UNIVERSITY OF CALIFORNIA, MERCED

High-Order Spherical Harmonics Methods for Radiative Heat Transfer and Applications in Combustion Simulations

by

Wenjun Ge

A dissertation submitted in partial satisfaction of the
requirements for the degree of
Doctor of Philosophy

in

Mechanical Engineering

Committee in charge:
Professor Michael F. Modest, Chair
Professor Gerardo C. Diaz
Professor Yanbao Ma
Professor Francois Blanchette

Spring 2017

The dissertation of Wenjun Ge is approved:

Michael F. Modest, Chair — Date

Gerardo C. Diaz — Date

Yanbao Ma — Date

Francois Blanchette — Date

University of California, Merced

*To my grandma Xiufang Ji (*01/07/1928 – 02/10/2017*),*

my mother Diying Xu

and my fiancée Lixia Jin

Acknowledgments

At the end of this thesis, I feel so indebted to all the people that helped and supported me accomplishing this research. First of all, I want to thank my supervisor, Prof. Michael F. Modest for his support and encouragement for my Ph.D. research. His enthusiasm in research has motivated me to work in earnest and persevere steadily when facing difficulties and disappointments. I am also grateful to my committee members, Prof. Gerardo C. Diaz, Prof. Yanbao Ma and Prof. Francois Blanchette not solely for their precious advice on my research and this thesis, but also for being role models for me.

I would also like to thank all the current and former group members, Dr. Tao Ren, Dr. Somesh P. Roy, Dr. Ricardo Marquez, Dr. Jian Cai, Dr. Pingyang Wang and Dr. Chaojun Wang. They are amazingly skillful and kind people to work with. Also, it has been a great privilege for me to have joined the TRI meetings together with Prof. Daniel C. Haworth and his group from the Pennsylvania State University for the past four years.

I also want to thank Prof. Sandip Mazumder from Ohio State University, Prof. Keisuke Kobayashi from Kyoto University and Prof. Edward Larsen from University of Michigan for their advice on the spherical harmonics methods.

I would also like to thank my friends, Alfred Fredette and his wife Tina, Dr. Zifan Wang and his wife Shurong, Dr. Lin Domizio and her husband Tony, Dr. Lun Jiang, Andrés Muñoz and his wife Eva, Kai Xiang Oh, Bennett Widyolar, Loan Nguyen, the Medefind family, the Winston family, Monika Modest, Dr. Mark Kerfoot, Dr. Dan Hu, Xiuming Shang, Donglei Yang, and many others whom I meet in Merced.

Financial support from Department of Energy and National Science Foundation through Grant No. NSF1258635 is greatly appreciated.

Last but not least, I would like to thank my family, especially my grandma Xiufang, my mother Diying, my father Lun, my fiancée, Lixia and my cousins Wei and Lois. Their unconditional love is the main source of happiness of my life.

Contents

List of Figures

List of Tables

Nomenclature

Roman symbols

$\mathbf{A}$	block-coupled matrix
a	nongray stretch function
d	distance; diameter; Wigner coefficients
G	incident radiation, W m^{-2}
g	fraction of the explicit term for the FVM implementation of Marshak's BC
H	hemispherical irradiation, W m^{-2}
I	radiative intensity, W m^{-2} sr
I_n^m	position dependent radiative intensity coefficient
I_b	blackbody radiative intensity, W m^{-2} sr
I_w	radiative intensity at wall, W m^{-2} sr
i	index of the boundary condition
k	turbulent kinetic energy, J/kg; absorption coefficient variable, m^{-1}
$\mathbf{I}$	vector containing I_n^m
$\mathcal{L}$	differential operator
$\hat{\mathbf{n}}$	unit surface normal vector
N	order of the spherical harmonics method
N_2	number of governing equations
N_3	number of computational cells
P_n^m	associated Legendre polynomial
p	pressure, Pa
$\mathbf{p}$	coefficient vector for I_w
$\mathbf{q}$	radiative heat flux, W m^{-2}
$\nabla \cdot \mathbf{q}$	negative radiative heat source, W m^{-3}

$\mathbf{q}_{(n,m)}$	row vectors of the coefficient matrices
$\mathbf{Q}$	coefficient matrices
$\dot{Q}_C$	heat release from combustion, W
$\dot{Q}_{emi}$	total emission, W
$\dot{Q}_{rad}$	net radiative heat loss, W
r	radius, m
$\mathbf{R}$	rotation matrix; coefficient matrix
$\mathbf{S}$	surface area vector
S_{rad}	radiative heat source, W m^{-3}
S_{emi}	emission, W m^{-3}
S_{abs}	absorption, W m^{-3}
T	temperature, K
u	velocity, m/s
$\hat{\mathbf{s}}$	unit direction vector
$\hat{\mathbf{t}}$	unit surface tangential vector
V	volume of the computational cell
w	face weighting factor, weight of a quadrature point
x	mole fraction of gases
Y_n^m	spherical harmonics
Y	mass fraction

Greek symbols

α	Euler rotation angle; time-blending factor
β	extinction coefficient, m^{-1}; Euler rotation angle
γ	Euler rotation angle;
δ_{ij}	Kronecker delta function

$\Delta^n_{mm'}$	rotation function
ϵ	surface emittance;Turbulence dissipation rate, J (kg s)$^{-1}$
θ	polar angle
ψ	azimuthal angle
κ	absorption coefficient, m^{-1}
ρ	density, m^{-3}; reflectivity
τ	optical coordinate, optical thickness
$\mathbf{\Phi}_i$	field of intensity coefficients I^m_n
Φ	scattering phase function
ϕ	the azimuthal angle of a position with respect to x-axis; symbol for I^m_n
χ	radiant fraction
ω	scattering albedo
Ω	solid angle

Superscripts and subscripts

a	number of discrete ordinates in azimuthal angle
C,F	center of a computational cell, center of a neighboring cell
f,b	face of an internal cell, face of a boundary cell
g	quadrature point for cumulative k distribution
d,s	diffuse, specular
i, j	indices for coefficient matrices and vectors
P	Planck-mean absorption coefficient
p	number of discrete ordinates in polar angle
x, y, z	global coordinates
$\bar{x}$, $\bar{y}$, $\bar{z}$	local coordinates
η	wavenumber

Acronyms

ADA	Advanced Differential Approximation
CFD	Computational Fluid Dynamics
CPU	Central Processing Unit
DOM	Discrete Ordinates Method
FDM	Finite Difference Method
FSK	Full-Spectrum k-Distribution
FVM	Finite Volume Method
LBL	Line-By-Line
MDA	Modified Differential Approximation
ODE	Ordinary Differential Equation
PaSR	Partially Stirred Reactor
PDE	Partial Differential Equation
PDF	Probability Density Function
TCI	Turbulence Chemistry Interaction
TRI	Turbulence Radiation Interaction
PMC	Photon Monte Carlo
RTE	Radiative Transfer Equation

Abstract

The study of radiative transfer within participating gaseous and particulate media has become increasingly important in the prediction of the combustion process of hydrocarbons for various scientific and industrial applications. The radiative transfer equation (RTE) is an integro-differential equation in five independent variables describing the physical process of radiative transfer. The angular dependency of the RTE makes it exceedingly difficult to solve by deterministic methods. Several approximate deterministic methods for the RTE have been developed over time. Two most promising candidates, the discrete ordinates method (DOM) and the spherical harmonics (P_N) method, are often used to solve the RTE even though both of them have their limitations. The DOM discretizes the entire solid angle by a finite number of ordinate directions and integrals over direction are replaced by numerical quadrature. DOM is relatively simple to implement but suffers from ray effects and false scattering and requires an iterative solution for scattering media or reflecting surfaces. On the other hand, the spherical harmonics P_N method is a spectral method that solves the RTE by approximating the angular distribution of the intensity by a truncated series of spherical harmonics. Despite the popularity of the lowest order of the P_N method, i.e., the P_1 method, the potential of high-order P_N methods has never been fully explored. This is partly due to cumbersome mathematics, and to lack of research in this area compared with the effort and progress made in its most popular counterpart, the DOM. Increasing of the order of P_N is expected to overcome the difficulty of optically thin and optically intermediate conditions or domains with optically thin and optically intermediate regions, which is the motivation for this research. The Photon Monte Carlo (PMC) method is so far the most accurate method; unlike the DOM/FVM and P_N methods, the stochastic PMC method gives an exact solution to the RTE. However, the PMC method can be computationally expensive since a large number of rays must be traced, which prevents it from wider applications in evaluating radiative transfer within combustion simulations.

This study focuses on a recently-developed general P_N formulation consisting of $N(N+1)/2$ second-order elliptic PDEs and their Marshak's boundary conditions for arbitrary 3-D geometries. The number of equations and unknowns can be further reduced to $(N+1)^2/4$ for two-dimensional geometries by taking advantage of the geometric characteristics of spherical harmonics. Special boundary conditions, including symmetry/specular reflection boundaries, walls with specified radiative flux, cyclic boundaries and mixed diffuse-specular surfaces have also been developed for high-order P_N methods. The high-order P_N methods (up to the order of 7) have been implemented within the finite volume-based `OpenFOAM`® open-source libraries. The performance of high-order P_N methods is demonstrated by solving a number of examples covering a wide range of different geometries and varying radiative properties including coupled simulations of a turbulent jet flame and a frozen snapshot study of a high-temperature oxy-natural gas burner. The goal of these examples is to test the performances of the high-order P_N methods with respect to all kinds of factors, e.g., order of P_N, overall optical thickness, geometry, homogeneity of radiative properties, etc., as well as to verify the finite volume implementations of the high-order P_N method on `OpenFOAM`®.

Chapter 1

Introduction

1.1 Background

The combustion of fossil fuels is the primary source of energy for society, the source of thrust for propulsion systems and at the same time the major cause of pollution. Understanding of the combustion process is essential to improve fossil energy utilization and reduce the pollutant emissions. Due to the complexity of combustion process, the design of combustion chambers used to be largely based on rules summarized from limited experimental data under limited thermodynamic conditions. Nowadays, successful design of the next generation of high-efficiency low-emission combustors, e.g., industrial burners, gas turbine combustors, internal combustion engines, pulverized coal combustors, etc., relies more and more on the capability of modeling the combustion process. Analysis based on effective modeling of the combustion process is much more efficient and insightful for carrying out parametric research and design optimizations, which can significantly reduce frequencies of costly experimental studies and prototype buildings [1]. Enormous computers equipped with Computational Fluid Dynamics (CFD) software are assisting scientists and engineers to simulate, diagnose, optimize and even control the combustion processes to meet the energy and environmental challenges of this century. Behind these powerful CFD tools, com-

prehensive modeling of combustion is still a developing research frontier with lots of unknowns and unsolved problems. Combustion is a process that involves interactions between fluid dynamics, chemical reactions and heat transfer in different temporal and spatial scales. Significant progress has been made over time [2–6], but the submodels, i.e., turbulent flow, chemical kinetics, thermal radiation, multi-phase flow and their interactions (e.g., turbulence-chemistry interaction: TCI and turbulence-radiation interaction: TRI, etc.), are still among the most challenging fundamental and practical problems of computational science and engineering.

Figure 1.1 is a general schematic illustrating the physical and chemical processes involved in the combustion inside of an industrial diesel engine chamber to show the complexity of combustion modeling in real applications. The fuel spray is injected from the nozzles at the center with high velocities and then evaporates and mixes with the high-pressure air while the piston is compressing the mixture. After ignition, the flow conditions turn highly turbulent, which can be observed visually, and at the same time hundreds of chemical reactions are taking place involving hundreds of species. The heat of combustion is transfered to the gases, soot and cylinder walls through both radiation and convection, and all these processes take place in a very short time scale.

To capture the complex characteristics of such flames and the generation of pollutants, such as NO_x and soot, which are very sensitive to the temperature fields, the simulation must be able to include physical and chemical processes as accurate as possible. On the other hand, due to constraints of computational power, different levels of simplifications of the corresponding physical and chemical models are necessary for most industrial applications. The selection of the approximate sub-models is critical to the validity of the overall simulation results, thus careful scrutiny is required before leaving out important physical processes or applying over-simplified approximations without knowing their effects.

The radiation emitted from the combustion products is proportional to differences in the fourth power of temperature, which indicates the importance of it in high-temperature applications. There are two major sources of radiation in hydrocarbon flames: (1) from the participating product

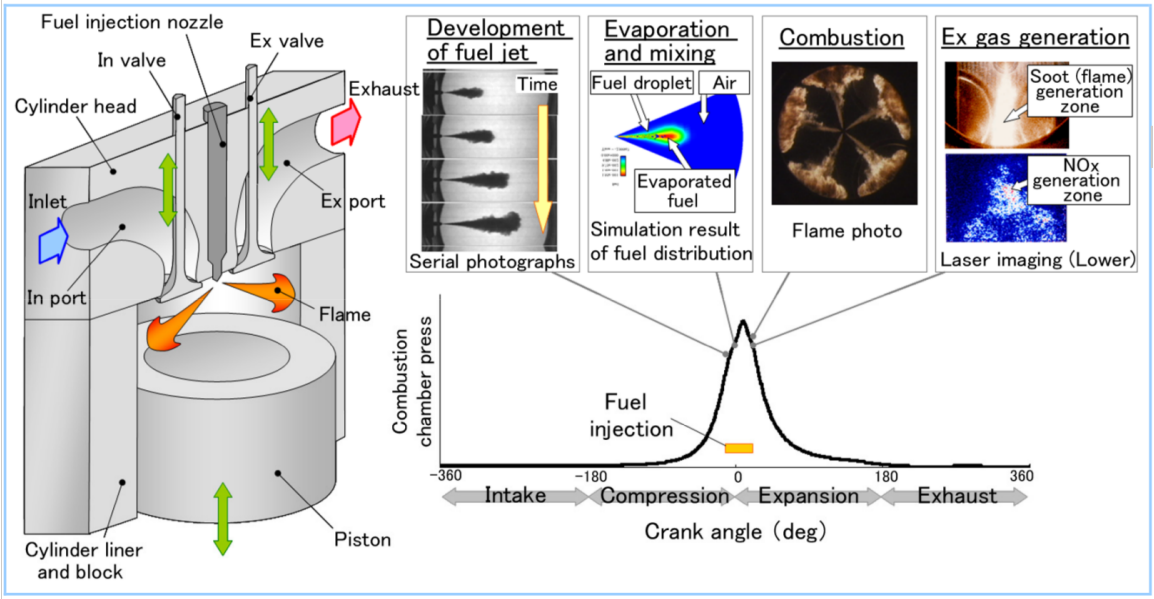

Figure 1.1: Combustion processes in an industrial diesel engine chamber [7].

gases; and (2) from in-flame soot and solid/liquid fuels. The combustion of hydrocarbons produces significant amounts of heat and radiating products such as CO_2, H_2O and soot. The gaseous products of a hydrocarbon flame mostly radiate and absorb across certain bands in the infrared spectrum, while soot if present usually dominates over gas radiation. However, radiative heat transfer, its interactions with turbulence, chemistry and soot formulation had been ignored or treated too simply for a long time in spite of the fact that it is the dominant mode of heat transfer for most combustors at industrial scales [6, 8–10]. This is partly due to the relatively small scale of laboratory flames so that scalars predicted from simple radiative models are sometimes close enough to the experimental measurements. Simplistic treatment of radiation is also a consequence of the fact that adding more realistic radiation models on top of the simulation of flames, which usually are extremely time-consuming already, is rarely practical. Therefore, simpler approximate models, such as optically thin or gray models, are common practice in most combustion simulations [11, 12].

A widely used indicator to quantify the importance of radiation for a flame that reaches steady-state is the radiant fraction χ_R [13] which is the ratio of net radiative heat loss Q_{rad} and

the heat of combustion released from chemical reactions $\dot{m}_F \Delta h_C$. It is usually determined from experimental data and can be very convenient once tabulated or fitted into correlations for different fuels, sizes of combustors and flow conditions. For example, Turns and Myher [14] relate the radiant fraction to a global residence time, which is the function of flame characteristics (flame density, flame volume, mass fraction of the fuel and inlet velocity etc.) for different fuels, flow conditions and burner sizes, and found that the correlation is capable of predicting the overall release of NO_x when scaling flames. But its analysis and other similar empirical studies [14–20] are based on the optically thin and gray approximations, which consequently affect the applicability of these correlations to other conditions. Theoretically, a small radiant fraction of a high temperature flame alone can either mean little emission or a large fraction of self-absorption and, therefore, the radiant fraction cannot be directly used to determine whether high-level radiation simulation is required.

The gray model uses a single mean absorption coefficient, usually the Planck-mean absorption coefficient κ_P, for radiation calculations, where κ_P is calculated by weighing the spectral absorption coefficient κ_η with the Planck function [21], which conserves total emission. The optically thin approximation, which neglects self-absorption, is valid when the optical thickness (τ_P), again evaluated in terms of κ_P, is very small ($\tau_P \ll 1$) [21]. The concept of optical thickness is just a rough estimation of the level of self-absorption and there is no clear border-line between optically thin and optically thick conditions. It is common to have totally different radiation regimes where the highly emitting-absorbing-scattering region at the center of a flame is surrounded by regions with almost no radiation in a real combustion chamber. The optically thin and gray models can be good tools to estimate the range of difference that adding radiation models could bring to the specific combustion problem, especially when the combustion simulation is still at the preliminary stage. But they tend to lead to substantial errors if the participating media are optically thick or nongray, as has been shown by both numerical and experimental studies [22–30]. A gray model is never appropriate unless the volume fraction of the in-flame soot exceeds about 0.1 ppm [31]. It has been shown in a methane flame that neglecting radiation in combustion systems under atmospheric pressure may

lead to over-prediction of temperature of up to 200°C, while employing optically thin or gray models can lead to under-prediction of temperatures about 100°C [32–34]. Keramida et al. [29] studied the effect of radiation of a typical industrial natural gas-fired furnace. The results have shown that accounting for radiation and applying the gray gas model in the combustion simulation significantly reduced the mean temperature in the furnace which gave a better agreement towards experimental data and the combustion gases leave the furnace with about 60% lower temperature than that of the model without radiation. Stefanidis et al. [30] simulated an industrial steam cracker (length: 12 m, width: 3 m and height: 8 m) with gray and nongray radiation models. As illustrated in Fig. 1.2, the temperature distributions calculated from gray and nongray models are significantly different, where the temperature differences at certain areas of the furnace exceed 150 K. Radiation also significantly affects the propagation speed and extinction characteristics of laminar premixed flames [35, 36]. The laminar burning velocity was increased up to 150% when large amounts of nongray gases, i.e, CO_2 and H_2O, are present [36] . Also, the nongray effects of participating gases have been carefully measured in laboratory-scale nonluminous turbulent methane jet flames. The comparative study showed that optically thin assumption may over-predict the radiative heat loss by more than a factor of two [37].

Most industrial flames are turbulent, thus the interactions between radiation and turbulence, or turbulence–radiation interaction (TRI), also plays an important role in real combustion processes. The nonlinear interaction can significantly change the global and local flame characteristics. Turbulence influences radiation through fluctuations in temperature T, pressure p and species concentrations X, and therefore affect both the emission and absorption through the Planck function (a function of temperature) and spectral absorption coefficients (determined by temperature, pressure and gas composition). Experiments on laboratory-scale flames [38–40] have shown that radiative emission can be as much as 50% to 300% higher than that expected based on mean values of temperatures and absorption coefficients. Modeling of nonluminous flames [33, 41, 42] also predicted a 30% to 50% increase in radiative emission and reduction in peak temperature of about 100 K when

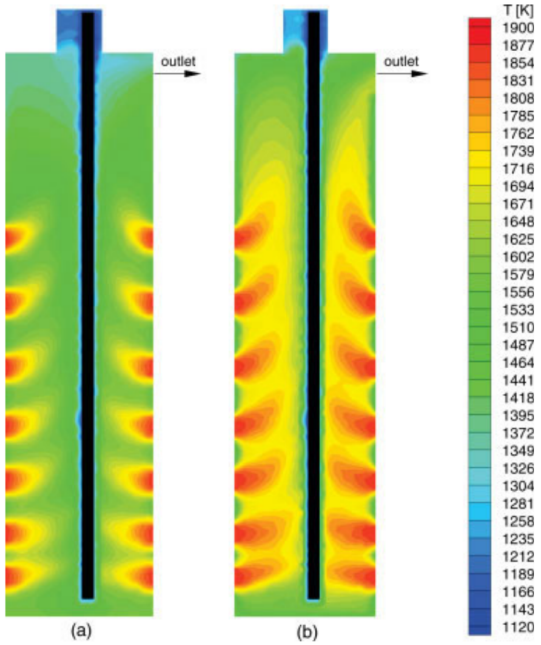

Figure 1.2: Temperature contour plots in a vertical cross section in the middle of the simulation of an industrial furnace [30]; (a) Gray radiation model; (b) Nongray radiation model.

comparing simulations with and without TRI. Mehta et al. [31] investigated TRI in luminous turbulent jet flames and the results show that TRI increased the emission from the flames by 30–60% and the net heat loss from the flame increased by 45–90%. Different models and implementations to treat TRI have been reviewed in [43]. And the systematic isolation study by Mehta et al. [31] showed that emission TRI is more important than absorption TRI and the latter can be safely ignored for laboratory-scale flames.

More uncertainty is involved, if particulate media in combustion, such as soot, coal and fly-ash particles, fuel sprays, etc., are also present. Soot is the product resulting from incomplete combustion of hydrocarbons in fuel-rich parts of flames. Experiments have shown that soot emission in most cases is much stronger than gas emission. Although the radiative properties of soot materials are also functions of wavelength [44], usually the gray approximation for soot is fairly good for most combustion conditions. Adams and Smith [45] showed that the radiation contributions of the soot particles are of the same order of magnitude as that of the gases, while self-absorption by the soot

is lower than that of gases for a turbulent methane flame. Wang et al. [46] studied the interactions between soot formulation and radiation in an oxygen-enriched turbulent propane flame. The results show that soot radiation lowered the average flame temperature, especially in the flame-tip region. Metha et al. [31] studied the radiation effects of soot in six turbulent jet flames and found that soot emission can contribute as much as 70% to the total emission from the flames and more than 90% of the soot emission escaped the domain, which is due to the much narrower absorption band of gases than that of soot.

Radiation in pulverized coal combustions is the principal mode of heat transfer and critical to furnace efficiency. It also plays an important role in the preheating of the coal particles and their ignition [47]. Compared with soot, coal and fly-ash particles are spread throughout the combustion chamber and scattering of coal cannot be ignored. Recent experimental and numerical studies of a 100 kW burner of pulverized coal under oxy-fuel conditions from the research groups of Chalmers and DTU [48] showed that modeling results, which applied the Lorenz–Mie theory for coal particles, are in accordance with experiment results, and the gray approximation is reasonable for both coal and fly-ash, which is consistent with the study of Clements [49] of a scaled 250 kW burner, but is contrary to the conclusions of Edge et al. [50] drawn from the simulation of a 0.5 MW scale burner. Significant progress on the modeling side has been made by Modest's group at University of California, Merced. Cai et al. [51–53] and Marquez et al. [54] have developed relevant multi-phase models, energy splitting schemes and nongray treatment of the radiative properties of coals for different applications, and they obtained promising results when comparing with experimental measurements and references.

The radiative effects of hydrocarbon fuel sprays in practical combustion systems have been rarely studied even though the flame dynamics are very sensitive to spray evolution [55]. The burning rate of fuel sprays is determined by the heat gain from the flame and hot walls via convection and radiation and the heat loss by evaporation, which is an important parameter for combustion analysis [13]. Tseng and Viskanta [56] examined the effects of radiation on the evaporation of single

isolated *n*-heptane droplets with different diameters and surrounding temperatures and found that radiation contributes as much as 15% of the convective heating with the surrounding temperature at 1000 K for the *n*-heptane droplets with a diameter of 100 μm. The radiation contribution was found to be in equal convection scale for the larger *n*-heptane droplets (1000 μm). The size of the fuel droplets in real applications, such as diesel engines, tends to be smaller (1–100 μm), which may have lesser radiation effects. Pioneering numerical simulations [57, 58] of diesel engines have shown limited radiation effects on spray evaporation, overall flow fields and ignition. However, a rough theoretical estimation of Roy et al. [57] predicts that radiative and convective heat transfer may be comparable under some conditions, which will require more experimental and modeling studies.

1.2 The Radiative Transfer Equation

Radiative heat transfer in an absorbing, emitting and scattering medium can be formulated by considering conservation of radiative energy, known as the radiative transfer equation (RTE), which is an integro-differential equation with spatial and directional dependency [21]:

$$\hat{\mathbf{s}} \cdot \nabla_\tau I_\eta + I_\eta = (1 - \omega_\eta) I_{b\eta} + \frac{\omega_\eta}{4\pi} \int_{4\pi} I_\eta(\hat{\mathbf{s}}') \Phi_\eta(\hat{\mathbf{s}} \cdot \hat{\mathbf{s}}') d\Omega' \tag{1.1}$$

where $I_\eta(\boldsymbol{\tau}, \hat{\mathbf{s}})$ is the spectral radiative intensity, which is defined as the spectral radiative energy flow per unit solid angle and unit area normal to the photon rays. $\boldsymbol{\tau} = \int \beta_\eta \mathrm{d}\mathbf{r}$ is an optical coordinate and β_η is the spectral extinction coefficient, which is the sum of spectral absorption coefficients κ_η and scattering coefficients $\sigma_{s\eta}$; $I_{b\eta}$ is the blackbody intensity or Planck function; $\omega_\eta = \sigma_{s\eta}/\beta_\eta$ is the spectral scattering albedo; and $\Phi_\eta(\hat{\mathbf{s}} \cdot \hat{\mathbf{s}}')$ is the scattering phase function. The RTE mathematically describes augmentation and extinction of spectral intensity along a path in the direction of $\hat{\mathbf{s}}$.

The net energy balance at any location in the medium is obtained by integrating the spectral intensity over all directions and all wavenumbers. The net radiative heat source S_{rad}, is the

difference between local absorption S_{abs} and emission S_{emi}:

$$S_{rad} = -\nabla \cdot \mathbf{q}_{rad} = -(S_{emi} - S_{abs}) = -4\kappa_P \sigma T^4 + \int_0^\infty \kappa_\eta G_\eta d\eta, \qquad G_\eta = \int_{4\pi} I_\eta(\boldsymbol{\tau}, \hat{\mathbf{s}}) d\Omega \tag{1.2}$$

where the spectral incident radiation G_η is defined as the directional integral of spectral radiative intensity. The radiative heat flux crossing any surface, with surface normal vector $\hat{\mathbf{n}}$, is evaluated by

$$\mathbf{q}_{rad} \cdot \hat{\mathbf{n}} = \int_0^\infty \mathbf{q}_{rad,\eta} \cdot \hat{\mathbf{n}} d\eta = \int_0^\infty \int_{4\pi} I_\eta(\boldsymbol{\tau}, \hat{\mathbf{s}}) \hat{\mathbf{n}} \cdot \hat{\mathbf{s}} d\Omega d\eta \tag{1.3}$$

Solution methods for the RTE can be divided into two categories: deterministic methods and the stochastic methods. A deterministic solution of the RTE usually requires further approximation of the angular dependency, since analytical solutions of the RTE by direct integration with respect to location and solid angle are rarely practical except for a small number of problems [21].

1.2.1 Photon Monte Carlo Method

In stochastic methods, or Photon Monte Carlo (PMC) methods, physically meaningful photons are statistically traced from their points of emission to their points of absorption. With enough photon bundles being traced, the resulting radiative distribution in the solution domain is statistically determined. The Monte Carlo method was first applied to radiative heat transfer problems by Howell and Perlmutter [59–61]. Modest and Poon [62] and Modest [63] improved the basic ray-tracing scheme by applying the concept of energy partitioning to alleviate efficiency problems for optically thin and optically thick media or when the walls are highly reflective. The PMC has been successfully applied to radiative transfer in participating media [34, 64–67] and stochastic media generated by probability density function (PDF) methods [68, 69]. Recently, it was extended to flames with Lagrangian coal particles [54] and fuel sprays [57]. The PMC provides an exact solution if sufficient photon bundles are traced, and its solution is commonly used to verify other approximate methods.

An advantage of the PMC method is its ability to accommodate arbitrary multidimensional geometries and spectral variations. PMC codes used to be very time-consuming, but with the recent development of computer parallelizations and graphic processing units (GPU) , it can be reasonably fast if photons and computational domains are assigned properly among processors [70, 71]. The only drawback is the inherent statistical errors which might be incompatible with other deterministic sub-models when they are strongly coupled [72].

1.2.2 Approximate Methods

Several approximate deterministic methods for the five-dimensional RTE, Eq (1.1), have been developed over time, such as spherical harmonics (P_N) methods, the zonal method, the discrete transfer method and discrete ordinates method (DOM or S_N). The zonal method is a semi-analytical method developed by Hottel and Cohen [73], which is able to give accurate results but is limited to simple geometries, and large computational resources are required to invert a full matrix of exchange factors. The discrete transfer method [74–76] is very similar to DOM but also incorporates some features from PMC, which tends to combine the disadvantages of both methods [21]. The most widely used approximate methods today are the discrete ordinates method or its finite volume version [1] [77–81] and the lowest-order spherical harmonics (P_1) method [21]. The DOM discretizes the entire solid angle by a finite number of ordinate directions and integrals over direction are replaced by numerical quadrature. DOM is relatively simple to implement and thus is widely regarded as a standard solver for radiative heat transfer in modern CFD software packages [82–84]. Preliminary comparisons of P_3 and S_4 results have shown the superiority of DOM for non-scattering media [85]. But an iterative solution is required for scattering media or reflecting surfaces, and computational cost is high for optically thick media. The method also suffers from ray effects and false scattering due to the angular discretization [86–88]. Despite the popularity of the lowest order of the P_N method, i.e., the P_1 method, the potential of high-order P_N methods has

[1] To not be confused with the finite volume numerical method which shares the same name, the alias FVM is not used.

never been fully explored. This is partly due to the cumbersome mathematics, and also due to lack of research in this area compared with the effort and progress made in its most popular counterpart, the DOM. The P_N approximation is a spectral method that assumes the unknown radiative intensity I can be approximated by a truncated series of spherical harmonics that decouples the directional and spatial variations of the intensity field. It is potentially more accurate than DOM at comparable computational cost while preserving the rotational invariance [89] of the RTE. The lowest order of the P_N family, the P_1 approximation, has been extensively applied to radiative transfer problems. However, it loses accuracy when intensity is directionally very anisotropic [21], as is often the case in optically thin media. Increasing of the order of P_N is expected to overcome this difficulty.

Many modifications of the P_1 method have been proposed to improve the accuracy significantly, including the modified differential approximation (MDA) [90, 91] and the advanced differential approximation (ADA) [92]. The principle is to split the intensity into two components, i.e., a ballistic part and a diffusive part. The ballistic component is easily solved by direct integration, while the diffusive component is suitable to be solved by the P_1 method. However, their applications are limited to specific simple geometries where the numerical integration can be carried out easily. These modifications can also be applied to any order of P_N approximation as well whenever it improves the results for P_1.

1.2.3 High-Order Spherical Harmonics (P_N) Method

The spherical harmonics method, or (P_N) method, is perhaps the oldest way among the approximate methods to solve the transport equations. It was first formulated by astrophysicists to describe radiative transfer in stars [93, 94], and was then further studied and developed for neutron-transport theory [95–98]. Davidson [96] found that approximations of odd orders P_{2n-1} are more accurate than even ones of next highest order P_{2n}, so that only approximations of odd orders should be employed. One of the difficulties in the spherical harmonics method is the formulation of the boundary conditions. Mark [99, 100] and Marshak [101] developed two different approximations

of the boundary conditions of the P_N method for neutron transport problems. Gelbard [102] compared the results of an absorption-free Milne problem [103] applying the P_N methods with Mark's and Marshak's boundary conditions, and found that (1) Marshak's boundary condition provides better results; (2) though the accuracy improvement from P_3 approximation to that of P_1 is great, the P_N methods converge rather slowly with increase of N due to the vacuum condition at the boundary. Attempts to develop the boundary conditions through variational methods have been proposed by Pomraning and Clark [104, 105]. However, the variational approach is more involved and Davis [106] showed that actually with proper choice of the functional, the boundary conditions derived from variational principle are identical to that of the Marshak's. One modification of the P_N method, called double-P_N method, was proposed by Yvon [107], who noticed the difficulty of P_N method when a function of the directional cosine μ (cosine of the polar angle) has a discontinuity at interfaces or walls. The idea of the double-P_N method is to have two expansions, instead of one, of the function for each angular range of $\mu > 0$ and $\mu < 0$, which allows accounting for discontinuities of the angular distributions. Gelbard [108] compared the double-P_1 method with DOM methods of 12 ordinates (as reference) and solutions of P_1 and P_3 for a number of 1-D cases, the results showed that the double-P_1 method is more accurate than that of P_3. Schmidt and Gelbard [109] and Wang [110] further developed the double-P_N method for cylindrical and spherical geometries, and the double-P_1 method still outperformed the P_3 results. However, the double-P_N method is considerably more complicated even for a 1-D formulation and more approximations are required in the derivation, which prevented it from further developments.

Cheng [111, 112] applied the P_N methods to analyze radiative transfer in a 1-D compressible flow of a nonscattering radiating gray gas. Although the governing equations were obtained for arbitrary order of N, only the lowest order, P_1, is applied to the solution of the RTE. Arpaci and Gozum [113] applied the P_3 and P_5 methods to the Bénard problem (natural convection studies between horizontal parallel plates) and found that the results of P_3 and P_5 are increasingly more accurate than P_1, although the accuracy improvement of P_5 is unexpectedly small. Canosa and Pe-

nafiel [114] and Dave and Canosa [115] used the P_N method with the consideration of anisotropic scattering for atmospheric problems, which showed the potential of P_N methods to solve realistic scattering problems efficiently. Bayazitoglu and Higenyi [116] tested the P_3 method on 1-D problems in Cartesian, cylindrical and spherical coordinates. The P_3 solvers proved to give much better results than those of P_1 for all coordinates systems. Higenyi [117] extended the formulation of the P_N method to the order of P_5 and applied it to 1-D problems in cylindrical coordinates and found great improvements for the P_3 approximation over the P_1 approximation and less improvements for P_5. In addition, the P_N approximations in cylindrical and spherical coordinates were shown to be less accurate than in Cartesian coordinates. Tong and Swathi [118] reported the results from P_2 to P_{11} methods for a 1-D hollow sphere confining emitting-absorbing-scattering gases. The results of the examples without scattering were compared with other accurate methods. And examples with linear anisotropic scattering were compared to analytical solutions of lower-order P_N methods (P_1, P_2 and P_3) and numerical solutions of higher-order ones (P_7 and P_{11}). It was found that lower-order P_N solutions converge faster at the outer wall than near the inner wall and only when the optical thickness is close to 10 did the lower order solutions converge closer to higher-order solutions. Their conclusion was confirmed by the recent study of Ymeli and Kamdem [119], who applied the P_N methods, up to the order of P_{105}, to a similar 1-D hollow sphere with different optical thicknesses and aspect ratios.

The P_N methods have also been developed to solve multidimensional problems, which result in more coupled governing equations. Detailed derivations of the general 3-D formulation in Cartesian coordinates have been given by Davison [96] and by Cheng [111, 112]. The formulation in general coordinate systems has been given by Ou and Liou [120]. Another general three-dimensional derivation was given by Condiff [121] by expanding the intensity in terms of polyadic Legendre polynomials [122], whose arguments are tensors rather than scalars. However, the number of equations and unknowns as well as the mathematical complexity of the method increases rapidly with the order in multidimensional problems, so that the order of approximation has mostly been limited

to P_3 ([123–127] in radiative transfer and [128–132] in neutron transport). Fletcher [133–136] developed the first general computer program for arbitrary order of P_N in 2-D and 3-D geometries for neutron transport problems. The program was successfully applied to various classic neutron transport problems, but limited by the magnitude of the scattering cross section. Further studies based on Fletcher's implementation for more general neutron transport applications were conducted by Kobayashi [137,138], Inanc [139,140] and Khouaja et al. [141]. Brunner [142,143] and Eaton [144] applied the P_N method to time-dependent simulations of neutron transport processes, and Mark's boundary conditions are applied which can be implemented relatively easier within the framework of the Riemann solver. The development of higher-order P_N method for radiative heat transfer had been very limited, until recently. Modest and Yang [145, 146] and Modest [147] have developed, so far, the most general three-dimensional P_N formulation consisting of $N(N+1)/2$ second-order elliptic PDEs and their Marshak's boundary conditions for arbitrary 3-D geometries. The formulation is relatively easy to apply to arbitrary geometries, which is ready for implementation in modern software packages. The new formulation ignites a resurgence of research interests in high-order P_N methods [148–154] for solving radiative transfer problems.

Another currently popular concept is to apply filters [89, 155] to give different weights for different orders of spherical harmonics to avoid the oscillations of P_N method for problems with void regions next to a strongly emitting–absorbing region, which is popular in meteorology studies and summarized by Boyd [156]. The Filtered-P_N method has also been applied to determine the effect of radiation on the propagation of coal dust flames [157] and reasonable results were obtained. So far, it is still a developing research topic and careful tuning of filter parameters for different problems is required due to the lack of generality.

1.3 Radiative Properties

The spectral variation of the radiative properties adds another layer of difficulty to radiation simulations. The treatment of spectral variations of radiative properties determines how many times

and in what manner the RTE needs to be evaluated for realistic simulations of practical combustion systems. The overall accuracy of the radiation simulation cannot be expected to be better than the accuracy of the models employed to obtain the radiative properties of radiating gases, particles or sprays.

1.3.1 Radiative Properties of Participating Gases

The absorption coefficient of the gaseous products (CO_2, H_2O, CO etc.) from the combustion of hydrocarbons varies dramatically across the entire spectrum [21]. An example of the pressure-based absorption coefficients for the most important wavenumber range of these participating gases is shown in Fig. 1.3. The strong spectral variations of the absorption coefficient, which are non-linearly related to temperature and pressure, make them very difficult to deal with. The most accurate method is to solve the RTE with line-by-line (LBL) [158, 159] calculations based on absorption coefficients calculated from high-resolution databases, such as HITRAN, HITEMP and CDSD [160–162]. LBL calculations require roughly one million spectral solutions of the RTE, which is impractical for industrial applications. Therefore, mostly they are used as references to validate other spectral models.

Closer inspection of the spectral distribution of gaseous absorption coefficients reveals that the oscillatory absorption coefficient has the same value at many different wavenumbers. This fact can be taken advantage of by applying the concept of reordering the reoccurring absorption coefficients at different wavenumbers (k-distribution method) [164], which is much more efficient to store and compute. Several models have been developed over time, including the spectral-line-based weighted-sum-of-gray-gases (SLW) method [165], the absorption distribution function (ADF) method [166] and the full-spectrum k-distribution (FSK) method [167]. While the former two methods are approximate schemes, the FSK is an exact method for homogeneous media and the assumption of a correlated absorption coefficient is made for nonhomogeneous media (FSCK) [168]. The FSK can reduce the number of evaluations of the RTE from 1 million times to as low as eight

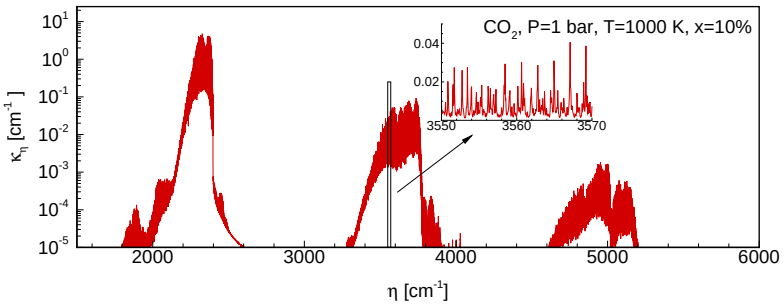

(a)

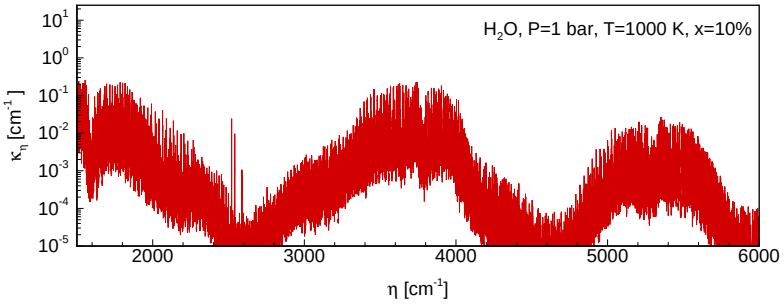

(b)

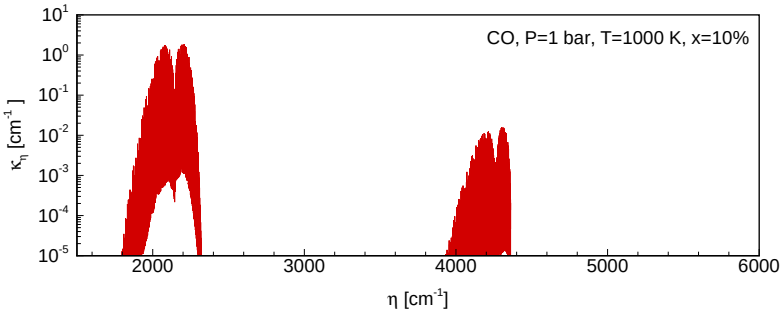

(c)

Figure 1.3: Spectral absorption coefficients for combustion gases: (a) CO_2 (b) H_2O and (c) CO [163].

times with high accuracy. Wang and Modest [169] and Cai and Modest [170] generated a narrow-band database for individual species, from which FSKs can be assembled with appropriate mixing models [171] on the fly. Such narrow-band database is very compact and seems ideal; however, the mixing calculations are still computationally prohibitive when large numbers of FSKs are calcu-

lated per time step [172]. Recent development of Wang et al. [173] solved this problem by tabulating precalculated k-distributions of gas mixtures into a full spectrum k-distribution (FSK) look-up table, which reduces computational cost significantly without sacrificing accuracy. Such table can be easily customized for different applications and specific thermodynamic ranges. Applications of FSK look-up tables for gas-soot mixtures can be found in [174] and further development based on quadrature transformation is described in [175].

1.3.2 Radiative Properties of Particulate Media

The absorption and scattering coefficients of particulate media depend on a variety of factors, including their temperatures, complex indices of refraction, diameters, shapes and spatial locations, etc.. Usually, radiative properties of particulate media are relatively more benign as compared to those of participating gases resulting in less error if approximated as gray. While absorption coefficients of gases can be precisely calculated from quantum mechanics, the radiative properties of particles and sprays more or less depend on semi-empirical correlations with more assumptions involved, such as assuming the shape of particles to be spherical and homogeneous.

The range of soot diameters tends to be between 5–80 nm and volume fractions (f_v) are between 10^{-8}–10^{-5} [176–179]. Soot particles are observed to have the same temperature as the gas phase [180] and are usually treated as a dilute continuum. Early experiments [181] have confirmed that scattering of soot may be neglected, as predicted by Rayleigh's theory for small particles, and it leads to an absorption coefficient of

$$\kappa_\lambda = C\frac{f_v}{\lambda^a} \tag{1.4}$$

where C and a (dispersion exponent) are empirical constants. The value of a directly reflects the spectral dependence of the complex index of refraction, ranging from 0.7 to 2.4 [182–185]. Earlier theories explained that the different values of dispersion exponent are due to particle sizes, because the fact that the values of dispersion exponent are different from different soot particles is incompatible with Rayleigh's theory. Later experiments [182–184] have shown that the differences are mainly

because of different complex indices of refraction. The complex index of refraction of soot is found to be mainly related to chemical composition and the porosity, while it is insensitive to temperature. The most widely accepted correlation is the polynomial fitting from Chang and Charalampopoulos [44] for propane soot. Studies [186, 187] also found agglomeration of soot may increase the sizes up to where Rayleigh's theory no longer holds. A brief introduction of special treatments of such soot is offered in [21].

Pulverized coal particles have sizes of 5–400 μm [47] and therefore the Lorenz–Mie theory [21] is usually applied to calculate absorption and scattering coefficients. Reviews of radiative properties of coal particles can be found in [8, 188, 189]. Buckius and Hwang [190] carried out a large number of calculations based on Lorenz–Mie theory and found that the absorption and scattering coefficients of coal particles are almost independent of the particle size distributions and types of coals but solely dependent on the mean particle diameter. Their conclusion was confirmed by the calculations of Foster and Howarth [191] and Viskanta et al. [192] with the exception of mid-sized particles. In most applications, the correlation parameters developed by Buckius and Hwang [190] are sufficient for the prediction of radiative properties of coals.

Compared to soot and coal, the radiative properties of liquid fuel sprays have not yet been systematically studied. The current status of research in this field has been summarized in the text book of Dombrovsky and Baillis [193]. In terms of practical applications, the absorption coefficient of Diesel sprays in an engine combustion environment has been evaluated by Roy et al. [57]. Three optical approximations, i.e., the normal incidence approximation [21], Dunkle's model [194] and a size-based correlation for semi-transparent droplets [195] are employed, while the complex indices of refraction are determined by the correlations of Dombrovsky et al. [196] , a LBL table by Dombrovsky and Baillis [193] and a gray model, respectively. The results show that the absorption coefficients of sprays from different spectral models are quite different, and further experimental investigations are required to draw any conclusion.

Coal particles and fuel sprays are sometimes treated as Lagrangian phases in combustion sim-

ulations [6, 197, 198]. Except for the PMC method of Wang et al. [68], which is able to treat discrete Lagrangian particles naturally [68], deterministic expressions of RTE all require the framework of a Eulerian coordinate system, where all radiative properties are treated in the sense of cell-averaged values, or bulk values. The bulk absorption and scattering coefficients from the dispersed phase can be calculated as the sum of the absorption and scattering coefficients of individual particles in that cell divided by the cell volume. Theoretically, such treatment is valid only when the volume fraction of the fuel spray is small, for which the assumption of independent scattering holds. Roy et al. [57] verified the validity of semi-Lagrangian calculations by comparing them with true Lagrangian formulations, and the results were almost identical while the true Lagrangian formulation takes considerably more CPU time. Similar semi-Lagrangian treatment for coal particles has been carried out in [51–53], which showed the potential of high-fidelity simulations of coal properties.

1.4 Reacting Flow Simulation

The starting point of reacting flow simulation is to solve the Navier-Stokes equations [6, 199, 200]. These equations describe how velocity, pressure, temperature and density of the fluid are related while supplemented by the equations of thermodynamic state and properties of the fluid. Submodels, such as turbulence, chemical reaction and radiation, also reside in the Navier-Stokes equations through additional terms and by changing fluid properties. Using Cartesian tensor notation, the set of conservation equations for turbulent reacting flows in the convertional RANS-based (Reynolds-Averaged Navier-Stokes) formulation can be presented as follows:

$$\frac{\partial\langle\rho\rangle}{\partial t}+\frac{\partial\langle\rho\rangle\tilde{u}_i}{\partial x_i}=0 \tag{1.5a}$$

$$\frac{\partial\langle\rho\rangle\tilde{u}_j}{\partial t}+\frac{\partial\langle\rho\rangle\tilde{u}_j\tilde{u}_i}{\partial x_i}=\frac{\partial(\langle\rho\rangle\tilde{u}_j\tilde{u}_i-\langle\rho\rangle\widetilde{u_ju_i})}{\partial x_i}+\frac{\partial\langle\tau_{ij}\rangle}{\partial x_i}-\frac{\partial\langle p\rangle}{\partial x_j}+\langle\rho\rangle g_j \quad (j=1,2,3) \tag{1.5b}$$

$$\frac{\partial\langle\rho\rangle\tilde{Y}_\alpha}{\partial t}+\frac{\partial\langle\rho\rangle\tilde{Y}_\alpha\tilde{u}_i}{\partial x_i}=\frac{\partial(\langle\rho\rangle\tilde{Y}_\alpha\tilde{u}_i-\langle\rho\rangle\widetilde{Y_\alpha u_i})}{\partial x_i}-\frac{\partial\langle J_i^\alpha\rangle}{\partial x_i}+\langle S_{\alpha,\mathrm{chem}}\rangle \quad (\alpha=1,2,...,N_S) \tag{1.5c}$$

$$\frac{\partial\langle\rho\rangle\tilde{h}}{\partial t}+\frac{\partial\langle\rho\rangle\tilde{h}\tilde{u}_i}{\partial x_i}=\frac{\partial(\langle\rho\rangle\tilde{h}\tilde{u}_i-\langle\rho\rangle\widetilde{hu_i})}{\partial x_i}-\frac{\partial\langle J_i^h\rangle}{\partial x_i}+\frac{D\langle p\rangle}{Dt}+\langle\tau_{ij}\frac{u_j}{x_i}\rangle+\langle S_{rad}\rangle \tag{1.5d}$$

where a Roman index denotes a component of coordinates and a Greek index denotes a chemical species; $\mathbf{u}$ is the velocity, $\mathbf{Y}$ is the mass fractions of the N_S chemical species, h is the specific enthalpy, ρ is the mixture mass density, p is the pressure, $\mathbf{g}$ is the body force per unit mass; $\boldsymbol{\tau}$, $\mathbf{J}^\alpha$ and $\mathbf{J}^h$ are the viscous stress tensor, the molecular flux of species and enthalpy, respectively. The angle brackets $\langle\rangle$ and the tilde $\sim$ operators denote the Reynolds averaging and Favre averaging, respectively. To fully define the physical system, the state equations, $p = p(\mathbf{Y}, T, \rho)$ and $T = T(\mathbf{Y}, h, p)$, are also required and sometimes in the form of databases.

The fourth equation, Eq. (1.5d), is regarded as the energy equation. The effect of radiation is represented by adding a radiative heat source term S_{rad} (ignoring the averaging operators since TRI is not the focus of this thesis), i.e., the negative divergence of radiative heat flux $-\nabla \cdot q_{rad}$, as a source term to the energy equation. In turn, the scalar fields ($\mathbf{Y}$, T and p) obtained from the Navier-Stokes equations are then used to determine the radiative properties, such as the blackbody radiative intensity I_b and absorption coefficient κ.

The chemical production rate for species α, $\langle S_{\alpha,\mathrm{chem}}\rangle$ in the species transport equation, Eq. (1.5c), is in principle a known function of local thermal properties ($\mathbf{Y}$, T and p). However, a detailed reaction mechanism sometimes involves a lot of species and reactions for hydrocarbon fuels, which is still not trivial even with advanced computational capacity. For instance, a very detailed methane reaction would involve 325 reactions and 53 species as given by GRI–Mech 3.0 [201] and a de-

tailed reaction mechanism for n-heptane would include 654 species and 5935 reactions [202]. Each reaction will give one first-order ODE and the size of the stoichiometric coefficient matrix of such chemistry kinematics would be the size of number of species times the number of reactions [13]. The source term $\langle \mathbf{S}_{\text{chem}} \rangle$ needs to be evaluated for each time step and therefore a very large and stiff system of ODEs are to be solved at each time step for every computational cell where there are reactions. Reduced mechanism is often employed to reduce the computational costs in practice. Another level of complexity is added to the combustion model by considering the turbulence-chemistry interaction (TCI), which is based on the reality that for turbulent flames $\langle \mathbf{S}_{\text{chem}}(\mathbf{Y}, T, p) \rangle \neq \mathbf{S}_{\text{chem}}(\langle \mathbf{Y} \rangle, \langle T \rangle, \langle p \rangle)$. That is because the closure problems from averaging the highly nonlinear chemical source terms. Different methods, such as Eddy Break-Up model (EBU) [203], laminar flamelet model [204], Partially Stired Reactor (PaSR) [205], Eddy-Dissipation Concept (EDC) [206] and Probability Density Function (PDF) [207], have been developed over time to address the TCI. Among these, the PDF approach is the most capable of reproducing the finite-rate chemistry effects and the occurrence of localized extinction and re-ignition for turbulent flames. The discussion of TCI can be found in the textbooks on combustion modeling [208, 209].

1.5 Objectives

This thesis focuses on the solutions of the radiative transfer equation (RTE) with high-order spherical harmonics (P_N) approximations for the angular dependency and finite volume method for the spatial discretization and their applications in modeling radiative heat transfer in realistic combustion simulations. The aim of this study is to develop and implement the high-order spherical harmonics P_N method up to P_7, which has never been comprehensively explored and applied to real multidimensional combustion conditions. Accurate evaluation of radiative transfer in real combustion processes involves full-spectrum calculations including both optically thin and optically thick regions. The high-order P_N methods are expected to improve the accuracy of the P_1 method under these conditions. The new elliptic P_N formulation of Modest and Yang [145, 146] and Modest [147]

will be implemented (up to P_7) within the finite volume-based OpenFOAM® open-source libraries. Since 2-D geometries are often encountered in practical combustion simulations, a 2-D Cartesian version and a 2-D axisymmetric version of the elliptic formulation will be reviewed and also implemented in OpenFOAM®, which can reduce the computational cost for special geometries. In addition, special boundary conditions, including symmetry/specular reflection boundaries, walls with specified radiative flux, cyclic boundaries and mixed diffuse-specular surfaces will be developed for arbitrary geometries by applying the geometrical properties of spherical harmonics. The high-order P_N methods will be demonstrated by solving a number of examples covering a wide range of different geometries and varying radiative properties including a 2-D axisymmetric turbulent jet flame and a 2-D axisymmetric high-temperature oxy-fuel flame. The solutions obtained are then to be compared with exact solutions and other standard methods.

1.6 Outline of the Chapters to Follow

Chapter 2 provides a review of the theory of the general elliptic formulation of high-order spherical harmonics (P_N) methods for arbitrary geometries. Chapter 3 starts with the review and documentation of the derivations of a 2-D Cartesian version and a 2-D axisymmetric version of the elliptic formulation of the high-order P_N methods and their Marshak's boundary conditions. Then, the development of special boundary conditions, including symmetry/specular reflection boundaries, walls with specified radiative flux, cyclic boundaries and mixed diffuse-specular surfaces will also be described. The implementation of these formulations in finite volume-based open-source OpenFOAM® is discussed in detail in Chapter 4. Chapter 5 shows the verification of the code and the performance of the high-order P_N methods for a wide range of conditions presenting the strengths and drawbacks of P_N methods, which is followed by applications to real combustion simulations in Chapter 6. Finally in Chapter 7, conclusions will be drawn and future work will be briefly proposed.

Chapter 2

Elliptic Formulation of the High-Order Spherical Harmonics (P_N) Method

Spherical harmonics P_N approximation is a spectral method that assumes distribution of the unknown radiative intensity I can be approximated by a finite series of spherical harmonics that decouples the directional and spatial dependencies of the intensity fields. The original RTE is converted into a system of coupled PDEs solving for the spatial-dependent coefficients of the spherical harmonics series. In this chapter, the development of the second-order elliptic formulation of arbitrary order of spherical harmonics P_N methods will be reviewed with the original developments found in [145–147]. Critical steps of the derivation of the second-order elliptic formulation will be discussed, and the resulting $N(N+1)/2$ governing equations and Marshak's boundary conditions will be presented. In order to show the derivations with clarity, only isotropic scattering is considered [1]. The spectral dependence of the intensity and the RTE is ignored for now since the extension to the nongray forms are straightforward.

[1] The inclusion of anisotropic scattering is presented in [145, 146], but it will not be discussed in this thesis.

2.1 Second-Order Elliptic Formulation

The spherical harmonics, or P_N, methods are based on expanding the radiative intensity field $I(\mathbf{r}, \hat{\mathbf{s}})$ into an orthogonal series of spherical harmonics $Y_n^m(\hat{\mathbf{s}})$, whereby the spatial and the directional dependencies are decoupled. While the full infinite series is an exact representation, a truncated series of order N is used in practice:

$$I(\boldsymbol{\tau}, \hat{\mathbf{s}}) = \sum_{n=0}^{N} \sum_{m=-n}^{n} I_n^m(\boldsymbol{\tau}) Y_n^m(\hat{\mathbf{s}}) \tag{2.1}$$

where $I_n^m(\boldsymbol{\tau})$ are the intensity coefficients and are functions of space only and $Y_n^m(\hat{\mathbf{s}})$ are the spherical harmonics, which are functions of direction only. A few low-order intensity coefficients have physical interpretations; I_0^0 has the physical meaning of the incident radiation per solid angle, while I_1^1, I_1^{-1}, and I_1^0 are components of the radiative heat flux; I_2^m are related to the radiation pressure after division by the speed of light. Intensity coefficients with higher orders ($n > 2$) do not have clear physical significance.

The most common closure for the P_N approximation is to truncate the series at a certain odd order of N as:

$$I_n^m(\boldsymbol{\tau}) = 0 \quad \text{for} \quad n > N \tag{2.2}$$

this truncation will preserve rotational invariance, which means different spherical harmonics series expanded from rotations of coordinates give identical results. The spherical harmonics $Y_n^m(\psi, \theta)$ satisfy Laplace's equation in spherical coordinates and their real forms are defined as [210],

$$Y_n^m(\psi, \theta) = \begin{cases} \cos(m\psi) P_n^m(\cos\theta) & \text{for} \quad m \geq 0 \\ \sin(|m|\psi) P_n^m(\cos\theta) & \text{for} \quad m < 0 \end{cases} \tag{2.3}$$

where θ and ψ are polar and azimuthal angles, respectively; $P_n^m(\cos\theta)$ are associated Legendre

polynomials [210], given by

$$P_n^m(\mu) = (-1)^m \frac{(1-\mu^2)^{|m|/2}}{2^n n!} \frac{d^{n+|m|}}{d\mu^{n+|m|}} (\mu^2 - 1)^n \tag{2.4}$$

where μ denotes $\cos\theta$. Some examples of associated Legendre polynomials are shown in Table. 2.1. The properties of associated Legendre polynomials can be found in handbooks of mathematics [211, 212], and one important property is its orthogonality. The associated Legendre polynomials are mutually orthogonal, i.e.,

Table 2.1: Table of associated Legendre polynomials

n	m=0	m=1	m=2	m=3
0	1	-	-	-
1	$\cos\theta$	$-\sin\theta$	-	-
2	$(3\cos^2\theta - 1)/2$	$-3\cos\theta\sin\theta$	$3\sin^2\theta$	-
3	$(5\cos^3\theta - 3\cos\theta)/2$	$-(15\cos^2\sin\theta - 3\sin\theta)/2$	$15\cos\theta\sin^2\theta$	$-15\sin^3\theta$

$$\int_{-1}^{1} P_n^m(\mu) P_{n'}^{m'}(\mu) d\mu = \delta_{mm'}\delta_{nn'} \frac{2(n+|m|)!}{(2n+1)(n-|m|)!} \tag{2.5}$$

which leads to the orthogonality of spherical harmonics:

$$\int_{4\pi} Y_n^m Y_{n'}^{m'} d\Omega = \delta_{mm'}\delta_{nn'} \frac{2\pi(n+|m|)!(1+\delta_{m,0})}{(n-|m|)!(2n+1)} \tag{2.6}$$

Another important property is its function parity: associated Legendre polynomials are even functions when $(m+n)$ are even and odd functions when $(m+n)$ are odd, which is critical for developing special boundary conditions.

Substituting Eq. (2.1) into the RTE, Eq. (1.1), and assuming the scattering is isotropic, we obtain:

$$\hat{\mathbf{s}} \cdot \nabla_{\boldsymbol{\tau}} \sum_{n=0}^{N} \sum_{m=-n}^{n} I_n^m(\boldsymbol{\tau}) Y_n^m(\hat{\mathbf{s}}) + \sum_{n=0}^{N} \sum_{m=-n}^{n} I_n^m(\boldsymbol{\tau}) Y_n^m(\hat{\mathbf{s}}) - \omega I_0^0(\boldsymbol{\tau}) = (1-\omega) I_b \tag{2.7}$$

To develop the governing equations with respect to the intensity coefficients I_n^m, Eq. (2.7) is multi-

plied by $Y_{n'}^{m'}$ and integrated over a solid angle of 4π. Exploiting the orthogonality of the spherical harmonics, Eq. (2.6), one obtains a system of $(N+1)^2$ first-order PDEs in the unknown intensity coefficients $I_n^m(\boldsymbol{\tau})$ with respect to spatial locations only. The number of governing equations can be further reduced by eliminating the odd order intensity coefficients (I_n^m with odd n) by their relation to the gradients of I_{n+1}^m and I_{n-1}^m [145], which transforms the governing equations of the P_N method from $(N+1)^2$ first-order PDEs into $N(N+1)/2$ second-order elliptic PDEs. The intensity coefficients I_n^m of the second-order elliptic formulation are listed in Table. 2.2.

Table 2.2: Intensity coefficients employed for 3-D Cartesian formulation

n	Intensity Coefficients												
0						I_0^0							
2					I_2^{-2}	I_2^{-1}	I_2^0	I_2^1	I_2^2				
4			I_4^{-4}	I_4^{-3}	I_4^{-2}	I_4^{-1}	I_4^0	I_4^1	I_4^2	I_4^3	I_4^4		
6	I_6^{-6}	I_6^{-5}	I_6^{-4}	I_6^{-3}	I_6^{-2}	I_6^{-1}	I_6^0	I_6^1	I_6^2	I_6^3	I_6^4	I_6^5	I_6^6
n	I_n^{-n}	$\cdots$	$\cdots$	I_n^{-3}	I_n^{-2}	I_n^{-1}	I_n^0	I_n^1	I_n^2	I_n^3	$\cdots$	$\cdots$	I_n^n

To solve the $N(N+1)/2$ elliptic PDEs, $N(N+1)/2$ boundary conditions are required. Physically, the incoming intensity should be specified at the boundary faces, i.e., the boundary condition is of the type:

$$I(\mathbf{r}_w, \hat{\mathbf{s}}) = I_w(\mathbf{r}_w, \hat{\mathbf{s}}), \quad \text{for} \quad \hat{\mathbf{n}} \cdot \hat{\mathbf{s}} > 0$$

where I_w is the radiative intensity at the boundary wall, which represents the sum of the intensities leaving the wall due to both emission and reflection; $\hat{\mathbf{n}}$ is the outward surface normal of the boundary faces. Since the radiative intensity I is truncated at the order of N, the boundary condition can no longer be satisfied exactly. Instead, the truncated I can either satisfy Eq. (2.8) along particular direction $\hat{\mathbf{s}}$ (Mark [99, 100]) or in an integral sense (Marshak [101]). Mark's boundary conditions are to assign the value of the zeros of the Legendre polynomial of order $N+1$, while Marshak's are based on the incoming half moments of the intensity. Davison [96] theoretically speculated

that for low-order P_N methods, Marshak's boundary conditions would give more accurate results while Mark's would be better for high-order P_N methods. However, Pellaud [213] and Schmidt and Gelbard [102, 109] proved that Marshak's boundary conditions gave superior results even for high-order P_N approximations. More recent studies of Brunner [142,143], Eaton [144] and McClarren [214] for transient problems employed Mark's boundary condition and get reasonable results, but no comparison was made between Mark's and Marshak's boundary conditions in their studies. The developments of Modest and Yang [145, 146] and Modest [147] followed Marshak's approximation and they extended the Marshak's boundary conditions for multidimensional problems.

The general Marshak's boundary conditions [101] are stated as:

$$\int_{\hat{\mathbf{n}}\cdot\hat{\mathbf{s}}>0} I\bar{Y}^m_{2i-1}(\hat{\mathbf{s}})d\Omega = \int_{\hat{\mathbf{n}}\cdot\hat{\mathbf{s}}>0} I_w\bar{Y}^m_{2i-1}(\hat{\mathbf{s}})d\Omega, \quad i = 1, 2, ..., \frac{1}{2}(N+1), \text{ all relevant } m \tag{2.8}$$

where the $\bar{Y}^m_{2i-1}(\hat{\mathbf{s}})$ are expressed in terms of local coordinates systems, in which $\hat{\mathbf{s}}$ is represented by the local polar angle $\bar{\theta}$ measured from the surface normal and the local azimuthal angle $\bar{\psi}$. One well-known difficulty of applying Marshak's boundary conditions is that it leads to more boundary conditions than the number of governing equations. Equation (2.8) gives $(N+1)(N+2)/2$ boundary conditions for all m within the range of $-i \leq m \leq +i$, while there are only $N(N+1)/2$ governing equations. Davison [96] suggests that for $i \leq (N-1)/2$, Eq. (2.8) be satisfied for all m while for $i = (N+1)/2$, as many m as possible from the smallest $|m|$. This is simply assuming the normal moments are more relevant than tangential ones in local coordinates at the boundary faces. Modest and Yang [145, 146] adopted this method with a modification, i.e., they chose all the even $|m|$ for $i = (N+1)/2$ instead of the smallest $|m|$ to avoid implementation difficulties. Modest [147] showed this to be the only consistent set of boundary conditions.

2.2 Governing Equations

The set of $N(N+1)/2$ second-order elliptic PDEs of the P_N method for isotropic scattering in 3-D Cartesian coordinates as given by [147] are:

For each $Y_n^m : n = 0, 2, \ldots, N-1,\ 0 \le m \le n$:

$$\begin{aligned}
&\sum_{k=1}^{3}\Bigg\{(\mathcal{L}_{xx}-\mathcal{L}_{yy})\left[(1+\delta_{m2})a_k^{nm}I_{n+4-2k}^{m-2}+\frac{\delta_{m1}}{2}c_k^{nm}I_{n+4-2k}^{m}+e_k^{nm}I_{n+4-2k}^{m+2}\right]\\
&\quad+(\mathcal{L}_{xz}+\mathcal{L}_{zx})\left[(1+\delta_{m1})b_k^{nm}I_{n+4-2k}^{m-1}+d_k^{nm}I_{n+4-2k}^{m+1}\right]\\
&\quad+(\mathcal{L}_{xy}+\mathcal{L}_{yx})\left[-(1-\delta_{m2})a_k^{nm}I_{n+4-2k}^{-(m-2)}+\frac{\delta_{m1}}{2}c_k^{nm}I_{n+4-2k}^{-m}+e_k^{nm}I_{n+4-2k}^{-(m+2)}\right]\\
&\quad+(\mathcal{L}_{yz}+\mathcal{L}_{zy})\left[-(1-\delta_{m1})b_k^{nm}I_{n+4-2k}^{-(m-1)}+d_k^{nm}I_{n+4-2k}^{-(m+1)}\right]\\
&\quad+(\mathcal{L}_{xx}+\mathcal{L}_{yy}-2\mathcal{L}_{zz})c_k^{nm}I_{n+4-2k}^{m}\Bigg\}\\
&\quad+\left[\mathcal{L}_{zz}-(1-\omega\delta_{0n})\right]I_n^m=-(1-\omega)I_b\delta_{0n}
\end{aligned}\tag{2.9a}$$

and for each $Y_n^{-m} : n = 2, \ldots, N-1,\ 1 \le m \le n$:

$$\begin{aligned}
&\sum_{k=1}^{3}\Bigg\{(\mathcal{L}_{xy}+\mathcal{L}_{yx})\left[(1+\delta_{m2})a_k^{nm}I_{n+4-2k}^{m-2}+\frac{\delta_{m1}}{2}c_k^{nm}I_{n+4-2k}^{m}-e_k^{nm}I_{n+4-2k}^{m+2}\right]\\
&\quad+(\mathcal{L}_{yz}+\mathcal{L}_{zy})\left[(1+\delta_{m1})b_k^{nm}I_{n+4-2k}^{m-1}-d_k^{nm}I_{n+4-2k}^{m+1}\right]\\
&\quad+(\mathcal{L}_{xx}-\mathcal{L}_{yy})\left[(1-\delta_{m2})a_k^{nm}I_{n+4-2k}^{-(m-2)}-\frac{\delta_{m1}}{2}c_k^{nm}I_{n+4-2k}^{-m}+e_k^{nm}I_{n+4-2k}^{-(m+2)}\right]\\
&\quad+(\mathcal{L}_{xz}+\mathcal{L}_{zx})\left[(1-\delta_{m1})b_k^{nm}I_{n+4-2k}^{-(m-1)}+d_k^{nm}I_{n+4-2k}^{-(m+1)}\right]\\
&\quad+(\mathcal{L}_{xx}+\mathcal{L}_{yy}-2\mathcal{L}_{zz})c_k^{nm}I_{n+4-2k}^{-m}\Bigg\}\\
&\quad+(\mathcal{L}_{zz}-1)\,I_n^{-m}=0
\end{aligned}\tag{2.9b}$$

where $a_k^{nm}, b_k^{nm}, c_k^{nm}, d_k^{nm}$, and e_k^{nm} are constant coefficients tabulated in Table 2.3, and δ_{ij} is the Kronecker delta function. The $\mathcal{L}$ operators are denoting the derivatives. For example,

$$\mathcal{L}_{xy} = \frac{1}{\beta}\frac{\partial}{\partial x}\left(\frac{1}{\beta}\frac{\partial}{\partial y}\right) \tag{2.10a}$$

$$\mathcal{L}_{zz} = \frac{1}{\beta}\frac{\partial}{\partial z}\left(\frac{1}{\beta}\frac{\partial}{\partial z}\right) \tag{2.10b}$$

Table 2.3: Elliptic P_N approximation coefficients [21]

	k=1	k=2	k=3
$a_k^{nm(a)}$	$\frac{1}{4(2n+5)(2n+3)}$	$-\frac{1}{2(2n+3)(2n-1)}$	$\frac{1}{4(2n-1)(2n-3)}$
$b_k^{nm(b)}$	$\frac{n+m+1}{2(2n+5)(2n+3)}$	$-\frac{2m-1}{2(2n+3)(2n-1)}$	$-\frac{n-m}{2(2n-1)(2n-3)}$
c_k^{nm}	$-\frac{\pi_2(n+m+1)}{4(2n+5)(2n+3)}$	$\frac{n^2+n-1+m^2}{(2n+3)(2n-1)}$	$-\frac{\pi_2(n-m-1)}{2(2n-1)(2n-3)}$
d_k^{nm}	$-\frac{\pi_3(n+m+1)}{2(2n+5)(2n+3)}$	$-\frac{(2m+1)(n+m+1)(n-m)}{2(2n+3)(2n-1)}$	$\frac{\pi_3(n-m-2)}{2(2n-1)(2n-3)}$
e_k^{nm}	$\frac{\pi_4(n+m+1)}{4(2n+5)(2n+3)}$	$-\frac{\pi_2(n+m+1)\pi_2(n-m-1)}{2(2n+3)(2n-1)}$	$\frac{\pi_4(n-m-3)}{4(2n-1)(2n-3)}$

$\pi_k(n) = \prod_{j=0}^{k-1}(n+j)$

[a] $a_k^{nm} = 0$ for $m \leq 1$;
[b] $b_k^{nm} = 0$ for $m = 0$.

2.3 Boundary Conditions

$N(N+1)/2$ boundary conditions are required and determined from the general Marshak's boundary condition, Eq. (2.8). Substitution of Eq. (2.1) in terms of local coordinates into Eq. (2.8)

leads to

$$(1+\delta_{m,0})\pi \sum_{n=0}^{N} p_{n,2i-1}^{m} \bar{I}_{n}^{m} = \int_{0}^{2\pi} \int_{0}^{1} I_w \bar{Y}_{2i-1}^{m} d\bar{\mu} d\bar{\psi} \tag{2.11}$$

with the relevant i and m pairs of

$$m = \begin{cases} -i, -i+1, \cdots, i & i = 1, 2, \cdots, (N-1)/2 \\ -N+1, -N+3, \cdots, N-1 & i = (N+1)/2 \end{cases} \tag{2.12}$$

where each i and m pair gives one individual boundary condition. As discussed in the previous section, for the largest value of i, only the even values of m are employed for a consistent set of $N(N+1)/2$ boundary conditions. The $p_{n,j}^{m}$ in Eq. (2.11) are the half-moments of associated Legendre polynomials, which are defined as

$$p_{n,j}^{m} = p_{j,n}^{m} = \int_{0}^{1} P_{n}^{m}(\bar{\mu}) P_{j}^{m}(\bar{\mu}) d\bar{\mu} \quad \text{and} \quad p_{n,j}^{m} = 0 \quad \text{if } n < |m| \text{ or } j < |m| \tag{2.13}$$

and tabulated in Table 2.4, which are calculated by the recursion formula [147]. Note that n and j are always positive and the sign of m does not affect the evaluation of $p_{n,j}^{m}$ since the evaluation of associated polynomial $P_{n}^{m}(\bar{\mu})$ is taking the absolute value of m, Eq. (2.4). Appendix A gives more details of the half-moments calculation and it follows that:

$$p_{n,j}^{m} = 0 \quad n + j \text{ even}, n \neq j \tag{2.14}$$

If I_w is diffuse, Eq. (2.11) simplifies to

$$\sum_{n=0}^{N} p_{n,2i-1}^{m} \bar{I}_{n}^{m} = \delta_{m,0} p_{0,2i-1}^{0} I_w \tag{2.15}$$

In order to obtain a generic boundary condition for arbitrary geometries, the spherical harmonics

Table 2.4: Half-moments of associated Legendre polynomials, $\times 10^{-m}$

m	$n \setminus j$	0	1	2	3	4	5	6	7
0	0	1.00000							
	1	0.50000	0.33333						
	2	0.00000	0.12500	0.20000					
	3	-0.12500	0.00000	0.12500	0.14286				
	4	0.00000	-0.02083	0.00000	0.07031	0.11111			
	5	0.06250	0.00000	-0.03906	0.00000	0.07031	0.09091		
	6	0.00000	0.00781	0.00000	-0.01562	0.00000	0.04883	0.07692	
	7	-0.03906	0.00000	0.02188	0.00000	-0.02279	0.00000	0.04883	0.06667
1	1		0.06667						
	2		0.07500	0.12000					
	3		0.00000	0.07500	0.17143				
	4		-0.04167	0.00000	0.14062	0.22222			
	5		0.00000	-0.02344	0.00000	0.14062	0.27273		
	6		0.03281	0.00000	-0.06562	0.00000	0.20508	0.32308	
	7		0.00000	0.01312	0.00000	-0.04557	0.00000	0.20508	0.37333
2	2			0.04800					
	3			0.07500	0.17143				
	4			0.00000	0.14062	0.40000			
	5			-0.06563	0.00000	0.39375	0.76364		
	6			0.00000	-0.06525	0.00000	0.57422	1.29231	
	7			0.07088	0.00000	-0.24609	0.00000	1.10742	2.0160
3	3				0.10286				
	4				0.19687	0.56000			
	5				0.0000	0.55125	1.83273		
	6				-0.23625	0.00000	2.06719	4.65231	
	7				0.0000	-0.34453	0.00000	3.98672	10.0800
4	4					0.44800			
	5					0.99225	3.29891		
	6					0.00000	3.72094	13.9569	
	7					-1.51594	0.00000	17.5416	44.3520
5	5						3.29891		
	6						8.18606	30.7052	
	7						0.00000	38.5914	159.667
6	6							36.8463	
	7							100.338	415.135
7	7								581.189

expressed in local coordinates must be rotated back to global coordinates. This is achieved by adopting Euler's rotation theorem [215] stating that any Cartesian coordinates with a common origin are

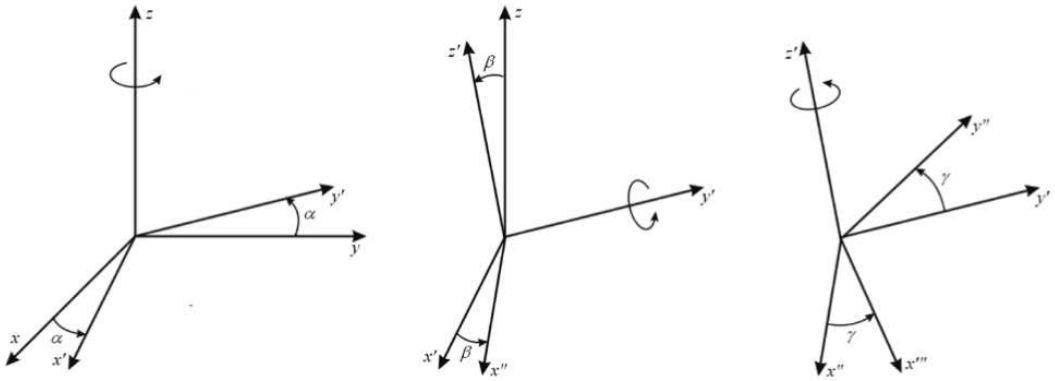

Figure 2.1: Definition of Euler angles for an arbitrary rotation.

related by rotations about fixed axes. Here three Euler angles (α, β, γ) are employed following Varshalovich's definition [216] [2], i.e., the first rotation of an angle α is about the global z-axis, the second is by an angle β about the y'-axis and the third is about the z'-axis by an angle of γ, as indicated in Fig. 2.1. The Euler angles can be obtained from the surface normal $\hat{\mathbf{n}}$ of the boundary faces in arbitrary geometries as

$$\begin{aligned} \alpha &= \tan^{-1}(n_y/n_x) \\ \beta &= \cos^{-1}(n_z) \\ \gamma &= \tfrac{\pi}{2} \end{aligned} \tag{2.16}$$

where n_x, n_y, and n_z are the x, y, and z components of the surface normal vector $\hat{\mathbf{n}}$, respectively. And γ is arbitrarily defined. With given Euler angles a coordinate rotation matrix $\mathbf{R}$ [217] can be determined as

$$\mathbf{R} = \begin{bmatrix} -\sin\alpha & -\cos\alpha\cos\beta & \cos\alpha\sin\beta \\ \cos\alpha & -\sin\alpha\cos\beta & \sin\alpha\sin\beta \\ 0 & \sin\beta & \cos\beta \end{bmatrix} \tag{2.17}$$

allowing the evaluation of tangential directional vectors as

[2] Although angle β shares the same greek letter with the extinction coefficients, it only appears in the coordinates rotation and hopefully will not cause any confusion.

$$\hat{\mathbf{t}}_{\overline{x}} = \mathbf{R} \cdot \hat{\mathbf{i}} \quad \hat{\mathbf{t}}_{\overline{y}} = \mathbf{R} \cdot \hat{\mathbf{j}} \tag{2.18}$$

For a given rotation of Euler angles, the spherical harmonics in local coordinates can be rotated back to global coordinates through a rotation matrix $\overline{\Delta}^n_{mm'}(-\gamma, -\beta, -\alpha)$ [217], which leads to a linear combination of spherical harmonics in global coordinates:

$$\bar{I}^m_n = \sum_{m'=-n}^{n} \bar{\Delta}^n_{mm'} I^{m'}_n \tag{2.19}$$

where the rotation matrix $\bar{\Delta}^n_{mm'}$ is calculated from

$$\begin{aligned}\bar{\Delta}^n_{m,m'}(-\gamma, -\beta, -\alpha) = \operatorname{sign}(m')\Psi_m(-\gamma)\Psi_{m'}(-\alpha)\left[d^n_{|m|,|m'|}(-\beta) + (-1)^{m'} d^n_{|m|,-|m'|}(-\beta)\right] \\ - \operatorname{sign}(m)\Psi_{-m}(-\gamma)\Psi_{-m'}(-\alpha)\left[d^n_{|m|,|m'|}(-\beta) - (-1)^{m'} d^n_{|m|,-|m'|}(-\beta)\right]\end{aligned} \tag{2.20}$$

with

$$\operatorname{sign}(m) = \begin{cases} -1 & m < 0 \\ 1 & m \geq 0 \end{cases} \tag{2.21}$$

and the function Ψ_m is defined as

$$\Psi_m(\theta) = \begin{cases} \cos m\theta & m \geq 0 \\ \sin |m|\theta & m < 0 \end{cases} \tag{2.22}$$

$d^n_{mm'}$ is the real parts of the modified Wigner-D function, i.e.,

$$\begin{aligned} d^n_{mm'}(\beta) = & \frac{(-1)^{m+m'}(n-|m|)!(n+|m|)!}{1+\delta_{m,0}} \\ & \times \sum_{k=\max(0,m'-m)}^{\min(n-m,n+m')} \frac{(-1)^k \left(\cos\frac{\beta}{2}\right)^{2n-2k-m+m'} \left(\sin\frac{\beta}{2}\right)^{2k+m-m'}}{k!(n-m-k)!(n+m'-k)(m-m'+k)!} \end{aligned} \tag{2.23}$$

Since the elliptic formulation is based on I^m_n with even n, the local $\bar{I}^m_n$ in the boundary conditions

with odd n must be eliminated through their relations to the derivatives of $\bar{I}^m_{n+1}$ and $\bar{I}^m_{n-1}$ [145]. Then the $\bar{I}^m_{n+1}$ and $\bar{I}^m_{n-1}$ are rotated back to the global coordinates through Eq. (2.19). The final form of the Marshak's boundary conditions for the second-order elliptic formulation are shown below in terms of a local coordinate system $\bar{x}$, $\bar{y}$ (tangential to the surface), and $\bar{z}$ (surface normal) [147].

For each $\overline{Y}^0_{2i-1}$, $i = 1, 2, \cdots, (N+1)/2$;

$$
\begin{aligned}
I_w p^0_{0,2i-1} = &\sum_{l=0}^{\frac{N-1}{2}} \sum_{m'=-2l}^{2l} p^0_{2l,2i-1} \overline{\Delta}^{2l}_{0,m'} I^{m'}_{2l} + \frac{\partial}{\partial \tau_{\bar{x}}} \sum_{l=1}^{\frac{N-1}{2}} \sum_{m'=-2l}^{2l} v^0_{l,i} \overline{\Delta}^{2l}_{1,m'} I^{m'}_{2l} \\
&+ \frac{\partial}{\partial \tau_{\bar{y}}} \sum_{l=1}^{\frac{N-1}{2}} \sum_{m'=-2l}^{2l} v^0_{l,i} \overline{\Delta}^{2l}_{-1,m'} I^{m'}_{2l} - \frac{\partial}{\partial \tau_{\bar{z}}} \sum_{l=0}^{\frac{N-1}{2}} \sum_{m'=-2l}^{2l} w^0_{l,i} \overline{\Delta}^{2l}_{0,m'} I^{m'}_{2l}
\end{aligned}
\tag{2.24a}
$$

and for each $\overline{Y}^{\pm m}_{2i-1}$, $i = 1, 2, \cdots, (N+1)/2$:

$$
\begin{aligned}
0 = &\sum_{l=0}^{\frac{N-1}{2}} \sum_{m'=-2l}^{2l} p^m_{2l,2i-1} \overline{\Delta}^{2l}_{\pm m,m'} I^{m'}_{2l} \\
&- \frac{\partial}{\partial \tau_{\bar{x}}} \sum_{l=l_1}^{\frac{N-1}{2}} \sum_{m'=-2l}^{2l} \left[(1 \pm \delta_{m,1}) u^m_{l,i} \overline{\Delta}^{2l}_{\pm(m-1),m'} - v^m_{l,i} \overline{\Delta}^{2l}_{\pm(m+1),m'} \right] I^{m'}_{2l} \\
&\pm \frac{\partial}{\partial \tau_{\bar{y}}} \sum_{l=l_2}^{\frac{N-1}{2}} \sum_{m'=-2l}^{2l} \left[(1 \mp \delta_{m,1}) u^m_{l,i} \overline{\Delta}^{2l}_{\mp(m-1),m'} + v^m_{l,i} \overline{\Delta}^{2l}_{\mp(m+1),m'} \right] I^{m'}_{2l} \\
&- \frac{\partial}{\partial \tau_{\bar{z}}} \sum_{l=0}^{\frac{N-1}{2}} \sum_{m'=-2l}^{2l} w^m_{l,i} \overline{\Delta}^{2l}_{\pm m,m'} I^{m'}_{2l}
\end{aligned}
\tag{2.24b}
$$

where l_1 and l_2 are defined as

$$
l_1 = 1 - l_2 = \begin{cases} 0 & \text{for} \quad \overline{Y}^m_{2i-1} \\ 1 & \text{for} \quad \overline{Y}^{-m}_{2i-1} \end{cases}
\tag{2.25}
$$

and the constant coefficients $u^m_{l,i}$, $v^m_{l,i}$, $w^m_{l,i}$ are defined as

$$u^m_{l,i} = \frac{p^m_{2l-1,2i-1} - p^m_{2l+1,2i-1}}{2(4l+1)} \tag{2.26a}$$

$$v^m_{l,i} = \frac{\pi_2(2l+m)p^m_{2l-1,2i-1} - \pi_2(2l-m)p^m_{2l+1,2i-1}}{2(4l+1)} \tag{2.26b}$$

$$w^m_{l,i} = \frac{(2l+m)p^m_{2l-1,2i-1} + (2l-m+1)p^m_{2l+1,2i-1}}{4l+1} \tag{2.26c}$$

Following Eq. (2.14), $u^m_{l,i}$, $v^m_{l,i}$, $w^m_{l,i}$ are zero when $i \neq l$ and $i - l \neq 1$.

The partial derivatives in Eq. (2.24) are expressed in local optical coordinates as

$$\frac{\partial}{\partial \tau_{\overline{x}}} = \frac{1}{\beta}\frac{\partial}{\partial \overline{x}} \tag{2.27a}$$

$$\frac{\partial}{\partial \tau_{\overline{y}}} = \frac{1}{\beta}\frac{\partial}{\partial \overline{y}} \tag{2.27b}$$

$$\frac{\partial}{\partial \tau_{\overline{z}}} = \frac{1}{\beta}\frac{\partial}{\partial \overline{z}} \tag{2.27c}$$

Finally, the radiative intensity at the boundary wall I_w is determined from:

$$I_w = \epsilon I_{bw} + (1-\epsilon)\frac{H}{\pi} \tag{2.28}$$

where ϵ is the surface emittance, and H is the hemispherical irradiation. For black walls, $\epsilon = 1$, this leads to $I_w = I_{bw}$. For clarity, here the definition of I_w, Eq (2.28), is limited to diffusely reflecting walls. More explanation and further development for walls with more complicated properties will be presented in the special boundary condition section.

2.4 Solutions

In the previous sections, the RTE was converted into $N(N+1)/2$ second-order elliptic PDEs and the corresponding boundary conditions were obtained adopting Marshak's formulation. The

governing equations, Eq. (2.9), with their boundary conditions, Eq. (2.24), are ready to be solved as a linear simultaneous system of PDEs if the extinction coefficients β and the blackbody radiative intensity I_b are specified. Analytical solutions only exist for simple 1-D geometry problems [21] and are very difficult if not impossible for multidimensional problems. Thus numerical solutions are necessary for multidimensional applications, which was originally implemented up to P_5 for 2-D geometries in the finite-element-based PDE solver FlexPDE [145–147, 218]. A better implementation platform is required before the elliptic formulation of high-order P_N method can be applied to more complicated problems.

The solutions of the described systems of PDEs, I_n^m, are rarely reconstructed back to the radiative intensity I. Instead, only ones with physical significance are used to describe the state of radiative heat transfer. The incident radiation G is obtained from

$$G(\boldsymbol{\tau}) = \int_{4\pi} I(\boldsymbol{\tau}, \hat{\mathbf{s}}) d\Omega = 4\pi I_0^0(\boldsymbol{\tau}) \tag{2.29}$$

and the radiative heat flux $\mathbf{q}$ is evaluated as

$$\mathbf{q}(\boldsymbol{\tau}) = \int_{4\pi} I(\boldsymbol{\tau}, \hat{\mathbf{s}}) \hat{\mathbf{s}} d\Omega = \frac{4\pi}{3}(-I_1^1, -I_1^{-1}, I_1^0) \tag{2.30}$$

where the I_1^m are given by

$$I_1^0 = -\frac{\partial I_0^0}{\partial \tau_z} - \frac{2}{5}\frac{\partial I_2^0}{\partial \tau_z} + \frac{3}{5}\frac{\partial I_2^1}{\partial \tau_x} + \frac{3}{5}\frac{\partial I_2^{-1}}{\partial \tau_y} \tag{2.31a}$$

$$I_1^1 = +\frac{\partial I_0^0}{\partial \tau_x} - \frac{1}{5}\frac{\partial I_2^0}{\partial \tau_x} - \frac{3}{5}\frac{\partial I_2^1}{\partial \tau_z} + \frac{6}{5}\frac{\partial I_2^2}{\partial \tau_x} + \frac{6}{5}\frac{\partial I_2^{-2}}{\partial \tau_y} \tag{2.31b}$$

$$I_1^{-1} = +\frac{\partial I_0^0}{\partial \tau_y} - \frac{1}{5}\frac{\partial I_2^0}{\partial \tau_y} - \frac{3}{5}\frac{\partial I_2^{-1}}{\partial \tau_z} - \frac{6}{5}\frac{\partial I_2^2}{\partial \tau_y} + \frac{6}{5}\frac{\partial I_2^{-2}}{\partial \tau_x} \tag{2.31c}$$

Equations (2.30) and (2.31) are valid for both the global coordinates system (x-y-z, I_n^m) as well as a local coordinates system at the boundary face ($\bar{x}$-$\bar{y}$-$\bar{z}$, $\bar{I}_n^m$).

Chapter 3

Further Development of the High-Order Spherical Harmonics (P_N) Method

In this chapter, the high-order spherical harmonics (P_N) method for 2-D Cartesian and 2-D axisymmetric domains will be developed from the 3-D formulation by employing geometric relations between the spherical harmonics. The number of equations and unknowns reduces to $(N+1)^2/4$ in the 2-D formulations compared with $N(N+1)/2$ for the general 3-D P_N formulation. Also, the Marshak's boundary conditions are extended to solve problems with nonblack and mixed diffuse-specular surfaces. Additional boundary conditions for specified radiative wall flux, for symmetry/specular reflection boundaries and for cyclic boundaries are also formulated.

3.1 2-D Formulations

3.1.1 Formulation for 2-D Cartesian Geometry

The formulation of the 2-D Cartesian P_N is derived from the 3-D formulation by applying the parity properties of the the associated Legendre polynomials $P_n^m(\mu)$, Eq. (2.4). For two-dimensional Cartesian geometry in the x-y plane with polar angle θ measured from the z-axis, one

obtains $I(\theta,\psi) = I(\pi-\theta,\psi)$ or $I(\mu,\psi) = I(-\mu,\psi)$ with $\mu = \cos\theta$. As seen from Eqs. (2.3) and (2.4), the associated Legendre polynomials $P_n^m(\mu)$ are odd functions when $(m+n)$ are odd and thus I_n^m with $(m+n)$ being odd must vanish. Since the governing equations are formulated with even n only, all terms in the governing equation with odd m vanish. The remaining intensity coefficients I_n^m are listed in Table. 3.1. Based on this, and eliminating all derivatives into the z-direction, the remaining $(N+1)^2/4$ governing equations for order N are:

For each $Y_n^m : n = 0, 2, \ldots, N-1,\ m = 0, 2, \ldots n$:

$$\begin{aligned}
&\sum_{k=1}^{3}\Big\{(\mathcal{L}_{xx}-\mathcal{L}_{yy})\left[(1+\delta_{m2})a_k^{nm}I_{n+4-2k}^{m-2}+e_k^{nm}I_{n+4-2k}^{m+2}\right]\\
&\quad+(\mathcal{L}_{xy}+\mathcal{L}_{yx})\left[-(1-\delta_{m2})a_k^{nm}I_{n+4-2k}^{-(m-2)}+e_k^{nm}I_{n+4-2k}^{-(m+2)}\right]\\
&\quad+(\mathcal{L}_{xx}+\mathcal{L}_{yy})c_k^{nm}I_{n+4-2k}^{m}\Big\}\\
&\quad-(1-\omega\delta_{0n})I_n^m=-(1-\omega)I_b\delta_{0n}
\end{aligned} \tag{3.1a}$$

and for each $Y_n^{-m} : n = 2, \ldots, N-1,\ m = 2, \ldots n$:

$$\begin{aligned}
&\sum_{k=1}^{3}\Big\{(\mathcal{L}_{xy}+\mathcal{L}_{yx})\left[(1+\delta_{m2})a_k^{nm}I_{n+4-2k}^{m-2}-e_k^{nm}I_{n+4-2k}^{m+2}\right]\\
&\quad+(\mathcal{L}_{xx}-\mathcal{L}_{yy})\left[(1-\delta_{m2})a_k^{nm}I_{n+4-2k}^{-(m-2)}+e_k^{nm}I_{n+4-2k}^{-(m+2)}\right]\\
&\quad+(\mathcal{L}_{xx}+\mathcal{L}_{yy})c_k^{nm}I_{n+4-2k}^{-m}\Big\}\\
&\quad-I_n^{-m}=0
\end{aligned} \tag{3.1b}$$

The boundary conditions again are expressed in local coordinates in terms of the surface normal and tangential vectors. The local coordinates can be set up as in Fig. 3.1, so that $\bar{I}_n^m$ is independent of $\bar{y}$ (pointing into the global z-direction). Meanwhile, the $\bar{x}$ direction can be found from Euler angles, and Fig. 3.1 shows both the arrangements of the global and local coordinates for a general 2-D Cartesian geometry in the x-y plane.

Table 3.1: Intensity coefficients employed for 2-D Cartesian formulation in x-y plane.

n	Intensity Coefficients						
0				I_0^0			
2			I_2^{-2}	I_2^0	I_2^2		
4		I_4^{-4}	I_4^{-2}	I_4^0	I_4^2	I_4^4	
6	I_6^{-6}	I_6^{-4}	I_6^{-2}	I_6^0	I_6^2	I_6^4	I_6^6
n	I_n^{-n}	$\cdots$	I_n^{-2}	I_n^0	I_n^2	$\cdots$	I_n^n

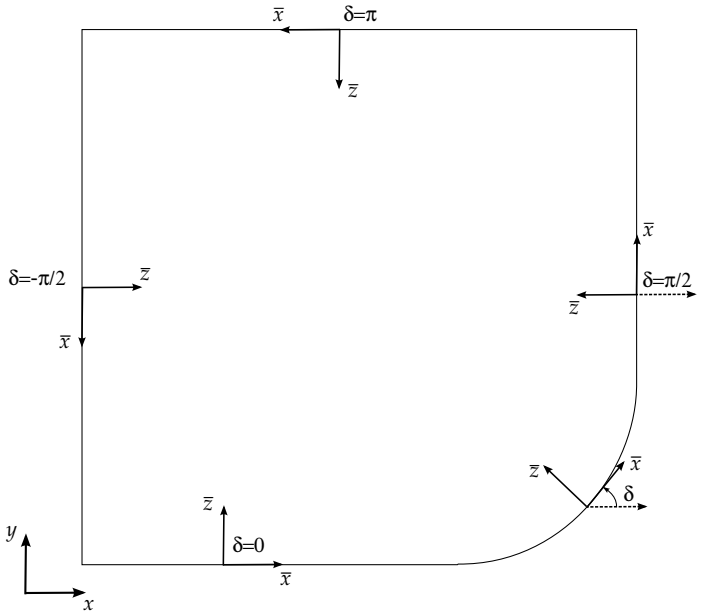

Figure 3.1: Schematic of the global coordinate system and the local coordinate system in x-y plane.

The Euler angles are calculated from [216]

$$\alpha = \tan^{-1}\left(\frac{n_y}{n_x}\right) = \delta + \frac{\pi}{2} \tag{3.2a}$$

$$\beta = \frac{\pi}{2} \tag{3.2b}$$

$$\gamma = -\frac{\pi}{2} \tag{3.2c}$$

resulting in

$$\hat{\mathbf{n}} = \cos\alpha\hat{\mathbf{i}} + \sin\alpha\hat{\mathbf{j}} = -\sin\delta\hat{\mathbf{i}} + \cos\delta\hat{\mathbf{j}} \tag{3.3a}$$

$$\hat{\mathbf{t}}_{\bar{x}} = \sin\alpha\hat{\mathbf{i}} - \cos\alpha\hat{\mathbf{j}} = \cos\delta\hat{\mathbf{i}} + \sin\delta\hat{\mathbf{j}} \tag{3.3b}$$

Because of the two-dimensionality, we have $I(\bar{\theta},\bar{\psi}) = I(\bar{\theta},-\bar{\psi})$ with the local azimuthal angle $\bar{\psi}$ defined in the $\bar{x}$-$\bar{y}$ plane and measured from the local $\bar{x}$-axis, which leads to the elimination of $\bar{I}_n^m$ with negative m, which in turn leads to zero identities for the $\bar{Y}_{2i-1}^{-m}$ boundary conditions. Together with the elimination of the I_n^m with odd m in global coordinates, the remaining $(N+1)^2/4$ boundary conditions for 2-D problems become

For each $\bar{Y}_{2i-1}^0$, $i = 1, 2, \cdots, (N+1)/2$:

$$\begin{aligned} I_w p_{0,2i-1}^0 = &\sum_{l=0}^{\frac{N-1}{2}} \sum_{m'=-l}^{l} p_{2l,2i-1}^0 \bar{\Delta}_{0,2m'}^{2l} I_{2l}^{2m'} + \frac{\partial}{\partial\tau_{\bar{x}}} \sum_{l=1}^{\frac{N-1}{2}} \sum_{m'=-l}^{l} v_{l,i}^0 \bar{\Delta}_{1,2m'}^{2l} I_{2l}^{2m'} \\ &- \frac{\partial}{\partial\tau_{\bar{z}}} \sum_{l=0}^{\frac{N-1}{2}} \sum_{m'=-l}^{l} w_{l,i}^0 \bar{\Delta}_{0,2m'}^{2l} I_{2l}^{2m'} \end{aligned} \tag{3.4a}$$

and for each $\bar{Y}_{2i-1}^m$,

$i = 1, 2, \cdots, (N-1)/2$, $m = 1, 2, \cdots, 2i-1$; $i = (N+1)/2$, $m = 2, 4, \cdots, 2i-2$:

$$\begin{aligned} 0 = &\sum_{l=0}^{\frac{N-1}{2}} \sum_{m'=-l}^{l} p_{2l,2i-1}^m \bar{\Delta}_{\pm m,2m'}^{2l} I_{2l}^{2m'} \\ &- \frac{\partial}{\partial\tau_{\bar{x}}} \sum_{l=0}^{\frac{N-1}{2}} \sum_{m'=-l}^{l} \left[(1+\delta_{m,1}) u_{l,i}^m \bar{\Delta}_{m-1,2m'}^{2l} - v_{l,i}^m \bar{\Delta}_{m+1,2m'}^{2l} \right] I_{2l}^{2m'} \\ &- \frac{\partial}{\partial\tau_{\bar{z}}} \sum_{l=0}^{\frac{N-1}{2}} \sum_{m'=-l}^{l} w_{l,i}^m \bar{\Delta}_{\pm m,2m'}^{2l} I_{2l}^{2m'} \end{aligned} \tag{3.4b}$$

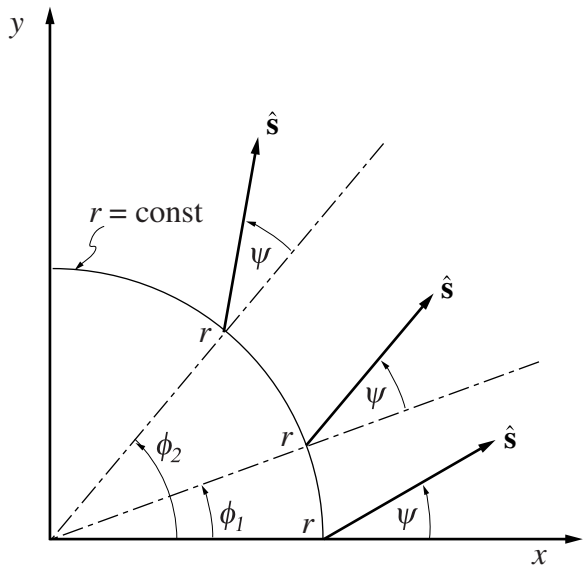

Figure 3.2: Illustration of the invariance of intensity with respect to azimuthal angle ψ at different locations for axisymmetric conditions.

3.1.2 Formulation for 2-D Axisymmetric Geometry

The elliptic formulation of high-order P_N method for 2-D axisymmetric geometries can also be directly derived from the general 3-D formulations. For axisymmetric problems, physical quantities such as temperature, heat flux, radiative intensity, chemical species concentrations, etc., vary only radially and axially and are, therefore, two-dimensional. As a result, for many of these applications, the transport equations are solved on a 2-D or a 3-D thin-wedge computational domain in order to reduce the computational effort. The radiative intensity depends on position $\mathbf{r}(r, \phi, z)$ and direction $\hat{\mathbf{s}}(\theta, \psi)$ where θ is the polar angle (measured from the z-axis), and ψ is the azimuthal angle (measured counter-clockwise from the x-axis). If the physical system is axisymmetric, then the radiative intensity varies with r and axially with z, but not azimuthally with ϕ. Figure 3.2 illustrates several location-direction combinations, which have identical intensities for axisymmetric conditions. At a fixed location $\mathbf{r}(r, \phi_1, z)$ the radiative intensity in the direction $\hat{\mathbf{s}}(\theta, \psi + \phi_1)$ is equal to the radiative intensity at some other location $\mathbf{r}(r, \phi_2, z)$ in the direction $\hat{\mathbf{s}}(\theta, \psi + \phi_2)$, which has the

same deflection angle relative to its position vector **r**. One may conclude from Fig. 3.2 that

$$I(r, \phi, z; \theta, \psi + \phi) = I(r, 0, z; \theta, \psi) \tag{3.5}$$

for any ϕ, as long as the problem is axisymmetric. When $\phi = 0$, the radiative intensity is evaluated along the x-axis. Considering the general case at some arbitrary ϕ and a reference case when $\phi = 0$, the radiative intensity as approximated by the spherical harmonic series expansion Eq. (2.1) yields, for a given n, the equality

$$\begin{aligned}
&I_n^0(r, \phi, z) P_n^0(\theta) + \sum_{m=1}^{n} I_n^m(r, \phi, z) \left[\cos m\psi \cos m\phi - \sin m\psi \sin m\phi\right] P_n^m(\theta) \\
&+ \sum_{m=1}^{n} I_n^{-m}(r, \phi, z) \left[\sin m\psi \cos m\phi + \cos m\psi \sin m\phi\right] P_n^m(\theta) \\
&= I_n^0(r, 0, z) P_n^0(\theta) + \sum_{m=1}^{n} I_n^m(r, 0, z) \cos m\psi P_n^m(\theta) + \sum_{m=1}^{n} I_n^{-m}(r, 0, z) \sin m\psi P_n^m(\theta)
\end{aligned} \tag{3.6}$$

By comparing the I_n^0 terms, it follows that for $m = 0$

$$I_n^0(r, \phi, z) = I_n^0(r, 0, z) \tag{3.7}$$

which implies that the intensity coefficients with $m = 0$ must be functions of r and z only and are thus axisymmetric. Now comparing other like terms, $\cos m\psi P_n^m(\cos\theta)$ and $\sin m\psi P_n^m(\cos\theta)$ in Eq. (3.6), yields the following relations for intensity coefficients with $m > 0$.

$$I_n^m(r, 0, z) = I_n^m(r, \phi, z) \cos m\phi + I_n^{-m}(r, \phi, z) \sin m\phi \tag{3.8a}$$

$$I_n^{-m}(r, 0, z) = -I_n^m(r, \phi, z) \sin m\phi + I_n^{-m}(r, \phi, z) \cos m\phi \tag{3.8b}$$

Inverting these relations to express $I_n^m(r,\phi,z)$ and $I_n^{-m}(r,\phi,z)$ in terms of the $I_n^m(r,0,z)$ and $I_n^{-m}(r,0,z)$ gives

$$I_n^m(r,\phi,z) = I_n^m(r,0,z)\cos m\phi - I_n^{-m}(r,0,z)\sin m\phi \tag{3.9a}$$

$$I_n^{-m}(r,\phi,z) = I_n^m(r,0,z)\sin m\phi + I_n^{-m}(r,0,z)\cos m\phi \tag{3.9b}$$

Also, by symmetry at $\phi = 0$, $I(r,0,z;\theta,\psi) = I(r,0,z;\theta,-\psi)$, or

$$\sum_{m=1}^{n} I_n^m(r,0,z)Y_n^m(\psi,\theta) = \sum_{m=1}^{n} I_n^m(r,0,z)Y_n^m(-\psi,\theta) \tag{3.10}$$

which leads to $I_n^{-m}(r,0,z) = 0$ for any m. Thus, according to Eq. (3.9), the intensity coefficients for arbitrary ϕ are related to the same r and z-dependent variable $I_n^m(r,0,z)$ as

$$I_n^m(r,\phi,z) = I_n^m(r,0,z)\cos m\phi, \tag{3.11a}$$

$$I_n^{-m}(r,\phi,z) = I_n^m(r,0,z)\sin m\phi. \tag{3.11b}$$

For axisymmetric problems, the dependence on ϕ of intensity coefficients with $m > 0$ are trigonometric factors (sines and cosines with periodicity equal to m) that multiply the same axisymmetric variable $I_n^m(r,0,z)$. Hereafter, this axisymmetric variable will be denoted as $\hat{I}_n^m(r,z)$. From Eq. (3.11), it can be seen that the number of intensity coefficient variables of the P_N approximation is reduced from $N(N+1)/2$ to $(N+1)^2/4$. The employed intensity coefficients are listed in Table 3.2.

The starting point of the 2-D axisymmetric formulation is the 3-D Cartesian formulation given by Eq. (2.9) in Chapter 2. To obtain the transformation of the PDEs to cylindrical coordinates, the

Table 3.2: Intensity coefficients employed for 2-D axisymmetric formulation

n	Intensity Coefficients						
0	$\hat{I}_0^0$						
2	$\hat{I}_2^0$	$\hat{I}_2^1$	$\hat{I}_2^2$				
4	$\hat{I}_4^0$	$\hat{I}_4^1$	$\hat{I}_4^2$	$\hat{I}_4^3$	$\hat{I}_4^4$		
6	$\hat{I}_6^0$	$\hat{I}_6^1$	$\hat{I}_6^2$	$\hat{I}_6^3$	$\hat{I}_6^4$	$\hat{I}_6^5$	$\hat{I}_6^6$
n	$\hat{I}_n^0$	$\hat{I}_n^1$	$\hat{I}_n^2$	$\hat{I}_n^3$	$\cdots$	$\cdots$	$\hat{I}_n^n$

relations of the differential operators are employed,

$$\mathcal{L}_x = \frac{1}{\beta}\frac{\partial}{\partial x} = \frac{\cos\phi}{\beta}\frac{\partial}{\partial r} - \frac{\sin\phi}{\beta r}\frac{\partial}{\partial \phi} \tag{3.12a}$$

$$\mathcal{L}_y = \frac{1}{\beta}\frac{\partial}{\partial y} = \frac{\sin\phi}{\beta}\frac{\partial}{\partial r} + \frac{\cos\phi}{\beta r}\frac{\partial}{\partial \phi} \tag{3.12b}$$

$$\mathcal{L}_z = \frac{1}{\beta}\frac{\partial}{\partial z} \tag{3.12c}$$

Together with the coordinate transformation, the $(N+1)^2/4$ governing equations of the 2-D, axisymmetric formulation of the P_N approximation can be derived from the general 3-D P_N governing equations with the axisymmetric relations of the intensity coefficients. Substituting Eq. (3.11) for the $I_n^{\pm m}$ of the 3-D P_N governing equations, Eq. (2.9), after considerable algebra (Appendix B[1]), leads to a transformed set of PDEs for axisymmetric variables $\hat{I}_n^m$ as:

[1]Appendix B is summarized and reorganized from the personal communications with the authors of [219].

For each Y_n^m: $n = 0, 2, 4, ..., (N-1)$ and $m = 0, 1, 2, ..., n$:

$$\begin{aligned}
\sum_{k=1}^{3} \Bigg\{ & (1+\delta_{m2}) a_k^{nm} \cos m\phi \left[\mathcal{L}_{rr} - \frac{2m-3}{\beta r}\mathcal{L}_r + \frac{m(m-2)}{\beta^2 r^2} - \frac{m-2}{r}\mathcal{L}_r\left(\frac{1}{\beta}\right) \right] \hat{I}_{n+4-2k}^{m-2} \\
& + (1+\delta_{m1}) b_k^{nm} \cos m\phi \left[\mathcal{L}_{rz} + \mathcal{L}_{zr} - \frac{2(m-1)}{\beta r}\mathcal{L}_z - \frac{m-1}{r}\mathcal{L}_z\left(\frac{1}{\beta}\right) \right] \hat{I}_{n+4-2k}^{m-1} \\
& + \frac{\delta_{m1}}{2} c_k^{nm} \cos\phi \left[\mathcal{L}_{rr} + \frac{1}{\beta r}\mathcal{L}_r - \frac{1}{r^2\beta^2} + \frac{1}{r}\mathcal{L}_r\left(\frac{1}{\beta}\right) \right] \hat{I}_{n+4-2k}^{m} \\
& + d_k^{nm} \cos m\phi \left[\mathcal{L}_{rz} + \mathcal{L}_{zr} + \frac{2(m+1)}{\beta r}\mathcal{L}_z + \frac{m+1}{r}\mathcal{L}_z\left(\frac{1}{\beta}\right) \right] \hat{I}_{n+4-2k}^{m+1} \\
& + e_k^{nm} \cos m\phi \left[\mathcal{L}_{rr} + \frac{2m+3}{\beta r}\mathcal{L}_r + \frac{m(m+2)}{\beta^2 r^2} + \frac{m+2}{r}\mathcal{L}_r\left(\frac{1}{\beta}\right) \right] \hat{I}_{n+4-2k}^{m+2} \\
& + c_k^{nm} \cos m\phi \left(\mathcal{L}_{rr} + \frac{1}{\beta r}\mathcal{L}_r - \frac{m^2}{\beta^2 r^2} - 2\mathcal{L}_{zz} \right) \hat{I}_{n+4-2k}^{m} \Bigg\} \\
& + \cos m\phi \left[\mathcal{L}_{zz} - (1 - \omega\delta_{0n}) \right] \hat{I}_n^m = -(1-\omega) I_b \delta_{0n}
\end{aligned} \tag{3.13}$$

The differential operators in cylindrical coordinates are defined as

$$\mathcal{L}_r = \frac{1}{\beta}\frac{\partial}{\partial r} \tag{3.14a}$$

$$\mathcal{L}_{rr} = \frac{1}{\beta}\frac{\partial}{\partial r}\left(\frac{1}{\beta}\frac{\partial}{\partial r}\right) \tag{3.14b}$$

$$\mathcal{L}_{rz} = \frac{1}{\beta}\frac{\partial}{\partial r}\left(\frac{1}{\beta}\frac{\partial}{\partial z}\right) \tag{3.14c}$$

$$\mathcal{L}_{zr} = \frac{1}{\beta}\frac{\partial}{\partial z}\left(\frac{1}{\beta}\frac{\partial}{\partial r}\right) \tag{3.14d}$$

and $\mathcal{L}_r(1/\beta)$ is a material property calculated from Eq. (3.14a) as

$$\mathcal{L}_r\left(\frac{1}{\beta}\right) = -\frac{1}{\beta^3}\frac{\partial \beta}{\partial r} \tag{3.15}$$

It is noted that each term contains $\cos m\phi$, which may, therefore, be canceled (including the case of $m = 0$, for which $\cos m\phi = 1$). Each Y_n^{-m} ($m = 1, 2, ..., n$) returns the same equation as the corresponding Y_n^m, but with $\sin m\phi$ in each term instead of the $\cos m\phi$. Thus, the set of governing

equations, like the number of unknowns $\hat{I}_n^m$, are reduced to

For each $Y_n^m : n = 0, 2, ..., N+1$ and $m = 0, 1, 2, ..., n$:

$$\begin{aligned}
\sum_{k=1}^{3} \Big\{ & (1+\delta_{m2}) a_k^{nm} \left[\mathcal{L}_{rr} - \frac{2m-3}{\beta r}\mathcal{L}_r + \frac{m(m-2)}{\beta^2 r^2} - \frac{m-2}{r}\mathcal{L}_r\left(\frac{1}{\beta}\right) \right] \hat{I}_{n+4-2k}^{m-2} \\
& + (1+\delta_{m1}) b_k^{nm} \left[\mathcal{L}_{rz} + \mathcal{L}_{zr} - \frac{2(m-1)}{\beta r}\mathcal{L}_z - \frac{m-1}{r}\mathcal{L}_z\left(\frac{1}{\beta}\right) \right] \hat{I}_{n+4-2k}^{m-1} \\
& + \frac{\delta_{m1}}{2} c_k^{nm} \left[\mathcal{L}_{rr} + \frac{1}{\beta r}\mathcal{L}_r - \frac{1}{r^2\beta^2} + \frac{1}{r}\mathcal{L}_r\left(\frac{1}{\beta}\right) \right] \hat{I}_{n+4-2k}^{m} \\
& + d_k^{nm} \left[\mathcal{L}_{rz} + \mathcal{L}_{zr} + \frac{2(m+1)}{\beta r}\mathcal{L}_z + \frac{m+1}{r}\mathcal{L}_z\left(\frac{1}{\beta}\right) \right] \hat{I}_{n+4-2k}^{m+1} \\
& + e_k^{nm} \left[\mathcal{L}_{rr} + \frac{2m+3}{\beta r}\mathcal{L}_r + \frac{m(m+2)}{\beta^2 r^2} + \frac{m+2}{r}\mathcal{L}_r\left(\frac{1}{\beta}\right) \right] \hat{I}_{n+4-2k}^{m+2} \\
& + c_k^{nm} \left(\mathcal{L}_{rr} + \frac{1}{\beta r}\mathcal{L}_r - \frac{m^2}{\beta^2 r^2} - 2\mathcal{L}_{zz} \right) \hat{I}_{n+4-2k}^{m} \Big\} \\
& + \left[\mathcal{L}_{zz} - (1 - \omega\delta_{0n}) \right] \hat{I}_n^m = -(1-\omega) I_b \delta_{0n}
\end{aligned} \tag{3.16}$$

$(N+1)^2/4$ boundary conditions are required and are derived from the 3-D P_N formulation of Marshak's boundary conditions, Eq. (2.24). As for the Cartesian formulation, the boundary conditions are expressed in terms of local coordinates $\overline{x}$, $\overline{y}$ (tangential to the surface) and $\overline{z}$ (along surface normal $\hat{\mathbf{n}}$), and a rotation function $\overline{\Delta}(-\gamma, -\beta, -\alpha)$, Eq. (2.20), is utilized to rotate local coordinates back to global coordinates for the calculation of boundary conditions.

Figure 3.3 shows both the arrangements of the global and local coordinates for a general 2-D axisymmetric geometry. β can be calculated from surface normal $\hat{\mathbf{n}}$ as

$$\beta = \cos^{-1}(n_z) \tag{3.17}$$

The tangential directions of the boundary surfaces are defined in such a way that one tangential direction ($\hat{\mathbf{t}}_x$ or $\overline{x}$) is within the r-z plane and perpendicular to the r-axis, and $\hat{\mathbf{t}}_y$ (or $\overline{y}$) is perpendicular to the r-z plane. Therefore, the Eulerian angle α is related to the azimuthal angle ϕ, Fig. 3.3(a), as

$$\alpha = \pi + \phi \tag{3.18}$$

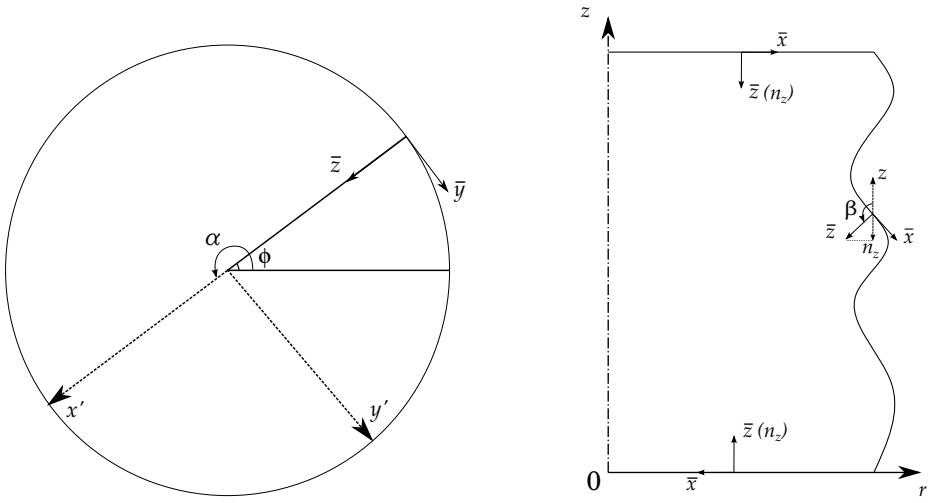

(a) (b)

Figure 3.3: Schematic of the global coordinate system and the local coordinate system in a general axisymmetric geometry; (a) *r*-ϕ plane and (b) *r*-*z* plane.

In order to keep $\hat{\mathbf{t}}_y$ (or $\overline{y}$) in the *r*-ϕ plane, $\gamma = 0$. With the above conditions, the relationship between the local Cartesian coordinates and the global cylindrical coordinates are

$$\hat{\mathbf{n}} = -\sin\beta\ \hat{\mathbf{r}} + \cos\beta\ \hat{\mathbf{z}} \tag{3.19a}$$

$$\hat{\mathbf{t}}_{\overline{x}} = -\cos\beta\ \hat{\mathbf{r}} - \sin\beta\ \hat{\mathbf{z}} \tag{3.19b}$$

$$\hat{\mathbf{t}}_{\overline{y}} = -\hat{\boldsymbol{\phi}} \tag{3.19c}$$

from which the derivatives are found as

$$\frac{\partial}{\partial \overline{z}} = -\sin\beta \frac{\partial}{\partial r} + \cos\beta \frac{\partial}{\partial z} \tag{3.20a}$$

$$\frac{\partial}{\partial \overline{x}} = -\cos\beta \frac{\partial}{\partial r} - \sin\beta \frac{\partial}{\partial z} \tag{3.20b}$$

$$\frac{\partial}{\partial \overline{y}} = -\frac{1}{r}\frac{\partial}{\partial \phi} \tag{3.20c}$$

As an example for the most common case of a fixed-radius cylinder (or wedge), for the vertical wall

faces the Eulerian angle $\beta = \pi/2$, and from Eq. (3.19),

$$\hat{\mathbf{n}} = -\hat{\mathbf{r}} \tag{3.21a}$$

$$\hat{\mathbf{t}}_{\bar{x}} = -\hat{\mathbf{z}} \tag{3.21b}$$

$$\hat{\mathbf{t}}_{\bar{y}} = -\hat{\boldsymbol{\phi}} \tag{3.21c}$$

Equation (3.19) is also consistent for the bottom and top boundaries of the wedge, where the Eulerian angle β equals 0 and π, respectively.

In order to derive the boundary conditions for the 2-D axisymmetric formulation from the $N(N+1)/2$ boundary conditions of the 3-D formulation, Eq. (2.9), the $\overline{\Delta}(-\gamma, -\beta, -\alpha) = \overline{\Delta}(0, -\beta, \pi - \phi)$ in their expanded form Eq. (2.20), are substituted into the full set of Marshak's boundary conditions. In addition, Eqs. (3.7) and (3.11) are employed, and the derivatives in the $\bar{y}$-direction are evaluated with Eq. (3.20c). After tedious derivation (Appendix B), it is found that all $\overline{Y}_n^{-m}$ related boundary conditions become zero identities, which reduces the total number of equations from $N(N+1)/2$ to $(N+1)^2/4$. The $(N+1)^2/4$ remaining boundary conditions are associated with the local spherical harmonics $\overline{Y}_{2i-1}^{m}$, where $i = (n+1)/2$, for certain combinations of m and i indices, i.e.,

$$m = \begin{cases} 0, 1, \cdots, i & i = 1, 2, \cdots, (N-1)/2 \\ 0, 2, \cdots, N-1 & i = (N+1)/2 \end{cases} \tag{3.22}$$

For example, the boundary conditions for axisymmetric P_3, where $(N+1)^2/4 = 4$, are associated with the local spherical harmonics $\overline{Y}_1^0$, $\overline{Y}_1^1$, $\overline{Y}_3^0$ and $\overline{Y}_3^2$.

The complete set of axisymmetric P_N boundary conditions, with the i and m pairs from

Eq. (3.22), then becomes

$$
\begin{aligned}
I_w p^0_{0,n} = &\sum_{l=0}^{\frac{N-1}{2}} \sum_{m'=0}^{2l} p^m_{2l,2i-1} D^{2l}_{|m||m'|}(-\beta) \hat{I}^{m'}_{2l} \\
&- \frac{1}{\beta r} \sum_{l=0}^{\frac{N-1}{2}} \sum_{m'=0}^{2l} \left(\delta^-_m u^m_{li} B^{2l}_{|m-1||m'|}(-\beta) + v^m_{li} B^{2l}_{|m+1||m'|}(-\beta) \right) \hat{I}^{m'}_{2l} \\
&- \frac{\partial}{\partial \tau_{\bar{x}}} \sum_{l=0}^{\frac{N-1}{2}} \sum_{m'=0}^{2l} \left(\delta^+_m u^m_{li} D^{2l}_{|m-1||m'|}(-\beta) - v^m_{li} D^{2l}_{|m+1||m'|}(-\beta) \right) \hat{I}^{m'}_{2l} \\
&- \frac{\partial}{\partial \tau_{\bar{z}}} \sum_{l=1}^{\frac{N-1}{2}} \sum_{m'=0}^{2l} w^m_{li} D^{2l}_{|m||m'|}(-\beta) \hat{I}^{m'}_{2l}
\end{aligned} \tag{3.23}
$$

where $\delta^{\pm}_m = (1 \pm \delta_{m1})(1 - \delta_{m0})$, and the constant coefficients u^m_{li}, v^m_{li}, w^m_{li}, and $p^m_{2l,n}$ are the same as in the 3-D formulation, while the $D^n_{|m||m'|}(\beta)$ and $B^n_{|m||m'|}(\beta)$ are

$$
D^n_{|m||m'|}(\beta) = (-1)^{m'} d^n_{|m|,|m'|}(\beta) + d^n_{|m|,-|m'|}(\beta) \tag{3.24a}
$$

$$
B^n_{|m||m'|}(\beta) = m' \left[(-1)^{m'} d^n_{|m|,|m'|}(\beta) - d^n_{|m|,-|m'|}(\beta) \right] \tag{3.24b}
$$

where the d are Wigner coefficients as given by the 3-D Marshak formulation in Eq. (2.23). The partial derivatives in these boundary conditions are expressed in local optical coordinates.

3.2 Special Boundary Conditions

3.2.1 Boundary Condition for Mixed Diffuse-Specular Surfaces

In this section, the general boundary condition for mixed diffuse-specular surfaces is derived, which then is readily reduced to simpler cases, such as a diffuse or a specular surface.

For a partially-diffuse and partially-specular surface, the emittance can be expressed as

$$\epsilon = 1 - \rho^s - \rho^d \tag{3.25}$$

where ρ^s and ρ^d are the specular and diffuse components of the reflectance, respectively. The outgoing intensity $I_w(\mathbf{r}_w, \hat{\mathbf{s}})$ along the direction $\hat{\mathbf{s}}$, in terms of local polar angle $\bar{\theta}$ and local azimuthal angles $\bar{\psi}$, for partially-diffuse and partially-specular surfaces consists of two components: one part is due to the intensity from diffuse emission $I_{bw}(\mathbf{r}_w)$ as well as the diffuse fraction of reflected energy $H(\mathbf{r}_w)/\pi$, while the other is the specular fraction of reflected energy $I^s(\mathbf{r}_w, \hat{\mathbf{s}})$. At the wall $\mathbf{r}_w$, the outgoing intensity can be expressed by

$$I_w(\bar{\theta}, \bar{\psi}) = \epsilon I_{bw} + \rho^d \frac{H}{\pi} + \rho^s I^s(\bar{\theta}, \bar{\psi}) \tag{3.26}$$

The hemispherical irradiation H in the P_N context is evaluated by multiplying Eq. (2.1) by $\bar{Y}_1^0$ (or $\cos\bar{\theta}$) and integrating over the hemisphere, or

$$H = -\int_{\hat{\mathbf{n}}\cdot\hat{\mathbf{s}}<0} \bar{I}\bar{Y}_1^0 d\Omega = -\sum_{n=0}^{N}\sum_{m=-n}^{n}\int_0^{2\pi}\int_{\frac{\pi}{2}}^{\pi} \bar{I}_n^m \bar{Y}_n^m(\bar{\mu}, \bar{\psi})\bar{Y}_1^0 d\bar{\mu}d\bar{\psi} = 2\pi\sum_{n=0}^{N}(-1)^n p_{n,1}^0 \bar{I}_n^0 \tag{3.27}$$

Substituting Eqs. (3.26) and (3.27) into the general Marshak's boundary condition (2.11), we have

$$(1+\delta_{m,0})\pi\sum_{n=0}^{N} p_{n,2i-1}^m \bar{I}_n^m = 2\pi\delta_{m,0}p_{0,2i-1}^0\left[\epsilon I_{bw} + 2\rho^d\sum_{n=0}^{N}(-1)^n p_{n,1}^0\bar{I}_n^0\right] + \rho^s\int_0^{2\pi}\int_0^1 I^s\bar{Y}_{2i-1}^m d\bar{\mu}d\bar{\psi} \tag{3.28}$$

I^s can be found by the law of specular reflection, which is

$$I^s(\bar{\theta}, \bar{\psi}) = I(\pi - \bar{\theta}, \bar{\psi}) = \sum_{n=0}^{N}\sum_{m=-n}^{n}\bar{I}_n^m\bar{Y}_n^m(\pi - \bar{\theta}, \bar{\psi}) = \sum_{n=0}^{N}\sum_{m=-n}^{n}\bar{I}_n^m\bar{Y}_n^m(-\bar{\mu}, \bar{\psi}) \tag{3.29}$$

The associated Legendre polynomials, given by Eq. (2.4), are even functions when $(m+n)$ are even

and odd functions when $(m+n)$ are odd, which leads to

$$I^s(\bar{\theta},\bar{\psi}) = \sum_{n=0}^{N}\sum_{m=-n}^{n}(-1)^{(m+n)}\bar{I}_n^m\bar{Y}_n^m(\bar{\mu},\bar{\psi}) \tag{3.30}$$

Therefore, Eq. (3.28) becomes

$$\sum_{n=0}^{N}\Big\{\underbrace{[1-(-1)^{m+n}\rho^s]p_{n,2i-1}^m}_{\text{(a) specular reflection}} - \underbrace{2(-1)^n\delta_{m,0}\rho^d p_{0,2i-1}^0 p_{n,1}^0}_{\text{(b) diffuse reflection}}\Big\}\bar{I}_n^m = \underbrace{\delta_{m,0}p_{0,2i-1}^0\epsilon I_{bw}}_{\text{(c) emission}} \tag{3.31}$$

$$i = 1,2,...,\frac{1}{2}(N+1),\quad \text{all relevant } m$$

Following Eq. (2.12), all m are employed for $i = 1,2,3,\cdots,(N-1)/2$ and only even m are employed for $i = (N+1)/2$. When $\epsilon = 1$, $\rho^s = 0$ and $\rho^d = 0$, Eq. (3.31) is simply the original Marshak's boundary conditions for black walls, Eq. (2.24), as expected; when $\rho^d = 0$ or $\rho^s = 0$, Eq. (3.31) gives the boundary conditions for purely specular or purely diffuse surfaces, respectively; when $N = 1$, there is no distinction between diffuse and specular surface reflectivities for P_1 approximation (Appendix C), which is consistent with the conclusion obtained in [220].

Before Eq. (3.31) can be applied to the elliptical formulation described in this thesis, the $\bar{I}_n^m$ with odd n need to be eliminated and the local $\bar{I}_n^m$ need to be rotated back to global I_n^m. Expanding part (b) of Eq. (3.31), we get

$$-2p_{0,2i-1}^0\rho^d\sum_{n=0}^{N}(-1)^n p_{n,1}^0\bar{I}_n^0 = -2p_{0,2i-1}^0\rho^d\left[(p_{0,1}^0 I_0^0 + p_{2,1}^0\bar{I}_2^0 + p_{4,1}^0\bar{I}_4^0 + p_{6,1}^0\bar{I}_6^0 + \cdots) - p_{1,1}^0\bar{I}_1^0\right] \tag{3.32}$$

According to Eq. (2.13), $p_{n,j}^m \equiv 0$ when $n+j$ is even and $n \neq j$, therefore $p_{n,1}^0 = 0$ when n is odd and $n \neq 1$. When $n = 1$, $\bar{I}_1^0$ is calculated as Eq. (2.31a) in terms of local $\bar{I}_n^m$:

$$\bar{I}_1^0 = -\frac{\partial\bar{I}_0^0}{\partial\tau_{\bar{z}}} - \frac{2}{5}\frac{\partial\bar{I}_2^0}{\partial\tau_{\bar{z}}} + \frac{3}{5}\frac{\partial\bar{I}_2^1}{\partial\tau_{\bar{x}}} + \frac{3}{5}\frac{\partial\bar{I}_2^{-1}}{\partial\tau_{\bar{y}}}$$

The local intensity coefficients $\bar{I}_n^m$ in Eq. (2.31a) are then rotated back to global I_n^m through the

rotation function, Eq. (2.19), which are

$$\bar{I}_2^0 = \bar{\Delta}_{0,-2}^2 I_2^{-2} + \bar{\Delta}_{0,-1}^2 I_2^{-1} + \bar{\Delta}_{0,0}^2 I_2^0 + \bar{\Delta}_{0,1}^2 I_2^1 + \bar{\Delta}_{0,2}^2 I_2^2 \tag{3.33a}$$

$$\bar{I}_2^1 = \bar{\Delta}_{1,-2}^2 I_2^{-2} + \bar{\Delta}_{1,-1}^2 I_2^{-1} + \bar{\Delta}_{1,0}^2 I_2^0 + \bar{\Delta}_{1,1}^2 I_2^1 + \bar{\Delta}_{1,2}^2 I_2^2 \tag{3.33b}$$

$$\bar{I}_2^{-1} = \bar{\Delta}_{-1,-2}^2 I_2^{-2} + \bar{\Delta}_{-1,-1}^2 I_2^{-1} + \bar{\Delta}_{-1,0}^2 I_2^0 + \bar{\Delta}_{-1,1}^2 I_2^1 + \bar{\Delta}_{-1,2}^2 I_2^2 \tag{3.33c}$$

The rotation matrices $\bar{\Delta}_{m,m'}^n$ are fixed values for a given boundary location and thus are not affected by the differentiation in Eq. (2.31a). Similarly, the other $\bar{I}_n^0$ with even n in Eq. (3.32) are also rotated back to global I_n^m through Eq. (2.19). Physically, $\bar{I}_1^0$ gives the normal heat flux at the wall,

$$\mathbf{q} \cdot \hat{\mathbf{n}} = q_w = \frac{4\pi}{3} \bar{I}_1^0 \tag{3.34}$$

It is seen that part (b) of Eq. (3.31) only requires $\bar{I}_n^0$ for local spherical harmonics $\bar{Y}_n^0$ and the heat flux at the wall, q_w, while the specular reflection, part (a) of Eq. (3.31), requires all of the $\bar{I}_n^m$.

The specular reflection, part (a) of Eq. (3.32), adds no extra terms but changes the coefficients of $\bar{I}_n^m$. Comparing Eq. (3.32) with Eq. (2.15), we find it convenient to define

$$\hat{p}_{n,2i-1}^m = [1 - (-1)^{m+n} \rho^s] p_{n,2i-1}^m - 2\delta_{m,0} \rho^d p_{0,2i-1}^0 p_{n,1}^0 \tag{3.35}$$

and the coefficients $\hat{u}_{l,i}^m$, $\hat{v}_{l,i}^m$ and $\hat{w}_{l,i}^m$ as

$$\hat{u}_{l,i}^m = [1 + (-1)^{(m+l)} \rho^s] u_{l,i}^m \tag{3.36a}$$

$$\hat{v}_{l,i}^m = [1 + (-1)^{(m+l)} \rho^s] v_{l,i}^m + \frac{2}{5} \delta_{m,0} \delta_{l,1} \rho^d p_{0,2i-1}^0 \tag{3.36b}$$

$$\hat{w}_{l,i}^m = [1 + (-1)^{(m+l)} \rho^s] w_{l,i}^m + \frac{2}{3} \delta_{m,0} (\delta_{l,0} + \frac{2}{5} \delta_{l,1}) \rho^d p_{0,2i-1}^0 \tag{3.36c}$$

With these abbreviations and following the relations in [145, 146], i.e., to express the $\bar{I}_n^m$ with odd n in terms of the derivatives of $\bar{I}_n^m$ with even n, and then rotating $\bar{I}_n^m$ back to global coordinates,

Eq. (3.31) is converted into $N(N+1)/2$ boundary conditions for mixed diffuse-specular surfaces: For each $\overline{Y}^m_{2i-1}$, $i = 1, 2, \cdots, (N+1)/2$,

$m = 0$:

$$\begin{aligned}\epsilon I_{bw} p^0_{0,2i-1} = &\sum_{l=0}^{\frac{N-1}{2}} \sum_{m'=-2l}^{2l} \hat{p}^0_{2l,2i-1} \bar{\Delta}^{2l}_{0,m'} I^{m'}_{2l} \\ &+ \frac{\partial}{\partial \tau_{\bar{x}}} \sum_{l=1}^{\frac{N-1}{2}} \sum_{m'=-2l}^{2l} \hat{v}^0_{l,i} \bar{\Delta}^{2l}_{1,m'} I^{m'}_{2l} + \frac{\partial}{\partial \tau_{\bar{y}}} \sum_{l=1}^{\frac{N-1}{2}} \sum_{m'=-2l}^{2l} \hat{v}^0_{l,i} \bar{\Delta}^{2l}_{-1,m'} I^{m'}_{2l} \\ &- \frac{\partial}{\partial \tau_{\bar{z}}} \sum_{l=0}^{\frac{N-1}{2}} \sum_{m'=-2l}^{2l} \hat{w}^0_{l,i} \bar{\Delta}^{2l}_{0,m'} I^{m'}_{2l} \end{aligned} \tag{3.37a}$$

$m \neq 0$:

$$\begin{aligned} 0 = &\sum_{l=0}^{\frac{N-1}{2}} \sum_{m'=-2l}^{2l} \hat{p}^m_{2l,2i-1} \bar{\Delta}^{2l}_{\pm m,m'} I^{m'}_{2l} \\ &- \frac{\partial}{\partial \tau_{\bar{x}}} \sum_{l=l'}^{\frac{N-1}{2}} \sum_{m'=-2l}^{2l} \left[(1 \pm \delta_{m,1}) \hat{u}^m_{l,i} \bar{\Delta}^{2l}_{\pm(m-1),m'} - \hat{v}^m_{l,i} \bar{\Delta}^{2l}_{\pm(m+1),m'} \right] I^{m'}_{2l} \\ &\pm \frac{\partial}{\partial \tau_{\bar{y}}} \sum_{l=1-l'}^{\frac{N-1}{2}} \sum_{m'=-2l}^{2l} \left[(1 \mp \delta_{m,1}) \hat{u}^m_{l,i} \bar{\Delta}^{2l}_{\mp(m-1),m'} + \hat{v}^m_{l,i} \bar{\Delta}^{2l}_{\mp(m+1),m'} \right] I^{m'}_{2l} \\ &- \frac{\partial}{\partial \tau_{\bar{z}}} \sum_{l=0}^{\frac{N-1}{2}} \sum_{m'=-2l}^{2l} \hat{w}^m_{l,i} \overline{\Delta}^{2l}_{\pm m,m'} I^{m'}_{2l} \end{aligned} \tag{3.37b}$$

where we define l' as

$$l' = \begin{cases} 0 \quad \text{for} \quad \overline{Y}^m_{2i-1} \\ 1 \quad \text{for} \quad \overline{Y}^{-m}_{2i-1} \end{cases} \tag{3.38}$$

and again, for $i = (N+1)/2$ only even m are employed Eq. (2.12). The form of Eq. (3.37) is identical to the boundary conditions for black walls, Eq. (2.24). Thus the implementation process will stay the same as the black wall with the newly defined coefficients $\hat{p}^m_{n,2i-1}$, $\hat{u}^m_{l,i}$, $\hat{v}^m_{l,i}$ and $\hat{w}^m_{l,i}$.

For the 2-D Cartesian formulation:

Following the 2-D Cartesian formulation in this thesis, Eq. (3.37) can also be applied to 2-D problems by eliminating the I_n^m with odd m in global coordinates and the $\bar{I}_n^m$ with negative m in the local coordinates. This leads to

$$\bar{I}_2^0 = \bar{\Delta}_{0,-2}^2 I_2^{-2} + \bar{\Delta}_{0,0}^2 I_2^0 + \bar{\Delta}_{0,2}^2 I_2^2 \tag{3.39a}$$

$$\bar{I}_2^1 = \bar{\Delta}_{1,-2}^2 I_2^{-2} + \bar{\Delta}_{1,0}^2 I_2^0 + \bar{\Delta}_{1,2}^2 I_2^2 \tag{3.39b}$$

Then Eq. (3.37) reduces to

For each $\overline{Y}_{2i-1}^m$, $i = 1, 2, \cdots, (N+1)/2$:

$m = 0$:

$$\begin{aligned}\epsilon I_{bw} p_{0,2i-1}^0 = &\sum_{l=0}^{\frac{N-1}{2}} \sum_{m'=-l}^{l} \hat{p}_{2l,2i-1}^0 \bar{\Delta}_{0,2m'}^{2l} I_{2l}^{2m'} + \frac{\partial}{\partial \tau_{\bar{x}}} \sum_{l=1}^{\frac{N-1}{2}} \sum_{m'=-l}^{l} \hat{v}_{l,i}^0 \bar{\Delta}_{1,2m'}^{2l} I_{2l}^{2m'} \\ &- \frac{\partial}{\partial \tau_{\bar{z}}} \sum_{l=0}^{\frac{N-1}{2}} \sum_{m'=-l}^{l} \hat{w}_{l,i}^0 \bar{\Delta}_{0,2m'}^{2l} I_{2l}^{2m'}\end{aligned} \tag{3.40a}$$

$m \neq 0$:

$$\begin{aligned}0 = &\sum_{l=0}^{\frac{N-1}{2}} \sum_{m'=-l}^{l} \hat{p}_{2l,2i-1}^m \bar{\Delta}_{\pm m,2m'}^{2l} I_{2l}^{2m'} \\ &- \frac{\partial}{\partial \tau_{\bar{x}}} \sum_{l=0}^{\frac{N-1}{2}} \sum_{m'=-l}^{l} \left[(1 \pm \delta_{m,1}) \hat{u}_{l,i}^m \bar{\Delta}_{\pm(m-1),m'}^{2l} - \hat{v}_{l,i}^m \bar{\Delta}_{\pm(m+1),2m'}^{2l} \right] I_{2l}^{2m'} \\ &- \frac{\partial}{\partial \tau_{\bar{z}}} \sum_{l=0}^{\frac{N-1}{2}} \sum_{m'=-l}^{l} \hat{w}_{l,i}^m \bar{\Delta}_{\pm m,2m'}^{2l} I_{2l}^{2m'}\end{aligned} \tag{3.40b}$$

the form of Eq. (3.40) is identical to the boundary conditions (2.24) for black walls except for the new definitions of coefficients $\hat{p}_{n,2i-1}^m$, $\hat{u}_{l,i}^m$, $\hat{v}_{l,i}^m$ and $\hat{w}_{l,i}^m$.

For the 2-D axisymmetric formulation:

Since the coefficients $p^m_{n,2i-1}$, $u^m_{l,i}$, $v^m_{l,i}$ and $w^m_{l,i}$ stay unchanged from the general 3-D formulation to the 2-D axisymmetric formulation of the Marshak's boundary conditions for the black walls, the boundary conditions for mixed diffuse-specular surfaces in 2-D axisymmetric formulation can be directly obtained by replacing the coefficients $p^m_{n,2i-1}$, $u^m_{l,i}$, $v^m_{l,i}$ and $w^m_{l,i}$ with the newly defined ones $\hat{p}^m_{n,2i-1}$, $\hat{u}^m_{l,i}$, $\hat{v}^m_{l,i}$ and $\hat{w}^m_{l,i}$:

$$\begin{aligned}
\epsilon I_w p^0_{0,n} = & \sum_{l=0}^{\frac{N-1}{2}} \sum_{m'=0}^{2l} \hat{p}^m_{2l,2i-1} D^{2l}_{|m||m'|}(-\beta) \hat{I}^{m'}_{2l} \\
& - \frac{1}{\beta r} \sum_{l=0}^{\frac{N-1}{2}} \sum_{m'=0}^{2l} \left(\delta^-_m \hat{u}^m_{li} B^{2l}_{|m-1||m'|}(-\beta) + \hat{v}^m_{li} B^{2l}_{|m+1||m'|}(-\beta) \right) \hat{I}^{m'}_{2l} \\
& - \frac{\partial}{\partial \tau_{\bar{x}}} \sum_{l=0}^{\frac{N-1}{2}} \sum_{m'=0}^{2l} \left(\delta^+_m \hat{u}^m_{li} D^{2l}_{|m-1||m'|}(-\beta) - \hat{v}^m_{li} D^{2l}_{|m+1||m'|}(-\beta) \right) \hat{I}^{m'}_{2l} \\
& - \frac{\partial}{\partial \tau_{\bar{z}}} \sum_{l=1}^{\frac{N-1}{2}} \sum_{m'=0}^{2l} \hat{w}^m_{li} D^{2l}_{|m||m'|}(-\beta) \hat{I}^{m'}_{2l}
\end{aligned} \tag{3.41}$$

3.2.2 Boundary Condition for Specified Radiative Heat Flux at the Wall

The Marshak's boundary conditions can be modified to develop the boundary conditions for specified radiative heat flux at the wall. This is achieved through elimination of I_w by combining the Marshak's boundary condition Eq. (2.24) with the equations expressing the heat flux at the wall which are Eqs. (2.30) and (2.31). It will be shown in Chapter 4 that after the Marshak's boundary conditions are transformed to Robin-type boundary conditions, only the boundary condition for I^0_0 includes the radiative intensity I_w from the wall. Based on the relation between the radiative flux and local intensity coefficients, Eqs. (2.30) and (2.31), the specified radiative wall flux condition is implemented by replacing the equation for I^0_0 with Eq. (2.31a), where the $\bar{I}^0_1$ is given by Eq. (2.31a). For a given q_w, this leads to a boundary condition of the Neumann type,

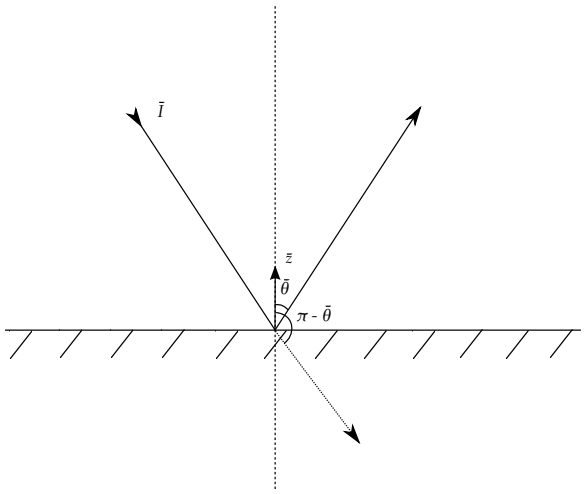

Figure 3.4: Schematic of a wall that specularly reflects incident radiation.

$$\frac{\partial I_0^0}{\partial \tau_{\bar{z}}} = \frac{\partial \bar{I}_0^0}{\partial \tau_{\bar{z}}} = -\frac{2}{5}\frac{\partial \bar{I}_2^0}{\partial \tau_{\bar{z}}} + \frac{3}{5}\frac{\partial \bar{I}_2^1}{\partial \tau_{\bar{x}}} + \frac{3}{5}\frac{\partial \bar{I}_2^{-1}}{\partial \tau_{\bar{y}}} - \frac{3}{4\pi}q_w \tag{3.42}$$

if $q_w = 0$ (insulated boundary),

$$\frac{\partial \bar{I}_0}{\partial \tau_{\bar{z}}} = -\frac{2}{5}\frac{\partial \bar{I}_2^0}{\partial \tau_{\bar{z}}} + \frac{3}{5}\frac{\partial \bar{I}_2^1}{\partial \tau_{\bar{x}}} + \frac{3}{5}\frac{\partial \bar{I}_2^{-1}}{\partial \tau_{\bar{y}}} \tag{3.43}$$

Again, the local intensity coefficients $\bar{I}_n^m$ in Eq. (3.43) are rotated back to global I_n^m through the rotation function (2.19), which expands to Eq. (3.33) for the 3-D formulation and Eq. (3.39) for the 2-D formulation.

3.2.3 Symmetry/Specular Boundaries

Specular reflection is one common type of reflection of light, in which the angle of incidence is equal to the angle of reflection with respect to the surface normal, as has been shown in Fig. 3.4. At such symmetry/specular reflection boundary, the local polar angle $\bar{\theta}$ is measured from the local $\bar{z}$-axis, and, therefore,

$$\bar{I}(\bar{\theta}, \bar{\psi}) = \bar{I}(\pi - \bar{\theta}, \bar{\psi}) \tag{3.44}$$

Equation (2.4) shows the odd-power dependence on $\cos\bar{\theta}$ when $n + m$ is odd, thus all $\bar{I}_n^m = 0$ when $n + m$ is odd, which provides the required $N(N + 1)/2$ boundary conditions. For example, for P_3 approximation, the corresponding boundary conditions are $\bar{I}_1^0 = 0$, $\bar{I}_2^{\pm 1} = 0$, $\bar{I}_3^0 = 0$ and $\bar{I}_3^{\pm 2} = 0$. Since only I_n^m with even n are solved for, $\bar{I}_n^m$ with odd n must be expressed in terms of $\bar{I}_{n+1}^m$ and $\bar{I}_{n-1}^m$. Applying the relationship between $\bar{I}_n^m$, $\bar{I}_{n+1}^m$ and $\bar{I}_{n-1}^m$ [145], while connecting the global I_n^m with the local $\bar{I}_n^m$ through the rotation function Eq. (2.19), the $N(N + 1)/2$ boundary conditions are found as: For all even n ($n = 0, 2, \cdots, N - 1$),

when m is even:

$$\frac{\partial \bar{I}_n^m}{\partial \tau_{\bar{z}}} = \frac{\partial}{\partial \tau_{\bar{z}}} \sum_{m'=-n}^{n} \bar{\Delta}_{m,m'}^n I_n^{m'} = 0 \tag{3.45a}$$

when m is odd:

$$\bar{I}_n^m = \sum_{m'=-n}^{n} \bar{\Delta}_{m,m'}^n I_n^{m'} = 0 \tag{3.45b}$$

It is worth mentioning that the above derivation is not based on Marshak's boundary condition, while it gives the same boundary conditions as Eq. (3.37) for perfectly specular surfaces ($\rho_s = 1$), as it must (Appendix C).

For the case of m=0, $\bar{I}_0^0 = I_0^0$, and Eq. (3.45a) is a boundary condition of the second type, which can be applied directly. For the remainder of the boundary conditions, the variables I_n^m and their surface normal derivatives, $\partial I_n^m / \partial \tau_{\bar{z}}$, are coupled through the summation terms in Eq. (3.45), and its implementation will be discussed in the Chapter 4 in detail.

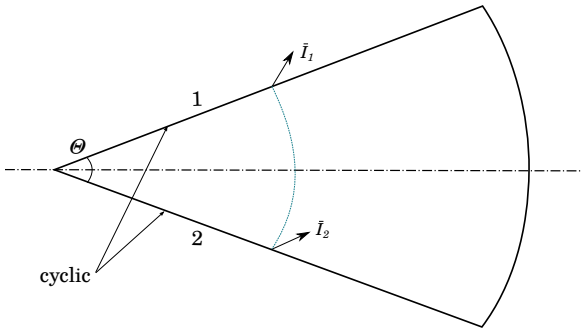

Figure 3.5: Schematic of two cyclic walls of a wedge geometry.

3.2.4 Cyclic Boundaries

Cyclic boundary conditions are frequently employed to reduce the computational cost for large-scale simulations where the physical fields vary in a periodic pattern. One might be temped to just let each intensity coefficients at one cyclic boundary face equal to their values at the other half of the cyclic boundary face. That happens to be correct only if there are no angular differences between the two cyclic faces. When being cyclic in the sense of rotating around an axis (Fig. 3.5), Eq. (3.7) when $m = 0$ and Eq. (3.9) when $m \neq 0$ must be applied as the boundary conditions, which involves the coupling of I_n^m and I_n^{-m} when $m \neq 0$. While the implementation of Eq. (3.7) is straightforward, implementation of Eq. (3.9) requires special treatment, which will be discussed in detail in the next chapter.

3.2.5 Axisymmetric Boundary Condition at Centerline ($r = 0$)

In finite volume-based grid systems, a wedge-shape grid with one node in the azimuthal direction is often used for axisymmetric applications. The tip of the wedge needs to be cut off to avoid a $(1/r)$-type singularity at the center where $r = 0$. At the centerline surface, boundary conditions for all intensity coefficients $\hat{I}_n^m$ need to be defined. The radiative intensity I is independent of the azimuthal angle ψ at the center of a cylinder and $\partial I/\partial r = 0$ at $r = 0$ for axisymmetric simulations. Therefore, the intensity coefficients at the centerline surface follow the relationship of

$$\left.\frac{\partial \hat{I}_n^m}{\partial r}\right|_{r=0} = 0, \quad m=0 \tag{3.46a}$$

$$\left.\hat{I}_n^m\right|_{r=0} = 0, \quad m \neq 0 \tag{3.46b}$$

which was applied in neutron transport problems in axisymmetric geometry [141].

Chapter 4

Implementation

This chapter describes the implementation of the high-order P_N methods. Solutions for the intensity coefficients of high-order P_N methods are obtained by numerical methods for the system of coupled elliptic PDEs and boundary conditions. Implementation consists of two parts: numerical discretization and solution. Discussion of the numerical method, primarily within the framework of the finite volume method (FVM) and, the segregated solution method on the `OpenFOAM®` platform will be presented in the following sections. The finite volume method [2, 221–224] is a major numerical method that transforms the partial differential equations into algebraic equations by representing conservation laws over cell-based control volumes. These resulting algebraic equations are then solved through matrix operations. Generally, the solution methods to solve the system of block matrices, resulting from the coupled PDEs can be roughly divided into two categories: one is to solve the system in a segregated manner [225, 226] in which each individual elliptic PDE can be efficiently solved by standard PDE solvers in many popular CFD softwares such as `OpenFOAM®`; the other is to solve the entire block-coupled matrix. The former requires outer iterations due to coupling between PDEs, while the latter is more experimental and requires more computational resources for practical applications.

`OpenFOAM®` (Open Field Operation and Manipulation), developed at Imperial College [84,

227], is a finite volume-based C++ software package that can add user-defined modules. It has been gradually gaining popularity among academic organizations and is widely used for fluid dynamics and heat transfer simulations. The main advantage of OpenFOAM® is its professional objective-oriented interface for coupling different modules, which is very convenient for multi-physics simulations, e.g., adding a radiative transfer module to the combustion simulations. The OpenFOAM® platform also provides support for parallelization at a fundamental level, so that user-defined modules can be parallelized almost effortlessly. The high-order P_N solver (up to the order of 7) is a part of a nongray radiative transfer module from Modest's group, which is currently being integrated into OpenFOAM® 2.2.x and 2.3.x. The module offers a variety of RTE solvers and spectral models, which are ready to be coupled with single-phase and multiphase combustion problems. The radiation module obtains its inputs (temperature, pressure, gas species, particles, etc.) from other existing OpenFOAM® libraries, and then returns the radiative heat source back to the energy equation within the Navier-Stokes module.

At the end of this chapter, a finite difference (FDM) implementation of high-order P_N methods in GNU Octave®[1] [228], limited to 1-D axisymmetric geometry will also be briefly introduced, which is used both for verification purposes and as an experiment of direct block-coupled solutions.

4.1 Implementation of High-Order P_N Methods in OpenFOAM®

4.1.1 Implementation of Governing Equations

The FVM implementation of the high-order P_N methods for three-dimensional geometries is presented first. The governing equations of their 3-D P_N formulation, Eq. (2.9), are comprised of $N_2 = N(N+1)/2$ second-order coupled elliptic PDEs. It is convenient to denote each governing equation characterized by spherical harmonic Y_n^m as Y_i, and the spatial field of each intensity coefficient $\mathbf{I}_n^m(\mathbf{r})$ as $\mathbf{\Phi}_i(\mathbf{r})$ and each symbol I_n^m as ϕ_i (Table. 4.1).

[1] a free high-level programming language which is similar to MATLAB®

Table 4.1: Denotations and indices of unknowns and governing equations.

i	ϕ_i	$\mathbf{I}_n^m$	Y_n^m	i	ϕ_i	$\mathbf{I}_n^m$	Y_n^m
1	ϕ_1	I_0^0	Y_0^0	15	ϕ_{15}	I_4^4	Y_4^4
2	ϕ_2	I_2^{-2}	Y_2^{-2}	16	ϕ_{16}	I_6^{-6}	Y_6^{-6}
3	ϕ_3	I_2^{-1}	Y_2^{-1}	17	ϕ_{17}	I_6^{-5}	Y_6^{-5}
4	ϕ_4	I_2^0	Y_2^0	18	ϕ_{18}	I_6^{-4}	Y_6^{-4}
5	ϕ_5	I_2^1	Y_2^1	19	ϕ_{19}	I_6^{-3}	Y_6^{-3}
6	ϕ_6	I_2^2	Y_2^2	20	ϕ_{20}	I_6^{-2}	Y_6^{-2}
7	ϕ_7	I_4^{-4}	Y_4^{-4}	21	ϕ_{21}	I_6^{-1}	Y_6^{-1}
8	ϕ_8	I_4^{-3}	Y_4^{-3}	22	ϕ_{22}	I_6^0	Y_6^0
9	ϕ_9	I_4^{-2}	Y_4^{-2}	23	ϕ_{23}	I_6^1	Y_6^1
10	ϕ_{10}	I_4^{-1}	Y_4^{-1}	24	ϕ_{24}	I_6^2	Y_6^2
11	ϕ_{11}	I_4^0	Y_4^0	25	ϕ_{25}	I_6^3	Y_6^3
12	ϕ_{12}	I_4^1	Y_4^1	26	ϕ_{26}	I_6^4	Y_6^4
13	ϕ_{13}	I_4^2	Y_4^2	27	ϕ_{27}	I_6^5	Y_6^5
14	ϕ_{14}	I_4^3	Y_4^3	28	ϕ_{28}	I_6^6	Y_6^6

The ϕ_i terms in each governing PDE Y_i are collected as

$$\begin{aligned}(\mathcal{L}_{xx} + \mathcal{L}_{yy} - 2\mathcal{L}_{zz})c_2^{nm}\phi_i + \mathcal{L}_{zz}\phi_i - (1 - \omega\delta_{1i})\phi_i \\ = c_2^{nm}\nabla_\tau^2\phi_i + (1 - 3c_2^{nm})\mathcal{L}_{zz}\phi_i - (1 - \omega\delta_{1i})\phi_i\end{aligned} \tag{4.1}$$

In the FVM, the domain is discretized into small finite volumes or computational cells (denoted as C), and each cell is bounded by a set of flat faces (denoted as f) and each face is shared with only one neighboring cell (denoted as F). Integrating over the computational cell, the governing equation Y_i becomes

$$\int_{V_C} \frac{c_2^{nm}}{\beta}\nabla\cdot\left(\frac{1}{\beta}\nabla\phi_i\right)\mathrm{d}V - (1 - \omega\delta_{1i})\int_{V_C}\phi_i\mathrm{d}V = \int_{V_C} E_i\mathrm{d}V \tag{4.2}$$

where E_i includes all the explicit terms including the constant source term $-(1 - \omega)\delta_{1i}I_b$, the re-

maining $(1 - 3c_2^{nm})\mathcal{L}_{zz}\phi_i$ term and all the double derivatives and cross derivatives of ϕ_j in the Y_i equation ($\mathcal{L}_{xx}\phi_j$, $\mathcal{L}_{xz}\phi_j$, etc.), i.e.,

$$E_i = -(1-\omega)\delta_{1i}I_b - (1 - 3c_2^{nm})\mathcal{L}_{zz}\phi_i + \sum_{j=1, j\neq i}^{N_2} f_j(\mathcal{L}\phi_j) \tag{4.3}$$

Following Gauss's divergence theorem,

$$\int_V \nabla \cdot \mathbf{J} \mathrm{d}V = \oint_S \mathbf{J} \cdot \hat{\mathbf{n}} \mathrm{d}S \tag{4.4}$$

Equation (4.1) becomes

$$c_2^{nm} \sum_f \left(\frac{1}{\beta}\nabla\phi_i\right)_f \cdot \mathbf{S}_f - (1 - \omega\delta_{1i})\beta_C\phi_{iC}V_C = \beta_C E_{iC} V_C \tag{4.5}$$

where $\mathbf{S}_f$ is the surface area vector which points outward and has the magnitude of the area of the face, V_C is the volume of the computational cell. For clarity, only orthogonal meshes are discussed in this section. The gradient/flux at the cell faces are discretized as

$$\left(\frac{1}{\beta}\nabla\phi\right)_f \cdot \mathbf{S}_f = \left(\frac{1}{\beta}\right)_f \frac{S_f}{d_{FC}}(\phi_F - \phi_C) \tag{4.6}$$

where d_{FC} is the distance of the center of the owner cell C, and that of the neighboring cell F. Applying the discretization as Eq. (4.6) to Eq. (4.5), Equation (4.5) is readily rearranged in the algebraic form to construct the coefficient matrix:

$$a_C\phi_C + \sum_F a_F\phi_F = b_C \tag{4.7}$$

with the coefficients representing the internal cell found as:

$$a_C = -c_2^{nm} \sum_f \left(\frac{1}{\beta}\right)_f \frac{S_f}{d_{FC}} - (1 - \omega\delta_{1i})\beta_C V_C \tag{4.8a}$$

$$a_F = c_2^{nm} \left(\frac{1}{\beta}\right)_f \frac{S_f}{d_{FC}} \tag{4.8b}$$

$$b_C = \beta_C E_{iC} V_C \tag{4.8c}$$

where E_{iC}, Eq. (4.3), requires the calculation of double derivatives and cross derivatives, which can be obtained by calculating the gradients twice through the Gauss's gradient theorem, i.e.,

$$\int_V \nabla J \mathrm{d}V = \oint_S J \mathrm{d}\mathbf{S} \tag{4.9}$$

therefore,

$$\nabla\phi_C = \frac{1}{V_C} \sum_f \phi_f \mathbf{S_f} \tag{4.10}$$

where ϕ_f is obtained by interpolating the surrounding values ϕ_C and ϕ_F.

$$\phi_f = w_f \phi_F + (1 - w_f)\phi_C \tag{4.11}$$

where w_f is the face weighting factor. If linear interpolation is employed, for an orthogonal grid:

$$\phi_f = \frac{d_{Ff}}{d_{FC}}(\phi_C - \phi_F) + \phi_F \tag{4.12}$$

where d_{Ff} is the distance between the neighboring cell center F and the center of the sharing face f.

4.1.2 Implementation of Marshak's Boundary Condition

Since the segregated solution method is employed, the boundary conditions expressed in Eq. (2.24) cannot be directly implemented efficiently. A matrix transformation is required so that individual Robin boundary conditions can be explicitly associated with each governing equation Y_i as

$$\phi_i + Z_{i,i}\frac{\partial \phi_i}{\partial \tau_{\overline{z}}} = \delta_{1i} I_w + f_i\left(\frac{\partial \phi_j}{\partial \tau_{\overline{x}}}, \frac{\partial \phi_j}{\partial \tau_{\overline{y}}}, \frac{\partial \phi_j}{\partial \tau_{\overline{z}}}\right) \tag{4.13}$$

at the boundary, where $Z_{i,i}$ is a constant scalar and f_i is a function of partial derivatives of other intensity coefficients ϕ_j, including the tangential derivatives of ϕ_j. Such a formulation can be efficiently obtained by first expressing the system of $N(N+1)/2$ boundary conditions in matrix form, and then transforming the matrices to generate one Robin-type boundary condition for each corresponding governing equation.

We will here take the Marshak's boundary conditions of the P_3 approximation as a demonstration to show the construction of coefficient matrices. The associated local spherical harmonics for Marshak's boundary condition for P_3 are $\overline{Y}_1^0, \overline{Y}_1^{-1}, \overline{Y}_1^1, \overline{Y}_3^0, \overline{Y}_3^{-2}$ and $\overline{Y}_3^2$. The coefficients in front of I_n^m and their derivatives for each boundary condition are determined from m and n pairs of the local spherical harmonics. Note that the rows of the coefficient matrices can be in any order, and here the rows are ordered by $|m|$. The first term on the right-hand side of boundary conditions (2.24a) for equation of $\overline{Y}_1^0$ $(n = 1, m = 0)$ is

$$\sum_{l=0}^{\frac{N-1}{2}} \sum_{m'=-2l}^{2l} p_{2l,1}^0 \overline{\Delta}_{0,m'}^{2l} I_{2l}^{m'} = \left[\ p_{0,1}^0 \overline{\Delta}_{0,0}^0, p_{2,1}^0 \overline{\Delta}_{0,-2}^2, p_{2,1}^0 \overline{\Delta}_{0,-1}^2, p_{2,1}^0 \overline{\Delta}_{0,0}^2, p_{2,1}^0 \overline{\Delta}_{0,1}^2, p_{2,1}^0 \overline{\Delta}_{0,2}^2\ \right] \cdot \boldsymbol{\phi} = \mathbf{q}_{(1,0)} \cdot \boldsymbol{\phi} \tag{4.14}$$

the subscripts of $\mathbf{q}_{(n,m)}$ show the n and m associated with $\overline{Y}_n^m$, and the vector $\boldsymbol{\phi}$ is defined as

$$\boldsymbol{\phi} = \begin{bmatrix} \phi_1 \\ \phi_2 \\ \phi_3 \\ \phi_4 \\ \phi_5 \\ \phi_6 \end{bmatrix} = \begin{bmatrix} I_0^0 \\ I_2^{-2} \\ I_2^{-1} \\ I_2^0 \\ I_2^1 \\ I_2^2 \end{bmatrix} \tag{4.15}$$

Applying the same formulation to the rest of the equations associated with the remaining $\overline{Y}_n^m$, the coefficients in front of I_n^m for the entire system of equations may be expressed as

$$\mathbf{Q} = \begin{bmatrix} \mathbf{q}_{(1,0)} \\ \mathbf{q}_{(3,0)} \\ \mathbf{q}_{(1,-1)} \\ \mathbf{q}_{(1,1)} \\ \mathbf{q}_{(3,-2)} \\ \mathbf{q}_{(3,2)} \end{bmatrix} = \begin{bmatrix} p_{0,1}^0 \overline{\Delta}_{0,0}^0 & p_{2,1}^0 \overline{\Delta}_{0,-2}^2 & p_{2,1}^0 \overline{\Delta}_{0,-1}^2 & p_{2,1}^0 \overline{\Delta}_{0,0}^2 & p_{2,1}^0 \overline{\Delta}_{0,1}^2 & p_{2,1}^0 \overline{\Delta}_{0,2}^2 \\ p_{0,3}^0 \overline{\Delta}_{0,0}^0 & p_{2,3}^0 \overline{\Delta}_{0,-2}^2 & p_{2,3}^0 \overline{\Delta}_{0,-1}^2 & p_{2,3}^0 \overline{\Delta}_{0,0}^2 & p_{2,3}^0 \overline{\Delta}_{0,1}^2 & p_{2,3}^0 \overline{\Delta}_{0,2}^2 \\ 0 & p_{2,1}^1 \overline{\Delta}_{-1,-2}^2 & p_{2,1}^1 \overline{\Delta}_{-1,-1}^2 & p_{2,1}^1 \overline{\Delta}_{-1,0}^2 & p_{2,1}^1 \overline{\Delta}_{-1,1}^2 & p_{2,1}^1 \overline{\Delta}_{-1,2}^2 \\ 0 & p_{2,1}^1 \overline{\Delta}_{1,-2}^2 & p_{2,1}^1 \overline{\Delta}_{1,-1}^2 & p_{2,1}^1 \overline{\Delta}_{1,0}^2 & p_{2,1}^1 \overline{\Delta}_{1,1}^2 & p_{2,1}^1 \overline{\Delta}_{1,2}^2 \\ 0 & p_{2,3}^2 \overline{\Delta}_{-2,-2}^2 & p_{2,3}^2 \overline{\Delta}_{-2,-1}^2 & p_{2,3}^2 \overline{\Delta}_{-2,0}^2 & p_{2,3}^2 \overline{\Delta}_{-2,1}^2 & p_{2,3}^2 \overline{\Delta}_{-2,2}^2 \\ 0 & p_{2,3}^2 \overline{\Delta}_{2,-2}^2 & p_{2,3}^2 \overline{\Delta}_{2,-1}^2 & p_{2,3}^2 \overline{\Delta}_{2,0}^2 & p_{2,3}^2 \overline{\Delta}_{2,1}^2 & p_{2,3}^2 \overline{\Delta}_{2,2}^2 \end{bmatrix} \tag{4.16}$$

Let $\mathbf{Q}_{\overline{x}}$, $\mathbf{Q}_{\overline{y}}$, $\mathbf{Q}_{\overline{z}}$ be the coefficient matrices for $\partial\boldsymbol{\phi}/\partial\tau_{\overline{x}}$, $\partial\boldsymbol{\phi}/\partial\tau_{\overline{y}}$ and $\partial\boldsymbol{\phi}/\partial\tau_{\overline{z}}$, respectively. The

resulting form for the $\mathbf{Q}_{\overline{x}}$ matrix is shown here:

$$\mathbf{Q}_{\overline{x}} = \begin{bmatrix} \mathbf{q}_{\overline{x}(1,0)} \\ \mathbf{q}_{\overline{x}(3,0)} \\ \mathbf{q}_{\overline{x}(1,-1)} \\ \mathbf{q}_{\overline{x}(1,1)} \\ \mathbf{q}_{\overline{x}(3,-2)} \\ \mathbf{q}_{\overline{x}(3,2)} \end{bmatrix} = \begin{bmatrix} 0 & v^0_{1,1}\overline{\Delta}^2_{1,-2} & v^0_{1,1}\overline{\Delta}^2_{1,-1} & \dots & v^0_{1,1}\overline{\Delta}^2_{1,2} \\ 0 & v^0_{1,2}\overline{\Delta}^2_{1,-2} & v^0_{1,2}\overline{\Delta}^2_{1,-1} & \dots & v^0_{1,2}\overline{\Delta}^2_{1,2} \\ 0 & v^1_{1,1}\overline{\Delta}^2_{-2,-2} & v^1_{1,1}\overline{\Delta}^2_{-1,-1} & \dots & v^1_{1,1}\overline{\Delta}^2_{-2,2} \\ v^1_{0,1}\overline{\Delta}^0_{2,0} & v^1_{1,1}\overline{\Delta}^2_{2,-2} & v^1_{1,1}\overline{\Delta}^2_{2,-1} & \dots & v^1_{1,1}\overline{\Delta}^2_{2,2} \\ 0 & v^2_{1,2}\overline{\Delta}^2_{2,-2} & v^2_{1,2}\overline{\Delta}^2_{2,-1} & \dots & v^2_{1,2}\overline{\Delta}^2_{2,2} \\ v^2_{0,2}\overline{\Delta}^0_{3,0} & v^2_{1,2}\overline{\Delta}^2_{3,-2} & v^2_{1,2}\overline{\Delta}^2_{3,-1} & \dots & v^2_{1,2}\overline{\Delta}^2_{3,2} \end{bmatrix}$$
$$- \begin{bmatrix} 0 & 0 & 0 & \dots & 0 \\ 0 & 0 & 0 & \dots & 0 \\ 0 & 0 & 0 & \dots & 0 \\ 2u^1_{0,1}\overline{\Delta}^0_{0,0} & 2u^1_{1,1}\overline{\Delta}^2_{0,-2} & 2u^1_{1,1}\overline{\Delta}^2_{0,-1} & \dots & 2u^1_{1,1}\overline{\Delta}^2_{0,2} \\ 0 & 2u^2_{1,2}\overline{\Delta}^2_{-1,-2} & 2u^2_{1,2}\overline{\Delta}^2_{-1,-1} & \dots & 2u^2_{1,2}\overline{\Delta}^2_{-1,2} \\ u^2_{0,2}\overline{\Delta}^0_{1,0} & u^2_{1,2}\overline{\Delta}^2_{1,-2} & u^2_{1,2}\overline{\Delta}^2_{1,-1} & \dots & u^2_{1,2}\overline{\Delta}^2_{1,2} \end{bmatrix} \tag{4.17}$$

Finally, let $\mathbf{p}$ be the coefficient vector for I_w on the left-hand side of Eq. (2.24a), which only has a nonzero value when $m = 0$:

$$\mathbf{p} = \begin{bmatrix} p_{(1,0)} \\ p_{(3,0)} \\ p_{(1,-1)} \\ p_{(1,1)} \\ p_{(3,-2)} \\ p_{(3,2)} \end{bmatrix} = \begin{bmatrix} p^0_{0,1} \\ p^0_{0,3} \\ 0 \\ 0 \\ 0 \\ 0 \end{bmatrix} \tag{4.18}$$

Two observations regarding the above matrices may be made. First, all coefficient matrices are functions of geometry only, and thus they only need to be calculated once. The second is that

the first column of matrix $\mathbf{Q}$ and vector $\mathbf{p}$ are identical, which leads to

$$\mathbf{Q}^{-1} \cdot \mathbf{p} = [1, 0, 0, 0, 0, 0]^T \tag{4.19}$$

which will be employed later in this section. Equation (4.19) can be proved by applying Gaussian elimination to the system of $\mathbf{Q} \cdot \mathbf{x} = \mathbf{p}$ where vector $\mathbf{p}$ equals the the first row of the invertible matrix $\mathbf{Q}$.

For general orders of P_N, the row vectors of the boundary condition are given by

$$\mathbf{q}_{(n,\pm m)} = \left[\delta_{m,0} p^m_{0,n}, p^m_{2,n}\overline{\Delta}^2_{\pm m,-2}, p^m_{2,n}\overline{\Delta}^2_{\pm m,-1}, \ldots, p^m_{2,n}\overline{\Delta}^2_{\pm m,2}, p^m_{4,n}\overline{\Delta}^4_{\pm m,-4}, \ldots, p^m_{N-1,n}\overline{\Delta}^{N-1}_{\pm m,N-1}\right] \tag{4.20a}$$

$$\mathbf{q}_{\overline{x}(n,0)} = \left[0, v^0_{1,i^*}\overline{\Delta}^2_{1,-2}, v^0_{1,i^*}\overline{\Delta}^2_{1,-1}, \ldots, v^0_{1,i^*}\overline{\Delta}^2_{1,2}, \ldots, v^0_{\frac{N-1}{2},i^*}\overline{\Delta}^{N-1}_{1,N-1}\right] \tag{4.20b}$$

$$\begin{aligned}\mathbf{q}_{\overline{x}(n,-m)} = &\left[0, v^m_{1,i^*}\overline{\Delta}^2_{-(m+1),-2}, v^m_{1,i^*}\overline{\Delta}^2_{-(m+1),-1}, \ldots, v^m_{1,i^*}\overline{\Delta}^2_{-(m+1),2}, \ldots, v^m_{\frac{N-1}{2},i^*}\overline{\Delta}^{N-1}_{-(m+1),N-1}\right] \\ &- (1-\delta_{m,1})\left[0, u^m_{1,i^*}\overline{\Delta}^2_{-(m-1),-2}, u^m_{1,i^*}\overline{\Delta}^2_{-(m-1),-1}, \ldots, u^m_{1,i^*}\overline{\Delta}^2_{-(m-1),2}, \ldots, u^m_{\frac{N-1}{2},i^*}\overline{\Delta}^{N-1}_{-(m-1),N-1}\right]\end{aligned} \tag{4.20c}$$

$$\begin{aligned}\mathbf{q}_{\overline{x}(n,+m)} = &\left[v^m_{0,i^*}\overline{\Delta}^0_{m+1,0}, v^m_{1,i^*}\overline{\Delta}^2_{m+1,-2}, v^m_{1,i^*}\overline{\Delta}^2_{m+1,-1}, \ldots, v^m_{1,i^*}\overline{\Delta}^2_{m+1,2}, \ldots, v^m_{\frac{N-1}{2},i^*}\overline{\Delta}^{N-1}_{m+1,N-1}\right] \\ &- (1+\delta_{m,1})\left[u^m_{0,i^*}\overline{\Delta}^0_{m-1,0}, u^m_{1,i^*}\overline{\Delta}^2_{m-1,-2}, u^m_{1,i^*}\overline{\Delta}^2_{m-1,-1}, \ldots, u^m_{1,i^*}\overline{\Delta}^2_{m-1,2}, \ldots, u^m_{\frac{N-1}{2},i^*}\overline{\Delta}^{N-1}_{m-1,N-1}\right]\end{aligned} \tag{4.20d}$$

$$\mathbf{q}_{\overline{y}(n,0)} = \left[0, v^0_{1,i^*}\overline{\Delta}^2_{-1,-2}, v^0_{1,i^*}\overline{\Delta}^2_{-1,-1}, \ldots, v^0_{1,i^*}\overline{\Delta}^2_{-1,2}, \ldots, v^0_{\frac{N-1}{2},i^*}\overline{\Delta}^{N-1}_{-1,N-1}\right] \tag{4.20e}$$

$$\begin{aligned}\mathbf{q}_{\overline{y}(n,-m)} = &-\left[v^m_{0,i^*}\overline{\Delta}^0_{m+1,0}, v^m_{1,i^*}\overline{\Delta}^2_{m+1,-2}, v^m_{1,i^*}\overline{\Delta}^2_{m+1,-1}, \ldots, v^m_{1,i^*}\overline{\Delta}^2_{m+1,2}, \ldots, v^m_{\frac{N-1}{2},i^*}\overline{\Delta}^{N-1}_{m+1,N-1}\right] \\ &-(1+\delta_{m,0})\left[u^m_{0,i^*}\overline{\Delta}^0_{m-1,0}, u^m_{1,i^*}\overline{\Delta}^2_{m-1,-2}, u^m_{1,i^*}\overline{\Delta}^2_{m-1,-1}, \ldots, u^m_{1,i^*}\overline{\Delta}^2_{m-1,2}\ldots, u^m_{\frac{N-1}{2},i^*}\overline{\Delta}^{N-1}_{m-1,N-1}\right]\end{aligned} \tag{4.20f}$$

$$\begin{aligned}\mathbf{q}_{\overline{y}(n,+m)} = &\left[0, v^m_{1,i^*}\overline{\Delta}^2_{-(m+1),-2}, v^m_{1,i^*}\overline{\Delta}^2_{-(m+1),-1}, \ldots, v^m_{1,i^*}\overline{\Delta}^2_{-(m+1),2}, \ldots, v^m_{\frac{N-1}{2},i^*}\overline{\Delta}^{N-1}_{-(m+1),N-1}\right] \\ &+(1-\delta_{m,1})\left[0, u^m_{1,i^*}\overline{\Delta}^2_{-(m-1),-2}, u^m_{1,i^*}\overline{\Delta}^2_{-(m-1),-1}, \ldots, u^m_{1,i^*}\overline{\Delta}^2_{-(m-1),2}, \ldots, u^m_{\frac{N-1}{2},i^*}\overline{\Delta}^{N-1}_{-(m-1),N-1}\right]\end{aligned} \tag{4.20g}$$

$$\mathbf{q}_{\overline{z}(n,\pm m)} = -\left[\delta_{m,0}w^m_{0,n}, w^m_{2,n}\overline{\Delta}^2_{\pm m,-2}, w^m_{2,n}\overline{\Delta}^2_{\pm m,-1}, \ldots, w^m_{2,n}\overline{\Delta}^2_{\pm m,2}, w^m_{4,n}\overline{\Delta}^4_{\pm m,-4}, , \ldots, w^m_{N-1,n}\overline{\Delta}^{N-1}_{\pm m,N-1}\right] \tag{4.20h}$$

where the case of $m = 0$ is included in the $\pm m$ notation for Eq. (4.20a), while for the rest, the $m = 0$ case is shown separately for clarity. $i^* = (n+1)/2$ and adding $*$ is just to avoid symbol conflict for this chapter.

The entire set of boundary equations (2.24) for general P_N boundary conditions may now be written in matrix form as

$$\mathbf{Q}\cdot\boldsymbol{\phi} + \mathbf{Q}_{\overline{x}}\cdot\frac{\partial\boldsymbol{\phi}}{\partial\tau_{\overline{x}}} + \mathbf{Q}_{\overline{y}}\cdot\frac{\partial\boldsymbol{\phi}}{\partial\tau_{\overline{y}}} + \mathbf{Q}_{\overline{z}}\cdot\frac{\partial\boldsymbol{\phi}}{\partial\tau_{\overline{z}}} = \mathbf{p}I_w \tag{4.21}$$

After all elements of the coefficient matrices are calculated, the next step is to convert Eq. (4.21) into individual Robin-type boundary conditions, Eq. (4.13), which can then be directly applied to each corresponding governing equation Y_i. For consistency of the notation, let i be the row index of the matrices, as given by Table. 4.1, the $(N+1)N/2$ Robin boundary conditions are

$$\phi_i + Z_{i,i}\frac{\partial\phi_i}{\partial\tau_{\overline{z}}} = \delta_{1i}I_w - \sum_{j=1,j\neq i}^{N_2}\left[X_{i,j}\frac{\partial\phi_j}{\partial\tau_{\overline{x}}} + Y_{i,j}\frac{\partial\phi_j}{\partial\tau_{\overline{y}}} + Z_{i,j}\frac{\partial\phi_j}{\partial\tau_{\overline{z}}}\right] \tag{4.22}$$

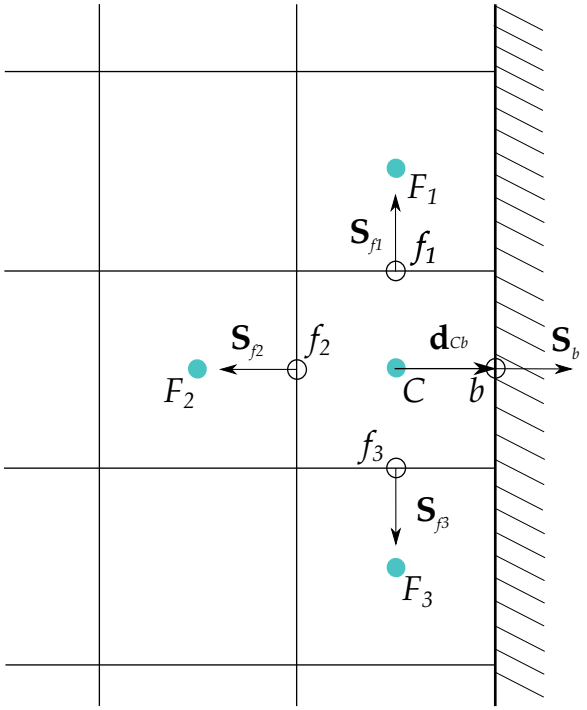

Figure 4.1: Schematic of one boundary cell and its neighboring cell.

where

$$\begin{aligned} \mathbf{X} &= \mathbf{Q}^{-1} \cdot \mathbf{Q}_{\bar{\mathbf{x}}} \\ \mathbf{Y} &= \mathbf{Q}^{-1} \cdot \mathbf{Q}_{\bar{\mathbf{y}}} \\ \mathbf{Z} &= \mathbf{Q}^{-1} \cdot \mathbf{Q}_{\bar{\mathbf{z}}} \end{aligned} \tag{4.23}$$

The coefficient matrix for the normal derivative $\partial\boldsymbol{\phi}/\partial\tau_{\bar{z}}$ is split into two parts. The diagonal elements of $\mathbf{Z}$ are kept on the left-hand side, and the rest are placed on the right-hand side. In order to calculate $\mathbf{X}$, $\mathbf{Y}$ and $\mathbf{Z}$, LU decomposition [229] of $\mathbf{Q}$ is employed. Equation (4.19) is readily shown to be valid for arbitrary orders of P_N, and thus the coefficient in front of I_w in Eq. (4.22) is 1 when $i = 1$ and equals zero for all other cases. Also, the diagonal elements of $\mathbf{X}$ and $\mathbf{Y}$, $X_{i,i}$ and $Y_{i,i}$, turn out to be zero for all Euler angles, which means there is no tangential derivatives of ϕ_i in the boundary conditions.

One feature of the finite volume method is the treatment of Robin-type boundary conditions. Since integration is performed over each control volume, the boundary conditions are never applied directly to the cell centers, but as fluxes at boundary faces. Therefore, boundary conditions of Robin-type cannot be satisfied simultaneously with the internal cells and the boundary face values have to be explicitly updated. The value of the dependent variable at the patch faces (b in Fig. 4.1) is found by

$$\phi_{ib} = g_i F_{ib} + (1 - g_i)\phi_{iC} \tag{4.24}$$

where F_{ib} is the right-hand side of Eq. (4.22).

$$F_{ib} = \delta_{1i} I_w - \sum_{j=1, j\neq i}^{N_2} \left[X_{i,j} \frac{\partial \phi_j}{\partial \tau_{\overline{x}}} + Y_{i,j} \frac{\partial \phi_j}{\partial \tau_{\overline{y}}} + Z_{i,j} \frac{\partial \phi_j}{\partial \tau_{\overline{z}}} \right]_b \tag{4.25}$$

The tangential derivatives in F_{ib} are explicitly calculated at the cell centers by Eq. (4.10) and then extrapolated to the boundary face (b). Usually the normal derivative is discretized with a first-order scheme for FVM implementations (adopted by, but not limited to, `OpenFOAM`®), i.e.,

$$\left. \frac{\partial \phi}{\partial \overline{z}} \right|_b = \frac{\phi_b - \phi_C}{d_{Cb}} \tag{4.26}$$

where d_{Cb} is the distance between face center b and neighboring cell center C for an orthogonal mesh, so that the fraction g_i is calculated by

$$g_i = \left[1 - \left(\frac{1}{\beta} \right)_b \frac{Z_{i,i}}{d_{Cb}} \right]^{-1} \tag{4.27}$$

Regarding the discretization in the finite volume method, the conservation law is applied to adjacent cells, where the gradients/fluxes on the cell-cell interfaces are discretized as before, Eq. (4.6), while the gradient/flux at the boundary face is specified according to the boundary conditions. The

gradient/flux at the boundary face is expressed by

$$(\nabla\phi_i)_b \cdot \mathbf{S}_b = \frac{\phi_{ib} - \phi_{iC}}{d_{Cb}} S_b = \frac{S_b}{d_{Cb}} \left[g_i F_{ib} + (1 - g_i)\phi_{iC} - \phi_{iC} \right] = \frac{S_b}{d_{Cb}} g_i F_{ib} - \frac{S_b}{d_{Cb}} g_i \phi_{iC} \tag{4.28}$$

At this point, the Marshak's boundary condition is ready to be integrated into the coefficient matrix, Eq. (4.7). Substituting Eq. (4.28) back to Eq. (4.8) for the cells adjacent to boundaries, the elements representing the boundary cells in the coefficients matrix are

$$a_C = -c_2^{nm} \sum_f \left(\frac{1}{\beta}\right)_f \frac{S_f}{d_{FC}} - c_2^{nm} \sum_b \left(\frac{1}{\beta}\right)_b \frac{S_b}{d_{Cb}} g_i - (1 - \omega\delta_{1i})\beta_C V_C \tag{4.29a}$$

$$b_C = \beta_C E_{iC} V_C - c_2^{nm} \sum_b \left(\frac{1}{\beta}\right)_b \frac{S_b}{d_{Cb}} g_i F_{ib} \tag{4.29b}$$

with a_F remains the same as for the internal cells, Eq. (4.8b). All information required to construct the coefficient matrices is contained in Eqs. (4.8) and (4.29).

4.1.3 Solution Method

The full coefficient matrix can be expressed as a single block-coupled matrix as

$$\begin{bmatrix} \mathbf{A}_{1,1} & \mathbf{A}_{1,2} & \cdots & \mathbf{A}_{1,j} & \cdots & \mathbf{A}_{1,N_2} \\ \mathbf{A}_{2,1} & \mathbf{A}_{2,2} & \cdots & \mathbf{A}_{2,j} & \cdots & \mathbf{A}_{2,N_2} \\ \vdots & \vdots & \ddots & \vdots & \ddots & \vdots \\ \mathbf{A}_{i,1} & \mathbf{A}_{i,2} & \cdots & \mathbf{A}_{i,j} & \cdots & \mathbf{A}_{i,N_2} \\ \vdots & \vdots & \ddots & \vdots & \ddots & \vdots \\ \mathbf{A}_{N_2,1} & \mathbf{A}_{N_2,2} & \cdots & \mathbf{A}_{N_2,j} & \cdots & \mathbf{A}_{N_2,N_2} \end{bmatrix} \begin{bmatrix} \mathbf{\Phi}_1 \\ \mathbf{\Phi}_2 \\ \vdots \\ \mathbf{\Phi}_i \\ \vdots \\ \mathbf{\Phi}_{N_2} \end{bmatrix} = \begin{bmatrix} \mathbf{b}^* \\ 0 \\ \vdots \\ 0 \\ \vdots \\ 0 \end{bmatrix} \tag{4.30}$$

where the block matrices in each row are obtained from numerical discretization of each governing equation of Y_i. The formulation of the block matrices has already been described in the last section, while the off-diagonal block matrices $\mathbf{A}_{i,j}$ represent the coefficient matrices discretized from the

double derivatives and cross derivatives in E_i (excluding the $\mathcal{L}_{zz}\phi_i$ term) and the surface derivatives in F_{ib}, even though they are calculated explicitly on the right-hand side for segregated solution method. Vector $\mathbf{b}^*$ represents the constant terms of $\mathbf{I}_b$ and $\mathbf{I}_w$.

Generally, the segregated solution method is preferable since all diagonal block matrices $\mathbf{A}_{i,i}$ are symmetric and sparse, which facilitates the iteration by employing stable and efficient symmetric matrix solvers. Also, the segregated method requires less memory (RAM). Let N_2 be the number of unknowns and N_3 be the number of cells of the mesh, the full matrix is of the size of $(N_2 \times N_3)^2$ (N_2 is the number of unknowns). The size of the whole matrix $\mathbf{A}$ increases quadratically with the increase of the number of unknowns, which makes the block-coupled method less attractive to real applications with a large RAM requirement. For the segregated method, N_2 diagonal matrices $\mathbf{A}_{i,i}$ of size of $N_3 \times N_3$ need to be iterated and the number of outer iterations required are problem dependent.

Since the segregated solution method is employed, all the $\mathbf{A}_{i,j}$ block matrices are moved to the right-hand side as

$$\begin{bmatrix} \mathbf{A}_{1,1} & 0 & \cdots & 0 & \cdots & 0 \\ 0 & \mathbf{A}_{2,2} & \cdots & 0 & \cdots & 0 \\ \vdots & \vdots & \ddots & \vdots & \ddots & \vdots \\ 0 & 0 & \cdots & \mathbf{A}_{i,i} & \cdots & 0 \\ \vdots & \vdots & \ddots & \vdots & \ddots & \vdots \\ 0 & 0 & \cdots & 0 & \cdots & \mathbf{A}_{N_2,N_2} \end{bmatrix} \begin{bmatrix} \mathbf{\Phi}_1 \\ \mathbf{\Phi}_2 \\ \vdots \\ \mathbf{\Phi}_i \\ \vdots \\ \mathbf{\Phi}_{N_2} \end{bmatrix} = \begin{bmatrix} \mathbf{b}_1 \\ \mathbf{b}_2 \\ \vdots \\ \mathbf{b}_i \\ \vdots \\ \mathbf{b}_{N_2} \end{bmatrix} \tag{4.31}$$

$$\begin{bmatrix} \mathbf{b}_1 \\ \mathbf{b}_2 \\ \vdots \\ \mathbf{b}_i \\ \vdots \\ \mathbf{b}_{N_2} \end{bmatrix} = - \begin{bmatrix} 0 & \mathbf{A}_{1,2} & \cdots & \mathbf{A}_{1,j} & \cdots & \mathbf{A}_{1,N_2} \\ \mathbf{A}_{2,1} & 0 & \cdots & \mathbf{A}_{2,j} & \cdots & \mathbf{A}_{2,N_2} \\ \vdots & \vdots & \ddots & \vdots & \ddots & \vdots \\ \mathbf{A}_{i,1} & \mathbf{A}_{i,2} & \cdots & 0 & \cdots & \mathbf{A}_{i,N_2} \\ \vdots & \vdots & \ddots & \vdots & \ddots & \vdots \\ \mathbf{A}_{N_2,1} & \mathbf{A}_{N_2,2} & \cdots & \mathbf{A}_{N_2,j} & \cdots & 0 \end{bmatrix} \begin{bmatrix} \mathbf{\Phi}_1 \\ \mathbf{\Phi}_2 \\ \vdots \\ \mathbf{\Phi}_i \\ \vdots \\ \mathbf{\Phi}_{N_2} \end{bmatrix} + \begin{bmatrix} \mathbf{b}^* \\ 0 \\ \vdots \\ 0 \\ \vdots \\ 0 \end{bmatrix} \tag{4.32}$$

In order to solve the entire system of block matrices, two loops of iterations are required: the iterations solving $\mathbf{A}_{i,i}\mathbf{\Phi}_i = \mathbf{b}_i$, Eq. (4.31), and outer iterations to resolve the coupling between $\mathbf{\Phi}_i$ and $\mathbf{\Phi}_j$. In this study, the incomplete Cholesky preconditioned conjugated gradient method (PCG) [230] is employed for inner iterations, while the Gauss-Seidel method is used for the outer iterations. The iteration processes can also be written in the form of:

$$\mathbf{\Phi}_i^{(k+1)} = \tilde{\mathbf{A}}_{i,i}^{-1} \left(- \sum_{j=1}^{i-1} \mathbf{A}_{i,j} \mathbf{\Phi}_j^{(k+1)} - \sum_{j=i+1}^{N_2} \mathbf{A}_{i,j} \mathbf{\Phi}_j^{(k)} + \delta_{1i} \mathbf{b}^* \right) \tag{4.33}$$

where the integer $k \geqslant 0$ denotes the sequence of outer iterations and $\tilde{\mathbf{A}}_{i,i}^{-1}$ is symbolizing the inner iterations. As mentioned in the last section, the boundary values $\mathbf{\Phi}_{ib}$ are not iterated in the inner iterations and are explicitly updated by Eq. (4.24). The $\mathcal{L}_{zz}\phi_i$ term is also explicitly updated during the outer iterations but is left outside of the expression in the whole matrix $\mathbf{A}$.

A numerical solution is obtained after the whole system has been iterated sufficiently. A normalized residual [231] is used to measure how well the solution satisfies the governing equations. For a system $\mathbf{A\Phi} = \mathbf{b}$, the residual R is calculated as

$$R = \frac{|\mathbf{b} - \mathbf{A\Phi}|_1}{|\mathbf{A\Phi} - \mathbf{A}\bar{\mathbf{\Phi}}|_1 + |\mathbf{b} - \mathbf{A}\bar{\mathbf{\Phi}}|_1} \tag{4.34}$$

where $|\cdot|_1$ denotes the L1-Norm. $\bar{\mathbf{\Phi}}$ is calculated from the arithmetic average of the elements of $\mathbf{\Phi}$. The convergence criteria ϵ_{inner} for all the inner iterations is $R < \epsilon_{inner} = 1 \times 10^{-5}$. In practice, it is not

necessary to have the inner iteration fully converged if the problem requires many outer iterations, so that the overall numbers of inner iterations can be decreased. Therefore, a changing convergence criteria is employed instead, which gradually decreases the ϵ_{inner}. Also, the maximum number of inner iterations for one single equation can be specified. A convergence criterion for outer iterations is also necessary to obtain meaningful results. Since ϕ_1 (I_0^0) is the incident radiation, the initial residual $R_{1,init}^{(k+1)}$ of $\mathbf{A}_{1,1}\mathbf{\Phi}_1^{(k+1)} = \mathbf{b}_1^{(k)}$ after (k) outer iterations is used to evaluate the convergence of outer iterations. It is often good enough if it is also observed that the initial residuals of all equations are decreasing monotonically. For stand-alone radiation simulations, $R_{1,init}^{(k+1)} < \epsilon_{outer} = 1 \times 10^{-3}$ is an appropriate choice. For unsteady combustion simulations, ϵ_{outer} of the P_N methods can be chosen close to the initial residuals of the energy equation between every time step. Since the radiative heat source S_{rad}, Eqs. (1.2) and (2.29), is the difference between emission and absorption, and the emission is constant for a single time step and absorption is related to I_0^0 by a factor of $4\pi\kappa$, it is also helpful to scale the ϵ_{outer} based on the maximum absorption coefficient κ_{max}.

The outer iterations with the Gauss-Seidel method is stable, if the spectral radius of the iterating matrices satisfies

$$\rho(\mathbf{A}_{i,i}^{-1} \cdot \mathbf{A}_{i,j}) = \max\{|\Lambda_1|, \cdots, |\Lambda_{N_3}|\} < 1 \tag{4.35}$$

where Λ are the eigenvalues of $\mathbf{A}_{i,i}^{-1} \cdot \mathbf{A}_{i,j}$. For example, if the full matrix $\mathbf{A}$ is symmetric positive definite (SPD) or $\mathbf{A}$ is strictly diagonally dominant, Eq. (4.35) will be unconditionally satisfied. Unfortunately the complete matrix $\mathbf{A}$ is not SPD, nor does it always have diagonal dominance. The diagonal dominance can be established when β is large, while the solver becomes less stable when β is small. The explicit derivative terms in the boundary condition are the major cause of instability. All the derivative operators in F_{ib}, Eq. (4.25), can be seen as the source of large coefficients in the $\mathbf{A}_{i,j}$ matrices when $\beta \to 0$.

An inertial damping technique is employed to slow down the outer iterations when $\beta \to 0$, which is implemented by adding $\lambda_i \phi_i$ to both sides of the boundary conditions, Eq. (4.22) followed

by division of the whole equation by $(1+\lambda_i)$, i.e.,

$$\phi_i + (\frac{1}{1+\lambda_i})Z_{i,i}\frac{\partial \phi_i}{\partial \tau_{\bar{z}}} = (\frac{1}{1+\lambda_i})I_w\delta_{1i} - (\frac{1}{1+\lambda_i})\sum_{j=1,j\neq i}^{N_2}\left[X_{i,j}\frac{\partial \phi_j}{\partial \tau_{\bar{x}}} + Y_{i,j}\frac{\partial \phi_j}{\partial \tau_{\bar{y}}} + Z_{i,j}\frac{\partial \phi_j}{\partial \tau_{\bar{z}}}\right] + (\frac{\lambda_i}{1+\lambda_i})\phi_i \tag{4.36}$$

the g_i in Eq. (4.27) is therefore replaced by

$$g_i = \left[1 - \left(\frac{1}{\beta}\right)_b \frac{Z_{i,i}}{(1+\lambda_i)d_{Cb}}\right]^{-1} \tag{4.37}$$

and F_{ib} is changed to

$$F_{ib} = (\frac{1}{1+\lambda_i})I_w\delta_{1i} - (\frac{1}{1+\lambda_i})\sum_{j=1,j\neq i}^{N_2}\left[X_{i,j}\frac{\partial \phi_j}{\partial \tau_{\bar{x}}} + Y_{i,j}\frac{\partial \phi_j}{\partial \tau_{\bar{y}}} + Z_{i,j}\frac{\partial \phi_j}{\partial \tau_{\bar{z}}}\right]\Bigg|_b + (\frac{\lambda_i}{1+\lambda_i})\phi_{ib} \tag{4.38}$$

Applying such inertial damping decreases the eigenvalues of $\mathbf{A}_{i,i}^{-1}\cdot\mathbf{A}_{i,j}$, and therefore stabilizes the outer iterations. The general idea is to relate λ_i to the local optical thickness τ, however, the optimum values of λ_i are problem dependent and require trial and error.

Other implementations of the boundary conditions are also possible, e.g., one can apply a Dirichlet type boundary condition by moving all derivatives to the right-hand side; or apply the boundary conditions as

$$\mathbf{Q}_{\bar{z}}^{-1}\cdot\mathbf{Q}\cdot\boldsymbol{\phi} + \mathbf{Q}_{\bar{z}}^{-1}\cdot\mathbf{Q}_{\bar{x}}\cdot\frac{\partial\boldsymbol{\phi}}{\partial\tau_{\bar{x}}} + \mathbf{Q}_{\bar{z}}^{-1}\cdot\mathbf{Q}_{\bar{y}}\cdot\frac{\partial\boldsymbol{\phi}}{\partial\tau_{\bar{y}}} + \frac{\partial\boldsymbol{\phi}}{\partial\tau_{\bar{z}}} = \mathbf{Q}_{\bar{z}}^{-1}\cdot\mathbf{p}I_w$$

or

$$\boldsymbol{\phi} + (\mathbf{D}^*)^{-1}\cdot\frac{\partial\boldsymbol{\phi}}{\partial\tau_{\bar{z}}} = (\mathbf{D}^*)^{-1}\cdot\left[\mathbf{Q}_{\bar{z}}^{-1}\cdot\mathbf{p}I_w - \mathbf{Q}_{\bar{z}}^{-1}\cdot\mathbf{Q}_{\bar{x}}\cdot\frac{\partial\boldsymbol{\phi}}{\partial\tau_{\bar{x}}} - \mathbf{Q}_{\bar{z}}^{-1}\cdot\mathbf{Q}_{\bar{y}}\cdot\frac{\partial\boldsymbol{\phi}}{\partial\tau_{\bar{y}}} - (\mathbf{Q}_{\bar{z}}^{-1}\cdot\mathbf{Q} - \mathbf{D}^*)\cdot\boldsymbol{\phi}\right] \tag{4.39}$$

where $\mathbf{D}^*$ denotes the diagonal matrix of $\mathbf{Q}_{\bar{z}}^{-1}\cdot\mathbf{Q}$. This implementation will eliminate the coupling between surface normal derivatives of ϕ_i and ϕ_j but adding the coupling between the surface values instead, so that stability can be improved wherever $\tau\to 0$ at the boundary. The major robustness

issue however is caused by the tangential derivatives, which cannot be resolved by this implementation. Since the number of equations increases quadratically, $N_2 = N(N+1)/2$, with the order of N, it is difficult to develop an unconditionally-stable high-order P_N solver based on relaxation and simple transformation of the boundary conditions. Designing a preconditioning matrix [232, 233] for the full matrix, which partially resolves the coupling between the block matrices, is a superior strategy, but is beyond the scope of this thesis. This method should be examined in future studies.

4.1.4 Implementation of Special Boundary Conditions

The finite volume implementation of special boundary conditions, including boundary conditions for mixed diffuse-specular reflective surfaces, specified radiative heat flux at the wall, specular reflection/symmetry boundary condition and cyclic boundary conditions will be described.

4.1.4.1 Boundary Conditions for Mixed Diffuse-Specular Surfaces

The implementation of boundary conditions for mixed diffuse-specular surfaces Eq. (3.37) is similar to that of the Marshak boundary condition for black walls, Eq. (2.24), since they almost have the same forms and can be converted to Robin-type boundary conditions in the same way. The original coefficients $p^m_{n,2i-1}$, Eq. (2.13) and Table. 2.4, $u^m_{l,i}$, $v^m_{l,i}$ and $w^m_{l,i}$,Eq. (2.26a), in $\mathbf{Q}, \mathbf{Q}_{\bar{x}}, \mathbf{Q}_{\bar{y}}, \mathbf{Q}_{\bar{z}}$, Eq. (4.21), are replaced by $\hat{p}^m_{n,2i-1}$, $\hat{u}^m_{l,i}$, $\hat{v}^m_{l,i}$ and $\hat{w}^m_{l,i}$ in Eqs. (3.35) and (3.36). Another change is to replace I_w in Eq. (2.24) with ϵI_{bw} as shown in Eq. (3.37). The rest is to follow the same implementation procedure of the Marshak's boundary condition for black walls.

4.1.4.2 Boundary Condition for Specified Radiative Heat Flux at the Wall

As discussed in Section 4.1.2, the Marshak's boundary conditions were transformed to Robin-type boundary condition as given by Eq. (4.22). Following this implementation, only the boundary condition for ϕ_1 (I^0_0) includes the radiative intensity I_w from the wall. The boundary condition for specified radiative flux at the wall is implemented by replacing Eq. (4.22) for ϕ_1 with Eq. (3.42)

while keeping the rest of Eq. (4.22) unchanged. When $i = 1$, let $F_{1b'}$ represents all the explicit calculations of the right-hand side of Eq. (3.42), the gradient/flux at the boundary face is then expressed by:

$$(\nabla\phi_1)_{b'} \cdot \mathbf{S}_{b'} = S_{b'} F_{1b'} \tag{4.40}$$

which is readily integrated into the coefficient matrix for $i = 1$ as:

$$b_C = \beta_C E_{1C} V_C - c_2^{00} \sum_{b'} \left(\frac{1}{\beta}\right)_{b'} S_{b'} F_{1b'} \tag{4.41}$$

where the expression of a_C and a_F are as the same as those for the internal cells, Eqs. (4.8a) and (4.8b).

4.1.4.3 Specular Reflection/Symmetry Boundary Condition

The equations describing specular reflection/symmetry boundary, Eq. (3.45), can also be written in matrix form similar to Eq. (4.20), because the variables $\boldsymbol{\phi}$ and their surface normal derivatives, $\partial\boldsymbol{\phi}/\partial\tau_{\tilde{z}}$, are also coupled through the summation terms. Let

$$\mathbf{q}_{(n,m)} = \begin{bmatrix} \bar{\Delta}^n_{m,-n} & \bar{\Delta}^n_{m,-n+1} & \cdots & \bar{\Delta}^n_{m,n} \end{bmatrix} \tag{4.42}$$

For even n (n= 0, 2,$\cdots$, N-1), when m is even, applying the discretization of the surface normal derivative as Eq. (4.26), Eq. (3.45a) can be expressed as

$$\mathbf{q}_{(n,m)} \cdot \boldsymbol{\phi}_{(n)b'} = \mathbf{q}_{(n,m)} \cdot \boldsymbol{\phi}_{(n)C} \tag{4.43}$$

and when m is odd, Eq. (3.45b) is reduced to

$$\mathbf{q}_{(n,m)} \cdot \boldsymbol{\phi}_{(n)b'} = 0 \tag{4.44}$$

with $\boldsymbol{\phi_{(n)}}$ defined as

$$\boldsymbol{\phi}_{(n)} = \begin{bmatrix} I_n^{-n} \\ I_n^{-n+1} \\ \vdots \\ I_n^{n-1} \\ I_n^{n} \end{bmatrix} \tag{4.45}$$

Considering each $\mathbf{q}_{(n,m)}$ vector as a row of a matrix, and denoting the matrix on the left-hand-side as $\mathbf{Q}_{b'}$, and the matrix on the right-hand side as $\mathbf{Q}_C$, one obtains

$$\mathbf{Q}_{b'} \cdot \boldsymbol{\phi}_{(n)b'} = \mathbf{Q}_C \cdot \boldsymbol{\phi}_{(n)C} \tag{4.46}$$

Taking P_3 as an example, the corresponding five boundary conditions resulting from Eqs. (3.45) become

$$\begin{bmatrix} \bar{\Delta}^2_{-2,-2} & \cdots & \cdots & \bar{\Delta}^2_{-2,2} \\ \bar{\Delta}^2_{-1,-2} & \cdots & \cdots & \bar{\Delta}^2_{-1,2} \\ \bar{\Delta}^2_{0,-2} & \cdots & \cdots & \bar{\Delta}^2_{0,2} \\ \bar{\Delta}^2_{1,-2} & \cdots & \cdots & \bar{\Delta}^2_{1,2} \\ \bar{\Delta}^2_{2,-2} & \cdots & \cdots & \bar{\Delta}^2_{2,2} \end{bmatrix} \begin{bmatrix} \phi_2 \\ \phi_3 \\ \phi_4 \\ \phi_5 \\ \phi_6 \end{bmatrix}_{b'} = \begin{bmatrix} \bar{\Delta}^2_{-2,-2} & \cdots & \cdots & \bar{\Delta}^2_{-2,2} \\ 0 & \cdots & \cdots & 0 \\ \bar{\Delta}^2_{0,-2} & \cdots & \cdots & \bar{\Delta}^2_{0,2} \\ 0 & \cdots & \cdots & 0 \\ \bar{\Delta}^2_{2,-2} & \cdots & \cdots & \bar{\Delta}^2_{2,2} \end{bmatrix} \begin{bmatrix} \phi_2 \\ \phi_3 \\ \phi_4 \\ \phi_5 \\ \phi_6 \end{bmatrix}_{C} \tag{4.47}$$

With the matrix formulation, $\boldsymbol{\phi}$ at boundary walls are calculated from

$$\boldsymbol{\phi}_{(n)b'} = \mathbf{Q}_{b'}^{-1} \mathbf{Q}_C \boldsymbol{\phi}_{(n)C} \tag{4.48}$$

or

$$\phi_{ib'} = V_{i,i} \phi_{iC} + F_{ib'} \tag{4.49}$$

where $\mathbf{V} = \mathbf{Q}_{b'}^{-1}\mathbf{Q}_C$ and $F_{ib'}$ is representing the sum of the relevant ϕ_{jC} terms as

$$F_{ib'} = \sum_{j=1, j\neq i}^{n} V_{i,j}\phi_{jC} \tag{4.50}$$

The gradient/flux at the specular/symmetry surface is calculated according to

$$(\nabla\phi_i)_{b'} \cdot \mathbf{S}_{b'} = \frac{\phi_{ib'} - \phi_{iC}}{d_{Cb'}} S_{b'} = \frac{S_{b'}}{d_{Cb'}}\left[V_{i,i}\phi_{iC} + F_{ib'} - \phi_{iC}\right] = \frac{S_{b'}}{d_{Cb'}}F_{ib'} - \frac{S_{b'}}{d_{Cb'}}(V_{i,i} - 1)\phi_{iC} \tag{4.51}$$

which leads to the expression for the elements of the coefficient matrix:

$$a_C = -c_2^{nm}\sum_f \left(\frac{1}{\beta}\right)_f \frac{S_f}{d_{FC}} - c_2^{nm}\sum_{b'}\left(\frac{1}{\beta}\right)_{b'} \frac{S_{b'}}{d_{Cb'}}(V_{i,i} - 1) - (1 - \omega\delta_{1i})\beta_C V_C \tag{4.52a}$$

$$b_C = \beta_C E_{iC} V_C - c_2^{nm}\sum_{b'}\left(\frac{1}{\beta}\right)_{b'} \frac{S_{b'}}{d_{Cb'}}F_{ib'} \tag{4.52b}$$

where the expression for a_F are as same as that of the internal cells, Eqs. (4.8b). The ϕ_1 (I_0^0) equation can be regarded as a special case, where $V_{1,1} = 1$ and $F_{ib'} = 0$, which results in a zero-gradient boundary condition. The above implementation is for pure specular reflection/symmetry surfaces.

4.1.4.4 Cyclic boundary conditions

The cyclic boundary condition for high-order P_N methods is implemented by manipulating the connectivity of the mesh. The two patches that are cyclic are mathematically connected to each other, even though they are not connected geometrically. The above implementation is achieved by first labeling the paired cells as neighbors and then solve the system as if they are internal cells. This is all that required for the cyclic boundary conditions of high-order P_N method Eq. (3.7) when $m = 0$.

However for $m \neq 0$, one needs to construct the elements of the coefficients matrix reflecting the mathematical relations of Eq. (3.9). The process can be better understood by the concept of

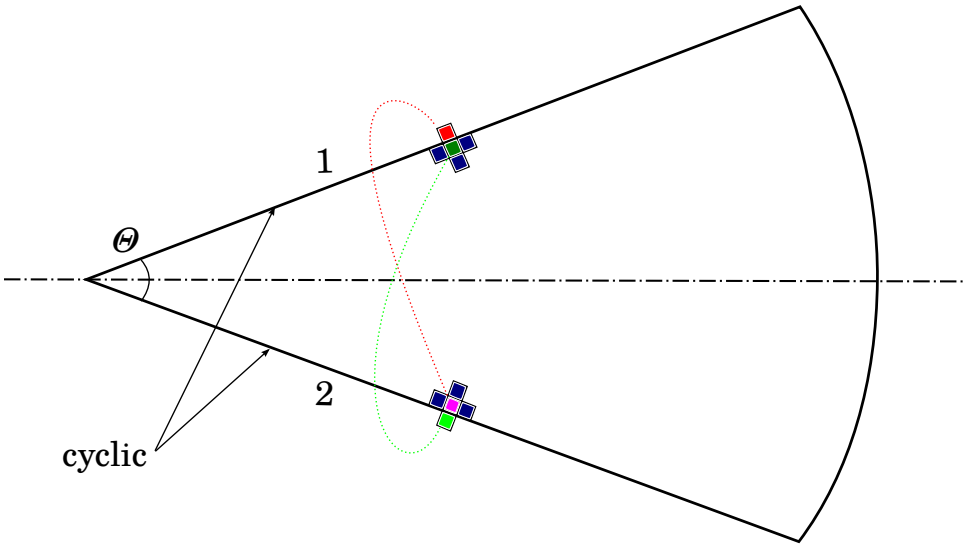

Figure 4.2: A schematic of cyclic boundary conditions for high-order P_N methods

ghost cells as shown in Fig. 4.2. The value of the ghost cell F' next to the boundary cell C is obtained from Eq. (3.9). The gradient/flux across the shared face b' is discretized as

$$\left(\frac{1}{\beta}\nabla\phi_i\right)_{b'} \cdot \mathbf{S}_{b'} = \left(\frac{1}{\beta}\right)_{b'} \frac{S_{b'}}{d_{F'C}}(\phi_{iF'} - \phi_{iC}) \tag{4.53}$$

following Eq. (3.9)

$$\phi_{iF'} = \cos m\Theta\phi_{iF} + L_{iF'} \tag{4.54}$$

where Θ is the angle (counter-clockwise) between patches shown in Fig. 4.2 and $L_{iF'}$ includes the term with $\phi_{jF} \sin m\Theta$ in Eq. (3.9). Substituting Eq. (4.54) into Eq. (4.53) and rearranging, one obtains the expression for the coefficient matrix as:

$$a_C\phi_C + \sum_F a_F\phi_F + a_{F'}\phi_{F'} = b_C \tag{4.55}$$

with the coefficients representing the cyclic boundary cells found from:

$$a_C = -c_2^{nm} \sum_f \left(\frac{1}{\beta}\right)_f \frac{S_f}{d_{FC}} - c_2^{nm} \left(\frac{1}{\beta}\right)_{b'} \frac{S_{b'}}{d_{F'C}} - (1 - \omega\delta_{1i})\beta_C V_C \tag{4.56a}$$

$$a_F = c_2^{nm} \left(\frac{1}{\beta}\right)_f \frac{S_f}{d_{FC}} \tag{4.56b}$$

$$a_{F'} = c_2^{nm} \left(\frac{1}{\beta}\right)_{b'} \frac{S_{b'}}{d_{F'C}} \cos m\Theta \tag{4.56c}$$

$$b_C = \beta_C E_{iC} V_C + c_2^{nm} \left(\frac{1}{\beta}\right)_{b'} \frac{S_{b'}}{d_{F'C}} L_{iF'} \tag{4.56d}$$

Normally, a discretization scheme has to satisfy a rule that demands opposite signs of a_C and a_F (or $a_{F'}$). This is to guarantee the boundedness of the discretization scheme, which requires ϕ_C changes with ϕ_F (or $\phi_{F'}$) in the same direction. In practice, it is not easy to tell whether breaking the boundedness rule damages the stabilities of iterations, because, for the high-order P_N method, the signs of the intensity coefficients (when $m \neq 0$) across the cyclic wall can be opposite as well.

4.1.5 Non-Orthogonality Correction

In previous sections, the discussion was limited to orthogonal meshes. A grid is orthogonal if, for all the cells in the computational domain, the surface normal vector $\mathbf{S}_f$ and vector $\mathbf{d}_{CF}$ joining the centers of the owner (C) and neighbor (F) cells are collinear. (By this definition, a 2-D or 3-D cylindrical mesh will also be considered nonorthogonal.) One example of one owner cell and one neighbor cell that are non-orthogonal to each other is shown in Fig. 4.3, where the non-orthogonality is measured by the angle between $\mathbf{S}_f$ and $\mathbf{d}_{CF}$. Non-orthogonality can introduce large errors and even cause instability issues, but is very common in numerical simulations of complex geometries, especially with unstructured grids. One advantage of the FVM is its flexibility in treating complex geometries, because of its innate compatibility with unstructured grids. `OpenFOAM`® is based on unstructured meshes and has adopted a deferred non-orthogonality correction in which the non-orthogonal contribution is treated explicitly [231]. The basic treatment of a non-orthogonal mesh

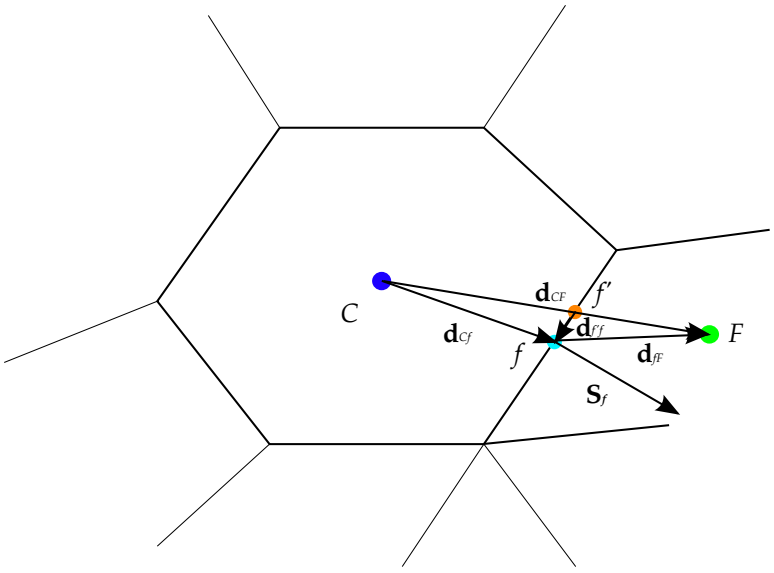

Figure 4.3: Schematic of non-orthogonality between center-to-center and face normal vectors.

in OpenFOAM® as related to the implementation of high-order P_N methods will be discussed in this section. Meanwhile, it is worthwhile to emphasize that creating a high-quality mesh is more important than finding better correction methods.

4.1.5.1 Laplacian operator

The Laplacian term in the governing equations of high-order P_N methods is discretized according to Gauss' divergence theorem, Eq. (4.4). The following discretization of $(\nabla\phi)_f \cdot \mathbf{S}_f$, as found in Eq. (4.5), requires its discretized expression in terms of ϕ_C and ϕ_F, as in Eq. (4.6) for two orthogonal cells. For a non-orthogonal mesh, Eq. (4.6) needs to be corrected. This is achieved by splitting the product $(\nabla\phi)_f \cdot \mathbf{S_f}$ into two parts:

$$(\nabla\phi)_f \cdot \mathbf{S_f} = (\nabla\phi)_f \cdot \mathbf{e}_f + (\nabla\phi)_f \cdot \mathbf{k}_f \tag{4.57}$$

Several decomposition methods exist [231], and OpenFOAM® adopted the following decomposition that constrains $\mathbf{k}_f$ to be normal to the surface normal $\mathbf{S}_f$, as shown in Fig. 4.4, i.e.,

$$\mathbf{e}_f = \frac{\mathbf{d}_{CF}}{\mathbf{d}_{CF} \cdot \mathbf{S}_f} S_f^2 \tag{4.58a}$$

$$\mathbf{k}_f = \mathbf{S}_f - \mathbf{e}_f \tag{4.58b}$$

The discretized Laplacian becomes

$$(\nabla\phi)_f \cdot \mathbf{S}_f = \frac{e_f}{d_{FC}}(\phi_F - \phi_C) + \left[(\nabla\phi)_f \cdot \mathbf{k}_f\right]_{\text{old}} \tag{4.59}$$

The first term on the right hand side of Eq. (4.59) is represented implicitly by the variable at the center of the adjacent cell, which is regarded as the orthogonal contribution of the gradient, while the second term on the right hand side represents a contribution of non-orthogonal correction part, which needs to be updated explicitly or, in another word, to use an old value from the former iteration. Therefore, the coefficient matrix for internal non-orthogonal cells is obtained as

$$a_C = -c_2^{nm} \sum_f \left(\frac{1}{\beta}\right)_f \frac{e_f}{d_{FC}} - (1 - \omega\delta_{1i})\beta_C V_C \tag{4.60a}$$

$$a_F = c_2^{nm} \left(\frac{1}{\beta}\right)_f \frac{e}{d_{FC}} \tag{4.60b}$$

$$b_C = \beta_C E_{iC} V_C - c_2^{nm} \sum_f \left(\frac{1}{\beta} \nabla\phi \cdot \mathbf{k}\right)_f \tag{4.60c}$$

Equation (4.60) reduces to Eq. (4.8) when the cells are orthogonal, i.e., when $e_f = S_f$ and $k_f = 0$.

4.1.5.2 Boundary Conditions

Consider a boundary cell with one face at the boundary, as shown in Fig. 4.5. The gradient at boundary surfaces needs to be corrected when the surface area vector $\mathbf{S}_b$ does not pass through the cell center C. To correct for the non-orthogonality, the surface normal vector $\mathbf{d}_{Cb'}$ between the cell

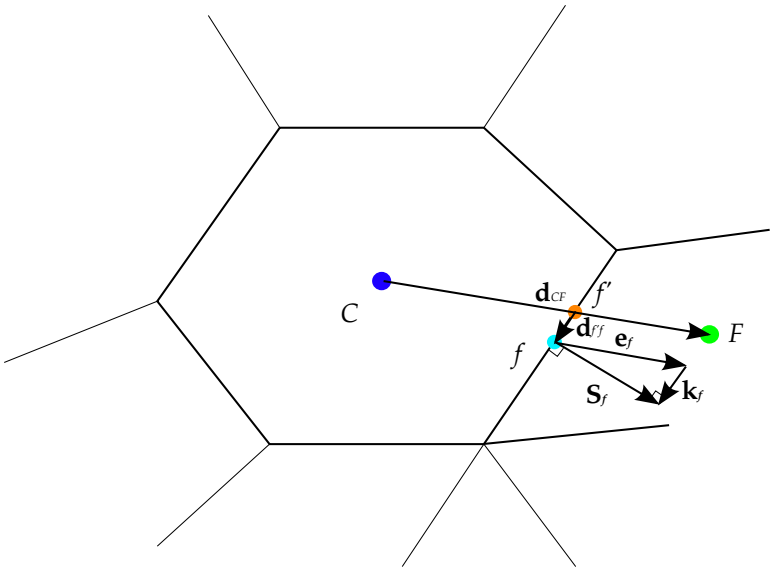

Figure 4.4: Schematic of correction vectors of non-orthogonal cells.

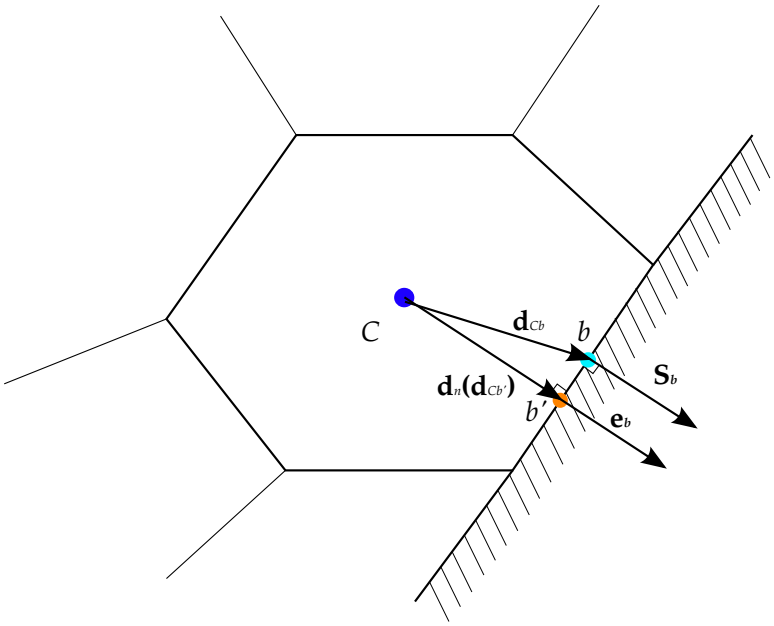

Figure 4.5: Schematic of non-orthogonality correction for non-orthogonal cells at the boundary.

center C and the boundary face is used instead of the vector $\mathbf{d}_{Cb}$ between C and the center of the boundary face b, which can be calculated from

$$\mathbf{d}_n = \mathbf{d}_{Cb'} = (\mathbf{d}_{Cb} \cdot \hat{\mathbf{s}}_b)\,\hat{\mathbf{s}}_b \tag{4.61}$$

where $\hat{\mathbf{s}}_b = \mathbf{S}_b/S_b = -\hat{\mathbf{n}}$ is the unit vector along surface area vector $\mathbf{S}_b$. For relatively traditional FVM implementations, including `OpenFOAM`®, the value of ϕ is assumed to be uniform on the entire boundary face, so that $\phi_{b'} = \phi_b$ and the discretization of the normal derivative at the boundary becomes

$$\left.\frac{\partial \phi}{\partial \bar{z}}\right|_b = \frac{\phi_b - \phi_C}{d_n} \tag{4.62}$$

therefore, the fraction $g_{i,NonOrth}$ for Marshak's boundary conditions (replacing Eq. (4.27) for the orthogonal grid) is now

$$g_{i,NonOrth} = \left[1 - \left(\frac{1}{\beta}\right)_b \frac{Z_{i,i}}{d_n}\right]^{-1} \tag{4.63}$$

with the coefficients matrix changed to

$$a_C = -c_2^{nm} \sum_f \left(\frac{1}{\beta}\right)_f \frac{S_f}{d_{FC}} - c_2^{nm} \sum_b \left(\frac{1}{\beta}\right)_b \frac{S_b}{d_n} g_{i,NonOrth} - (1 - \omega\delta_{1i})\beta_C V_C \tag{4.64a}$$

$$b_C = \beta_C E_{iC} V_C - c_2^{nm} \sum_b \left(\frac{1}{\beta}\right)_b \frac{S_b}{d_n} g_{i,NonOrth} F_{ib} \tag{4.64b}$$

Once again a_F remains the same as for internal cells, Eq. (4.8b).

Other boundary conditions can be corrected similarly by replacing the magnitude of vector $\mathbf{d}_{Cb}$ with the magnitude of face normal vector $\mathbf{d}_n$.

4.1.5.3 Face Interpolations

Explicit calculations of gradients within E_{iC} in Eqs. (4.60) and (4.64) require interpolation of the variable and its gradient to the face centers through Gauss's gradient theorem, Eq. (4.9). In non-orthogonal grids, the intersection of $\mathbf{d}_{CF}$ with the shared face, f', is not at the face center f, shown in Fig. 4.4. As can be seen, another correction, which is called skewness correction, is sometimes necessary. In the `OpenFOAM`® implementation, the skewness correction is integrated into

the interpolation as

$$\phi_f = w_f \phi_F + (1 - w_f)\phi_C + \left[(\nabla\phi)_f \cdot \mathbf{d}_{f'f}\right]_{\text{old}} \tag{4.65}$$

where $\mathbf{d}_{f'f}$ is shown in Fig. 4.3 and the interpolation weight w_f in Eq. (4.65) is calculated as

$$w_f = \frac{\mathbf{S}_f \cdot \mathbf{d}_{Cf}}{\mathbf{S}_f \cdot \mathbf{d}_{Cf} + \mathbf{S}_f \cdot \mathbf{d}_{fF}} \tag{4.66}$$

$\mathbf{d}_{Cf}$ and $\mathbf{d}_{fF}$ are also shown in Fig. 4.3.

4.1.6 2-D Cartesian P_N Solver and 2-D Axisymmetric P_N Solver

FVM implementations of the 2-D Cartesian and 2-D axisymmetric versions of high-order P_N methods, with the number of governing equations reduced to $(N + 1)^2/4$, follow the same procedure as that of the 3-D solver described in this chapter. The corresponding indices are listed in Table 4.2. Since the governing equations for 2-D formulations are also second-order elliptic PDEs, the implementation steps are almost the same as for the 3-D solver, which are:

- Collect the unknown ϕ_i in governing equation Y_i on the left-hand-side, and move extra $\mathcal{L}_{zz}\phi_i$ terms, if they exist, to the right-hand side together with the derivatives of other unknowns ϕ_j similar to Eq. (4.1);
- Construct the boundary matrices for Marshak's boundary conditions similar to Eqs. (4.20) and (4.21);
- Generate $N_2 = (N + 1)^2/4$ Robin-type boundary conditions similar to Eq. (4.22);
- Each governing equation with its boundary condition is solved by the PCG method (inner iterations) and the Gauss-Seidel method is employed for the outer iterations until convergence is reached.

It is useful to summarize the equations that are critical for the implementations.

For 2-D Cartesian P_N solver:

Table 4.2: Denotations and indices of unknowns and governing equations for 2-D solvers.

		2-D Cart.		2-D Axis.	
i	ϕ_i	I_n^m	Y_n^m	$\hat{\mathbf{I}}_n^m$	Y_n^m
1	ϕ_1	I_0^0	Y_0^0	$\hat{I}_0^0$	Y_0^0
2	ϕ_2	I_2^{-2}	Y_2^{-2}	$\hat{I}_2^0$	Y_2^0
3	ϕ_3	I_2^0	Y_2^0	$\hat{I}_2^1$	Y_2^1
4	ϕ_4	I_2^2	Y_2^2	$\hat{I}_2^2$	Y_2^2
5	ϕ_5	I_4^{-4}	Y_4^{-4}	$\hat{I}_4^0$	Y_4^0
6	ϕ_6	I_4^{-2}	Y_4^{-2}	$\hat{I}_4^1$	Y_4^1
7	ϕ_7	I_4^0	Y_4^0	$\hat{I}_4^2$	Y_4^2
8	ϕ_8	I_4^2	Y_4^2	$\hat{I}_4^3$	Y_4^3
9	ϕ_9	I_4^4	Y_4^4	$\hat{I}_4^4$	Y_4^4
10	ϕ_{10}	I_6^{-6}	Y_6^{-6}	$\hat{I}_6^0$	Y_6^0
11	ϕ_{11}	I_6^{-4}	Y_6^{-4}	$\hat{I}_6^1$	Y_6^1
12	ϕ_{12}	I_6^{-2}	Y_6^{-2}	$\hat{I}_6^2$	Y_6^2
13	ϕ_{13}	I_6^0	Y_6^0	$\hat{I}_6^3$	Y_6^3
14	ϕ_{14}	I_6^2	Y_6^2	$\hat{I}_6^4$	Y_6^4
15	ϕ_{15}	I_6^4	Y_6^4	$\hat{I}_6^5$	Y_6^5
16	ϕ_{16}	I_6^6	Y_6^6	$\hat{I}_6^6$	Y_6^6

Left-hand-side of the governing equation:

$$\begin{aligned}(\mathcal{L}_{xx} + \mathcal{L}_{yy})c_2^{nm}\phi_i - (1 - \omega\delta_{1i})\phi_i \\ = c_2^{nm}\nabla_\tau^2\phi_i - (1 - \omega\delta_{1i})\phi_i\end{aligned} \tag{4.67}$$

Marshak's boundary conditions in matrix form:

$$\mathbf{Q}\cdot\boldsymbol{\phi} + \mathbf{Q}_{\bar{x}}\cdot\frac{\partial\boldsymbol{\phi}}{\partial\tau_{\bar{x}}} + \mathbf{Q}_{\bar{z}}\cdot\frac{\partial\boldsymbol{\phi}}{\partial\tau_{\bar{z}}} = \mathbf{p}I_w \tag{4.68}$$

where the matrices $\mathbf{Q}$, $\mathbf{Q}_{\bar{x}}$ and $\mathbf{Q}_{\bar{z}}$ are constructed from Eq. (3.4).

Robin-type boundary conditions after transformation:

$$\phi_i + Z_{i,i}\frac{\partial \phi_i}{\partial \tau_{\bar{z}}} = \delta_{1i} I_w - \sum_{j=1, j\neq i}^{N_2} \left(X_{i,j}\frac{\partial \phi_j}{\partial \tau_{\bar{x}}} + Z_{i,j}\frac{\partial \phi_j}{\partial \tau_{\bar{z}}} \right) \tag{4.69}$$

with $\mathbf{X}$, $\mathbf{Z}$ are defined as

$$\mathbf{X} = \mathbf{Q}^{-1} \cdot \mathbf{Q}_{\bar{\mathbf{x}}}, \quad \mathbf{Z} = \mathbf{Q}^{-1} \cdot \mathbf{Q}_{\bar{\mathbf{z}}} \tag{4.70}$$

For 2-D axisymmetric P_N solver:

Left-hand-side of the governing equation with $\mathcal{L}_{zz}\phi_i$ term:

$$\begin{aligned} &\frac{\delta_{m1}}{2} c_2^{nm} \left[\mathcal{L}_{rr} + \frac{1}{\beta r}\mathcal{L}_r - \frac{1}{\beta^2 r^2} + \frac{1}{r}\mathcal{L}_r\left(\frac{1}{\beta}\right) \right] \phi_i \\ &\quad + c_2^{nm} \left(\mathcal{L}_{rr} + \frac{1}{\beta r}\mathcal{L}_r - \frac{m^2}{\beta^2 r^2} - 2\mathcal{L}_{zz} \right) \phi_i \\ &\quad + \left[\mathcal{L}_{zz} - (1 - \omega\delta_{0n}) \right] \phi_i \\ &\quad = a_{nm}^* \nabla \cdot \left(\frac{1}{\beta} \nabla \phi_i \right) + b_{nm}^* \phi_i + c_{nm}^* \mathcal{L}_{zz} \phi_i \end{aligned} \tag{4.71}$$

where

$$a_{nm}^* = c_2^{nm} \frac{1 + \delta_{m1}/2}{\beta}, \tag{4.72a}$$

$$b_{nm}^* = c_2^{nm} \left[\frac{\delta_{m1}/2}{r} \mathcal{L}_r\left(\frac{1}{\beta}\right) - \frac{m^2 + \delta_{m1}/2}{\beta^2 r^2} \right] - (1 - \omega\delta_{1i}) \tag{4.72b}$$

$$c_{nm}^* = 1 - (3 + \delta_{m1}/2) c_2^{nm}. \tag{4.72c}$$

Marshak's boundary conditions in matrix form:

$$\mathbf{Q} \cdot \boldsymbol{\phi} + \frac{1}{\beta}\mathbf{Q}_r \cdot \boldsymbol{\phi} + \mathbf{Q}_{\bar{x}} \cdot \frac{\partial \boldsymbol{\phi}}{\partial \tau_{\bar{x}}} + \mathbf{Q}_{\bar{z}} \cdot \frac{\partial \boldsymbol{\phi}}{\partial \tau_{\bar{z}}} = \mathbf{p} I_w \tag{4.73}$$

where the matrices $\mathbf{Q}$, $\mathbf{Q}_r$, $\mathbf{Q}_{\bar{x}}$ and $\mathbf{Q}_{\bar{z}}$ are constructed from Eq. (3.23). The $\mathbf{Q}_r \cdot \boldsymbol{\phi}/\beta$ term is constructed from the second term on the right-hand side of Eq. (3.23). In order to leave $1/\beta$ outside of $\mathbf{Q}_r$ which only depends on the geometric information, the $\mathbf{Q}_r \cdot \boldsymbol{\phi}/\beta$ term is not combined with $\mathbf{Q} \cdot \boldsymbol{\phi}$ term.

Robin-type boundary conditions after transformation:

$$\phi_i + \frac{Z_{i,i}}{(1+R_{i,i})}\frac{\partial \phi_i}{\partial \tau_{\bar{z}}} = \frac{1}{(1+R_{i,i})}\left[\delta_{1i} I_w - \sum_{j=1, j\neq i}^{N_2}\left(X_{i,j}\frac{\partial \phi_j}{\partial \tau_{\bar{x}}} + Z_{i,j}\frac{\partial \phi_j}{\partial \tau_{\bar{z}}} + R_{i,j}\phi_j\right)\right] \tag{4.74}$$

where $\mathbf{X}$, $\mathbf{Z}$ and $\mathbf{R}$ are defined as

$$\begin{aligned} \mathbf{X} &= \mathbf{Q}^{-1} \cdot \mathbf{Q}_{\bar{\mathbf{x}}} \\ \mathbf{Z} &= \mathbf{Q}^{-1} \cdot \mathbf{Q}_{\bar{\mathbf{z}}} \\ \mathbf{R} &= \mathbf{Q}^{-1} \cdot \mathbf{Q}_{\mathbf{r}} \end{aligned} \tag{4.75}$$

4.2 Finite Difference Implementation of the 1-D Axisymmetric P_N Method

The procedure for the finite difference discretization of the 1-D axisymmetric P_N equations is presented in this section. The high-order spherical harmonics method in 1-D axisymmetric geometry can be derived from the 2-D axisymmetric formulation, i.e., Eqs. (3.13) and (3.16). Then the governing equations as well as the Marshak's boundary conditions are discretized by the finite difference method (FDM) with second-order accuracy. The FDM implementation of the axisymmetric P_3 method is shown here to demonstrate the discretization process, and the implementation of other higher-order P_N methods follows the same procedure. After the entire coefficient matrix is constructed, it is solved by direct inversion of the entire coefficient matrix in `GNU Octave`®.

4.2.1 FDM Discretization of the Governing Equations

The governing equations of the P_N formulation for 1-D axisymmetric geometry are obtained from Eq. (3.13) by picking only the relevant equations and intensity coefficients and eliminating any terms related to operators for z-direction derivatives, i.e., $\mathcal{L}_z$, $\mathcal{L}_{zz}$, $\mathcal{L}_{rz}$ and $\mathcal{L}_{zr}$. Similar to the P_N formulations for the 2-D Cartesian geometry, the associated Legendre polynomials $P_n^m(\mu)$ are odd functions when $(m+n)$ are odd and thus I_n^m with $(m+n)$ being odd must vanish also for the 1-D axisymmetric formulation of the P_N method. The governing equation for 1-D axisymmetric formulation of the P_N method becomes

For each Y_n^m : $n = 0, 2, ..., N+1$ and $m = 0, 2, 4, ..., n$:

$$\begin{aligned}
\sum_{k=1}^{3} \Bigg\{ & (1+\delta_{m2}) a_k^{nm} \left[\mathcal{L}_{rr} - \frac{2m-3}{\beta r}\mathcal{L}_r + \frac{m(m-2)}{\beta^2 r^2} - \frac{m-2}{r}\mathcal{L}_r\left(\frac{1}{\beta}\right) \right] \hat{I}_{n+4-2k}^{m-2} \\
& + \frac{\delta_{m1}}{2} c_k^{nm} \left[\mathcal{L}_{rr} + \frac{1}{\beta r}\mathcal{L}_r - \frac{1}{r^2\beta^2} + \frac{1}{r}\mathcal{L}_r\left(\frac{1}{\beta}\right) \right] \hat{I}_{n+4-2k}^{m} \\
& + e_k^{nm} \left[\mathcal{L}_{rr} + \frac{2m+3}{\beta r}\mathcal{L}_r + \frac{m(m+2)}{\beta^2 r^2} + \frac{m+2}{r}\mathcal{L}_r\left(\frac{1}{\beta}\right) \right] \hat{I}_{n+4-2k}^{m+2} \\
& + c_k^{nm} \left(\mathcal{L}_{rr} + \frac{1}{\beta r}\mathcal{L}_r - \frac{m^2}{\beta^2 r^2} \right) \hat{I}_{n+4-2k}^{m} \Bigg\} \\
& - (1-\omega\delta_{0n}) \hat{I}_n^m = -(1-\omega) I_b \delta_{0n}
\end{aligned} \tag{4.76}$$

The relevant governing equations and intensity coefficients for the P_3 method are Y_0^0, Y_2^0, Y_2^2 and $\hat{I}_0^0$, $\hat{I}_2^0$, $\hat{I}_2^2$. Denoting the intensity coefficients $\hat{I}_0^0$, $\hat{I}_2^0$ and $\hat{I}_2^2$ as ϕ_{I}, ϕ_{II} and ϕ_{III} and symbols for each governing equation Y_0^0, Y_2^0, Y_2^2 as Y_{I}, Y_{II} and Y_{III}, the governing equations for the P_3 method (with no scattering) for 1-D axisymmetric geometry become

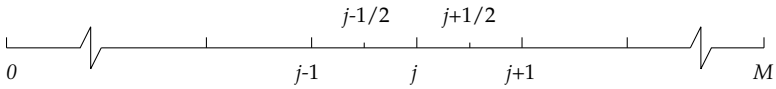

Figure 4.6: Schematic of a one-dimensional uniform mesh for the finite-difference discretization.

$$Y_{\mathrm{I}}: \quad \frac{1}{3}\left(\mathcal{L}_{rr}+\frac{1}{\beta r}\mathcal{L}_r\right)\phi_{\mathrm{I}}-\phi_{\mathrm{I}}-\frac{1}{15}\left(\mathcal{L}_{rr}+\frac{1}{\beta r}\mathcal{L}_r\right)\phi_{\mathrm{II}}+\frac{2}{5}\left[\mathcal{L}_{rr}+\frac{1}{\beta r}\mathcal{L}_r+\frac{2}{r}\mathcal{L}_r\left(\frac{1}{\beta}\right)\right]\phi_{\mathrm{III}}=-I_b \tag{4.77a}$$

$$Y_{\mathrm{II}}: \quad -\frac{1}{3}\left(\mathcal{L}_{rr}+\frac{1}{\beta r}\mathcal{L}_r\right)\phi_{\mathrm{I}}+\frac{5}{21}\left(\mathcal{L}_{rr}+\frac{1}{\beta r}\mathcal{L}_r\right)\phi_{\mathrm{II}}-\phi_{\mathrm{II}}-\frac{4}{7}\left[\mathcal{L}_{rr}+\frac{1}{\beta r}\mathcal{L}_r+\frac{2}{r}\mathcal{L}_r\left(\frac{1}{\beta}\right)\right]\phi_{\mathrm{III}}=0 \tag{4.77b}$$

$$Y_{\mathrm{III}}: \quad \frac{1}{6}\left(\mathcal{L}_{rr}-\frac{1}{\beta r}\mathcal{L}_r\right)\phi_{\mathrm{I}}-\frac{1}{21}\left(\mathcal{L}_{rr}-\frac{1}{\beta r}\mathcal{L}_r\right)\phi_{\mathrm{II}}+\frac{9}{21}\left(\mathcal{L}_{rr}+\frac{1}{\beta r}\mathcal{L}_r-\frac{4}{\beta^2 r^2}\right)\phi_{\mathrm{III}}-\phi_{\mathrm{III}}=0 \tag{4.77c}$$

Before discretization, the governing equations are multiplied by β. For any internal node at j ($0<j<M$) shown in Fig. 4.6, the derivative terms $\beta\mathcal{L}_{rr}\phi$ and $\beta\mathcal{L}_r\phi$ are discretized as

$$\beta\mathcal{L}_{rr}\phi=\frac{d}{dr}\left(\frac{1}{\beta}\frac{d}{dr}\right)\phi: \quad \left(\frac{1}{\beta}\right)_{j+1/2}\frac{\phi_{j+1}-\phi_j}{\Delta r^2}-\left(\frac{1}{\beta}\right)_{j-1/2}\frac{\phi_j-\phi_{j-1}}{\Delta r^2} \tag{4.78a}$$

$$\beta\mathcal{L}_r\phi=\frac{d\phi}{dr}: \quad \frac{\phi_{j+1}-\phi_{j-1}}{2\Delta r} \tag{4.78b}$$

where the subscripts (I,II,III) to distinguish unknowns are omitted here for clarity and j is the index for a spatial node. The remaining term $\beta\mathcal{L}_r\left(1/\beta\right)\phi$ has two different options for discretization:

$$\beta\mathcal{L}_r\left(\frac{1}{\beta}\right)\phi=\frac{d}{dr}\left(\frac{1}{\beta}\right)\times\phi: \quad \frac{(1/\beta)_{j+1/2}-(1/\beta)_{j-1/2}}{\Delta r}\phi_j \tag{4.79a}$$

$$\beta\mathcal{L}_r\left(\frac{1}{\beta}\right)\phi=-\frac{1}{\beta^2}\frac{d\beta}{dr}\phi: \quad \left(\frac{1}{\beta}\right)_j^2\frac{\beta_{j+1/2}-\beta_{j-1/2}}{\Delta r}\phi_j \tag{4.79b}$$

For a smooth profile of β (and $1/\beta$) with a fine mesh, both discretization methods will give very similar coefficients for ϕ_j.

4.2.2 FDM Discretization of the Boundary Conditions

4.2.2.1 Marshak's boundary condition at the outer wall (at $j = M$ where $r = R$)

The Marshak boundary condition is applied to the outer wall where $j = M$ ($r = R$). Equation (3.23) of the 2-D axisymmetric formulation gives four boundary conditions from $\overline{Y}_1^0, \overline{Y}_1^1, \overline{Y}_3^0$ and $\overline{Y}_3^2$. The boundary equation characterized by $\overline{Y}_1^1$ gives one equation for the intensity coefficient of I_2^1 which is irrelevant for 1-D formulations. Thus, the $\overline{Y}_1^1$ boundary condition is not taken and the Marshak boundary condition for 1-D axisymmetric geometry reduced from Eq. (3.23) for P_3 are:

$$\overline{Y}_1^0: \quad \frac{1}{2}\phi_{\mathrm{I}} + \frac{1}{3\beta_M}\phi'_{\mathrm{I}} - \frac{1}{16}\phi_{\mathrm{II}} - \frac{1}{15\beta_M}\phi'_{\mathrm{II}} + \frac{3}{8}\phi_{\mathrm{III}} + \frac{2}{5\beta_M}\phi'_{\mathrm{III}} + \frac{1}{\beta_M R}\frac{4}{5}\phi_{\mathrm{III}} = \frac{1}{2}I_{bw} \tag{4.80a}$$

$$\overline{Y}_3^0: \quad -\frac{1}{8}\phi_{\mathrm{I}} - \frac{1}{16}\phi_{\mathrm{II}} - \frac{3}{70\beta_M}\phi'_{\mathrm{II}} + \frac{3}{8}\phi_{\mathrm{III}} + \frac{9}{35\beta_M}\phi'_{\mathrm{III}} - \frac{1}{\beta_M R}\frac{12}{35}\phi_{\mathrm{III}} = -\frac{1}{8}I_{bw} \tag{4.80b}$$

$$\overline{Y}_3^2: \quad \frac{15}{8}\phi_{\mathrm{II}} + \frac{6}{7\beta_M}\phi'_{\mathrm{II}} + \frac{15}{4}\phi_{\mathrm{III}} + \frac{12}{7\beta_M}\phi'_{\mathrm{III}} - \frac{1}{\beta_M R}\frac{48}{7}\phi_{\mathrm{III}} = 0 \tag{4.80c}$$

The surface normal gradient ϕ' in Eq. (4.80) needs also to be discretized. Coefficients for a second-order accurate numerical stencil for discretization of the surface normal gradient ϕ' at the boundary node M can be obtained by Tailor expansions:

$$\phi_{M-1} = \phi_M - \Delta r\phi'_M + \frac{\Delta r^2}{2!}\phi''_M + O(\Delta r^3) \tag{4.81a}$$

$$\phi_{M-2} = \phi_M - 2\Delta r\phi'_M + \frac{4\Delta r^2}{2!}\phi''_M + O(\Delta r^3) \tag{4.81b}$$

The second-order accurate difference formula using points (ϕ_{M-2}, ϕ_{M-1}, ϕ_M) by 4×(4.81a)−(4.81b) is:

$$\phi'_M = \frac{\phi_{M-2} - 4\phi_{M-1} + 3\phi_M}{2\Delta r} \tag{4.82}$$

Since a direct solution method will be used to solve the whole system of algebraic equations, it is not necessary to further transform Eq. (4.80) into individual Robin-type boundary condition for each unknown.

4.2.2.2 Boundary condition at the centerline (at $j = 0$ where $r = 0$)

The second boundary condition must be applied to the centerline where $j = 0$ ($r = 0$). There are two ways to apply the centerline boundary condition. One is to directly apply Eq. (3.46) at the centerline. Note that multiplying Eq. (4.77c) by r^2 will give the same equation as Eq. (3.46b), which is $\phi_{\text{III}} = 0$ at $r = 0$. Multiplying Eq. (4.77a) and (4.77b) by r and substituting $\phi_{\text{III}} = 0$ into Eq. (4.77a) and (4.77b) will lead to $\phi'_{\text{I}} = \phi'_{\text{II}} = 0$ at $r = 0$, which are consistent with Eq. (3.46a). A second-order accurate difference formula using points (ϕ_0, ϕ_1 and ϕ_2) similar to Eq. (4.82) is used to discretize ϕ'_0, which is

$$\phi'_0 = \frac{-3\phi_0 + 4\phi_1 - \phi_3}{2\Delta r} \tag{4.83}$$

Another way is to apply L'Hospital's rule:

$$\lim_{r\to 0^+} \frac{\beta}{r}\mathcal{L}_r\phi = \lim_{r\to 0^+} \frac{1}{r}\frac{d\phi}{dr} = \left.\frac{d^2\phi}{dr^2}\right|_{r=0}, \quad \text{when} \lim_{r\to 0} \frac{d\phi}{dr} = 0 \tag{4.84}$$

followed by substitution of Eq. (4.84) into the governing equations. L'Hospital's rule can be applied to the P_1 equation without any difficulty, but it is more difficult for high-order P_N methods. For the example of P_3, there is no simple way to apply L'Hospital's rule to all terms related to ϕ_{III} satisfying the governing equation Eq. (4.77) at $r = 0$. Therefore, the first method is used for the centerline boundary.

Another second-order accurate approach to discretize the surface normal gradient ϕ' at both

boundaries is by adding ghost nodes next to the boundary nodes, which the added ghost nodes are labeled as $j = -1$ and $j = M + 1$, and then use the central differencing scheme to discretize ϕ', which are:

$$\phi'_0 = \frac{\phi_1 - \phi_{-1}}{2\Delta r} \tag{4.85a}$$

$$\phi'_M = \frac{\phi_{M+1} - \phi_{M-1}}{2\Delta r} \tag{4.85b}$$

Applying both the discretized governing equations and boundary conditions at the boundary nodes with central differencing scheme results in a system of $M + 3$ equations.

4.2.3 Solution Method

The same procedure is followed for the FDM implementation of P_5 and P_7 methods for the 1-D axisymmetric geometry. The resulting coefficient matrix from the described second-order finite-difference discretization from the axisymmetric P_N equations is solved by direct inversion of the entire coefficient matrix in `GNU Octave`®. It is found that using different second-order differencing schemes at the boundaries does not affect the results much. Compared with the segregated solution method used previously in the finite volume implementation, the direct solution does not require iteration and is more competitive than the segregated solution method when the the unknowns are strongly coupled. For example, from Eq. (4.77), it can be seen that the coefficients in front of ϕ_{I} (or I_0^0) and ϕ_{II} (or I_2^0) are of the same order, while for ϕ_{III} (or I_2^2), coefficients are related to $(1/r)\mathcal{L}_r$ $(1/\beta)$ which can easily affect the level of coupling between the unknowns. In that sense, the direct solution method could also be a good direction to look at for future improvements of iterations of the P_N equations, especially for designing preconditioners to partially solve the whole matrix while leaving a diagonal dominant matrix to be solved by segregated iterative methods.

Chapter 5

Results

5.1 Examples for Gray Media

The accuracy and efficiency of high-order P_N methods (up to P_7) will be studied through a series of examples. The results in terms of radiative heat source $S_{rad} = -\nabla \cdot \mathbf{q}$ calculated from high-order P_N methods as implemented in the FVM-based platform OpenFOAM® will be compared to that of exact solutions, either from direct integration or the PMC method. Other reference solutions, including analytical solution of P_N for 1-D Cartesian geometry, finite difference method (FDM) solution of the P_N method for 1-D cylindrical geometries and DOM are also used in different examples for comparison.

The goal of these examples is to test the performance of the high-order P_N methods with respect to the order of P_N, overall optical thickness, geometry, homogeneity of radiative properties, etc., as well as to verify the FVM implementations of the high-order P_N methods on OpenFOAM®. Gray media are assumed in this chapter since spectral variations of real participating media will hinder the evaluation of the performances of the high-order P_N methods. For some examples the angular distribution of intensities will be reconstructed from the truncated spherical harmonics expansions to further study the mechanism behind the high-order spherical harmonics P_N methods.

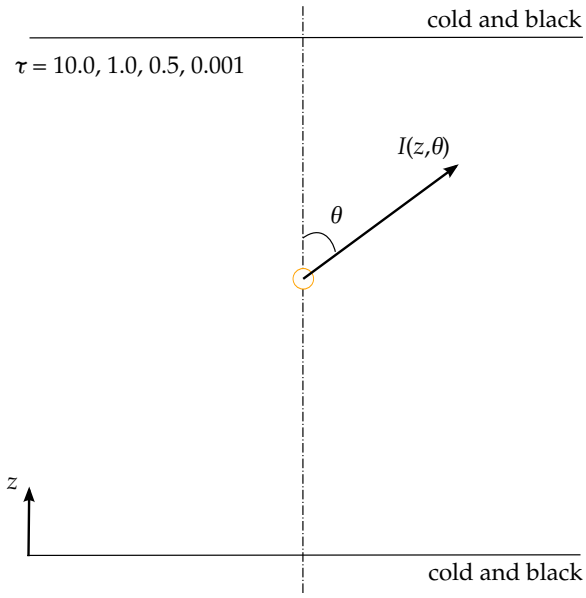

Figure 5.1: Diagram of the radiative transfer between two infinitely long parallel plates.

All calculations are carried out on a single 2.66 GHz Intel (R) Xeon (R) X7460 processor.

5.1.1 1-D Slab Geometry

The first geometry to test the high-order P_N methods is a 1-D slab, which represents the radiative transfer between two infinitely long parallel plates. An exact solution [21] by direct integration is available for 1-D radiative transfer problems and, therefore, used to evaluate the performance of the P_N methods. For 1-D Cartesian problems, analytical solutions for the P_N methods may also be found and are used to verify the numerical P_N solutions from `OpenFOAM`®. In the P_N FVM implementation, these 1-D slab examples are solved by treating walls at two suppressed dimensions as symmetry/specular boundaries as described by Eq. (3.45). For all three examples, the lower and upper walls are assumed to be cold and black ($I_w = 0.0, \epsilon = 1.0$).

5.1.1.1 Problem 1: 1-D slab with homogeneous radiative properties

The first group of examples are 1-D Cartesian problems with homogeneous radiative media of different optical thicknesses. A diagram of the problem is shown in Fig. 5.1. A $1 \times 1 \times 101$ slab is employed and four optical thicknesses τ are selected to test the performances of different orders of the P_N methods for these optical thicknesses. Four different orders of P_N approximations are tested i.e., P_1, P_3, P_5 and P_7.

The numerical results from different orders of P_N methods in terms of normalized quantities are presented in Figures 5.2–5.5. Since the medium is homogeneous, the resulting incident radiation G, radiative heat source $-\nabla \cdot \mathbf{q}$ and the intensity I are normalized by $4\pi I_b$, $4\pi\kappa I_b$ and I_b, respectively. In common applications, only the incident radiation G and the radiative heat source $-\nabla \cdot \mathbf{q}$, which are angular-integrated values of intensity I, are of interest. However, to show the performance of P_N methods for different optical thicknesses, the angular distribution of the normalized intensity at the center $\tau/2$ is also presented together with the exact angular distributions of the normalized intensity calculated from direct integration [21]. For the P_N methods, the angular distribution of intensity I is reconstructed by summing up the truncated spherical harmonics expansion, Eq. (2.1).

For the example of $\tau = 10$, which is shown in Fig. 5.2, all orders of the P_N methods give solutions close to the exact solution except that the normalized incident radiation and radiative heat source of P_1 are slightly off next to boundaries. This is because the angular distributions of the intensities are more isotropic for optically thick conditions, as shown in Fig. 5.2(b) for the normalized intensity at the center as a sampling point. At the optical thickness of 10, the normalized radiative heat source is almost zero close to the center (from z/L=0.3 to 0.7), which reflects the physics that the photons emitted close to the center are absorbed locally so that the net heat exchange at the center regions is a small portion of the total emission.

There is more energy escaping from the medium to the cold black walls for the example with $\tau = 1$ because the photons travel ten times longer distances compared with the example of $\tau = 10$, as shown in Fig. 5.3. The results in Fig. 5.3(a) show that P_1 incurs large errors predicting the

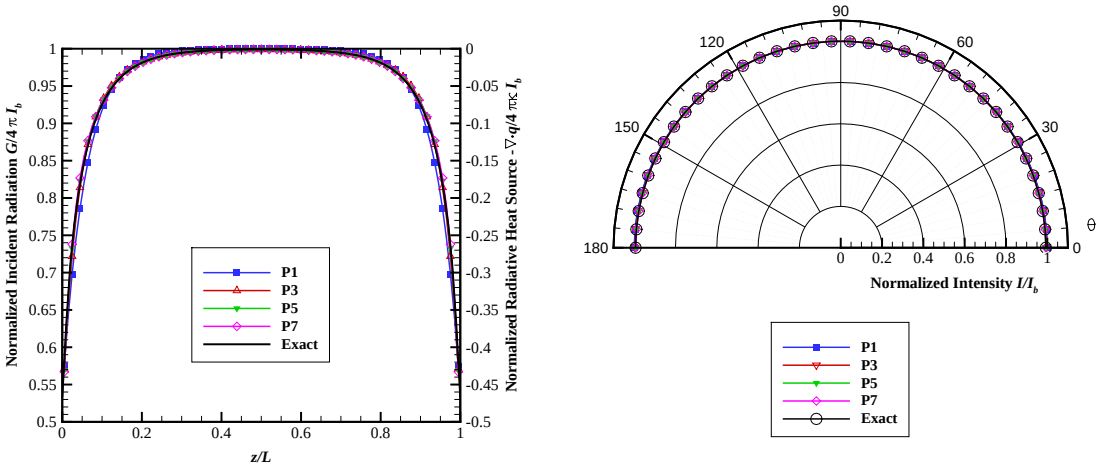

(a) (b)

Figure 5.2: Comparison of numerical P_N solutions to the exact solutions for the 1-D slab example with homogeneous medium for optical thickness τ=10; (a) normalized incident radiation $G/4\pi I_b$ and normalized radiative heat source $-\nabla \cdot \mathbf{q}/4\pi\kappa I_b$, and (b) normalized radiative intensity I/I_b.

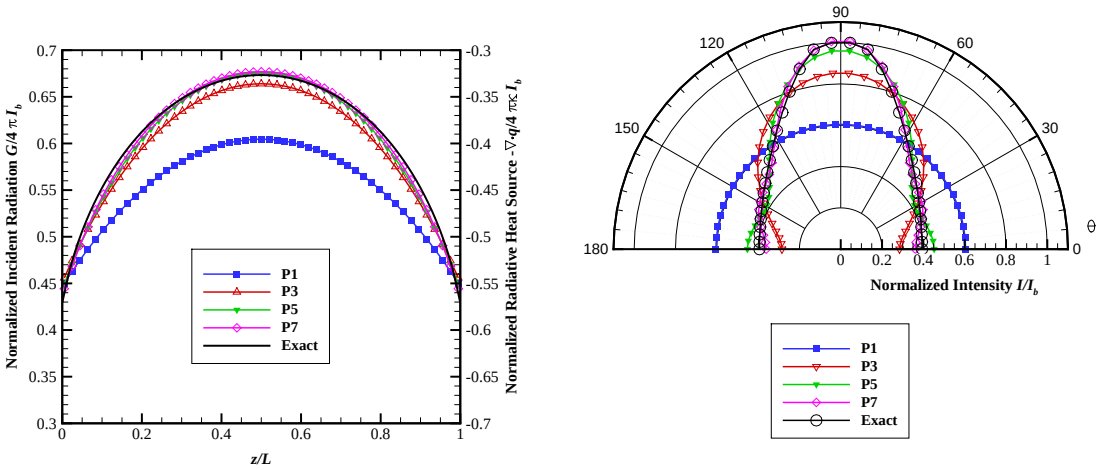

(a) (b)

Figure 5.3: Comparison of numerical P_N solutions to the exact solutions for the 1-D slab example with homogeneous medium for optical thickness τ=1; (a) normalized incident radiation $G/4\pi I_b$ and normalized radiative heat source $-\nabla \cdot \mathbf{q}/4\pi\kappa I_b$, and (b) normalized radiative intensity I/I_b.

normalized incident radiation and radiative heat source. P_3 increases the accuracy significantly over P_1 while the results from P_5 and P_7 are very close to the exact solution. The angular distribution of

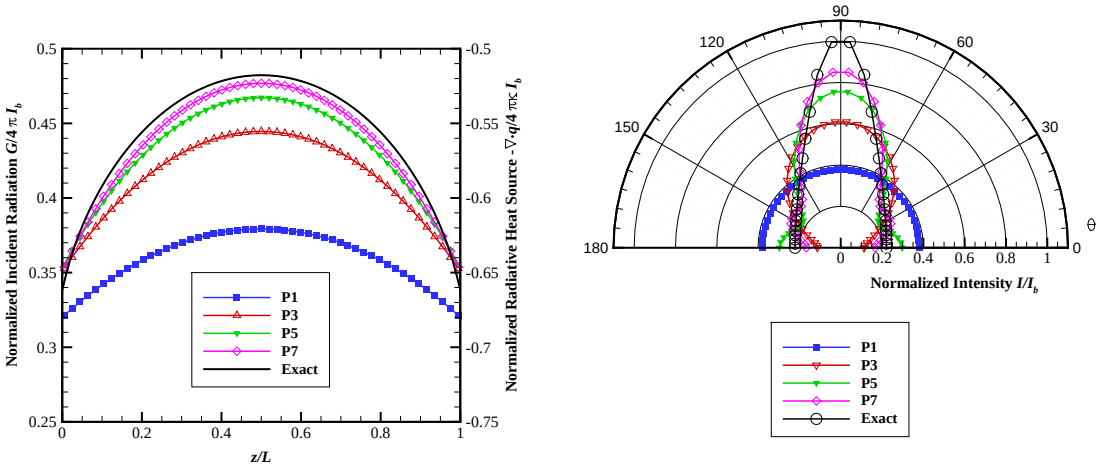

(a) (b)

Figure 5.4: Comparison of numerical P_N solutions to the exact solutions for the 1-D slab example with homogeneous medium for optical thickness τ=0.5; (a) normalized incident radiation $G/4\pi I_b$ and normalized radiative heat source $-\nabla \cdot \mathbf{q}/4\pi\kappa I_b$, and (b) normalized radiative intensity I/I_b.

intensity at the center in Fig. 5.3(b) is anisotropic since the emission path is longer close to $\theta = 90°$ (parallel to the surfaces) than that from $\theta = 0°$ (perpendicular to the surfaces). And P_1 predicts the angular distribution of intensity to be isotropic at the center since the expansion of spherical harmonics of order 1 has only the $I_0^0 Y_0^0$ term at the center (where I_1^m=0). As is shown in Fig. 5.3(b), increasing the order of P_N consistently improves the accuracy of the P_N method until the intensity predicted by P_7 at the center almost captures the exact angular distribution.

If one further decreases the optically thickness to $\tau = 0.5$, even P_7 fails to catch the peak of radiative intensity as shown in Fig. 5.4(b). Once again the angular distribution of intensity at the center predicted by P_1 method is isotropic, which fails to capture the nonisotropic feature of the exact intensity distribution. The gradually improving results in Fig. 5.4(b) for higher order ones are consistently closer to the exact solution, while more oscillations in the distributions are observed. As is seen from the forms of associated Legendre polynomials, Table 2.1, the high order spherical harmonics Y_n^m represent high-frequency bases of a function, and therefore, higher-order spherical harmonics expansions are able to closer approximate the exact anisotropic angular distributions

Table 5.1: Comparison of errors of normalized incident radiation at the center point ($z/L = \tau/2$) for different orders of P_N methods for the example of τ=0.5

Order	$\epsilon_{abs.}$	$\mu_{N,N-2}$
1	-0.102987	/
3	-0.037692	-63.4 %
5	-0.015087	-60.0 %
7	-0.005431	-64.0 %
Exact	0.482256	

while introducing more oscillations of the solution with regard to angular distributions of intensity. The integrated values, expressed by normalized incident radiation and radiative heat source in Fig. 5.4(a) also show consistent improvements of accuracies. Table 5.1 summarizes the absolute error $\epsilon_{abs.}$ of the normalized incident radiation comparing the results obtained from the P_N methods with the exact solution at the center. Another value $\mu_{N,N-2}$ is used to measure the error reduction rate, which is defined as

$$\mu_{N,N-2} = \frac{\epsilon_{abs.,N} - \epsilon_{abs.,N-2}}{\epsilon_{abs.,N-2}} \tag{5.1}$$

The errors are reducing at the rate about 60% for each increase of the order of the P_N methods.

Figure 5.5 shows the results for the condition of an optically thin example with $\tau = 0.001$. The predicted angular distribution of intensity from P_1 to P_7 in Fig. 5.5(b) is not showing a gradual convergence but rather step-wise improvements even with this step-shape distribution, while on the opposite, the normalized incident radiation and radiative heat sources from P_1 to P_7 in Fig. 5.5(a) seem to gradually converge to another value other than the exact solution. Table. 5.2 summarizes the absolute error $\epsilon_{abs.}$ and the error reduction rate $\mu_{N,N-2}$ of the normalized incident radiation comparing the results obtained from the P_N methods with the exact solution at the center. The error reduction is much slower than for the case of $\tau = 0.5$ and the reduction rate also becomes slower with the increase of the order N, which implies that a much higher order of P_N method is required to obtain an exact solution for optical-thin conditions. It is important to point out that the radiative

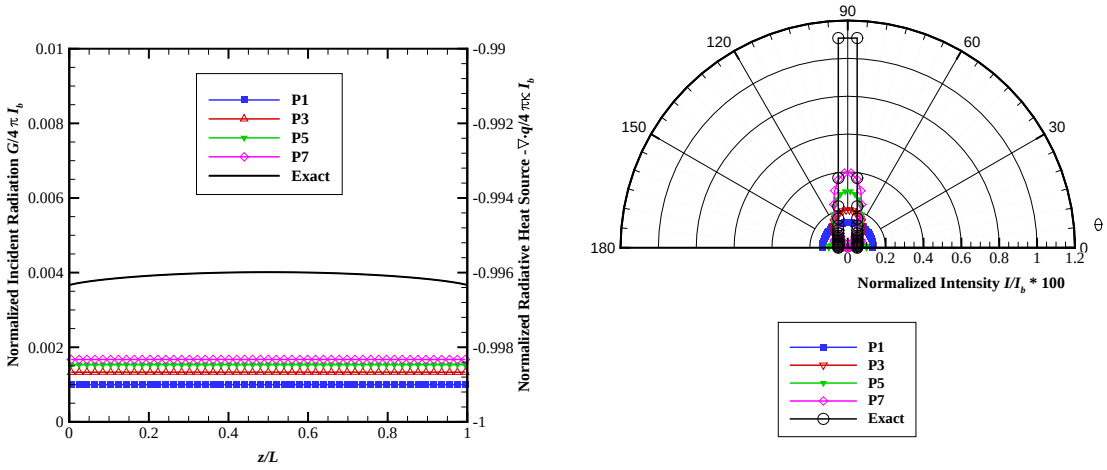

(a) (b)

Figure 5.5: Comparison of numerical P_N solutions to the exact solutions for the 1-D slab example with homogeneous medium for optical thickness τ=0.001; (a) normalized incident radiation $G/4\pi I_b$ and normalized radiative heat source $-\nabla \cdot \mathbf{q}/4\pi\kappa I_b$, and (b) normalized radiative intensity I/I_b.

heat source before normalization is what will eventually matter, and if one looks at the total scale of energy absorbed in Fig. 5.5(a), which is around 0.2-0.4% of the emitted energy, the error of the P_N method actually can be safely ignored since even an optically thin solution will be sufficient for this homogeneous optically thin example. This will be discussed further in the later problems. Furthermore, this example gives a reasonable minimum value of τ_{min}, which will be used to find a minimum κ_{min} for inhomogeneous cases with optically thin regions to avoid division by zeros.

All the above numerical P_N results have been verified against the analytical solution of P_N for 1-D Cartesian geometries. Figure 5.6 shows the comparison of the numerical solutions and the

Table 5.2: Comparison of errors of normalized incident radiation at the center point ($z/L = \tau/2$) for different orders of P_N methods for the example of τ=0.001

Order	$\epsilon_{abs.}$	$\mu_{N,N-2}$
1	-0.0030125717	/
3	-0.0026799798	-11.0 %
5	-0.0024807361	-7.4 %
7	-0.0023386386	-5.7 %
Exact	0.004012	

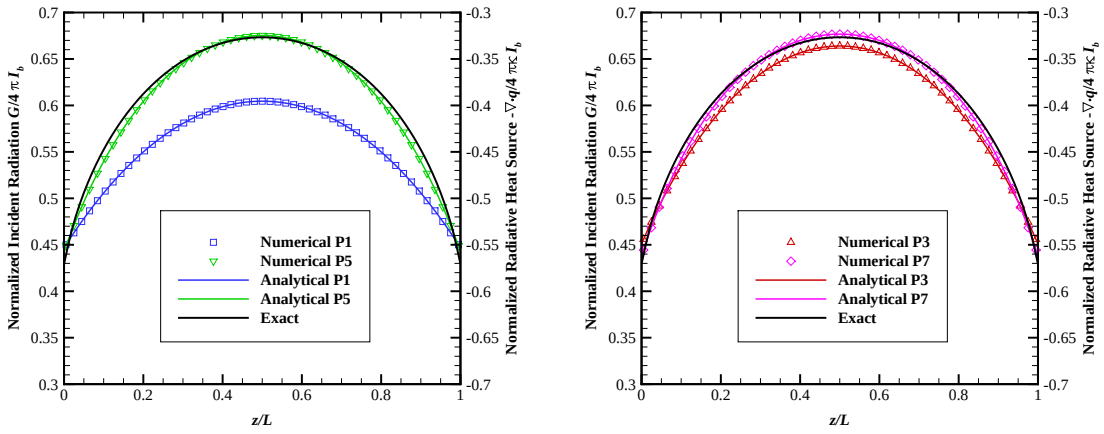

(a) (b)

Figure 5.6: Comparison of numerical and analytical solutions of the P_N methods for the example of $\tau = 1$; (a) P_1, P_5 and exact solutions and (b) P_3, P_7 and exact solutions.

analytical solutions of the P_N methods for the example of $\tau = 1$, where the numerical solutions of the P_N methods perfectly overlap the analytical solutions. Since the analytical solutions are dimensionless, the comparison can also be regarded as a grid independence check for the numerical solutions.

A CPU time comparison for Problem 1 is given in Table 5.3. The computational cost increases with the decreases of the optical thickness τ_L which is due to the stronger coupling between governing equations for the optically thinner case.

Table 5.3: Comparison of CPU time (s) for Problem 1: 1-D slab with homogeneous κ and I_b

No. of cells	τ_L	P_1	P_3	P_5	P_7
101	10	0.01	0.04	0.14	0.26
	1	0.01	0.04	0.14	0.26
	0.5	0.01	0.04	0.14	0.28
	0.001	0.01	0.05	0.15	0.33

5.1.1.2 Problem 2: 1-D slab with variable radiative properties

Problem 2 considers radiative transfer between two infinitely long plates with an inhomogeneous medium. For this example a $1 \times 1 \times 100$ slab is employed. The properties of the medium vary according to

$$I_b = 10(1 + 0.5y^2), \quad \mathrm{W \cdot m^{-3} \cdot sr^{-1}} \tag{5.2a}$$

$$\kappa = y, \quad \mathrm{m^{-1}} \tag{5.2b}$$

$$\tau_L = 0.5 \tag{5.2c}$$

where y is the perpendicular distance from the lower wall. The thickness of the slab is $L = 1$ m, and the optical thickness is $\tau_L = 0.5$. In optical coordinates the Planck function field (I_b) is linear, which is convenient for finding an analytical solution. For the numerical computations, a lower limit of $\kappa_{\min} = 10^{-3}$ m^{-1} was set for κ in order to avoid division by zero at the lower wall.

Since this example is 1-D and in Cartesian coordinates, the analytical solution can be obtained to verify certain aspects of the P_N approximation and the program implementation itself. For instance, by orienting the 1-D slab at different angles within each of the three coordinate planes (see Fig. 5.7), the 1-D slab can be used to verify that all partial derivatives are accounted for correctly in the implementation. For example, setting the configuration angle to $\phi = 0$ with the slab positioned in the x-y plane, one can test the $\mathcal{L}_{xx}$ derivatives, neglecting all mixed derivative, $\mathcal{L}_{yy}$, and $\mathcal{L}_{zz}$ terms from the PDEs. Similarly, setting $\phi = 90°$, the combination of $\mathcal{L}_{yy}$ derivatives can be singled out, and for $\phi = 45°$, the combination of $\mathcal{L}_{xx}$, $\mathcal{L}_{yy}$, $\mathcal{L}_{xy}$, and $\mathcal{L}_{yx}$ terms can be verified, etc.. In terms of solution profiles within the slab, the solutions for I_0^0 should be identical (and matching the analytical profiles) for arbitrary orientations of the 1-D slab. The numerical and analytical solution for incident radiation G and radiative heat source $-\nabla \cdot \mathbf{q}$, for the case of the slab oriented in the y-direction is shown in Fig. 5.8. The numerical results are found to perfectly overlap the analytical results for various orientations, which demonstrates that the P_N implementation correctly employs

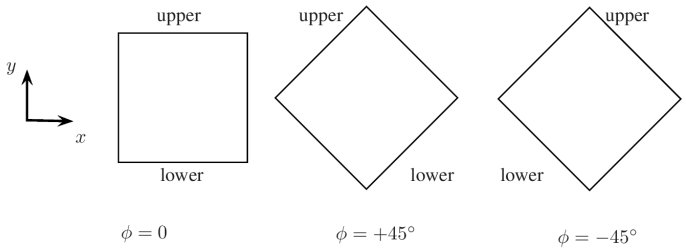

Figure 5.7: Rotations of 1-D slab at angles $\phi = 0, 45°, -45°$ in the *x*-*y* plane. The medium properties increase with low values at the lower wall to higher values at the upper wall.

Table 5.4: Comparison of errors of radiative heat source at two locations (y=0.1 m and y=0.8 m) for different orders of P_N methods for the example of τ=0.5

	y=0.1 m		y=0.8 m	
Order	$\epsilon_{abs.}$	$\mu_{N,N-2}$	$\epsilon_{abs.}$	$\mu_{N,N-2}$
1	-0.199823	/	-13.574682	/
3	0.219627	-209.9 %	-5.332582	-60.7 %
5	0.221957	+1.06 %	-2.402082	-55.0 %
7	0.168297	-24.2 %	-1.072482	-55.4 %
Exact	-7.499817		-71.567518	

all the terms in the PDEs. Comparing with the exact solution for this 1-D problem [21], higher order P_N generally produce more accurate results over the entire slab, except near the lower wall where the P_N methods incur larger errors for the incident radiation G. This is due to the optically thin region (small values of κ) close to the lower wall. Table 5.4 summarizes the absolute error $\epsilon_{abs.}$ and the error reduction rate $\mu_{N,N-2}$ for the radiative heat source comparing the results obtained from the P_N methods with the exact solution at two locations (y=0.1 m and y=0.8 m). At the position of y=0.8 m, the errors are dropping consistently at similar rates while at y=0.1 m the errors are dropping with oscillations. Nevertheless, the overall errors of the radiative heat source are reduced by approximately 55% every time the order is increased for this example.

This example has shown the rotational invariance of the P_N method in the *x*-*y* plane and the capability of the P_N methods predicting radiative heat source for 1-D Cartesian inhomogeneous case even with optically thin regions. The overall performance of the high-order P_N method in this

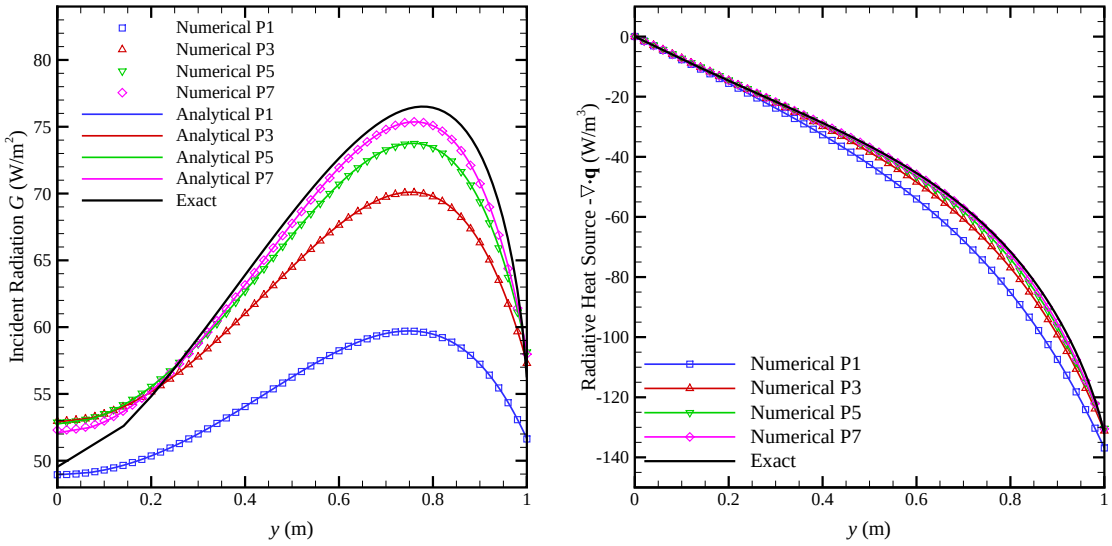

(a) (b)

Figure 5.8: Comparing incident radiation and radiative heat source with analytical solutions of P_N and exact solution for 1-D slab; (a) incident radiation G and (b) radiative heat source $-\nabla \cdot \mathbf{q}$.

Table 5.5: Comparison of CPU time (s) for Problem 2: 1-D slab with inhomogeneous κ and I_b

No. of cells	τ_L	P_1	P_3	P_5	P_7
100	0.5	0.01	0.04	0.15	0.27

inhomogeneous example has been shown to be similar to that of the homogeneous example at the same optical thickness $\tau_L = 0.5$.

The CPU time comparison for Problem 2 is given in Table 5.5. The computational cost does not differ much from that of the homogeneous case (Table 5.3) with the same optical thickness ($\tau_L = 0.5$).

5.1.1.3 Problem 3: 1-D slab with flame-like variable radiative properties

In this example, the radiative properties are flame-like with a strongly emitting and absorbing region in the center next to the optically thin regions. The computational domain is a 1-D slab ($1 \times 1 \times 200$) with length $L = 0.52 \times 2$ m. In the previous examples, the Planck function I_b was

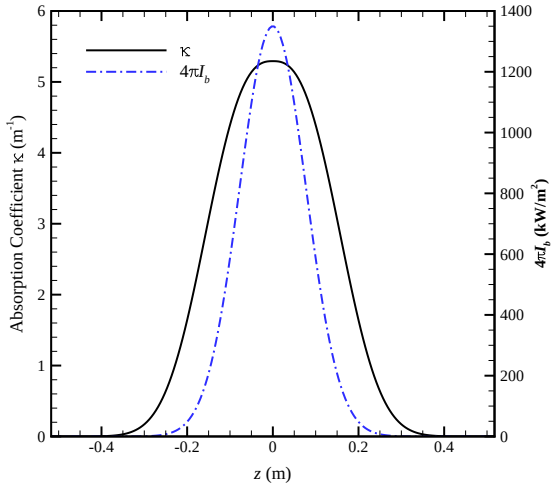

Figure 5.9: Flame-like variable radiative properties of Problem 3.

either normalized, as in Problem 1, or artificial values were used without physical significance, as in Problem 2. For this example a more physical scale of the Planck function $4\pi I_b$ is used to represent an exponential distribution of a flame with peak temperature around 1562 K. The corresponding radiative properties as shown in Fig. 5.9 are

$$4\pi I_b = 1.35 \times 10^3 e^{-83.333 z^2}, \quad \text{kW} \cdot \text{m}^{-3} \tag{5.3a}$$

$$\kappa = 5.293 e^{-83.333 |z|^{2.65}}, \quad \text{m}^{-1} \tag{5.3b}$$

$$-0.52 \leqslant z \leqslant 0.52, \quad \text{m} \tag{5.3c}$$

$$\tau_{L/2} = 0.886 \tag{5.3d}$$

Figure 5.10 shows the incident radiation G and the radiative heat source $-\nabla \cdot \mathbf{q}$ produced by P_N methods with different orders as well as the result from the exact solution. The sign of radiative heat source $-\nabla \cdot \mathbf{q}$ reflects the net radiative heat transfer from the medium, where negative radiative heat source indicates a loss of energy and vice versa. The radiative heat sources plotted in Fig. 5.10(b) show a negative peak (emission outstrips absorption) in the center ($z = 0$ m) with a rapid attenuation away from the peak until the net radiative heat transfer becomes positive (at $z = \pm 0.1$ m; absorption

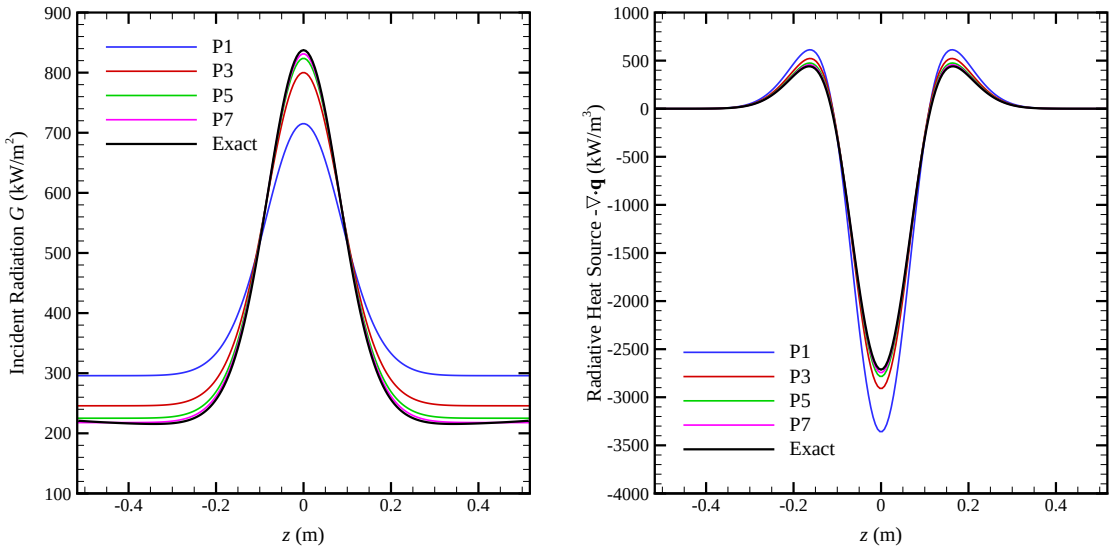

(a) (b)

Figure 5.10: Comparing incident radiation and radiative heat source with exact solution for 1-D slab with flame-like radiative properties; (a) incident radiation G and (b) radiative heat source $-\nabla \cdot \mathbf{q}$.

dominates). The results for the radiative heat source predicted by higher-order P_N methods become increasingly better in the central region ($|z| < 0.25$ m) and with P_7 result almost match the exact solution. And for optically thin regions ($|z| > 0.25$ m) where the radiative heat sources are relatively small, the differences between different orders of P_N methods seem unimportant, although the incident radiation G from different orders of P_N methods in Fig. 5.10(a) show relatively larger differences between different orders of P_N methods.

Figures. 5.11 and 5.12 present the angular distribution of radiative intensities at two locations (at $z = 0.0026$ m and $z = 0.455$ m). The plot at the central location ($z = 0.0026$ m) in Fig. 5.11 shows consistent improvements in accuracy from higher-order methods and is similar to what has been shown in Fig. 5.3(b) for the homogeneous example with $\tau = 0.5$. Since this location ($z = 0.0026$ m) is not exactly at the center, the plots are no longer symmetric. Therefore, P_1 gives nonisotropic results though it still incurs quite large errors. At the location of $z = 0.455$ m, it can be seen from Fig. 5.11(a) (the value 0 is a circle in this polar plot) that the magnitude of intensities in the upper

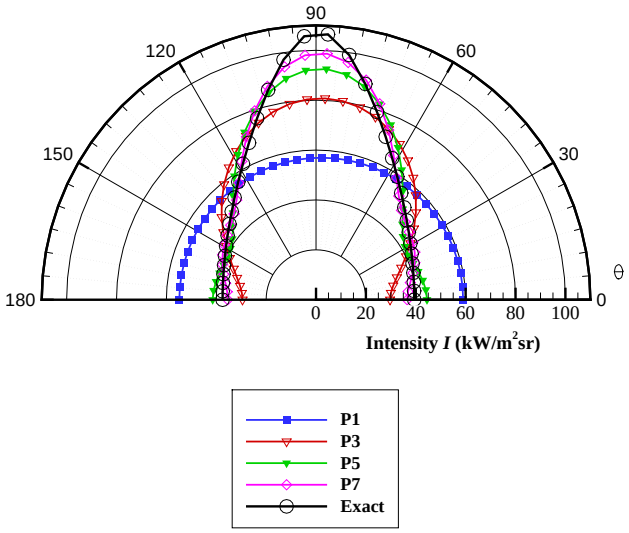

Figure 5.11: Comparison of intensity distributions calculated by P_N methods and exact solution at $z = 0.0026$ m.

hemisphere ($0° < \theta < 90°$) is still large with the magnitude of intensities being close to zero in the lower hemisphere. This is expected since the radiation mostly comes from the central emitting regions and there is no emission from the optically thin region and the wall. The performance of the P_N approximations becomes increasingly better with higher orders and P_7 almost catches the exact solution. Figure 5.12(a) is replotted in Cartesian coordinates as in Fig. 5.12(b) to show the oscillations of high-order P_N methods clearer. For this specific distribution of intensity, P_N methods with higher orders incur less errors but negative intensities are observed in the lower hemisphere. Though negative intensity is unphysical, and will never result from exact solutions of the RTE, it is inevitable for the P_N methods due to the oscillatory nature of finite-order spherical harmonics approximations when dealing with a jump discontinuity of intensity.

For the purpose of showing rotational invariance of the P_N methods and for code verification, the 1-D slab is then rotated by multiple random angles in a 3-D coordinate system. The I_0^0 and radiative heat sources are almost the same as expected, while the remainder of the I_n^m change according to the coordinate orientation. The P_7 results in direction (0 0 1) (along z-axis), direction

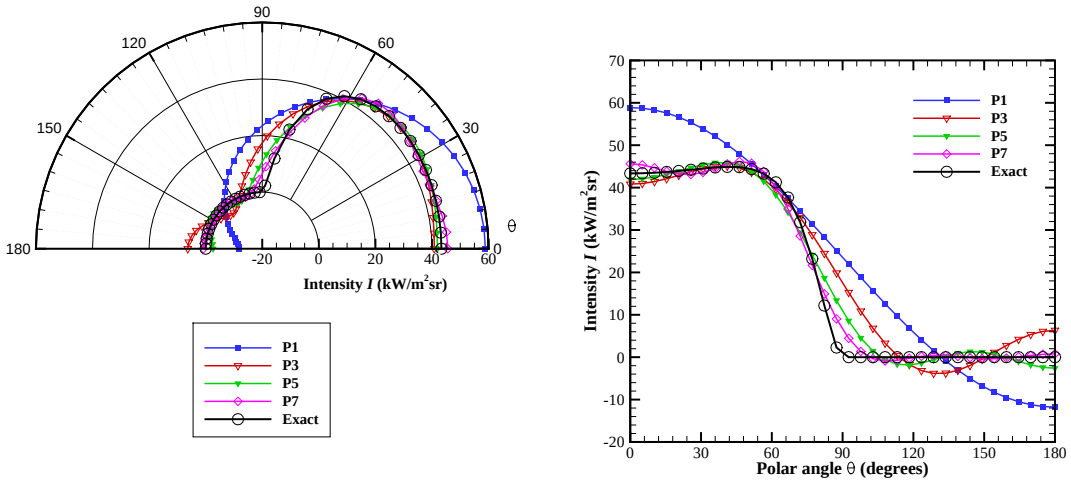

(a) (b)

Figure 5.12: Comparison of intensity distributions calculated by P_N methods and exact solution at z = 0.455 m; (a) in polar coordinates (b) in Cartesian coordinates.

(1 0 0) (along x-axis) and direction (-0.3756, 0.4631, 0.8027) are shown in Fig. 5.13.

Finally, the radiative heat source predicted by PMC results is also calculated and compared to the exact solution, which is shown in Fig. 5.14. The PMC result, which will be used as reference solution when exact solutions are no longer available for later examples. PMC is a stochastic method so that the accuracy and computational cost of PMC method depend on many factors such as the number of photon bundles that are traced, optical thickness of the problem, boundary conditions, mesh size, etc.. It is quite inconclusive to interpret a direct comparison of computational cost between other deterministic methods and PMC method. Furthermore, in the inhomogeneous examples in this thesis, as well as in real world applications, the emission and absorption may vary over several orders of magnitude across the domain, there is so far no general rule to determine the optimal number of photon bundles for any specific problem. For example, the results from Fig. 5.14 have shown that mean values predicted from 1-million-photon-bundle scheme are still not good enough at the center of the slab compared from that of the 50-million-photon-bundle scheme for this 1-D case, while the PMC results from 50-million-photon-bundle scheme are almost identical to

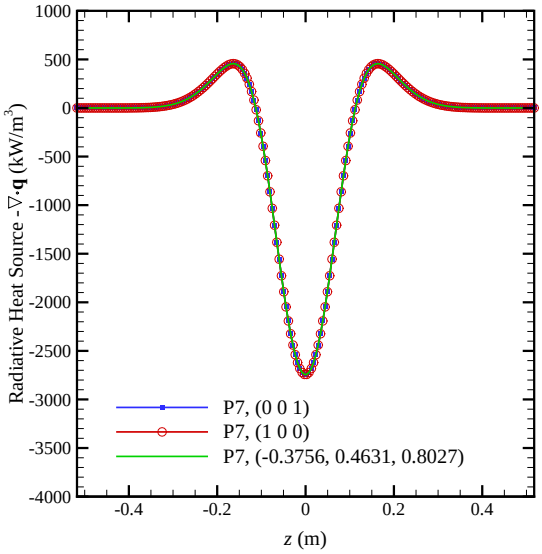

Figure 5.13: Comparing radiative heat source calculated from P_7 method with three orientations.

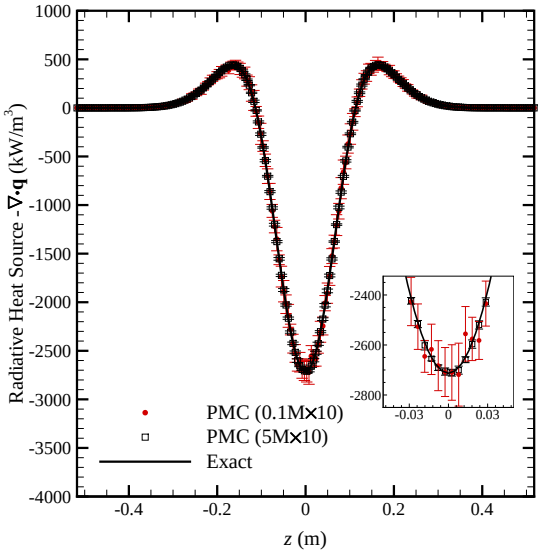

Figure 5.14: Comparing radiative heat source calculated from PMC method with the exact solution of 1-D slab for flame-like radiative properties.

the exact solution.

The CPU time comparison for Problem 3 for the P_N methods and the PMC is given in Table 5.6. The computational cost increases a lot especially for P_5 and P_7 from that of former 1-D

slab cases (Table 5.3 and 5.5).

Table 5.6: Comparison of CPU time (s) for Problem 3: 1-D slab with flame-like κ and I_b

Num. of cells	τ_L	P_1	P_3	P_5	P_7	PMC (0.1M×10)	PMC (5M×10)
200	0.886	0.01	0.10	0.52	1.34	45.7	2532.1

5.1.2 2-D Square or Rectangular Geometry

Like the 1-D slab case, radiative transfer in 2-D square or rectangular geometry is solved by treating the walls of a 3-D cube at one suppressed dimension as perfectly reflective (symmetry boundary). For examples in 2-D square or rectangular geometries, PMC will be used as the reference solution.

5.1.2.1 Problem 4: square enclosure with variable radiative properties

One example for a square enclosure is presented here to study the accuracy of the P_N methods for fields with strongly varying radiative properties in a two-dimensional geometry. The square in this 2-D example uses a $51 \times 51 \times 1$ mesh, and the four boundaries are assumed black and cold (the remaining two in the suppressed dimension use the specular reflection/symmetry boundary condition). The following radiative properties are chosen for the square enclosure:

$$4\pi I_b = 4\pi\left[1 + 5r^2(2 - r^2)\right], \quad \mathrm{W \cdot m^{-3}} \tag{5.4a}$$

$$\kappa = C_k\left[1 + 3.75(2 - r^2)^2\right], \quad \mathrm{m^{-1}} \tag{5.4b}$$

$$r^2 = x^2 + y^2, \quad -1 \le x \le 1, -1 \le y \le 1, \quad \mathrm{m} \tag{5.4c}$$

$$\tau_R = \int_0^R \kappa dr = 9\sqrt{2}C_k, R = \sqrt{2}, \quad \mathrm{m, along\ diagonal} \tag{5.4d}$$

The profiles of the Planck function and the absorption coefficients along the diagonal are shown in Fig. 5.15 and three values of C_k are investigated, i.e., C_k=0.01, 0.1 and 1.0, which represent optically thin, intermediate and thick conditions, respectively. Results predicted from high-order P_N methods

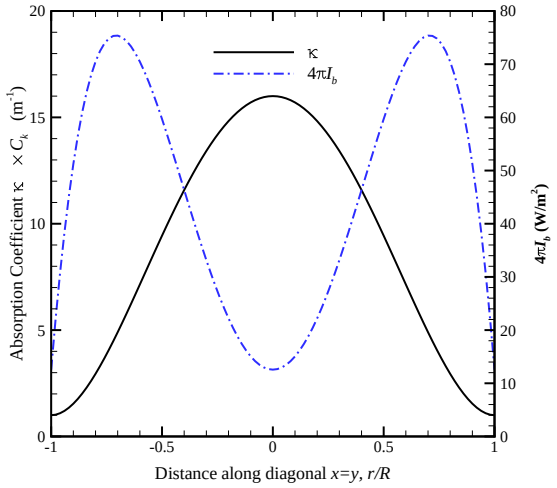

Figure 5.15: Radiative properties of Problem 4 along the diagonal.

as well as those from the PMC method for all three optical conditions in terms of both the negative radiative heat source $\nabla \cdot \mathbf{q}$ and the incident radiation G are shown in Fig. 5.16. Comparing results from the P_N methods with the PMC simulation for the optically thick case, Fig. 5.16(a) shows that all P_N methods except P_1 method do very well. In the optically intermediate case, Fig. 5.16(b), neither P_1 nor P_3 is able to catch the trend of peaks and valleys for the incident radiation G, while P_5 is very close to the PMC results and P_7 follows the variations in G well. For the optically thin case, Fig. 5.16(c), all P_N methods fail to follow the true variation of incident radiation G, with the higher-order methods performing marginally better than P_1; gratifyingly, the more important negative radiative heat source $\nabla \cdot \mathbf{q}$ is captured well even for the optically thin situation. This is because only a small portion of the radiative energy is absorbed ($G/4\pi I_b$) comparing the scale of G in Fig. 5.16(c) with that of the Planck function in Fig. 5.15.

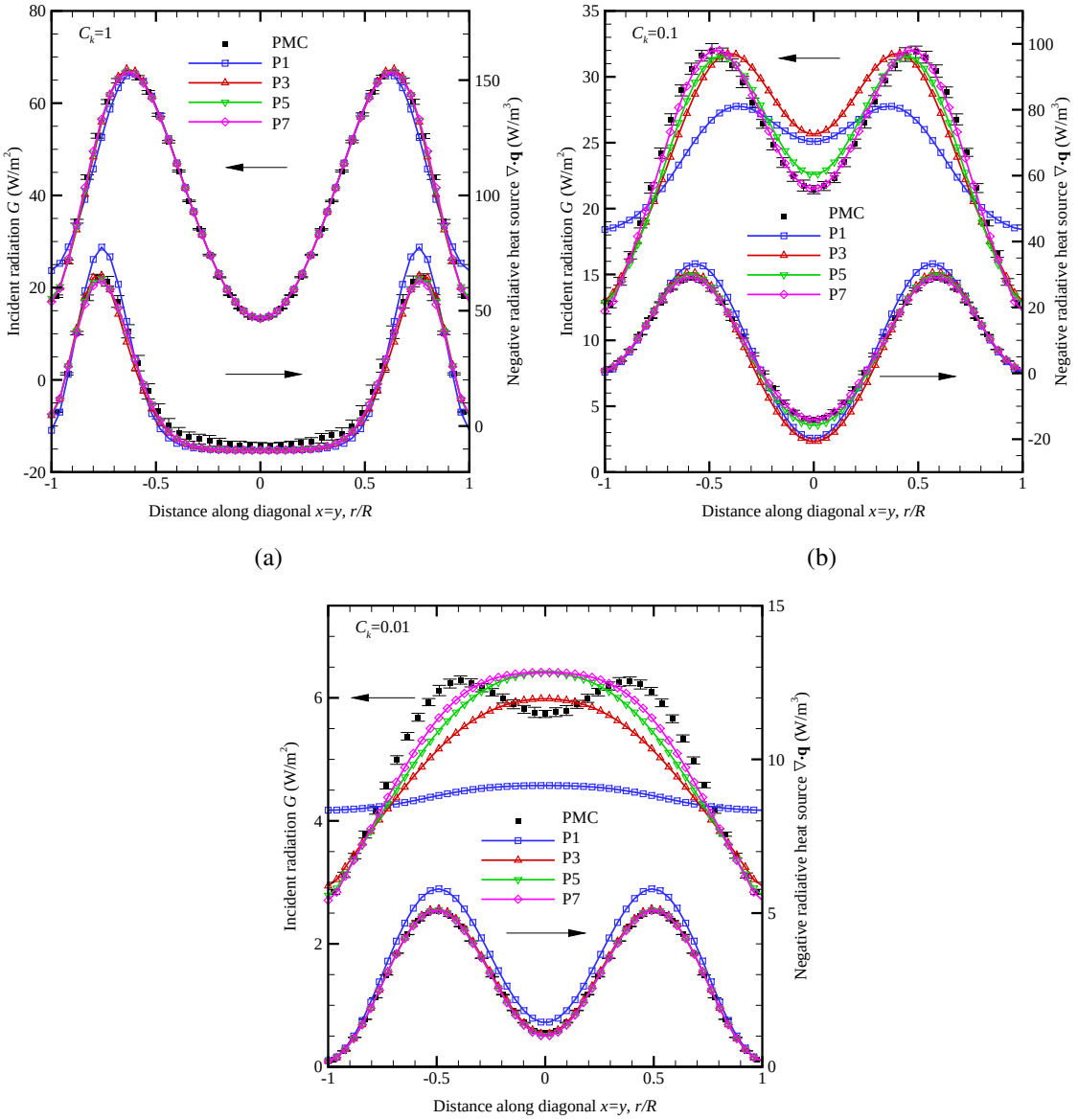

Figure 5.16: Incident radiation and radiative heat source for a square enclosure with various P_N approximations; (a) C_k=1, (b) C_k=0.1 and (c) C_k=0.01.

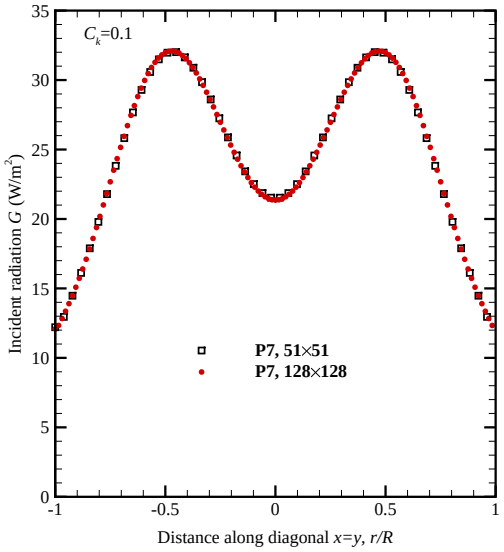

Figure 5.17: Incident radiation G from P_7 method obtained from two different meshes for the optically intermediate case ($C_k = 0.1$).

Mesh dependency test has been conducted to further verify the results. A uniform mesh with 128×128 computational cells is tested with the same distributions of radiative properties. The comparison of G from P_7 method for the $C_k = 0.1$ case with both meshes are shown in Fig. 5.17, and the results from both meshes are found to be overlapping with each other.

The 2-D square mesh is placed into different coordinate planes (x-y, x-z, y-z) to show the rotational invariance of the P_N methods as well as for code validation. It is found that, even though the relevant intensity coefficients are different for all three placements, the incident radiation $G = 4\pi I_0^0$ predicted are identical for all three placements and for all three optical conditions. As a demonstration, the contour profiles of the incident radiation G and the non-zero intensity coefficients I_2^m by the P_7 method from three different placements of the square mesh for the optically intermediate case (C_k=0.1) are shown in Figures 5.18–5.20. When the mesh is placed into the x-z plane (Fig. 5.19) and the y-z plane (Fig. 5.20), it is found that

$$\begin{bmatrix} I_0^0 \\ I_2^0 \\ I_2^1 \\ I_2^2 \end{bmatrix}_{x\text{-}z \text{ plane}} = \begin{bmatrix} I_0^0 \\ I_2^0 \\ I_2^{-1} \\ -I_2^2 \end{bmatrix}_{y\text{-}z \text{ plane}} \tag{5.5}$$

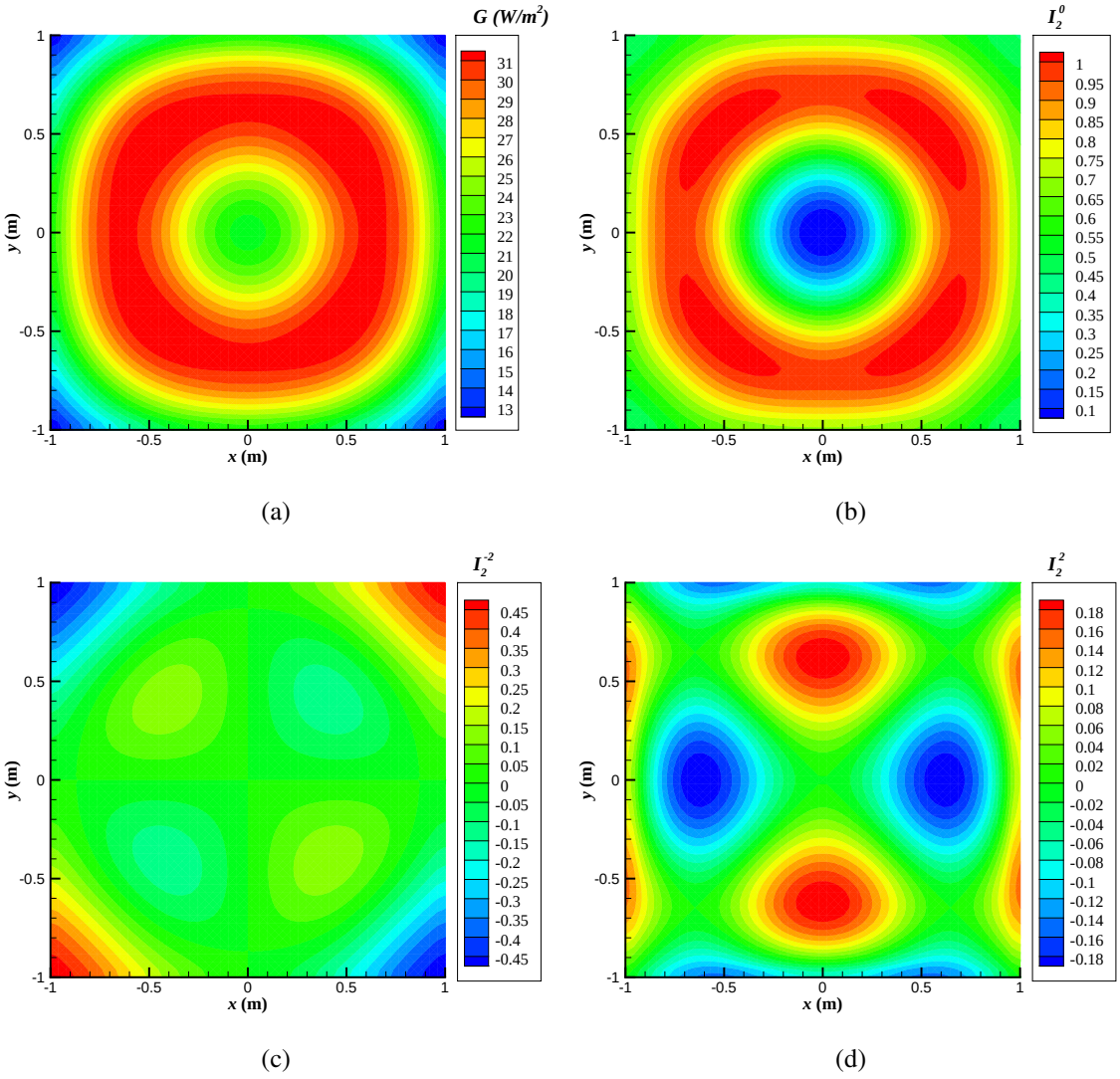

Figure 5.18: Incident radiation G and intensity coefficient I_2^m from P_7 method for Problem 4 when $C_k = 0.1$ in x-y plane; (a) $G(= 4\pi I_0^0)$, (b) I_2^0, (c) I_2^{-2} and (d) I_2^2.

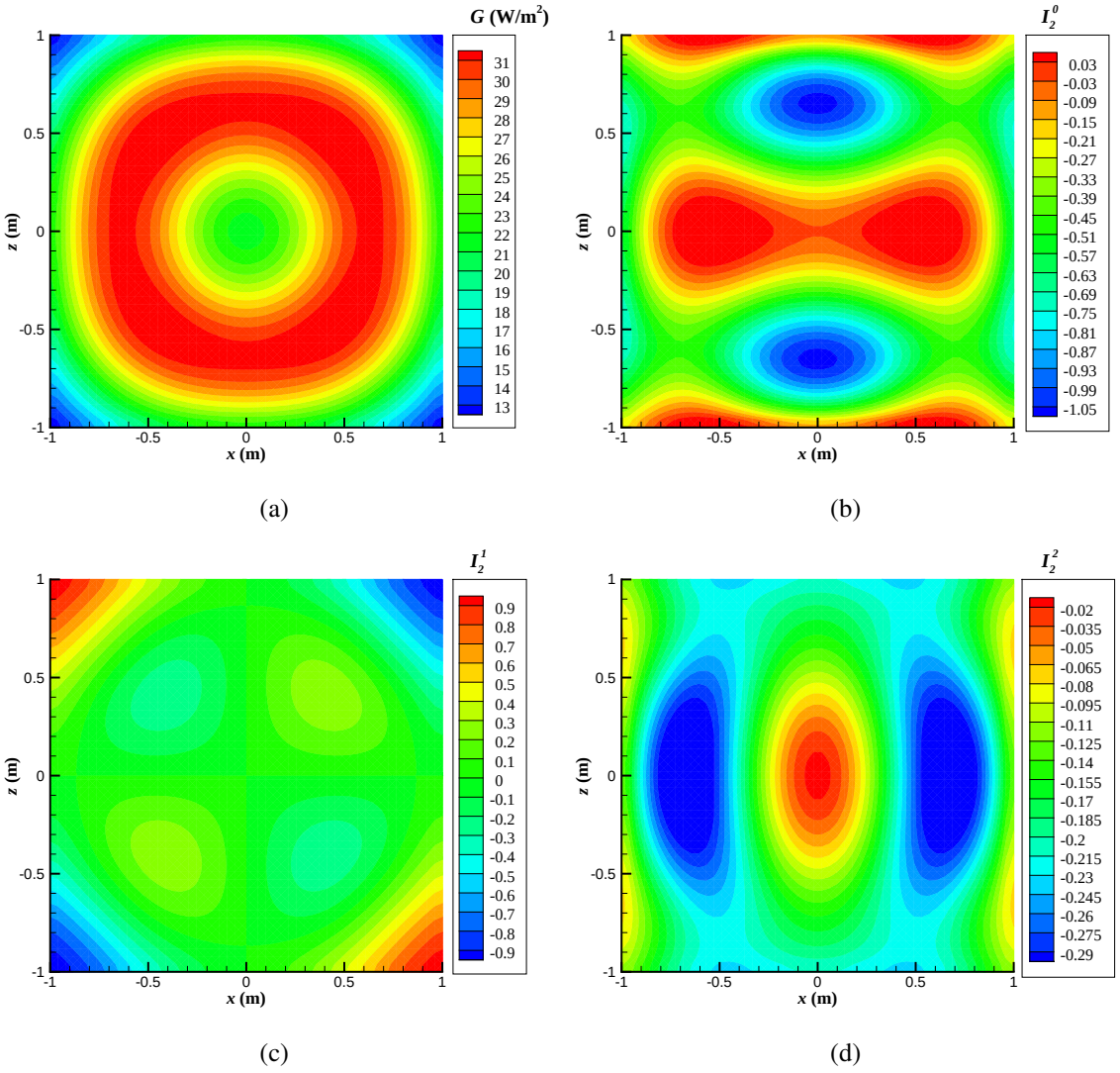

Figure 5.19: Incident radiation G and intensity coefficient I_2^m from P_7 method for Problem 4 when $C_k = 0.1$ in x-z plane; (a) $G(= 4\pi I_0^0)$, (b) I_2^0, (c) I_2^1 and (d) I_2^2.

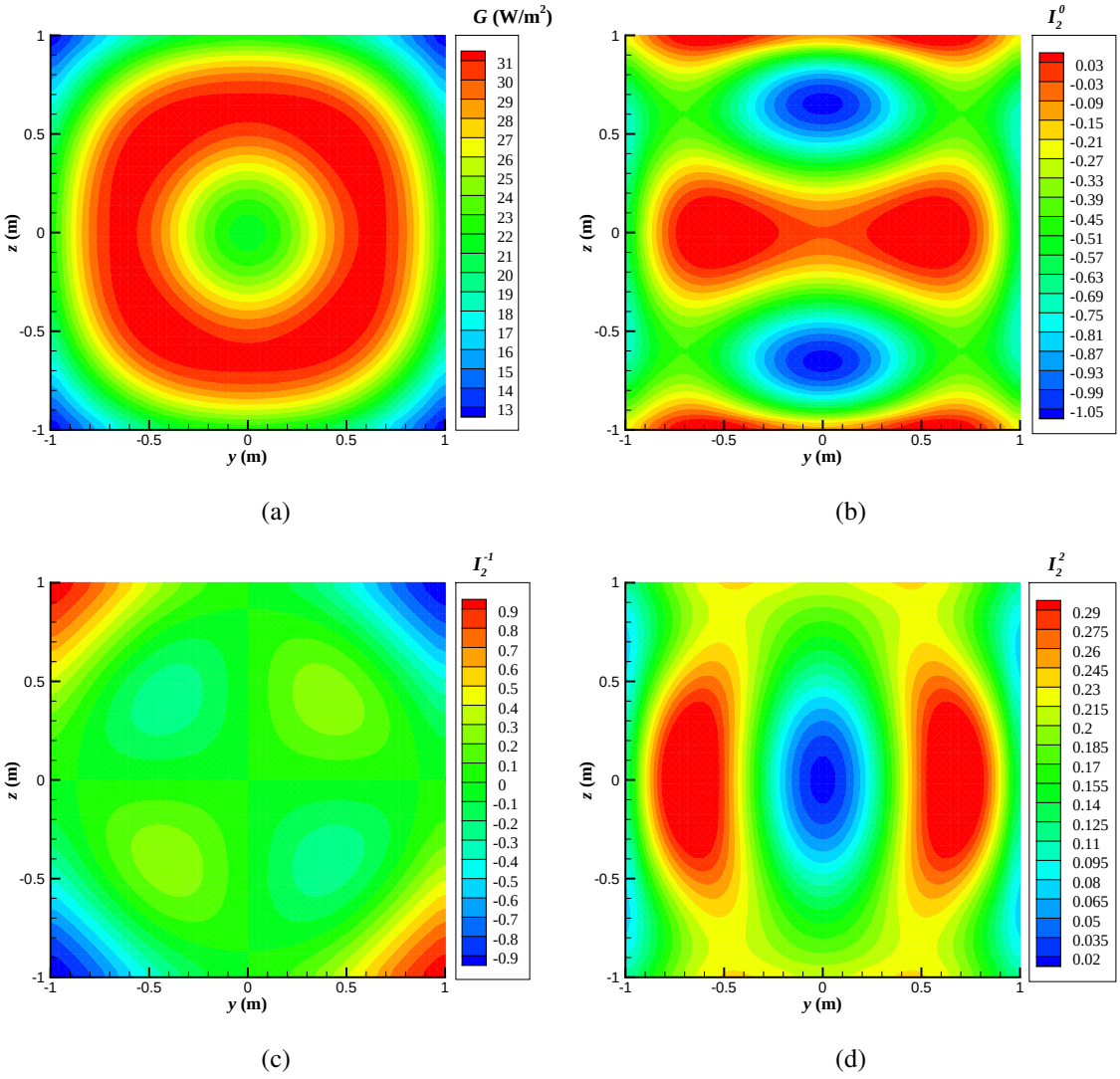

Figure 5.20: Incident radiation G and intensity coefficient I_2^m from P_7 method for Problem 4 when $C_k = 0.1$ in y-z plane; (a) $G(= 4\pi I_0^0)$, (b) I_2^0, (c) I_2^{-1} and (d) I_2^2.

Table 5.7: Comparison of CPU time (s) for Problem 3: 2-D square enclosure with variable κ and I_b

No. of cells	C_k	τ_R	P_1	P_3	P_5	P_7	PMC
2,601 (51×51)	C_k=1	12.7	0.02	0.75	4.71	7.0	459 (5M×10)
	C_k=0.1	1.27	0.02	0.87	5.05	9.33	125.5 (0.5M×10)
	C_k=0.01	0.127	0.02	1.78	7.09	19.2	21.2 (0.05M×10)

The CPU time comparison for Problem 4 for the P_N methods and the PMC is given in Table 5.7. For the computational cost of P_N methods, the overall optical thickness plays a more important role in this 2-D square problem. The CPU times for optically thick and intermediate cases do not differ much but the optically thin case consumes much more time. The computational cost of PMC method is also related to the overall optical thickness. More time is spent on ray tracing for optically thin case than that of the optically intermediate and thick cases. On the other hand, for optically thin case, it is not necessary to trace as many as photon bundles for optically intermediate and thick cases.

Figure 5.21 depicts the radiative flux q_w along one of the cold black walls for the same three optical conditions. Even for the optically thick case, P_1 is found to incur serious errors (6% at the center and 40% in the corners) while all high-order P_N methods perform well with a distinct improvement of accuracy from P_1 to P_3 and a small improvement from P_3 and P_5 to P_7 at the center of the wall. Similarly, for the optically intermediate case, P_1 again has large errors in the corners while P_3, P_5 and P_7 perform well against the PMC. Finally, P_1 predicts uniform heat flux for the optically thin case, while the high-order P_N methods predict almost the correct heat flux from the PMC method.

To test the specified-q_w boundary condition, one wall in each direction (x and y) is flagged as a specified-q_w boundary condition by inputting q_w according to the profile shown in Fig. 5.21 (first obtained by setting all walls to cold and black), while the opposite walls are kept as black and cold. Figure 5.22 shows the contour plot of $\nabla \cdot \mathbf{q}$ from the 2-D Cartesian P_7 solver with the specified-q_w boundary condition for the optically thick ($C_k = 1.0$) case. The differences between the cases with and without the the specified-q_w boundary condition are within 0.1%. The specified-q_w boundary

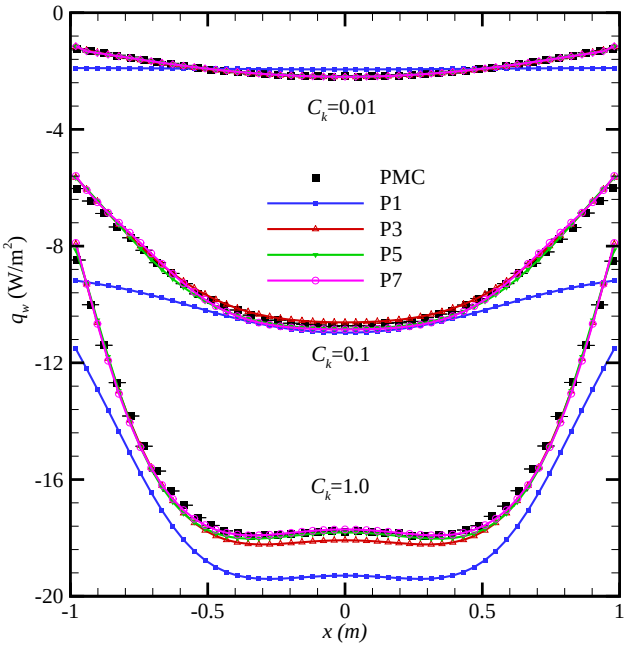

Figure 5.21: Radiative flux along the bottom wall (y=−1.0 m).

condition can be very useful which allows using experimental measurements as boundary values directly.

5.1.2.2 Problem 5: square enclosure with pure scattering radiative properties

A purely scattering medium in a square enclosure with a heated strip is studied next. This problem has formerly been studied by Modest and Yang [145] and Ravishankar and Mazumder [149] for P_1 and P_3 methods. The former had P_3 implemented in FlexPDE software [218] and the latter using in-house software. They found that the P_3 method is as inaccurate as the P_1 method for the optically thin and intermediate cases, and that higher-order P_N methods are expected to improve the solutions of P_N methods for this problem.

A square enclosure with the length of side being L, as shown in Fig. 5.24, with four black walls is considered, in which only the mid-section with the length of $0.2L$ of the bottom wall is hot, while the remainder of the bottom wall and the other three walls are cold. Since there is no

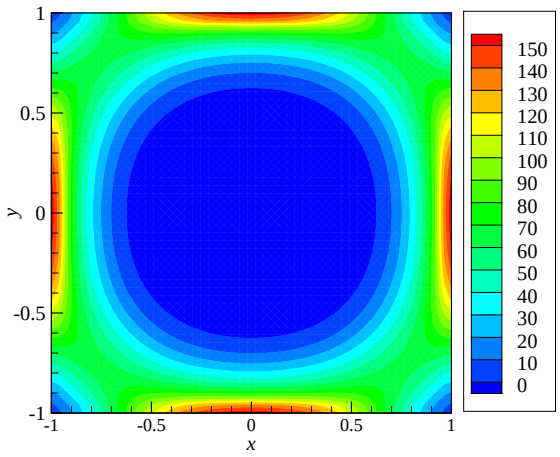

Figure 5.22: The radiative heat source $-\nabla\cdot\mathbf{q}$ from 2-D Cartesian P_7 solver with specified-q_w boundary condition for the $C_k = 1.0$ example. The upper wall ($y = 1.0$ m) and right wall ($x = 1.0$ m) employ specified-q_w boundary condition, while the other two are kept as black and cold wall.

medium absorption for this problem (where $\nabla \cdot \mathbf{q} = 0$ everywhere), the radiative energy emitted by the hot strip is redistributed to all four walls by scattering. A homogeneous and purely isotropically scattering medium with three different optical thickness ($\tau_L = \sigma_s L$= 0.1, 1.0 and 5.0; κ=0.0) is tested. The dimensionless irradiation ($H^* = H/\sigma T_h^4$) along the surfaces is plotted to evaluate the accuracy of different RTE solvers, including the spherical harmonics (P_N) method, the discrete ordinates method (DOM) and PMC. P_N methods with orders from P_1 to P_7 are tested and DOM$_{p\times a}$ for three discrete ordinates schemes with respect to the number of discrete polar ordinates p and azimuthal ordinates a, which are 4×8, 4×16 and 4×32, are tested. A 50×50 2-D grid is employed for all calculations.

Figure 5.24 shows the results for different optical thicknesses from (a) optically thin (τ_L = 0.1), to (b) optically intermediate ($\tau_L = 1.0$), and to (c) optically thick ($\tau_L = 5$). The dimensionless irradiation H^* is plotted along the top wall (on the left), along one of the side walls (in the middle) and along the bottom wall (on the right). The PMC results are regarded as exact. Neither DOM nor

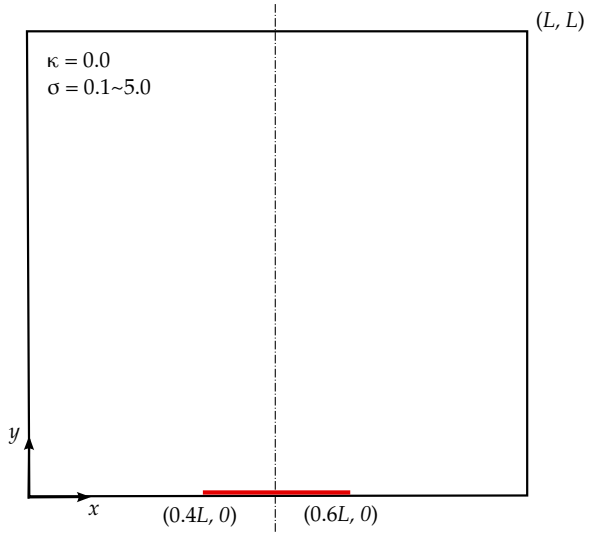

Figure 5.23: Diagram of the square enclosure with hot strip at the bottom center.

P_N can predict the irradiation well for optically thin and optically intermediate medium. As to be expected, the P_N methods predict irradiation H^* less accurately at the bottom surface, because of the discontinuity of intensity in the incoming and outgoing directions near the hot strip. The irradiation H^* calculated from P_N at the bottom wall may even obtain negative values for all optical thicknesses, which is physically impossible. In contrast, all DOM calculations provide decent results on the bottom wall but poorer results compared with P_N for the top and side walls due to ray effects.

P_1 and P_3 results are found to be as same as those of Modest and Yang [145] and Ravishankar and Mazumder [149], which had different implementations other than `OpenFOAM`® and used different meshes. P_5 and P_7 methods do not seem to improve the accuracy to a great extent. But consistent small improvements of H^* at the bottom wall, though still negative, for all three cases are observed. The trend of the convergence from P_1 to P_7 indicates that much higher orders of P_N method is required for the P_N method to match the PMC results for the optically thin and intermediate cases.

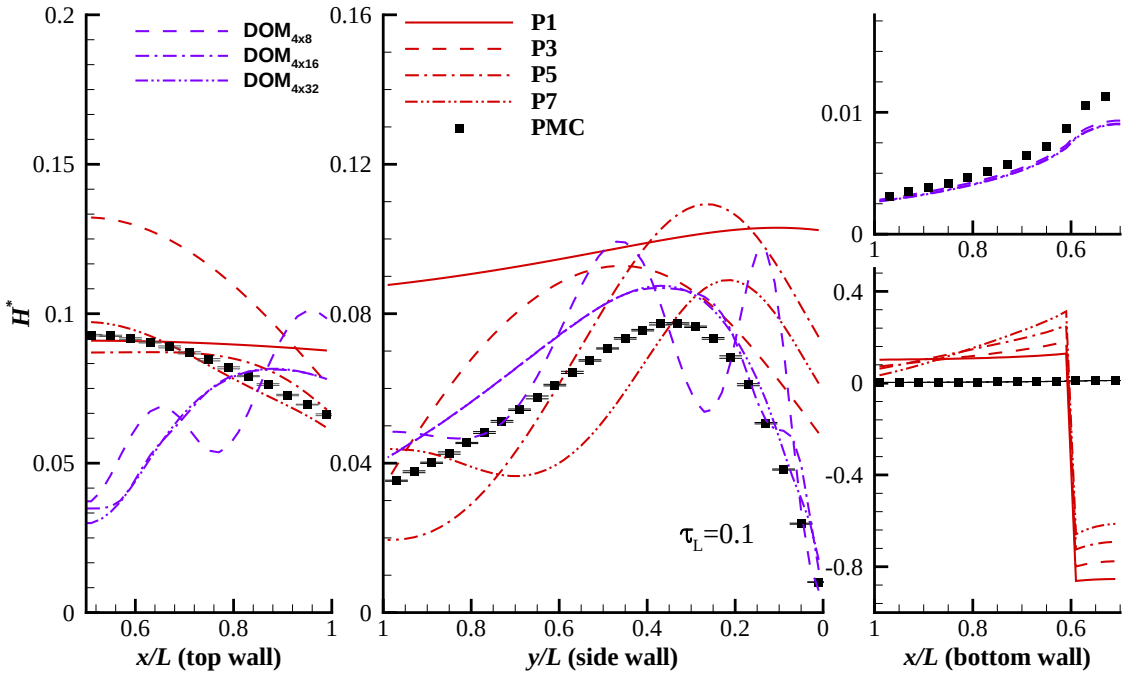
DOM4x8
DOM4x16
DOM4x32
P1
P3
P5
P7
PMC
H*
x/L (top wall)
y/L (side wall)
x/L (bottom wall)
τL=0.1

(a)

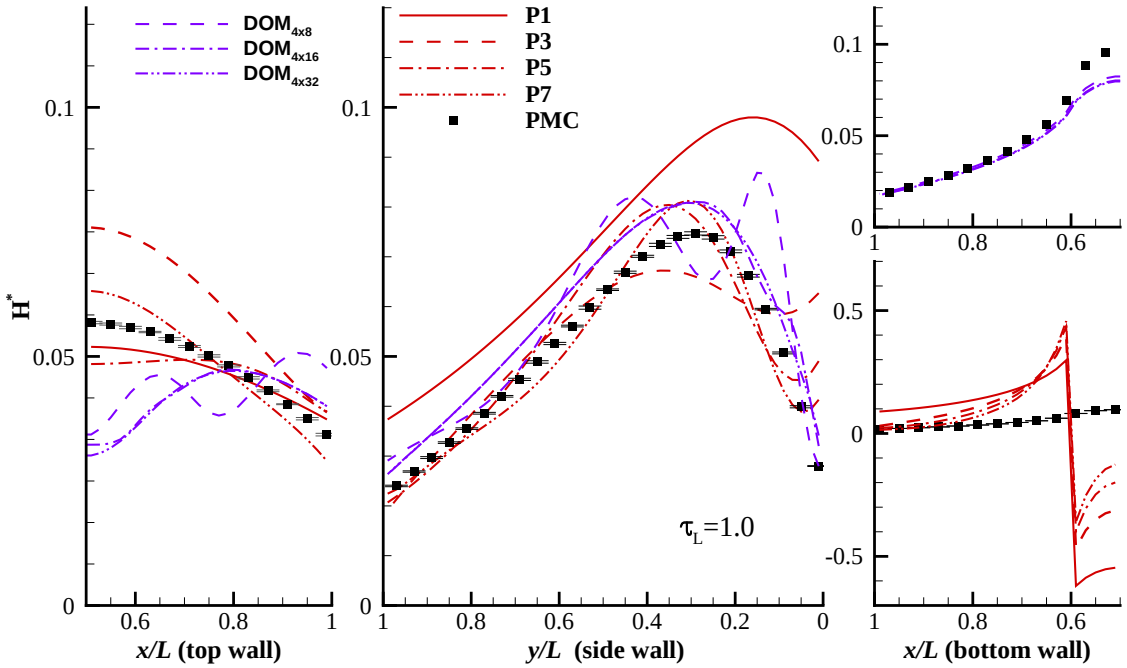

(b)

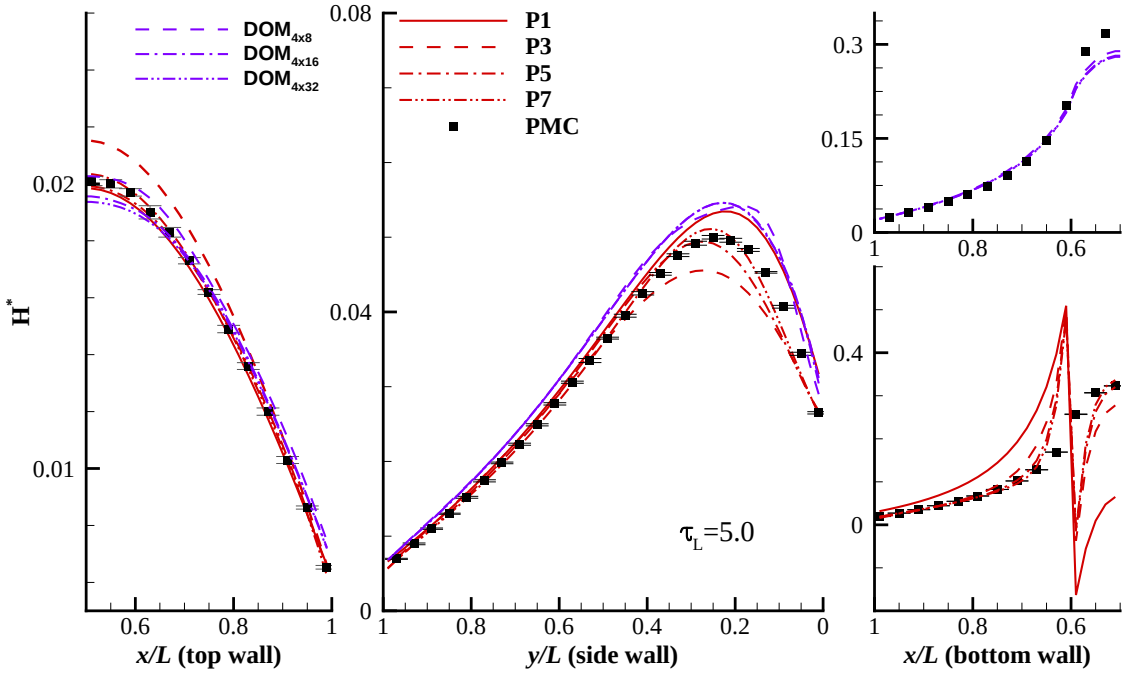

(c)

Figure 5.24: Comparison of different RTE solvers of dimensionless irradiation on surfaces; strip of bottom surfaces heated; (a) $\tau_L = 0.1$, (b) $\tau_L = 1.0$ and (c) $\tau_L = 5.0$.

Table 5.8: Dimensionless irradiation at the walls

$\tau_L = 1$	P_1	P_3	P_5	P_7	PMC
Q^*_{top}	0.0466874	0.0337713	0.0449401	0.0480993	0.0484804
Q^*_{side}	0.0725066	0.0528072	0.0540381	0.0514984	0.0521100
Q^*_{bottom}	0.00821792	0.0606176	0.0470249	0.0489417	0.0472123
$\epsilon_{rel.,t}$	−3.69 %	−30.3 %	−7.30 %	−0.786 %	/
$\epsilon_{rel.,s}$	+39.1 %	+1.34 %	+3.70 %	−1.17 %	/
$\epsilon_{rel.,b}$	−82.6 %	+28.4 %	−0.40 %	+3.66 %	/
$\tau_L = 5$	P_1	P_3	P_5	P_7	PMC
Q^*_{top}	0.0149507	0.0160292	0.0151374	0.0152146	0.0151887
Q^*_{side}	0.0333291	0.0299472	0.0309418	0.0310494	0.0312782
Q^*_{bottom}	0.118391	0.124077	0.122969	0.122677	0.122192
$\epsilon_{rel.,t}$	−1.57 %	+5.53 %	−0.338 %	+0.170 %	/
$\epsilon_{rel.,s}$	+6.56 %	−4.26 %	−1.08 %	−0.731 %	/
$\epsilon_{rel.,b}$	−3.11 %	+1.54 %	+0.636 %	0.397 %	/

Although the profiles of the dimensionless H^* predicted by the P_N methods are not good for the optically intermediate case, the overall energy distributions at the walls predicted by P_N methods are relatively better, which is shown in Table 5.8. Q^* is defined to be the integration of H^* along each wall and it is validated that $Q_{top} + 2Q_{side} + Q_{bottom} \approx 0.2$ (balancing emission) for all P_N and PMC results. The relative errors ϵ_{rel} are the errors of the P_N results with respect to the PMC results for each wall. Q^* and ϵ_{rel} for the optically thick case is also shown in Table 5.8 as a reference. Comparing Q^* from different orders of P_N methods with that from the PMC for the optically intermediate case, P_1 and P_3 are found to be totally off the correct answer but P_5 and P_7 have significantly reduced the levels of errors for all walls.

The CPU time comparison for Problem 5 for the P_N methods, the DOM and the PMC is given in Table 5.9. The computational costs of high-order P_N methods and the DOM show opposite trends as expected. DOM equations are coupled for scattering media and the computational costs of DOM increases with the optical thickness, while the elliptic PDEs of the high-order P_N methods are coupled more strongly for optically thinner media. It is also found that treating scattering is quite expensive for PMC method.

Table 5.9: Comparison of CPU time (s) for Problem 5: 2-D square, pure scattering

No. of cells	τ_L	P_1	P_3	P_5	P_7	$DOM_{4\times8}$	$DOM_{4\times16}$	$DOM_{4\times32}$	PMC (2M×10)
2,500	5.0	0.03	0.65	2.98	7.72	14.8	30.3	65.5	6621
	1.0	0.03	1.03	4.42	15.3	2.22	4.58	9.85	5645
	0.1	0.03	4.39	20.6	73.2	0.96	1.96	4.12	5549

Besides the results from the ordinary P_N methods, results from the modified P_N methods are also presented for comparison, as shown in Fig. 5.25. For comparison, results from non-modified P_7 and PMC are also included. The details of modified differential approximation (MDA) are described in [90,91] and will not be repeated here. The principle is to split the intensity into two components, i.e., one is a ballistic part related to wall emission, and a diffusive part. The ballistic component is easily solved by direct integration, while the diffusive component is suitable to be solved by the P_N method.

Excellent accuracy is achieved for the entire optical range when the MDA is applied to the P_N methods (the MPN method). For the top wall and side walls, the MPN methods are almost as accurate as the PMC results for all three optical conditions. Though the errors at the bottom wall by the MPN methods are still relatively large for the optically thin and intermediate cases, the improvement is significant and unphysical negative irradiation is no longer present. Further improvements can be achieved by the advanced differential approximation (ADA) [92], which will not be covered here.

The results in this example have shown the limits of P_N methods as well as the possibility of hybrid solution methods such as the MPN if the non-diffusive intensity fields can be evaluated separately when series of spherical harmonics cannot resolve them.

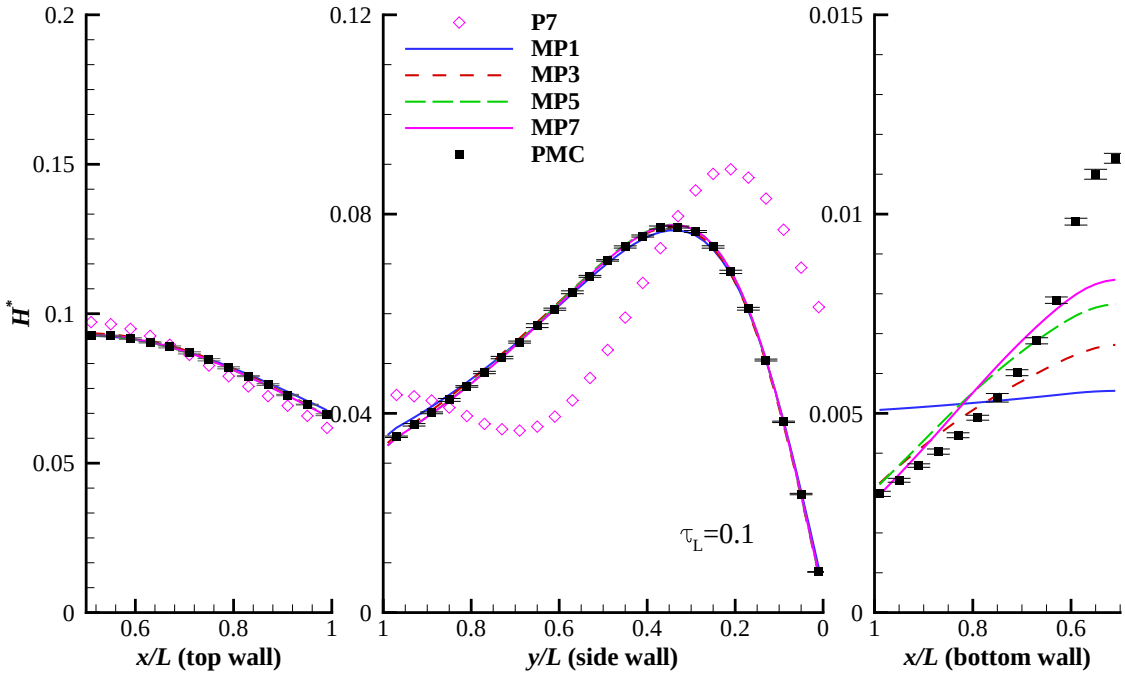
P7
MP1
MP3
MP5
MP7
PMC
τ_L=0.1
H^*
x/L (top wall)
y/L (side wall)
x/L (bottom wall)

(a)

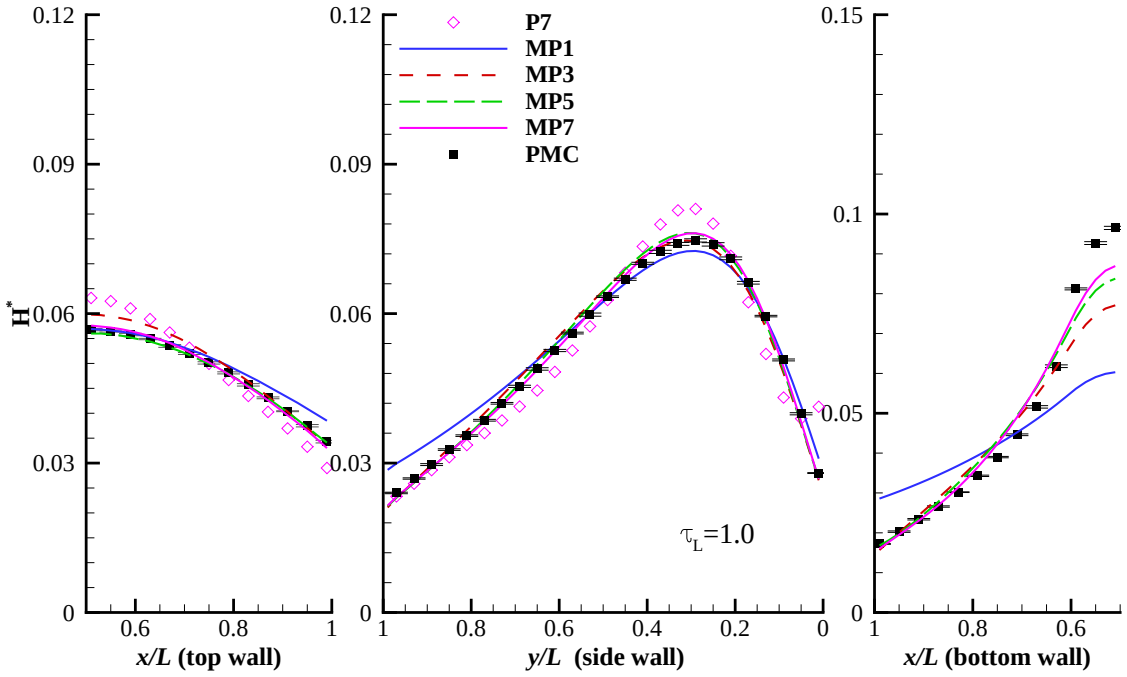

(b)

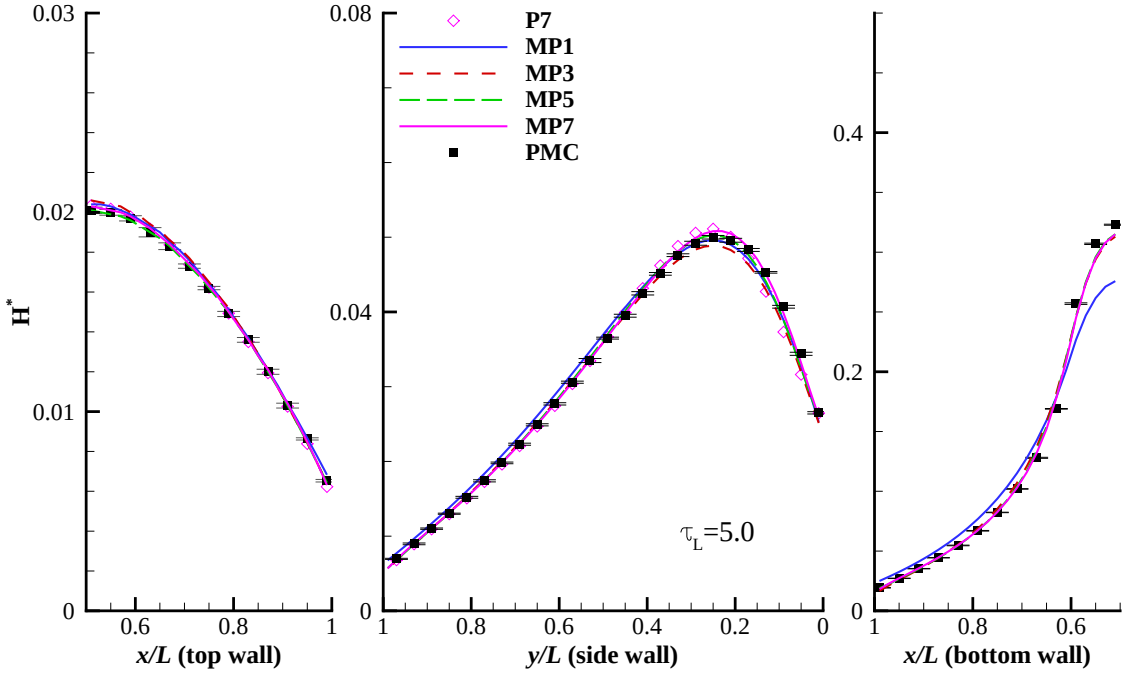

(c)

Figure 5.25: Comparison of different MPN solvers of dimensionless irradiation on surfaces; strip of bottom surfaces heated; (a) $\tau_L = 0.1$, (b) $\tau_L = 1.0$ and (c) $\tau_L = 5.0$.

5.1.2.3 Problem 6: rectangular enclosure with mixed diffuse-specular gray walls

Polished metals and glassy materials, which display strong specular reflection peaks, can effectively be approximated by a combination of diffuse reflection and specular reflection. Sample simulations to test the accuracy of the high-order P_N method for mixed diffuse-specular walls have been performed on a 2-D rectangular geometry enclosed by walls with different surface characteristics. The geometry and radiative properties are shown in Fig. 5.26, and the properties of the left and right walls make up four test cases, i.e.,

1. purely specular reflection ($\rho^s = 1$);
2. purely diffuse reflection ($\rho^d = 1$);
3. mixed diffuse-specular reflection without emission ($\epsilon = 0, \rho^s = 0.7, \rho^d = 0.3$);
4. mixed diffuse-specular reflection with emission ($\epsilon = 0.5, \rho^s = 0.2, \rho^d = 0.3$).

A 80×20 grid is employed for this problem.

The negative radiative heat source, $\nabla \cdot \mathbf{q}$ along the centerline ($x = 1$ m), and the heat flux at the top and bottom walls, q_w, calculated with different orders of P_N methods as well as the PMC method are shown in Figs. 5.27-5.30 for Cases 1–4. Generally speaking, good agreement is observed between the results from high-order P_N and those from PMC for all four cases, with results for heat flux at the corners showing the biggest discrepancies. For the pure-specular-reflection case, Case 1 as shown in Fig. 5.27, only the result from P_1 shows relatively large discrepancies compared to PMC results near the top and bottom walls. P_5 and P_7 methods even outperform the PMC on the heat fluxes predictions at the walls; since Case 1 is essentially a 1-D problem (even though the mesh is 2-D), the heat fluxes are supposed to be uniform along both top and bottom walls, and the uniformity of heat flux is successfully predicted by the P_N methods. In the pure-diffuse-reflection case, Case 2 as shown in Fig. 5.28, a clear gradual convergence from lower-order P_N methods to high-order P_N methods towards the PMC results is observed. P_7 gives the correct radiative heat source along

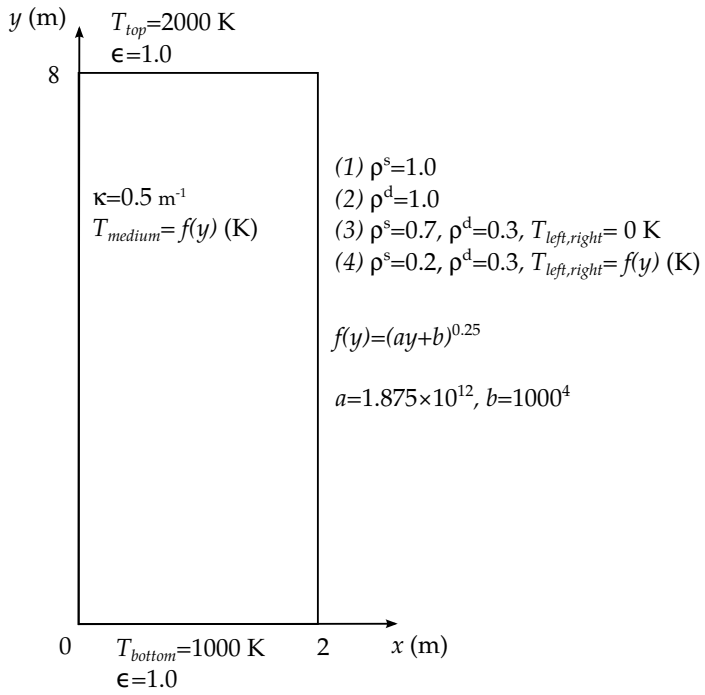

Figure 5.26: Schematic of rectangular enclosure for tests of specular, diffuse and mixed diffuse-specular surfaces; the bottom and top walls are black emitting walls and the left and right walls are following the configurations from (1) to (4).

the centerline but is still a little bit off for the heat flux predictions at both walls. P_1 gives the same results for both Case 1 and Case 2, because there is no difference in the P_1 formulation for treating specular and diffuse reflection as is shown in Appendix C. For Case 3 (Fig. 5.29), in which the left and right walls are mixed diffuse-specular surfaces, P_1 predicts the same uniform results as in the former two cases as expected. All high-order P_N methods are doing well for the prediction of radiative heat sources along the centerline. Compared with the performances of high-order P_N methods observed in Cases 1 and 2, it is found that more specular reflection (larger ρ^s) results in more accurate results from the high-order P_N methods. For the last case, Case 4 (Fig. 5.30), the left and right walls are two mixed diffuse-specular-emitting surfaces. This time P_1 predicts a non-uniform q_w at both walls and the performances of high-order P_N methods are similar to their performances in Case 2.

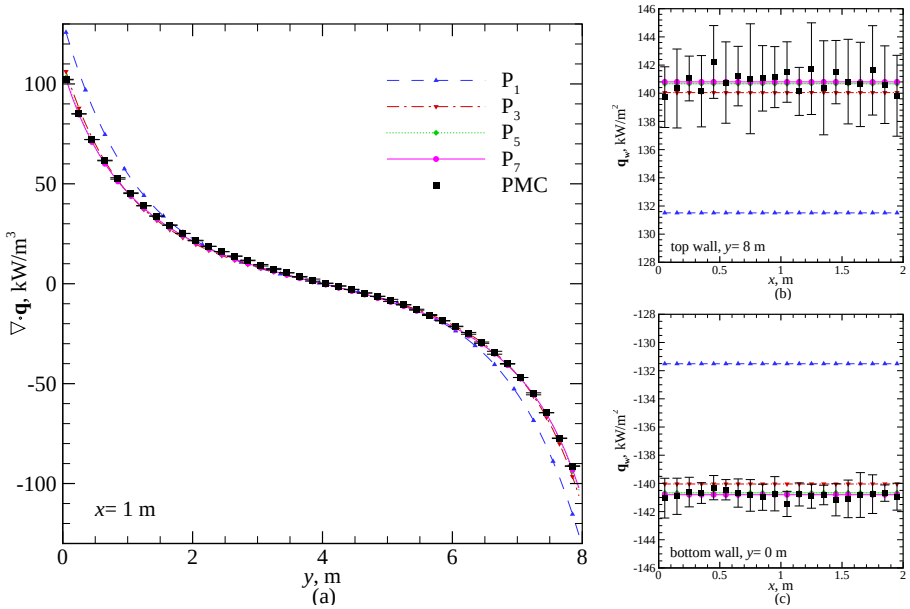

Figure 5.27: Radiative heat source $\nabla \cdot \mathbf{q}$ along $x = 1.0$ m and the heat flux q_w at top and bottom walls for Case 1; (a) $x = 1.0$ m, (b) $y = 8.0$ m and (c) $y = 0.0$ m.

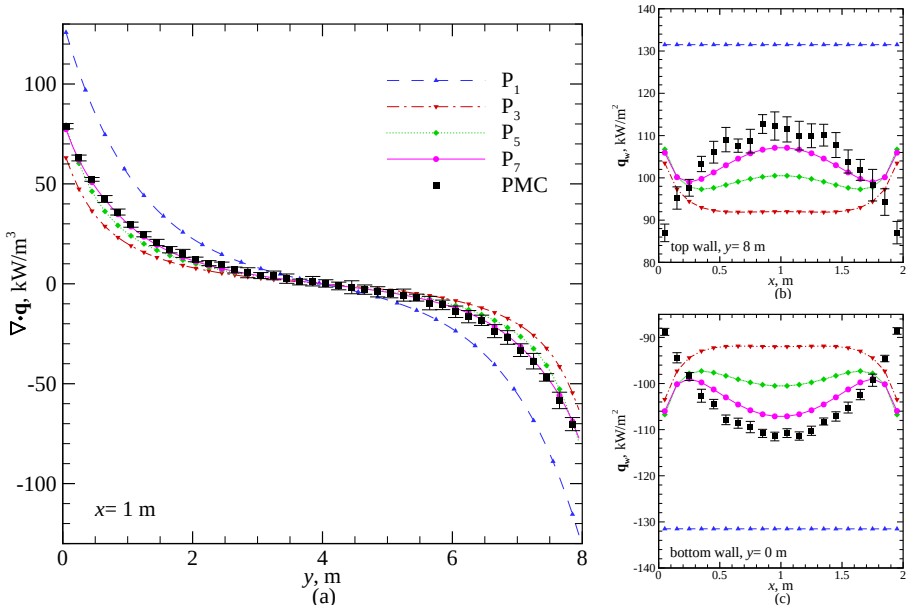

Figure 5.28: Radiative heat source $\nabla \cdot \mathbf{q}$ along $x = 1.0$ m and the heat flux q_w at top and bottom walls for Case 2; (a) $x = 1.0$ m, (b) $y = 8.0$ m and (c) $y = 0.0$ m.

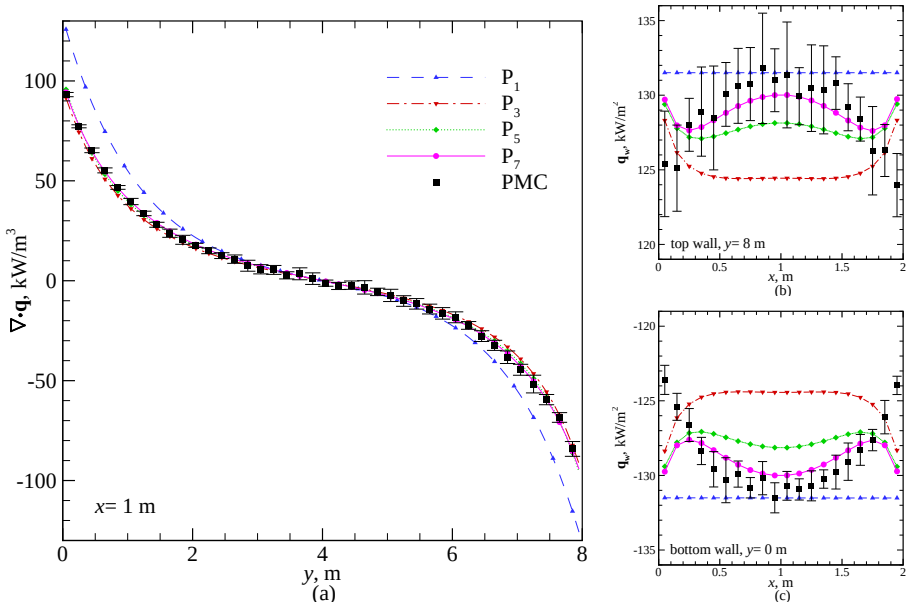

Figure 5.29: Radiative heat source $\nabla \cdot \mathbf{q}$ along $x = 1.0$ m and the heat flux q_w at top and bottom walls for Case 3; (a) $x = 1.0$ m, (b) $y = 8.0$ m and (c) $y = 0.0$ m.

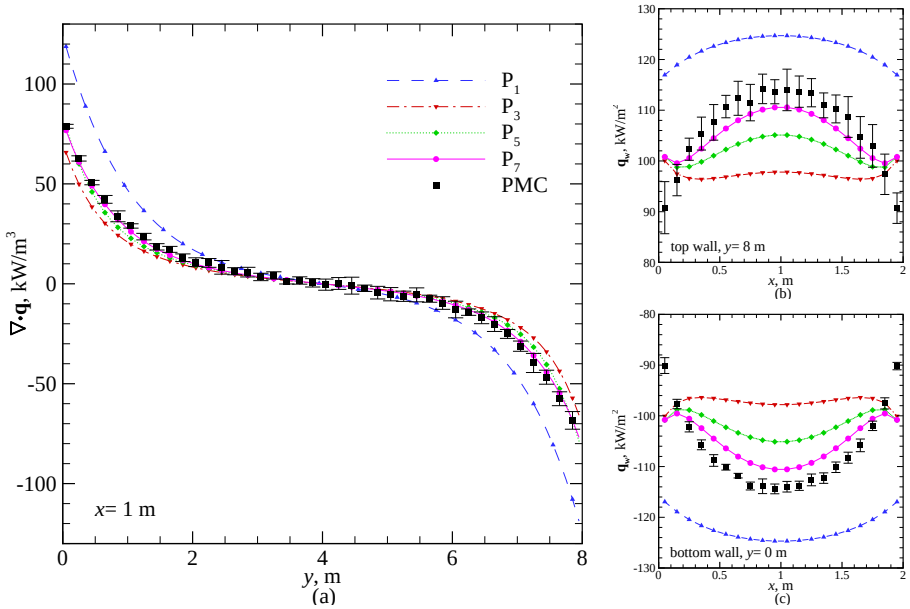

Figure 5.30: Radiative heat source $\nabla \cdot \mathbf{q}$ along $x = 1.0$ m and the heat flux q_w at top and bottom walls for Case 4; (a) $x = 1.0$ m, (b) $y = 8.0$ m and (c) $y = 0.0$ m.

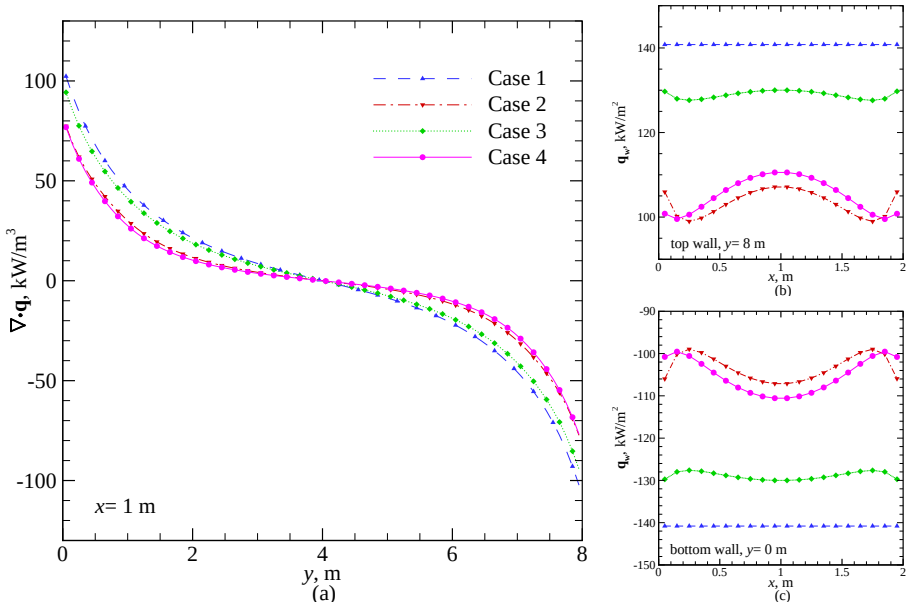

Figure 5.31: Comparison of radiative heat source $\nabla \cdot \mathbf{q}$ and the heat flux at the wall q_w from P_7 solver for four surface properties.

Figure 5.31 shows a comparison of the P_7 results for the four surface characteristics. The differences between the results from Case 1 and Case 2 show that the wall properties can significantly affect the radiative heat source distributions and the heat flux profiles at the wall especially for larger aspect ratios. The differences between the results from purely diffuse walls and purely specular walls are expected to increase with higher aspect ratio of the geometry. Also, it is expected that the radiative heat source in the medium and the heat flux at walls for Case 3 lie between that of Case 1 and Case 2.

The performance of P_N methods has been tested by this example in a rectangular geometry with mixed diffuse-specular walls. The error from P_1 in this example is not solely due to the optical-thickness but a physical phenomenon that cannot be formulated through the P_1 method. The high-order P_N methods are found to be capable of treating surfaces with mixed diffuse-specular properties which makes it a good tool for radiative transfer researches concerning wall properties.

Table 5.10: Comparison of CPU time (s) for Problem 6: 2-D rectangle, mixed diffuse-specular-emitting walls

No. of cells	τ_L	P_1	P_3	P_5	P_7	PMC (2M×10)
1,600	4.0	0.02	0.35	2.05	4.37	4660

The CPU time comparison for Problem 6 for the P_N methods and the PMC is given in Table 5.10. The computational costs for all four sets of surface properties are similar.

5.1.3 Cylindrical and Wedge Geometries

Axisymmetric geometries are common in general CFD applications, and thus also in the study of radiative transfer. In finite-volume applications, three different kinds of cylindrical meshes tend to be used. The first type of a computational domain is a full 3-D cylinder. The full 3-D cylindrical grid, which usually leads to a large number of computational cells, is nevertheless often used in flow field simulations by large eddy simulation (LES) and direct numerical simulation (DNS), because these problems by nature are three-dimensional. The second type is a thin wedge with single node in the circumferential direction, which is much more efficient than using a full cylinder for axisymmetric problems. Many combustion problems in a cylinder are axisymmetric, but most finite volume-based CFD codes rarely have cylindrical coordinates and/or axisymmetric capability. In those cases, such a thin-wedge mesh instead of the full cylinder is usually chosen to expedite the computation. The last one is a fan-shape wedge with multiple nodes in the circumferential direction, in order to reduce computational cost by recognizing periodic patterns in the circumferential direction within a cylinder.

In the coming sections, the radiative transfer predicted by the high-order P_N methods for all of these three grids will be studied. It is well-known that P_1 will perform poorer in a cylindrical geometry than in a Cartesian geometry [21], because radiative intensities tend to have more anisotropic angular distributions. The performance of high-order P_N methods in cylindrical geometry is to be demonstrated with three different examples.

5.1.3.1 Problem 7: Cylindrical enclosure and a 10° wedge enclosure with variable radiative properties

In this problem, a cylindrical geometry with axisymmetric radiative properties is considered. A long cylindrical enclosure ($R = 0.5$ m and $Z = 2.5$ m) with variable radiative properties is tested with the P_N methods as well as an exact solution obtained by direction integration [21]. The absorption coefficient κ varies both in the r-direction and z-direction described by Eq. (5.6):

$$I_b = 1 + \frac{20}{R^4} r^2 (R^2 - r^2), \quad \mathrm{W \cdot m^{-3}} \tag{5.6a}$$

$$\kappa = C_k \left[1 + \frac{15}{R^4} (R^2 - r^2)^2 \right], \quad \mathrm{m^{-1}} \tag{5.6b}$$

$$C_k = 0.3 + z \quad 0 \le r \le R = 0.5, 0 \le z \le 2.5, \quad \mathrm{m} \tag{5.6c}$$

$$\tau_R = \int_0^R \kappa dr = 3.75 C_k \tag{5.6d}$$

The radial optical thickness τ_R ranges from 1.125 (optically intermediate) to 10.5 (optically thick). The scale and dimension of the Planck-function I_b for this problem do not have any physical significance.

Radiative calculations are conducted on two meshes: a 2-D thin wedge and a full 3-D cylinder, with the same axisymmetric radiative medium. The computational meshes are shown in Fig. 5.32. The cylinder has 45 cells along the radius and 40 cells along the axis with a small square cuboid ($15 \times 15 \times 40$) at the center as shown in Fig. 5.32(a). The size of the square cuboid is 0.0156 m $\times$ 0.0156 m $\times$ 2.5 m. The size of the square is not very important for this example because the gradients of the radiative properties close to the center of the cylinder are small. The wedge has 84 cells along the radius and 40 cells along the axis as shown in Fig. 5.32(b). The tip of the wedge is cut off to avoid mathematical singularity at $r = 0$.

All walls of the full cylinder are cold and black. For the 2-D wedge, the top ($z = 2.5$ m), bottom ($z = 0$ m) and right ($r = 0.5$ m) walls are cold and black, the centerline boundary condition

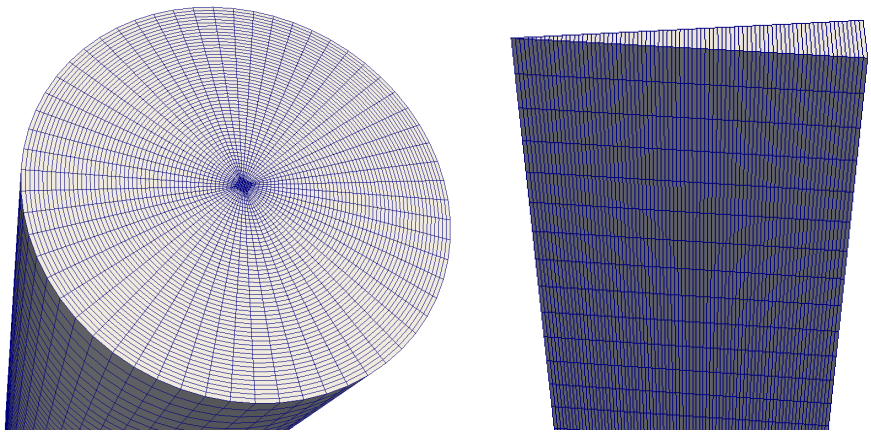

(a) (b)

Figure 5.32: The grids used for Problem 7 in (a) a full 3-D cylinder and (b) a 10° wedge.

for axisymmetric P_N method, Eq. (3.46) (the surface normal derivative of I_n^m are 0 when m=0, and I_n^m=0 when $m \neq 0$), is applied for the centerline of the wedge mesh.

Comparison of calculated incident radiation G for both the 3-D cylinder and the 2-D wedge meshes at two locations (z=0.71 m and z=1.60 m) are presented in Fig. 5.33. The P_N solutions from both geometries overlap each other, to within a maximum discrepancy of 2% close to the centerline of the wedge/cylinder.

Since both geometries produce the same results, results from only the wedge geometry are shown next. The results at two axial locations are shown in Fig. 5.34.

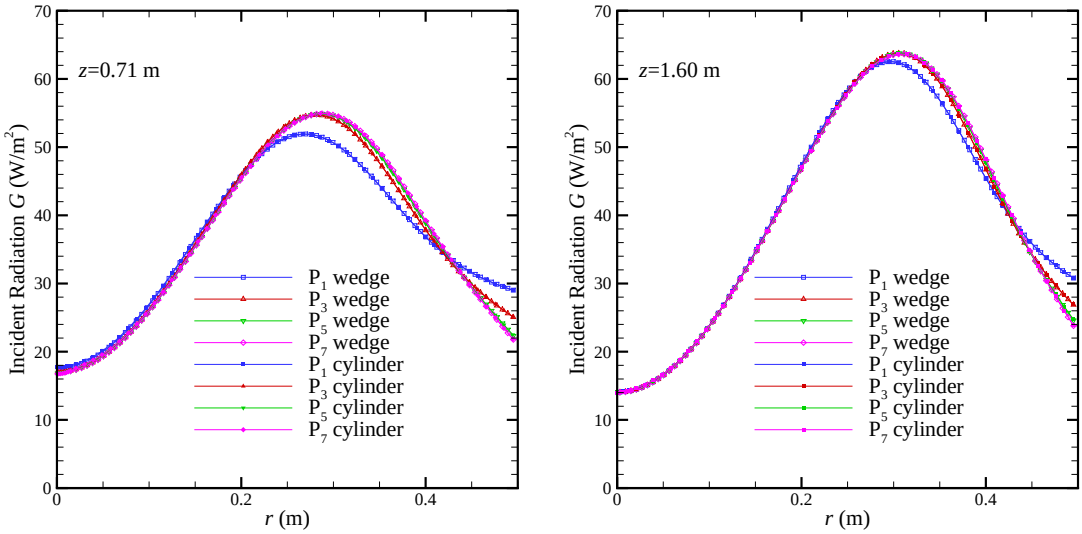

(a) (b)

Figure 5.33: Comparison of the numerical results for the 2-D P_N formulation on a wedge mesh and the 3-D P_N formulation on a cylinder mesh. (a) z=0.71 m and (b) z=1.60 m.

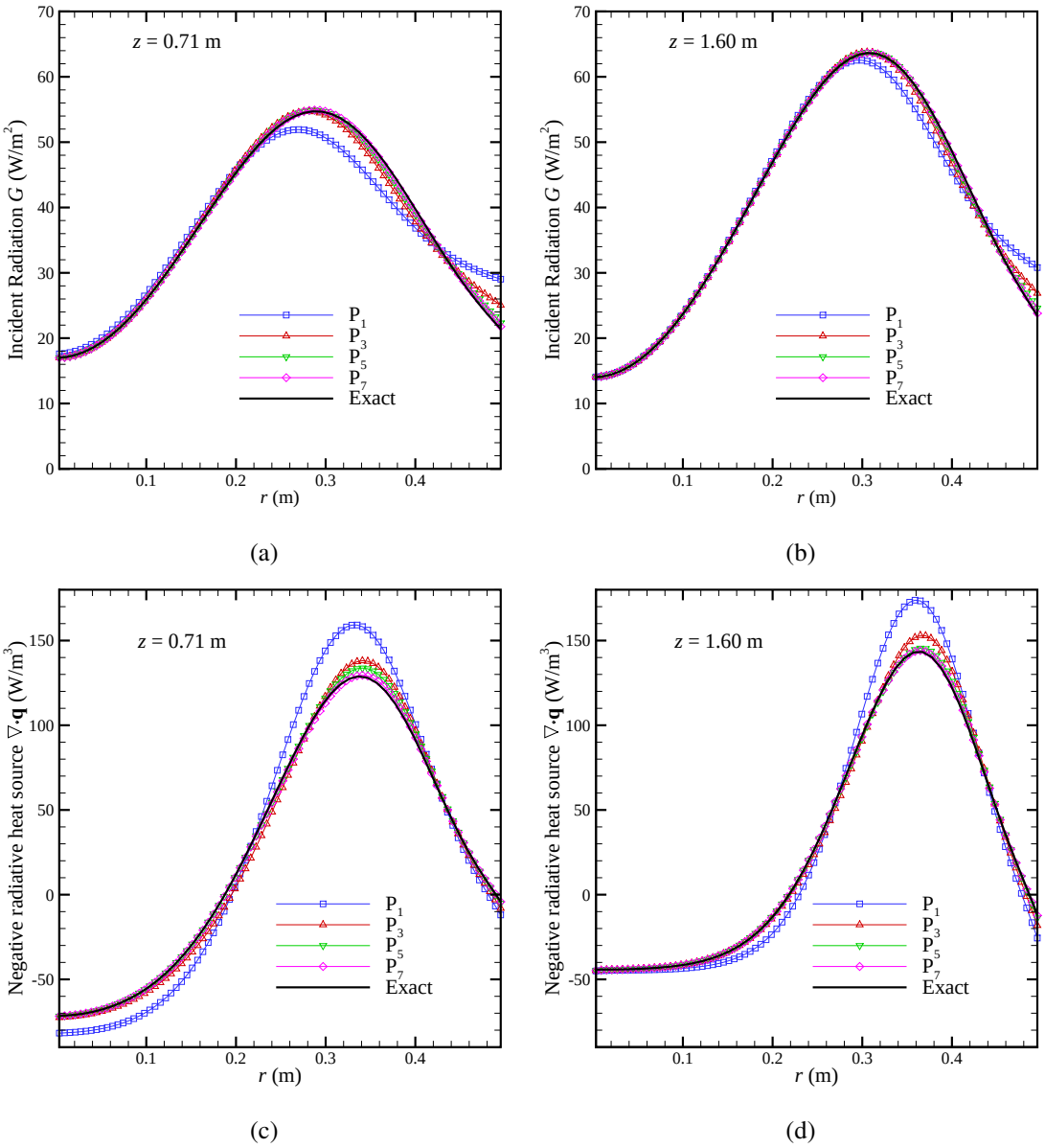

Figure 5.34: Incident radiation G and negative radiative heat source $\nabla \cdot \mathbf{q}$ for a wedge enclosure with variable radiative properties. (a) G at z=0.71 m, (b) G at z=1.60 m, (c) $\nabla \cdot \mathbf{q}$ at z=0.71 m and (d) $\nabla \cdot \mathbf{q}$ at z=1.60 m.

Table 5.11: Comparison of CPU time (s) for Problem 7: 3-D cylinder and 2-D 10° wedge with inhomogeneous κ and I_b

No. of cells	τ_R	P_1	P_3	P_5	P_7
131,400 (Cylinder)	1.125~10.5	1.01	90.5	269	727
3,360 (Wedge)	1.125~10.5	0.02	0.57	5.88	11.7

The incident radiation G and negative radiative heat source $\nabla \cdot \mathbf{q}$ are plotted and compared against the exact solution [21]. The incident radiation G predicted from P_3 to P_7 are very close to the exact solution, while P_1 has certain levels of discrepancies with the exact solution and this discrepancy decreases with increasing optical thickness. For the $\nabla \cdot \mathbf{q}$ predictions, only P_7 overlaps the exact solution at the axial location of $z = 0.71$ m while at $z = 1.60$ m both P_5 and P_7 essentially overlap the exact solution. This is also due to the overall optical thickness $\tau_R(z)$ at different axial locations, where larger–z locations have a larger τ_R. Both the incident radiation G and the negative radiative heat source $\nabla \cdot \mathbf{q}$ from P_7 correctly catch the sharp gradient near the cylinder wall.

The CPU time comparison for Problem 7 for the P_N methods is given in Table 5.11.

5.1.3.2 Problem 8: Cylindrical enclosure and a 10° wedge enclosure with flame-like radiative properties

In this example, the radiative properties are flame-like with a strongly emitting and absorbing region in the center of a cylinder surrounded by the optically thin regions. The radiative properties are exactly the same as in Problem 3 expressed by Eq. (5.3) and are shown in Fig. 5.9 by changing the coordinate z to r for this example. A 1-D thin wedge and a 2-D cylinder with the same radius ($R = 0.52$ m) are used to represent an infinitely-long cylinder. The P_N methods are tested on both meshes and the PMC method from the 2-D cylinder is used as the exact solution.

The cylinder has a large square (100×100) at the center and has 20 more cells along the radius as shown in Fig. 5.35. The size of the square is 0.294 m $\times$ 0.294 m covering the flame at the center. The wedge has 70 cells along the radius and again the tip of the wedge is cut off to avoid mathematical singularity at $r = 0$. The peripheral walls of the cylinder as well as the right

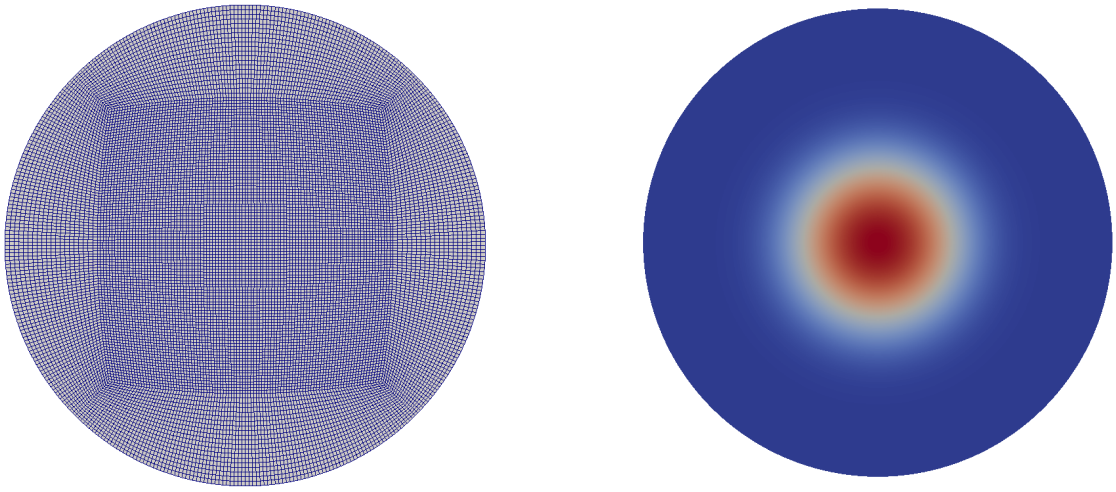

(a) (b)

Figure 5.35: The mesh of the 2-D cylinders with the square at the center covering the flame; (a) the mesh and (b) the contour plot shows the κ distribution according to Eq. (5.3).

wall ($r = R = 0.52$ m) of the wedge are set to black and cold, while the flat walls of the wedge, as well as the top and bottom walls of the cylinder are set to symmetry/specular reflection boundary condition; the centerline boundary condition for axisymmetric P_N method, Eq. (3.46) is applied to the centerline surface ($r \approx 0$) of the wedge.

Comparison of the negative radiative heat source $\nabla \cdot \mathbf{q}$ for both the 2-D cylinder and the 1-D wedge meshes is presented in Fig. 5.36(a). The P_1 method predicts a $\nabla \cdot \mathbf{q}$ about 30% larger compared to that predicted from the PMC method. High-order P_N methods are doing much better than the P_1 method. However, the results predicted by P_3, P_5 and P_7 are still not very accurate compared to the PMC predictions. It is found that even the P_7 result incurs a 12.5% error at the center compared to the PMC results, and the improvement of accuracy from P_5 and P_7 to P_3 is marginal. Although even high-order P_N method have problems converging to the PMC+LBL results, the overlapping P_N results from different geometries (Fig. 6.14) indicate the correctness of the implementation of the P_N methods in the finite-volume-method (FVM) based `OpenFOAM`®.

To further verify whether the errors of high-order P_N methods are due to the accuracy of the

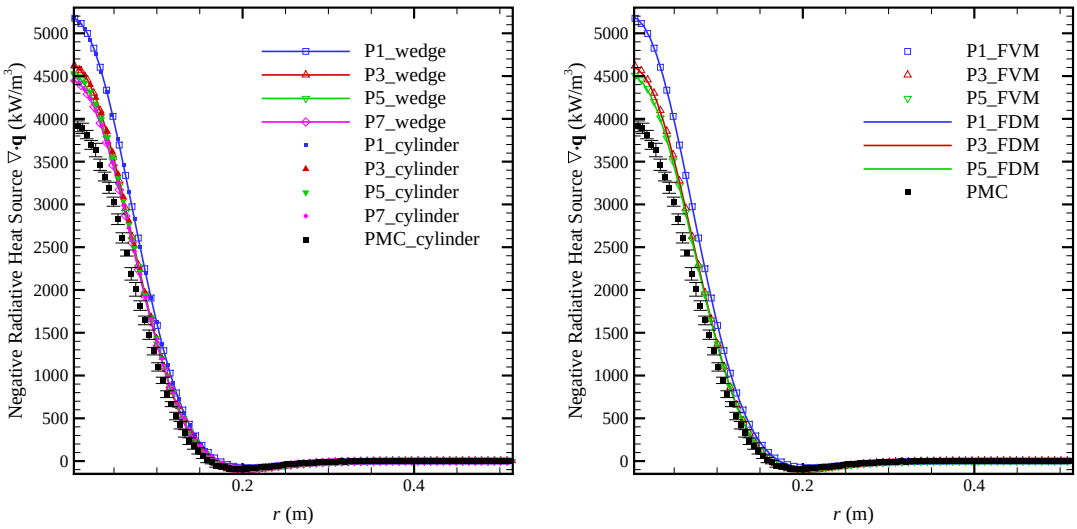

(a) (b)

Figure 5.36: Comparison of negative radiative heat source $\nabla \cdot \mathbf{q}$ (a) from the axisymmetric P_N solver on a wedge mesh and the P_N solver on a cylinder mesh and (b) from the axisymmetric P_N solver in FVM–OpenFOAM® and FDM–Octave® on the wedge.

spherical harmonics methods itself, or perhaps due to unknown issues in OpenFOAM®, results from a finite-difference-method (FDM) based solver implemented in Octave® for the 1-D axisymmetric P_N formulation was generated and is shown in Fig. 5.36(b). The results show that for this 1-D axisymmetric radiative transfer problem with flame-like radiative properties, the results from the FDM implementation of the P_N methods are almost the same as that from the FVM implementations in OpenFOAM®. The P_N methods up to the order of P_7 are proved to be not capable of accurate predictions for such profile of radiative properties in cylindrical geometry, and much higher order of the P_N methods would be required for the P_N methods to be as accurate as the PMC result for such problem. In the next chapter, the turbulent jet flame simulated in it will have a very similar distribution of radiative properties.

The CPU time comparison for Problem 8 for the P_N methods and the PMC is given in Table 5.12.

Table 5.12: Comparison of CPU time (s) for Problem 8: 2-D cylinder and 1-D 10° wedge with flame-like κ and I_b

No. of cells	τ_R	P_1	P_3	P_5	P_7	PMC (1M×10)
18000 (Cylinder)	0.886	0.12	8.29	25.5	68.8	9614
70 (Wedge)	0.886	0.01	0.18	1.0	3.8	/

5.1.3.3 Problem 9: Cylindrical enclosure and a 45° wedge enclosure with engine-combustion radiative properties

In this example, the P_N solver is applied to a 2-D cylinder and a fan-shape 45-degree wedge. Many combustion problems in a cylindrical domain, such as in a diesel engine (with multiple injectors along a circle), are periodically axisymmetric, in which the pattern of the azimuthal-angle-dependent flow field is repeated for every certain number of degrees. In these cases generally a fan-shape wedge mesh instead of a full cylinder is chosen to expedite the simulation. To test the performance of the high-order P_N methods (with radius r and azimuthal angle ϕ expressed in terms of x and y in Cartesian coordinates) as well as the symmetry/specular reflection boundary condition and cyclic boundary condition for the fan-shape wedge mesh, simulations are carried out on a 45° wedge and a full cylinder (Fig. 5.37) with specified absorption coefficients κ and the Plank function I_b:

$$I_b = 1 + \frac{20}{R^4} r^2 (R^2 - r^2), \quad \mathrm{W \cdot m^{-3}} \tag{5.7a}$$

$$\kappa = \left[1 + \frac{15}{R^4}(R^2 - r^2)^2\right]\left(1 + 0.5\frac{r}{R}\cos 8\phi\right), \quad \mathrm{m^{-1}} \tag{5.7b}$$

$$0 \le r \le R = 0.5, \quad \mathrm{m} \tag{5.7c}$$

$$-22.5^\circ \le \phi \le 22.5^\circ \quad \text{for the wedge} \tag{5.7d}$$

The wedge has 45 cells along the radius and 21 cells in the circumferential direction with the tip cut off to avoid stability issues; the cylinder contains 20 cells along the radius with a square (41×41) at the center. The peripheral walls of the cylinder as well as the outer peripheral walls of the wedge

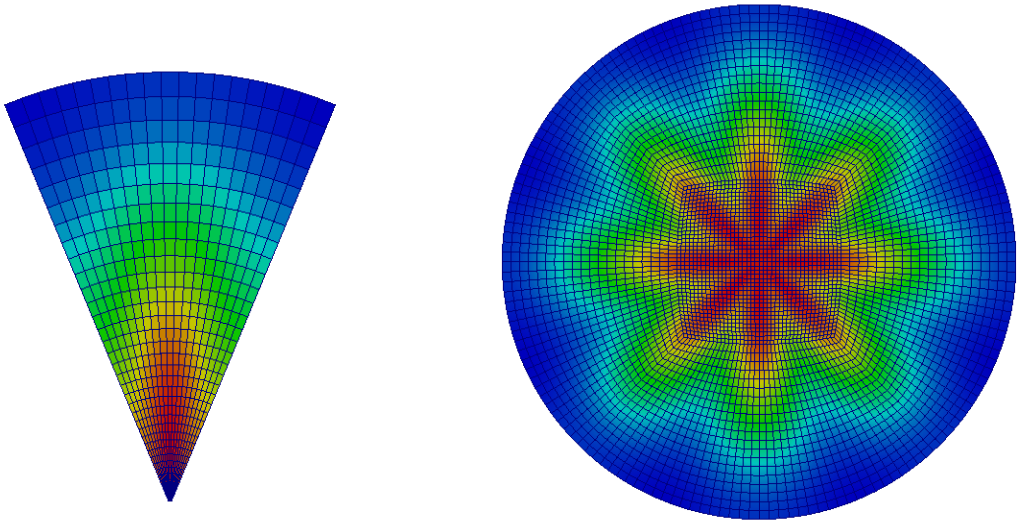

(a) (b)

Figure 5.37: The mesh of the 45° wedge (a) and the cylinder (b) in the analysis, the contour plot shows the κ distribution according to Eq. (5.7).

are set to black and cold, while the flat walls of the wedge and the top and bottom of the cylinder are set to symmetry/specular reflection boundary condition; the centerline boundary condition for axisymmetric P_N method, Eq. (3.46) is applied to the centerline surfaces ($r \approx 0$) of the fan-shape wedge.

Comparison of incident radiation, G, and radiative heat source, $-\nabla \cdot \mathbf{q}$, from P_1 to P_7 is shown in Fig. 5.38 for both meshes along the the radius (at 0°). The P_N results from the 45° wedge mesh (lines with hollow symbols) overlap the results from the full cylinder (lines with solid symbol) at this position. Figure 5.39 shows the contour plot of $-\nabla \cdot \mathbf{q}$ for P_7 from the 45° wedge. It is observed that the P_7 solutions from the 45° wedge match those from the cylinder (the differences are within 2% and mainly due to the grids), and similar comparison was made for other orders of P_N methods and the results are consistent. The results of P_7 are very close to that of the PMC except at the cylinder/wedge center and near $r = 0.35$ where incident radiation is maximum, as shown in Fig. 5.38(b). The larger uncertainties for the PMC close to the cylinder center are due to the small sizes of the cells at the cylinder center, and the discrepancy of P_7 at $r = 0.35$ maybe due

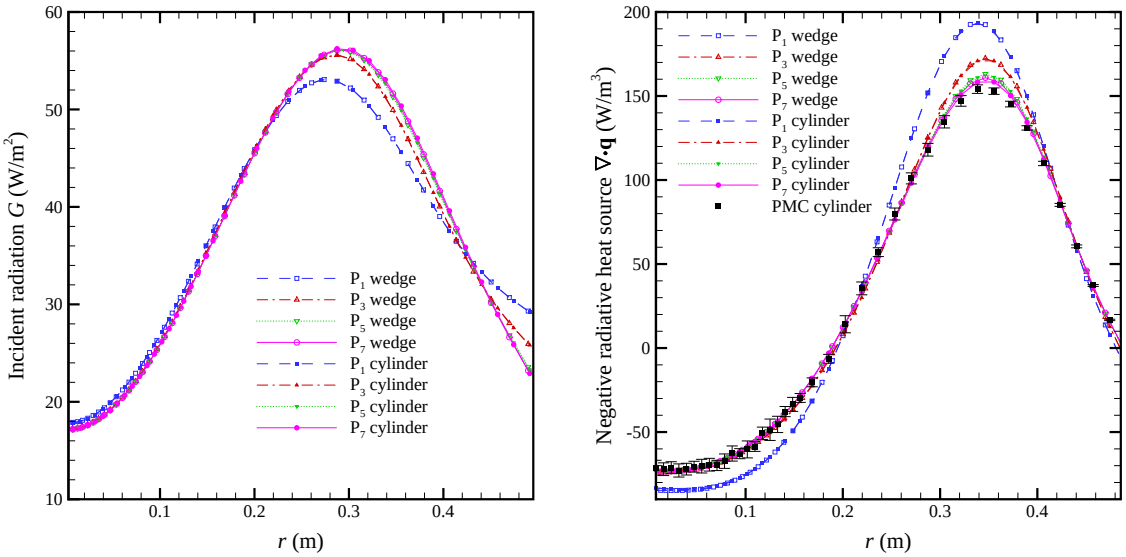

Figure 5.38: Incident radiation G and radiative heat source $-\nabla\cdot\mathbf{q}$ along the centerline of a 45° wedge enclosure and that of a cylinder; (a) Incident radiation G and (b) negative radiative heat source $\nabla\cdot\mathbf{q}$.

to its remaining approximations, or due to inaccuracies in the PMC method (a zeroth order method, assuming properties to be constant across cells).

The cyclic boundary condition is tested by rotating the wedge mesh by an angle of 10.714° clockwise which is shown in Fig. 5.40. This cyclic case is still representing 1/8 of the cylinder as shown in Fig. 5.37(b), but the symmetry/specular reflection boundary conditions can no longer be applied to the side walls. Both side walls use the cyclic P_N boundary conditions replacing the formerly used symmetry/specular reflection boundary conditions, with the rest of boundary conditions unchanged. The specific angle of 10.714° is to guarantee that the y-axis at $x = 0$ still overlaps the centerline of the artificial flame just as Fig. 5.37(a). Negative radiative heat sources $\nabla\cdot\mathbf{q}$ from P_N methods with the symmetric flame and the cyclic flame are found to overlap each other as expected.

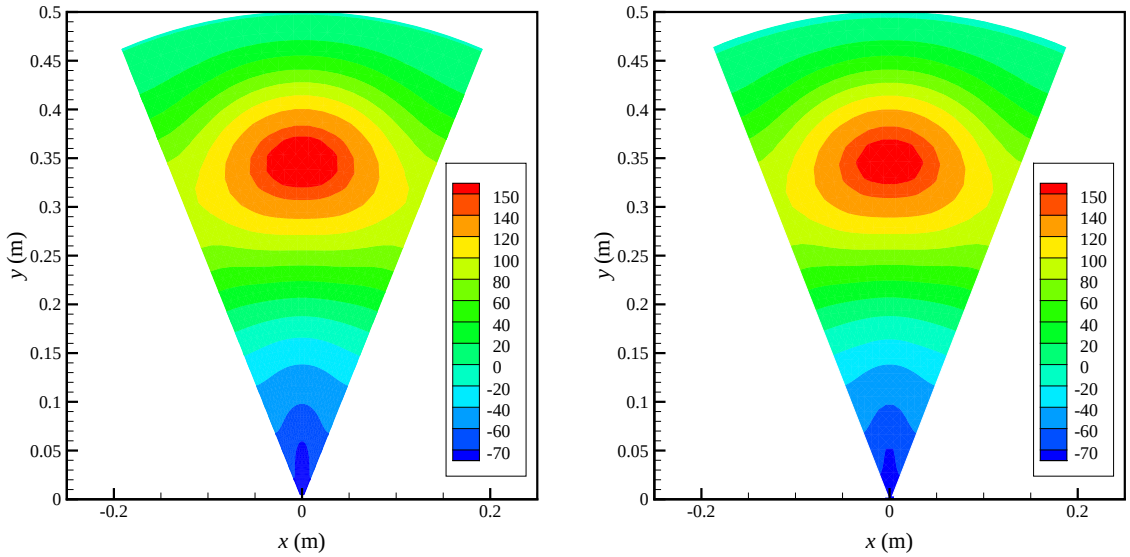

Figure 5.39: Comparison of negative radiative heat source $\nabla \cdot \mathbf{q}$ between a wedge mesh and part of a cylinder mesh; (a) a 45° wedge and (b) 1/8 of a full cylinder.

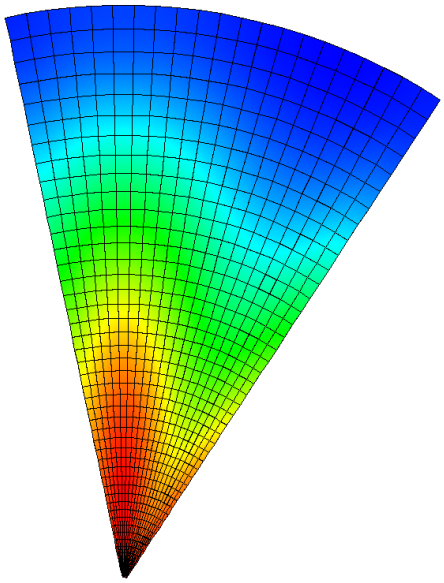

Figure 5.40: The mesh of the 45° wedge rotated by 10.714°, the contour plot shows the κ distribution.

Table 5.13: Comparison of CPU time (s) for Problem 9: 2-D cylinder and 2-D 45° wedge with engine-combustion radiative properties

No. of cells	$\tau_R(0°)$	P_1	P_3	P_5	P_7	PMC (2M×10)
4961 (Cylinder)	3.75	0.06	4.72	12.2	24.4	853
945 (Wedge)	3.75	0.01	0.56	1.35	2.57	/

The CPU time comparison for Problem 9 for the P_N methods and the PMC is given in Table 5.13.

5.2 Method of Manufactured Solutions

5.2.1 Introduction

The method of manufactured solutions (MMS) [234] has been employed to further validate the implementation of high-order P_N method in `OpenFOAM`®. MMS is a widely used technique to verify codes in numerical simulations of many scientific and engineering areas, e.g., the full Navier-Stokes equations in CFD simulations [235]. MMS can also be used to perform grid convergence tests for numerical discretization method. Comparison of results from different grids to the assumed analytical solution not only demonstrate the convergence of the numerical solution to the assumed analytical solution but also the order of accuracy of the numerical method. The procedure for the MMS for systems of PDEs is as follows:

1. Assume an analytical solution for each unknown. The solution should be continuous and smooth so that its derivatives exist and can be analytically calculated. The manufactured solution does not require any physical realism.

2. Substitute the manufactured solutions into the governing equations and obtain the resulting analytical expressions of source terms.

3. Add the obtained analytical source terms to the right-hand side of each governing equation, and then solve the whole system of PDEs numerically.

4. Comparing the calculated numerical solution for different mesh sizes with the assumed mesh-free analytical solution, one obtains the errors and the order of accuracy of the numerical method applied.

For the purpose of this thesis, the MMS has been carried out for the P_3 solvers in 2-D square meshes with four different mesh sizes to study the order of accuracy for the finite-volume discretizations. Dirichlet boundary conditions are employed instead of the original Robin-type ones to simplify the verification. The manufactured solutions are

$$I_n^m = \sin\left[\frac{(3+n/2)\pi x}{L} + \frac{m\pi}{4}\right]\cos\left[\frac{(3+n/2)\pi y}{L} + \frac{m\pi}{4}\right] \tag{5.8}$$

where L=1; And the extinction coefficient β=1 for all tests. The square is placed into the x-y plane and only four intensity coefficients are relevant, which are I_0^0, I_2^0, I_2^{-2} and I_2^2. The software package `Mathematica`® [236] is used to obtain the source terms S_n^m for each governing equation Y_n^m by substituting the analytical expressions of the manufactured solutions, Eq. (5.8), into the governing equations, Eq. (2.9). Then the generated analytical source terms are added to the P_N solver and the numerical solutions corresponding to these source terms are calculated. Four mesh sizes (Δ) are tested, which are Δ=0.02 (50×50), Δ=0.01 (100×100), Δ=0.005 (200×200) and Δ=0.0025 (400×400).

5.2.2 Results and Discussion

The results with mesh size of 0.005 (200×200) for all the relevant intensity coefficients I_0, I_2^{-2}, I_2^0 and I_2^2 from MMS are shown in Fig.5.41, which are close to the values directly calculated from Eq. (5.8). Figure 5.42 shows the L_2 norm of error between calculated numerical solution and analytical solution with increasing grid size of the P_3 method, where the L_2 norm is calculated from

$$L_2 = \left[\frac{1}{N_{cell}}\sum_{n=1}^{N_{cell}}\left(I^m_{n,numerical} - I^m_{n,analytical}\right)^2\right]^{0.5} \tag{5.9}$$

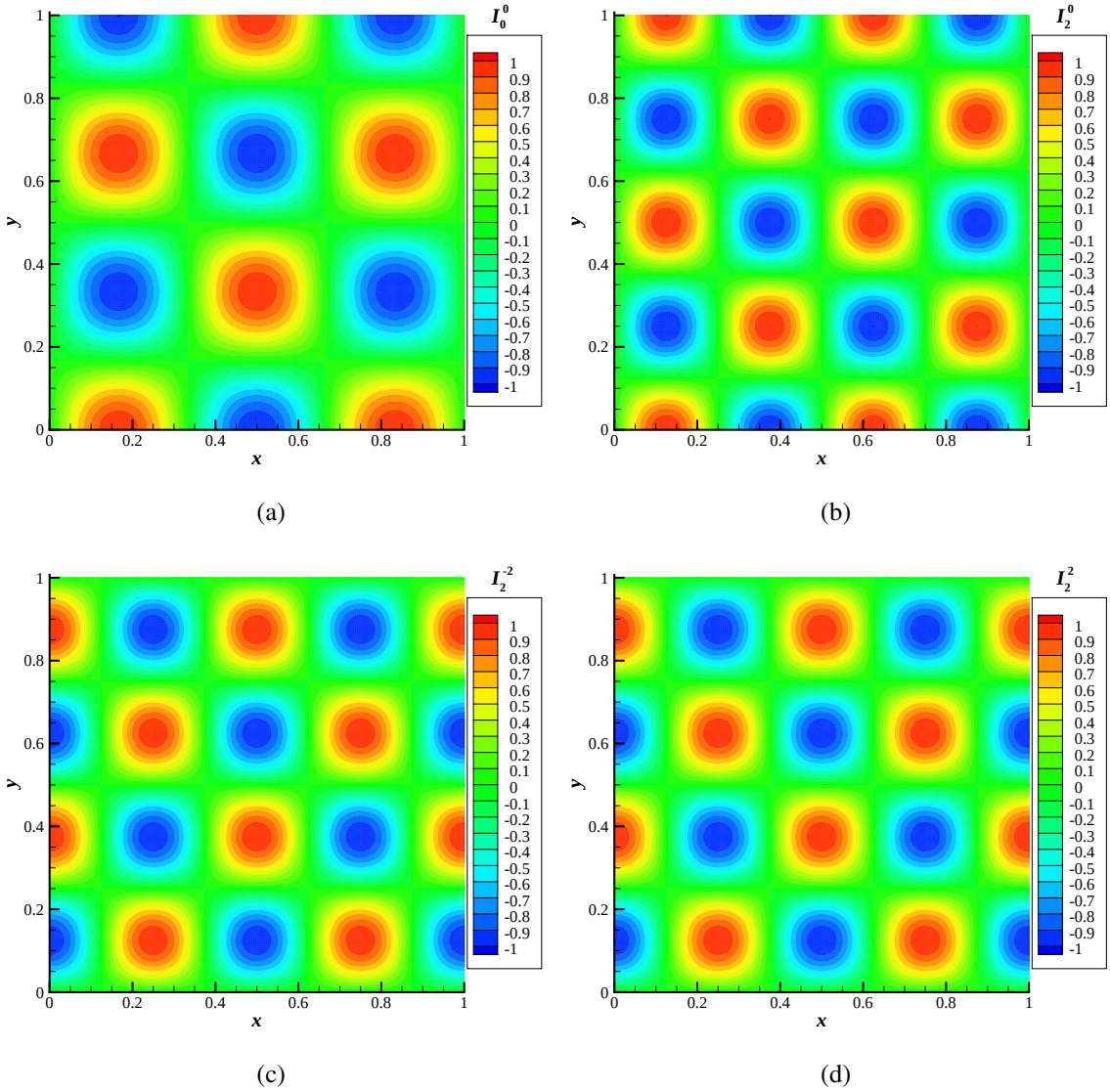

Figure 5.41: Contour plot for radiative intensity for MMS problem on 200×200 grid; (a) I_0^0, (b) I_2^0, (c) I_2^{-2} and (d) I_2^2.

With the finer mesh or the decrease of cell sizes, the numerical solutions get increasingly closer to the analytical solution. The finite-volume discretization methods is consistent since the error goes to 10^{-5} as the cell size δ goes to 0.0025. A line with the slope of 2.0 in the logarithmic coordinates is also drawn as a reference.

Table 5.14: Observed order of accuracy and L_2 norms for different unknowns from different grids for P_3 methods in the MMS study

Grid	Cell size, Δ	L_2 of I_0^0	L_2 of I_2^0	L_2 of I_2^{-2}	L_2 of I_2^2
50×50	0.02	0.015830	0.015009	0.004658	0.004803
100×100	0.01	0.004162	0.003793	0.001221	0.001302
200×200	0.005	0.001059	0.000947	0.000319	0.000342
400×400	0.0025	0.000269	0.000237	8.35E-005	9.02E-005
Observed Order	/	1.97	2.0	1.94	1.93

The observed orders of accuracy of I_0^0, I_2^0, I_2^{-2} and I_2^2 are close to 2.0 and shown in Table 5.14. The absolute values of the L_2 norms are not very important since they depend highly on the configuration of the profiles of the assumed solutions and the corresponding derived source terms. It is the converging trend and the orders of accuracy that are of the most interest, which are proved to be second-order accurate.

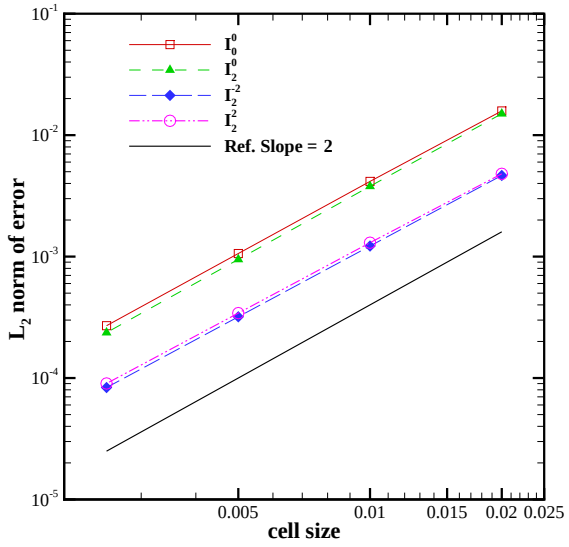

Figure 5.42: L_2 norm of error with increasing cell size.

5.3 Summary

This chapter has demonstrated the performance of high-order P_N methods (up to the order of P_7) in nine representative radiative transfer problems. For the purpose of assessing the high-order P_N methods as the RTE solver, all examples presented were limited to gray media in this chapter. These gray examples can be used as foundations for further analyzing radiative transfer problems in nongray media. Several conclusions were drawn from the results:

1. High-order P_N methods are accurate in terms of both incident radiation G and radiative heat source $-\nabla \cdot \mathbf{q}$ for generally optically thick problems in both Cartesian and cylindrical geometries.

2. High-order P_N methods do not improve the accuracy much from the P_1 method for radiative transfer in optically thin media in terms of incident radiation G or radiative intensity I. But all P_N methods are able to predict the correct radiative heat source $-\nabla \cdot \mathbf{q}$ for optically thin problems since there is very limited absorption, in which case the RTE solver is no longer important.

3. For the optically intermediate media, the performance of high-order P_N methods relies on the distribution of radiative properties in 3-D space (regardless of the dimension of computational grid). If the resulting intensities are not very anisotropic, which is usually the case for 1-D and 2-D Cartesian problems, constant but decreasing improvements of accuracy from higher-order P_N methods are expected and it is clear that the the P_N methods are gradually converging to the exact solution. If the intensities are very directionally anisotropic, for example in a cylinder where the maximum of both Planck functions and absorption coefficients are at the center of the cylinder surrounded by cold thin media, the improvements from high-order P_N methods are limited, i.e., P_3 improves results from P_1 to a certain extent, but P_5 and P_7 are only marginally better than P_3. And much higher order of the P_N method is required for such problems.

4. All P_N methods (including P_1) perform better in slab like geometries than in cylindrical geometry.

5. The second-order PDEs of P_N methods are weakly coupled for optically thick and intermediate examples while strongly coupled for optically thin examples. This does not cause any problem for coupled simulations since, once convergence is achieved, all the I_n^m can be stored and used as initial values for later iterations.

6. Considering the improvement of accuracy, computational cost and generality for applications, the P_3 method is often the optimal choice.

7. High-order P_N methods are able to accurately treat surfaces with mixed diffuse-specular reflections.

Chapter 6

Combustion Simulations

6.1 Nongray Radiation Model

6.1.1 Nongray Radiation Module

In this chapter, the high-order P_N methods are to be tested for examples with nongray participating media, which are mixtures of real combustion product gases (CO_2, H_2O, CO). The high-order P_N solvers are part of the nongray radiation module developed by Modest's group and implemented in `OpenFOAM`® 2.2.x. The module provides various choices of RTE solvers and spectral models with a user-friendly interface. All RTE solvers and spectral models supported by this module are shown in Fig. 6.1. The RTE solvers except the PMC are coded in C++ while the PMC and the spectral models are coded in FORTRAN90. The user can choose the RTE solver in conjunction with a spectral model through a generic interface of the nongray radiation module.

A pressure-based LBL absorption coefficient database generated from high-resolution molecular spectroscopic databases of HITEMP 2010 [160] and HITRAN 2012 [161] is used as the foundation of all spectral-based evaluations. The database includes 5 gas species, i.e., CO_2, H_2O, CO (from HITEMP 2010) as well as CH_4 and C_2H_2 (HITRAN 2012) at temperatures 300–3000 K and total pressures 0.1–80 bar. This database is used to calculate the Planck-mean absorption coefficient,

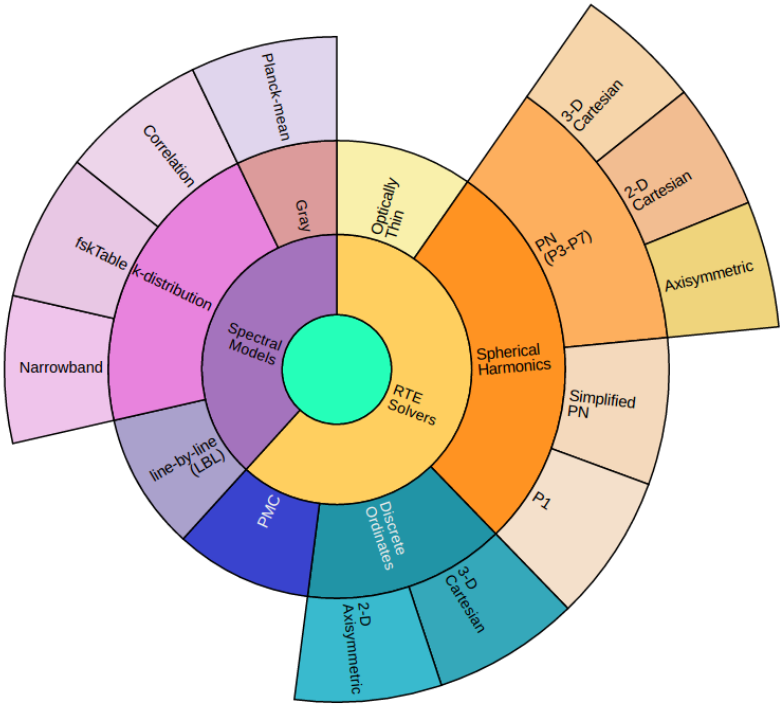

Figure 6.1: A schematic of supported RTE solvers and spectral models in the nongray radiation module.

narrow-band database, full-spectrum *k*-distribution (FSK) look-up table and LBL database for PMC to guarantee the consistency of all the spectral models.

The spectral models and RTE solvers of the nongray radiation module are briefly discussed in the following sub-section. The discussion is focused on their practical applications in combustion simulation.

6.1.1.1 Selection of spectral models and RTE solvers

Optically thin solver:

The optically thin solver (O.T.), employing the Planck-mean absorption coefficient, only predicts the emission from the flame. If the size of the flame is small, the O.T. may give correct radiation evaluations. However, for larger flames it will predict the lowest-possible temperature distribution

of a flame, which can be used as a reference to validate the results predicted by other RTEs and spectral models. Unfortunately, there is no strict definition of the size of a flame radiation-wise, and therefore, it is recommended to always run the O.T. model first: if the O.T. results are very close to the results with no radiation, it proves the flame to be a weakly radiating flame and there is no need to apply other models. If the temperature predicted by the O.T. result is much lower (50–500 K) than the no-radiation runs, then the next step is to pick better spectral models and RTE solvers.

PMC+LBL *solver*:

PMC+LBL [57, 67, 237] is the most accurate solver, which is regarded as an exact solution if enough photon bundles are traced. The computational cost is mainly scaled by the number of photon bundles traced. The current version supports loading the LBL database only at a single pressure due to the large memory demands when loading the LBL database. For example, the size of the LBL database at 1 bar is 2 GB. Loading a LBL database for multiple pressures is not recommended, and linear scaling for approximating the absorption coefficient at other pressures from the LBL database pressure is used instead.

Full-spectrum k-distributions* (FSK)*-based spectral models:

Three different implementations of the FSK method are currently available, i.e. a look-up table [169, 174], a narrow-band database [169, 170] and correlation functions [238–240].

The look-up table directly interpolates from a pre-calculated table of k-distributions for mixtures. The total size of the look-up table is 5 GB and can be dynamically loaded for individual applications. The current version is generated for three species (CO_2, H_2O and CO) plus soot. It was proved to be very accurate and is currently the optimal FSK implementation for combustion simulations.

Assembly of FSKs from a narrow-band database is another option, requiring much less storage and memory. The only bottleneck is that it needs to assemble the k-distributions for mixtures on the fly with a certain mixing scheme, which is computationally expensive for large grids. The current version supports five species (CO_2, H_2O, CO, CH_4 and C_2H_2) and is more easily expanded

to more species and wider range of thermodynamic states.

The idea of correlations is to fit k-distributions for single species into hyperbolic tangent functions. The current version supports CO_2 and H_2O at 1 bar, and an approximate mixing scheme must be employed. It requires the least amount of computer resources among the three FSK implementations, since it only needs to store a few coefficients for the correlations. However, the correlations in the current version are not as accurate as the other two FSK implementations.

Two mixing schemes are available for the narrow-band FSK and the correlations, which are the multiplicative scheme and the uncorrelated mixture scheme. The uncorrelated mixture scheme is more accurate but more expensive than the multiplicative scheme.

PN+FSK, SPN+FSK and DOM+FSK:

P1+FSK probably is the most cost-effective solver for its reasonable accuracy and small computational cost. P1+FSK usually predicts a temperature distribution between those predicted from O.T. and PMC+LBL methods for optically thin and intermediate flames and will be very close to PMC+LBL results for optically thick flames (again, there is no strict definition of the optical thickness of a flame). P1+FSK is computationally very fast, which makes it the optimal choice at the preliminary stage of a combustion simulation, when other sub-models (turbulence, chemistry, etc.) are still evolving.

The Simplified-P_N method [241, 242] (SP_3 and SP_5) is also provided, which is an asymptotic correction to the diffusion approximation. It is very efficient and sometimes gives very good results in an ad-hoc manner.

The accuracy and efficiency of the high-order PN+FSK and DOM+FSK solvers are to be compared and discussed in the examples in later sections of this chapter. Comparison between these two, in a general sense, is a much larger topic which requires careful design of numerical examples. In principle, it compares whether directional variation of intensity is better approximated by discrete points or by finite Fourier series. It is well known that DOM performs less efficiently in the presence of scattering and in optically thick cases and the high-order P_N is expected to have

Table 6.1: The number of second-order PDEs for different orders of the P_N method, and the number of first-order PDEs for different numbers of discrete ordinates for DOM

P_N		$\mathrm{DOM}_{p\times a}$	
P_1	1	$\mathrm{DOM}_{2\times4}$	8
P_3	6	$\mathrm{DOM}_{4\times4}$	16
P_5	15	$\mathrm{DOM}_{4\times8}$	32
P_7	28	$\mathrm{DOM}_{8\times8}$	64

trouble when the intensities are extremely anisotropic. What kind of combustion problems will produce the nongray radiative properties favoring either solver is still an open question. The number of second-order PDEs for different orders of P_N methods and the number of first-order PDEs for $\mathrm{DOM}_{p\times a}$, with respect to the number of discrete polar ordinates p and azimuthal ordinates a, are shown in Table 6.1. The coupling between the second-order PDEs for the high-order P_N depends on the problems, while for DOM, there is no coupling between the PDEs for non-scattering cases in principle.

6.1.2 Full-Spectrum *k*-Distribution (FSK) Look-Up Table

A full-spectrum k-distribution (FSK) look-up table is employed to treat the nongray participating gases for the simulations in this chapter. A full-spectrum k-distribution (FSK) look-up table has been constructed for gas–soot mixtures for three gas species, i.e., CO_2, H_2O and CO, and soot [174]. Since soot is not included in any of the calculations in this thesis, it will be excluded from the following description. The k-distribution of a mixture is assembled directly from the summation of the linear absorption coefficients of three gas species. The systematic approach to generate the table, including the generation of the pressure-based absorption coefficient and the generation of the k-distribution, is discussed in [173, 174]. To efficiently obtain accurate k-values for arbitrary thermodynamic states from tabulated values, a 6-D linear interpolation method is employed.

The idea of k-distribution of gaseous absorption coefficients is based on the fact that the oscillatory absorption coefficient has the same value at many different wavenumbers. The absorption coefficients with respect to the wavenumber can be reordered into corresponding k-distributions,

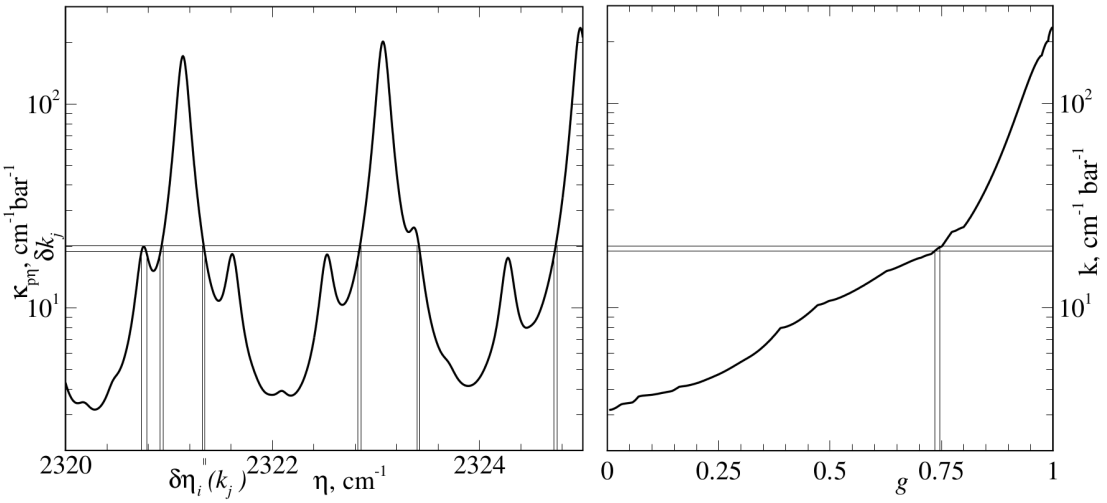

Figure 6.2: Extraction of k-distribution from spectral absorption coefficient data for small amounts of CO_2 in nitrogen, across a small part of its 4.3 μm band at p=1.0 bar, T=300 K; (a) actual absorption coefficient, (b) reordered equivalent k-distribution. [6]

which is illustrated in Fig. 6.2 showing a reordering process for in a narrow-band database.

A full-spectrum k-distribution is weighted by the Planck function and is defined as [21]

$$f_{\underline{\phi},T}(k;\underline{\phi},T) = \frac{1}{I_{b\eta}} \int_0^\infty I_{b\eta}(T)\delta(k-\kappa_\eta(\underline{\phi}))d\eta \tag{6.1}$$

where κ_η is the absorption coefficient calculated from a spectroscopic database, $\delta()$ is the Dirac-delta function, $\underline{\phi}$ is a vector of local thermodynamic state variables including pressure, temperature and species concentration, $f_{\underline{\phi},T}(k;\underline{\phi},T)$ is a Planck-function-weighted k-distribution with absorption coefficient evaluated at the local state $\underline{\phi}$ and a Planck function temperature T, $I_b(T)$ and $I_{b\eta}(T)$ are the Planck function and the spectral Planck function, respectively, at temperature T, and η is the wavenumber.

The cumulative full-spectrum k-distribution is defined as

$$g_{\underline{\phi},T}(k;\underline{\phi},T) = \int_0^k f_{\underline{\phi},T}(k';\underline{\phi},T)dk' \tag{6.2}$$

Thus, $g_{\underline{\phi},T}(k;\underline{\phi},T)$ represents the fraction of the spectrum whose absorption coefficient lies below the value of k and therefore, $0 \leq g_{\underline{\phi},T} \leq 1$. Inverting Eq. (6.2), a smooth, monotonically increasing function $k(g)$ can be obtained, with minimum and maximum values identical to those of κ_η. For a nonhomogeneous mixture, the spectral variable is reordered at a reference state $\underline{\phi}^0$. The RTE (ignoring scattering) can be reordered at the reference state $\underline{\phi}^0$ as

$$\frac{dI_g}{ds} = k_{\underline{\phi},T}(g_{\underline{\phi}^0,T})\left[a(g_{\underline{\phi}^0,T^0};T,T^0)I_b(T) - I_g\right] \tag{6.3}$$

where

$$I_g = \frac{\int_0^\infty I_\eta \delta(k-\kappa_\eta(\underline{\phi}^0))d\eta}{f_{\underline{\phi}^0,T^0}(k)} \tag{6.4}$$

$$a(g_{\underline{\phi}^0,T^0};T,T^0) = \frac{f_{\underline{\phi}^0,T^0}(k)}{f_{\underline{\phi}^0,T^0}(k)} = \frac{dg_{\underline{\phi}^0,T}(k)}{dg_{\underline{\phi}^0,T^0}(k)} \tag{6.5}$$

This is known as the full-spectrum correlated-k (FSCK) method. The total intensity is evaluated through the sum of a numerical quadrature (with quadrature points g and weights w_g)

$$I = \int_0^1 I_g dg_{\underline{\phi}^0,T^0} = \sum_{i=1}^{N} w_g I_{g_i} \tag{6.6}$$

and for each quadrature point g, Eq. (6.3) can be rewritten as

$$\frac{dI_g}{ds} = k_g\left[a_g I_b(T) - I_g\right] \tag{6.7}$$

where k_g is the k-value corresponding to the quadrature point g for a gas mixture and a_g is obtained from Eq. (6.5).

Usually, an eight-quadrature-point scheme is accurate enough for mixtures of major combustion products of hydrocarbon fuels. As can be seen from Eq. (6.7), by employing the FSK spectral model, eight RTEs are to be solved with eight different distributions of k_g. The value of k_g for one single cell with certain amounts of participating gases may differ by orders of magnitude depending

on the thermodynamic state of the mixture as is shown in Fig. 6.2(b) as an example. Therefore, the ideal RTE solver for nongray radiation simulation needs to be able to predict accurate results under a wide range of optical thicknesses. The performance of the RTE, especially the high-order P_N method, is sensitive to the overall optical thickness. The P_N method is expected to perform well for the larger quadrature points (if the size of the flame is not too small) but poorly for the middle quadrature points. For the small quadratures, where the k_g satisfies optically thin conditions, the RTE is no longer important since there is very little self-absorption.

6.2 1-D Slab Geometry with Nongray Media

This problem (Problem 10) demonstrates the performance of different RTE solvers for radiative transfer problems between two infinitely-large parallel plates. The hot medium between the two plates (L=1 m) consists of a mixture of CO_2, H_2O and CO. The thermodynamic properties of the mixture are listed in Eq. (6.8a):

$$p = 1, \quad \text{bar} \tag{6.8a}$$

$$T = 1600 \times \exp\left[-\left(\frac{x-0.2}{0.3}\right)^2\right] + 400, \quad \text{K} \tag{6.8b}$$

$$x_{CO_2} = 0.15 \times \exp\left[-\left(\frac{x-0.2}{0.3}\right)^2\right] \tag{6.8c}$$

$$x_{H_2O} = 0.15 \times \exp\left[-\left(\frac{x-0.2}{0.3}\right)^2\right] \tag{6.8d}$$

$$x_{CO} = 0.075 \times \exp\left[-\left(\frac{x-0.2}{0.3}\right)^2\right] \tag{6.8e}$$

The profile of temperature and mole fractions of the gases represents a realistic flame-like distribution. The 1-D slab has totally 100 cells. Both plates are treated as cold black walls. The P_N (From P_1 to P_7) methods and DOM with different number of discrete polar ordinates are coupled

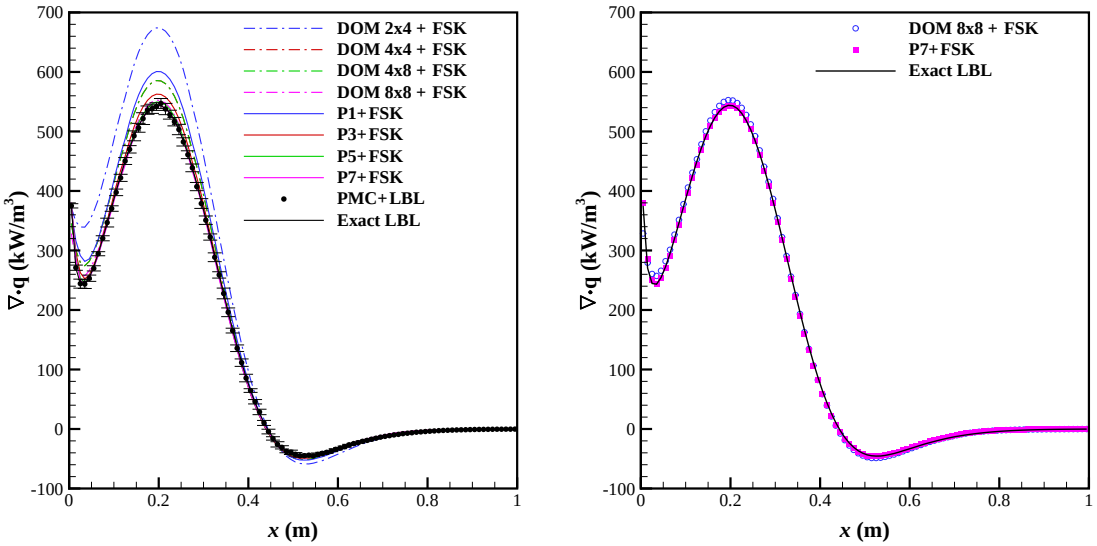

(a) (b)

Figure 6.3: Radiative heat source predicted by different solvers for a 1-D slab with nonhomogeneous gas mixture.

with the FSK look-up table as the spectral model with an 8-quadrature-point evaluation. PMC+LBL and an exact LBL solution are used as references. The exact LBL solution is obtained from direct integration of the RTE and LBL calculations for the whole spectrum.

The results in terms of radiative heat source are shown in Fig. 6.3. Figure 6.3(a) compares different RTEs, which illustrates the accuracy of P_N methods with respect to the order of N and of the $\mathrm{DOM}_{p\times a}$ with respect to the number of discrete polar ordinates p and azimuthal ordinates a. The predicted radiative heat sources are increasingly accurate with the increase of the order of P_N approximation and the number of discrete ordinates of DOM. The P7+FSK results are almost the same as the exact LBL results, which is clearer in Fig. 6.3(b). This is partly because of the similar distribution of the mole fractions of gases, where $x_{\mathrm{CO_2}} : x_{\mathrm{H_2O}} : x_{\mathrm{CO}} = const.$. It also proves that under these thermodynamic conditions, an eight-quadrature-point FSK model is as accurate as LBL calculations. Thus, any errors are mostly due to the accuracy of different RTEs. For this 1-D slab problem, results from $\mathrm{DOM}_{8\times8}$ is slightly above the exact LBL results.

Table 6.2: Comparison of CPU time (s) of RTEs for Problem 10: 1-D slab geometry with nongray radiative properties

No. of cells	PN				DOM				PMC
100	P_1	P_3	P_5	P_7	$DOM_{2\times4}$	$DOM_{4\times4}$	$DOM_{4\times8}$	$DOM_{8\times8}$	1M×10
CPU time (s)	0.02	0.41	2.07	5.37	0.02	0.06	0.12	0.25	706.7

The computational cost of different RTEs is shown in Table 6.2. All calculations were done on a single 2.66 GHz Intel (R) Xeon (R) X7460 processor. PMC+LBL employed 10 million photon bundles for this 1-D problem. Comparing the time costs from different orders of P_N methods, it is found that for this one-step calculation the time costs of the P_N methods do not scale with the PDE numbers solved due to a large number of outer iterations are required. At the same time, DOM does not require outer iteration for non-scattering media, thus turn out to be much more efficient than the P_N methods.

6.3 Scaled Sandia Flame D

6.3.1 Background

Accurate simulation of turbulent flames is a challenging task due to the fact that all sub-models, such as chemistry, turbulence and radiation are interacting with each other in a complicated way. Careful choices of approximate models can save a lot of effort and computational time. Since radiative transfer in combustion simulations has not been treated seriously until recently, the choice of the spectral model and RTE solver for radiative transfer in a specific flame is still an open question. It is important to identify relative accurate tools with acceptable computational cost for the radiation evaluation of a flame. In this section, the high-order P_N solvers are tested for an artificial jet flame, Sandia Flame D×4 (which is scaled from Sandia Flame D [243, 244]), for both a coupled combustion simulation and a snapshot simulation. The reason of scaling is to show more effects of radiation from the nongray participating gases, which is closer to the sizes of flames in real applications. The accuracy and computational cost of the high-order P_N methods for the coupled

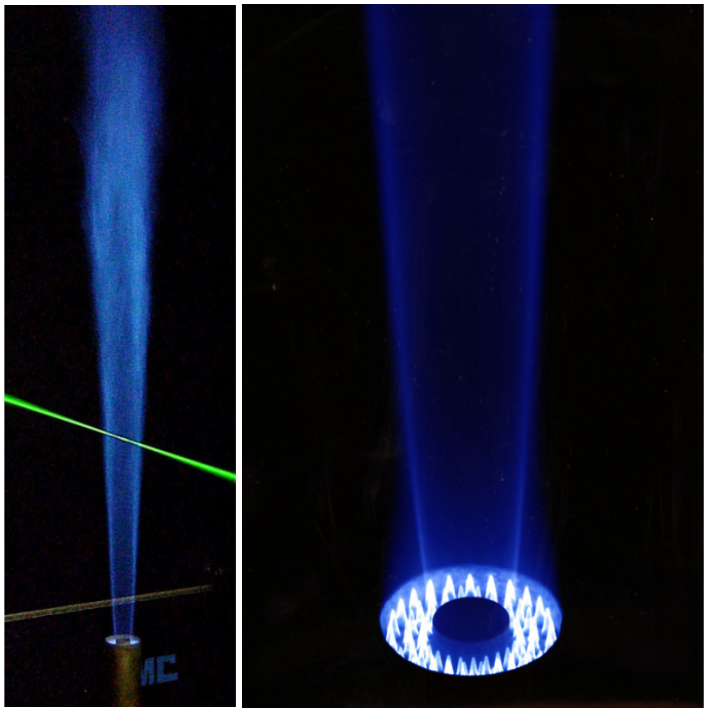

(a) (b)

Figure 6.4: Photographs of Flame D; (a) in full size and (b) close-up of the jet and pilot [243].

combustion simulation and the snapshot simulation are studied to show the limits and strengths of high-order P_N methods and their potential in coupled combustion simulations.

Sandia Flame D is a turbulent piloted jet flame [243] with a Reynolds number of Re_D=22,400. The fuel from the main jet is a mixture of methane and air with a ratio of 1:3 by volume. As is shown in Fig. 6.4, the main jet with a diameter of d_j = 7.2 mm at the center is surrounded by an annular pilot with a diameter of $2.62d_j$ to stabilize the main jet. The precise and careful measurement of Sandia Flame D provided a series of high quality experimental data [243] that makes it a standard benchmark of a turbulent jet flame to validate combustion models.

The effects of radiative transfer for the simulation of Sandia Flame D have been studied by Li [41], Wang [237] and Pal [34]. The importance of radiation and its interaction with turbulence (TRI) have been established by comparing the simulation results and the experimental measurements. Pal [34] also found that different spectral models and RTE solvers yield similar results

Table 6.3: Sizes of the main jet and the pilot and the inlet velocities in the simulation [245]

	Sandia Flame D		Sandia Flame D×4	
	d (mm)	u (m/s)	d (mm)	u (m/s)
main jet	7.2	49.89	28.8	12.4725
pilot	18.864	10.57	75.456	2.6425
co-flow	258.2	0.90	1032.8	0.2250

because of the relatively small size of Sandia Flame D. For this case, the P_1 RTE solver with a FSK spectral model is sufficient for the radiation calculations (though the small differences in predicted temperature resulted in totally different predictions of NO) [34]. Since the size of turbulent jet flames in real applications tends to be much larger, Sandia Flame D was scaled four times (Sandia Flame D×4) to study the effects of radiation for thicker turbulent jet flames [34, 41, 237]. Sandia Flame D is scaled up in such a way that the diameter of the main jet and the outer diameter of the pilot are quadrupled while decreasing the exit velocity of the mixture out of the jet and pilot to keep the Reynolds number Re_D unchanged. The geometric sizes of the main jet and the pilot and the inlet velocities of the original Sandia Flame D and Sandia Flame D×4 are shown in Table 6.3. The co-flow represents the environmental air entering the wind tunnel.

6.3.2 Coupled Simulations

So far, the high-order spherical harmonics (P_N) method has only been tested for non-coupled simulations. In this section, they are coupled to the RANS-based (Reynolds-Averaged Navier-Stokes) simulation models in `OpenFOAM`® 2.2.x. P_N methods from P_1 to P_7 as the RTE solver with the FSK look-up table as spectral models are tested in a coupled simulation of Sandia Flame D×4 partially-premixed jet flame. The optically thin, DOM+FSK and PMC+LBL solvers are also coupled to the reacting flow fields, respectively, as references. Turbulence–radiation interaction (TRI) is not considered here since the focus of this study is the performance of RTEs and only mean flow fields and mean radiative heat source will be discussed in this section. With the coupled simulation, it can be seen how the error of radiative heat source by the high-order P_N solvers or the

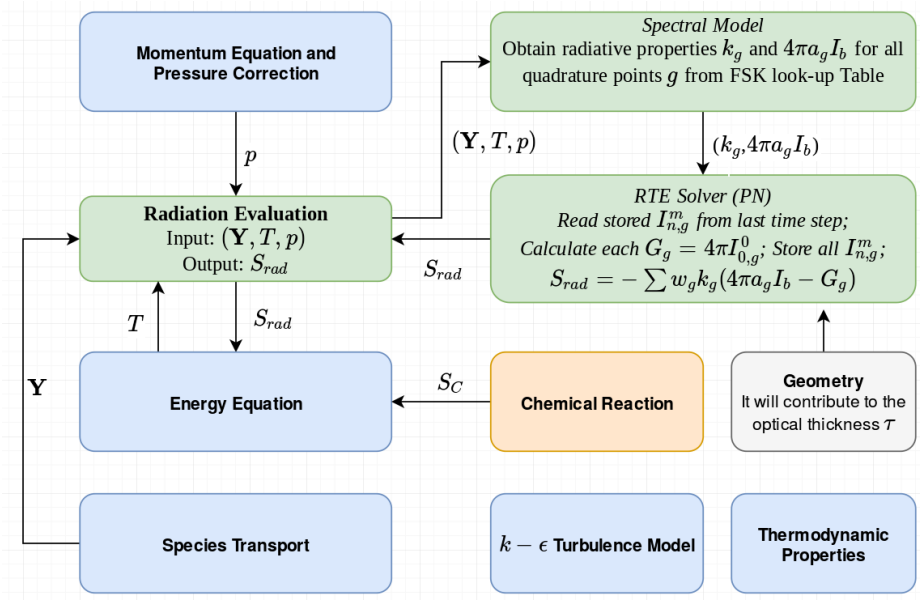

Figure 6.5: Schematic of the coupling between radiation and other sub-models; and between the radiation interface with P_N method as the RTE solver and FSK look-up table as the spectral model.

DOM solvers affect the resulting flow fields.

The coupling between the radiation sub-model and other sub-models is demonstrated in Fig. 6.5. There is no fundamental difference between P_N solvers and DOM solvers in terms of coupling with flow fields. In principle DOM equations are not coupled for non-scattering media while P_N equations are strongly coupled except for homogeneous optically thick media. The radiative heat source, S_{rad}, calculated from the radiation module is fed back to the energy equation, and in turn, the updated scalar fields ($\mathbf{Y}$, T and p) of the flow field will determine the radiative properties. From an overall energy balance, it is certain that considering radiative transfer will result in a flame with lower temperature, in general. Since the chemical reaction rate and thermodynamic properties of the gases are functions of temperature, the effects of radiation on the rest of the flow field other than temperature is hard to predict. The size of the flame is also critical to the role of radiation in overall flame simulations. A small flame will have very little total radiation (like the original Sandia Flame D) while a larger flame generally has more total radiation and self-absorption, which makes the influence of nongray spectral properties of the combustion gases more prominent.

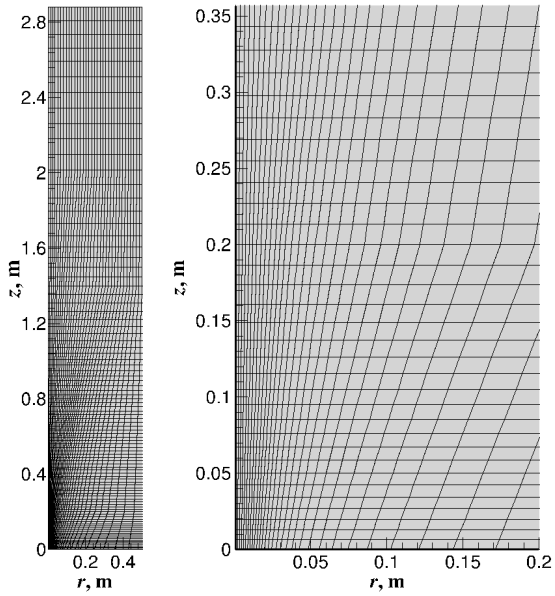

Figure 6.6: Grid system used in the axisymmetric flame simulation of Sandia Flame D.

6.3.2.1 Problem setup

In this study, a 10° wedge-shape grid consisting of 3325 cells (35 cells along the radial direction, or r-axis, and 95 cells along the axial direction, or z-axis) is employed as shown in Fig. 6.6. The full size of the computational domain is 0.516 m $\times$ 2.88 m and the mesh is optimized to have a finer mesh close to the jet to resolve the large local gradients there, and coarser in the air co-flow region and downstream of the flame to save computational time. Mesh dependency tests have been conducted by doubling the number of cells in both directions, and the results from two meshes for no-radiation reacting flows are compared with each other. It is found that the results are different for these two meshes. Although the grid independence of the mesh used for the coupled simulation can not be established for the mesh used as shown in Fig. 6.6, the current mesh is considered fine enough for the study of the effects of radiations in this thesis.

In this study, a pressure-based algorithm, i.e., PIMPLE or merged PISO (Pressure Implicit with Splitting of Operator)–SIMPLE (Semi-Implicit Method for Pressure Linked Equations) algorithm [223] in `OpenFOAM`® 2.2.x, is employed to resolve the coupling between pressure and velocity

for the RANS simulation. Since the maximum velocity of the reacting flow in the Sandia Flame D×4 is much smaller than a Mach number of 0.3, compressibility of the gases can be neglected, and therefore, PIMPLE is suitable for the flow simulation of Sandia Flame D×4. The pressure-coupled momentum equation, the energy equation in terms of sensible enthalpy, species transport equations and $k-\epsilon$ equations along with the chemical kinetics equations are iterated in sequence to predict the flow fields of the flame. A standard two-equation $k-\epsilon$ model is employed as the turbulence model with only $C_{\epsilon 1}$ being increased to 1.55 for a better representation of the turbulent flow field [1]. A 49 species and 277 reactions chemical reaction mechanism for methane, GRI–Mech 2.11 [246], is employed as chemistry mechanism and the SIBS (Semi-Implicit Bulirsch Stoer) ODE solver [229] is used to solve the chemical reaction equations. The PaSR (Partially Stirred Reactor) model [205] is employed for turbulence-chemistry interactions (TCI). The idea of PaSR is to assume only part of the gases in the computational cell are mixed. This sub-grid assumption is carried out by correcting the mean reaction rate by considering the turbulence mixing time scale (determined by the turbulent kinetic energy k and the turbulent dissipation ϵ) in addition to the chemical time scale. The nongray radiation models are integrated into `OpenFOAM®` 2.2.x and employed for the radiation evaluation. P_N RTE solvers with an FSK look-up table as the spectral model (PN+FSK), the DOM solvers with the same FSK table (DOM+FSK), the PMC solver with the line-by-line spectral model (PMC+LBL), and the optically thin solver with gray-Planck-mean spectral model (O.T.) are coupled to the reacting flow. The orders of the P_N solvers are from P_1 to P_7 and the combinations of numbers of discrete polar (p) and azimuthal (a) ordinates of the $\mathrm{DOM}_{p\times a}$ are $\mathrm{DOM}_{2\times 4}$, $\mathrm{DOM}_{4\times 4}$, $\mathrm{DOM}_{4\times 8}$ and $\mathrm{DOM}_{8\times 8}$. Three gas species, CO_2, H_2O and CO, are considered by the spectral models. All FSK calculations employ an eight-quadrature-point scheme, which means the RTE is solved eight times per radiation evaluation for the PN+FSK and DOM+FSK solvers. The P_N solver is the axisymmetric version, in which the total number of governing equations are reduced from $N(N+1)/2$ to $(N+1)^2/4$. The DOM solver is also an axisymmetric version [247] modified from the original

[1] This value of 1.55 is not discussed but actually used in [34]

DOM solvers in OpenFOAM®2.2.*x*.

The inlet boundary conditions for temperature, velocity and mass fractions of gases are listed in Table 6.4. For the radiative transfer, the outside boundaries are treated as cold and black and the top and bottom walls are treated as symmetry/specular reflection walls. The coupled simulation is carried out in the following manner: The simulation starts with no-radiation reacting flow. After running the no-radiation reacting flow for 2.2 s (about 9.5 flow-through times of the main jet or 2 flow-through times of the pilot), radiation models are activated. The radiation-coupled reacting flow keeps running for another 1.1 s until a time of 3.3 s. A constant time step of 8×10^{-6} s is used starting from 0 s to the end (3.3 s). Thus, from 2.2 s to 3.3 s, during which time the radiation models are considered, there are a total of 137,500 time steps. One advantage of the DOM and P_N methods in coupled combustion simulations is that they are able to use results of previous time steps as initial values for iterations at the new time step, which will reduce the computational cost of iterations required for DOM and P_N methods. The governing equations for DOM are not coupled for non-scattering media so that the benefit is limited. For the high-order P_N methods, since the governing equations are strongly coupled, storing the results from previous time steps will significantly reduce the total numbers of iterations required. The computational time for the P_N methods can be further improved by reducing the frequency of radiation evaluations for the coupled simulation. This is based on the fact that, in the multi-scale simulation of combustion, the time step is often determined by chemical models and, therefore, the change of the flow field may be small between time steps (this can also be taken advantage of by a time-blending scheme for the PMC solver). Therefore, four different frequencies are chosen: the PN+FSK and DOM+FSK scheme evaluates radiation every 1/10/100/250 time steps. The PMC+LBL calculation employs 5,000 photon bundles per time step with a recursive time-blending scheme, as given by:

$$(\nabla \cdot \mathbf{q})^{(k)} = (1-\alpha)(\nabla \cdot \mathbf{q})^{(k)} + \alpha(\nabla \cdot \mathbf{q})^{(k-1)} \quad \text{with} \quad (\nabla \cdot \mathbf{q})^{(0)} = 0 \tag{6.9}$$

with a blending factor $\alpha = 0.98$ and k is the time step. Time-blending can reduce the number

Table 6.4: Inlet boundary conditions of Sandia Flame D×4 [245]

	main jet	pilot	co-flow
T (K)	293	1880	291
u (m/s)	12.4725	2.6425	0.2250
Y_{CH_4}	0.15605	0.0	0.0
Y_{O_2}	0.1962	0.054	0.23113
Y_{H_2O}	0.0	0.0942	0.00581
Y_{CO_2}	0.00045	0.1098	0.00055
Y_{N_2}	0.6473	0.7377762	0.76251
Y_{CO}	0.0	0.00407	0.0
Y_{H_2}	0.0	0.000129	0.0
Y_H	0.0	0.0000248	0.0

of photon bundles required for each time step. This scheme is equal to employing about 1.25 million photon bundles for every 250 time steps (the contribution from 250 time steps ago is $0.02 \times (0.98)^{250} = 1.28 \times 10^{-4}$). Another scheme with the same blending factor but with 10,000 photon bundles per time step is also used as an accuracy validation for the former one. All computations are performed on twelve 2.66 GHz Intel (R) Xeon (R) X7460 processors. Simple domain decomposition into blocks with same number of cells along the axial direction is employed.

6.3.2.2 Results

The effects of radiation on the temperature predicted by different RTE solvers in the case of Sandia Flame D×4 are demonstrated in Fig. 6.7 in a 2-D contour plot followed by Fig. 6.8 showing centerline profiles. The PN/DOM+FSK results with different solving frequencies are found to be almost the same. Since the PMC+LBL results with different photon bundles per time step are also found to be very close to each other, only one PMC+LBL result is shown as the reference solution to be compared with. The profiles of radiative heat source and standard deviations of the PMC+LBL method (with 5000 photon bundles per time step) at three axial locations are shown in Fig. 6.9, as well, for reference. The standard deviation is obtained by splitting 5000 photon bundles into 10 sampling groups and keep running the PMC solver with the reacting flow for another 1000 time steps.

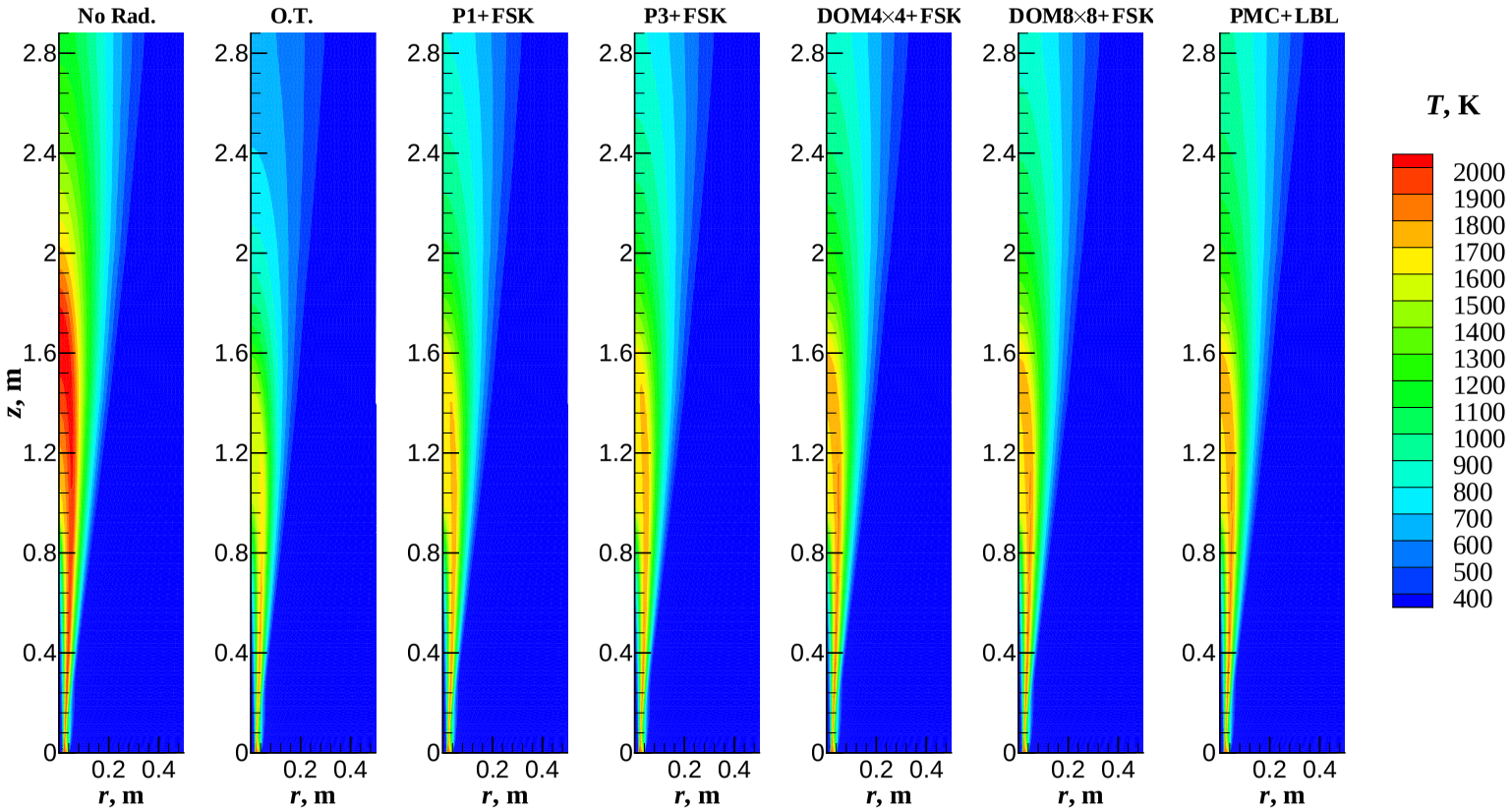

Figure 6.7: Effects of different RTE solvers on temperature distribution after two flow-through time (at 3.3 s).

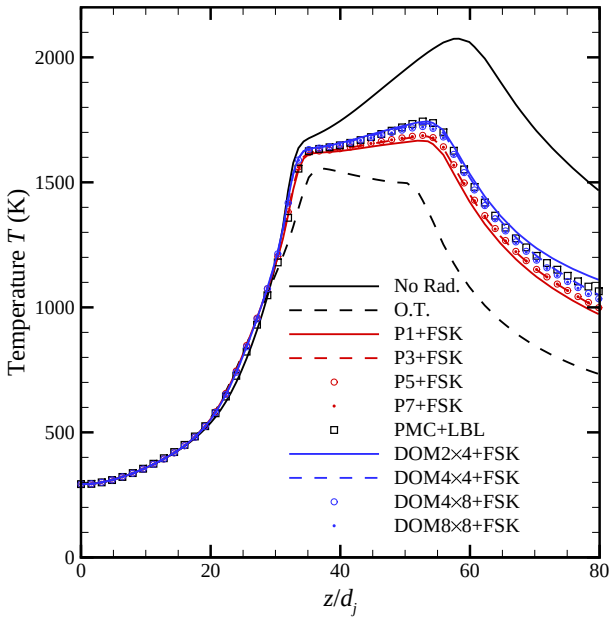

Figure 6.8: Centerline profiles of temperature.

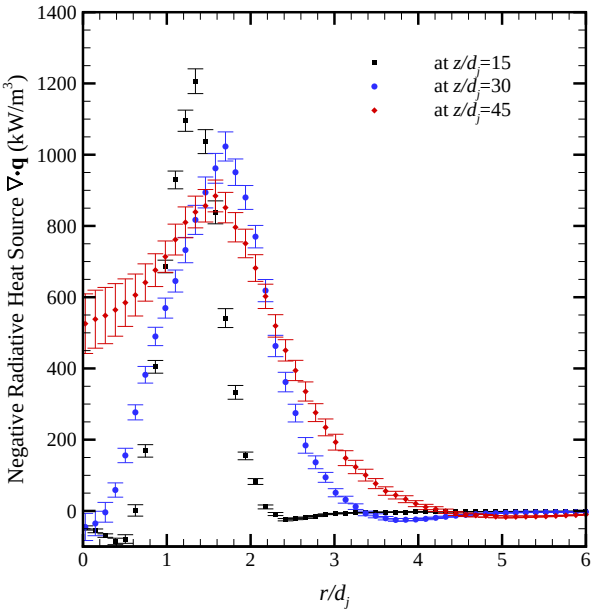

Figure 6.9: Negative radiative heat source $\nabla \cdot \mathbf{q}$ and the corresponding standard deviation from the PMC+LBL solver at three axial locations ($z/d_j = 15, 30, 45$).

Radiation and reacting flow are fully coupled in the simulations, so that different radiation models result in different radiative heat sources and, therefore, different temperature distributions, which in turn further lead to different chemical reaction rates and species concentrations. As expected, adding radiative transfer cools down the flame. It can be seen that for Sandia Flame D×4, the choice of radiation model plays a very important role. Totally ignoring radiation will introduce the largest error by over-predicting the flame temperature. The O.T. approximation ignores absorption and predicts the lowest temperature distribution; the PN+FSK, DOM+FSK and PMC+LBL predict considerably higher temperatures due to self-absorption. All DOM+FSK results are found to be very close to the PMC+LBL results, and only the temperature contours predicted from $\mathrm{DOM}_{4\times4}$+FSK and $\mathrm{DOM}_{8\times8}$+FSK are shown in Fig. 6.7 for reference. The small differences between the results predicted by $\mathrm{DOM}_{8\times8}$+FSK and PMC+LBL are believed to be partly due to the errors of FSK. P1+FSK performs much better than O.T., but it still under-predicts the flame temperatures compared with the results from high-order PN+FSK, DOM+FSK and PMC+LBL. P_3 only slightly improves the temperature profile compared with P_1 while P_5 and P_7 are very close to P_3 results. The temperature profiles predicted by high-order P_N methods are still quite different from the $\mathrm{DOM}_{8\times8}$ and PMC+LBL results, which will be further examined in a snapshot study in a later sub-section.

Peak temperatures along the centerline, $T_{p,c}$, predicted from different solvers as shown in Fig. 6.8, are summarized in Table 6.5. By comparing the peak temperatures, one can observe a decrease of temperature when employing different radiation models. The emission-only O.T. model predicts a drop of peak temperature of 520 K; the PMC+LBL predicts a drop of 329 K; the $\mathrm{DOM}_{p\times a}$+FSK predict the temperature drops of 330 K, 338 K, 350 K and 353 K with an increase in number of discrete ordinates; P1+FSK predicts a drop of 408 K, while the high-order PN+FSK models predict a peak temperature drop of around 386 K.

The radial distributions of two scalars, i.e., temperature (T) and mass fraction of nitrogen monoxide (Y_{NO}) at three axial locations $z/d_j = 15$, $z/d_j = 30$ and $z/d_j = 45$ are shown in Figs. 6.10

Table 6.5: The peak temperatures along the centerline $T_{p,c}$ predicted from different solvers at 3.3 s

Radiation Solvers	$T_{p,c}$ (K)	$\Delta T_{p,c}$ (K)	%
No Rad.	2074	/	/
O.T.	1554	-520	-25.1
P1+FSK	1666	-408	-19.7
P3+FSK	1683	-391	-18.8
P5+FSK	1688	-386	-18.6
P7+FSK	1689	-385	-18.6
DOM 2×4	1744	-330	-15.9
DOM 4×4	1736	-338	-16.3
DOM 4×8	1724	-350	-16.9
DOM 8×8	1721	-353	-17.0
PMC+LBL	1745	-329	-15.9

and 6.11, respectively. These two plots show the flame structure and local distribution of the pollutant NO. The radial profiles of both scalars predicted by DOM+FSK are very close to those from the PMC+LBL. For the temperature predictions, at upstream locations of $z/d_j = 15$ and 30, P1+FSK results are shown to be already very close to PMC+LBL results, while at the downstream location of $z/d_j = 45$, the errors of P_N methods are larger. The NO production is very sensitive to temperature, therefore resulting in larger differences between different radiation solvers.

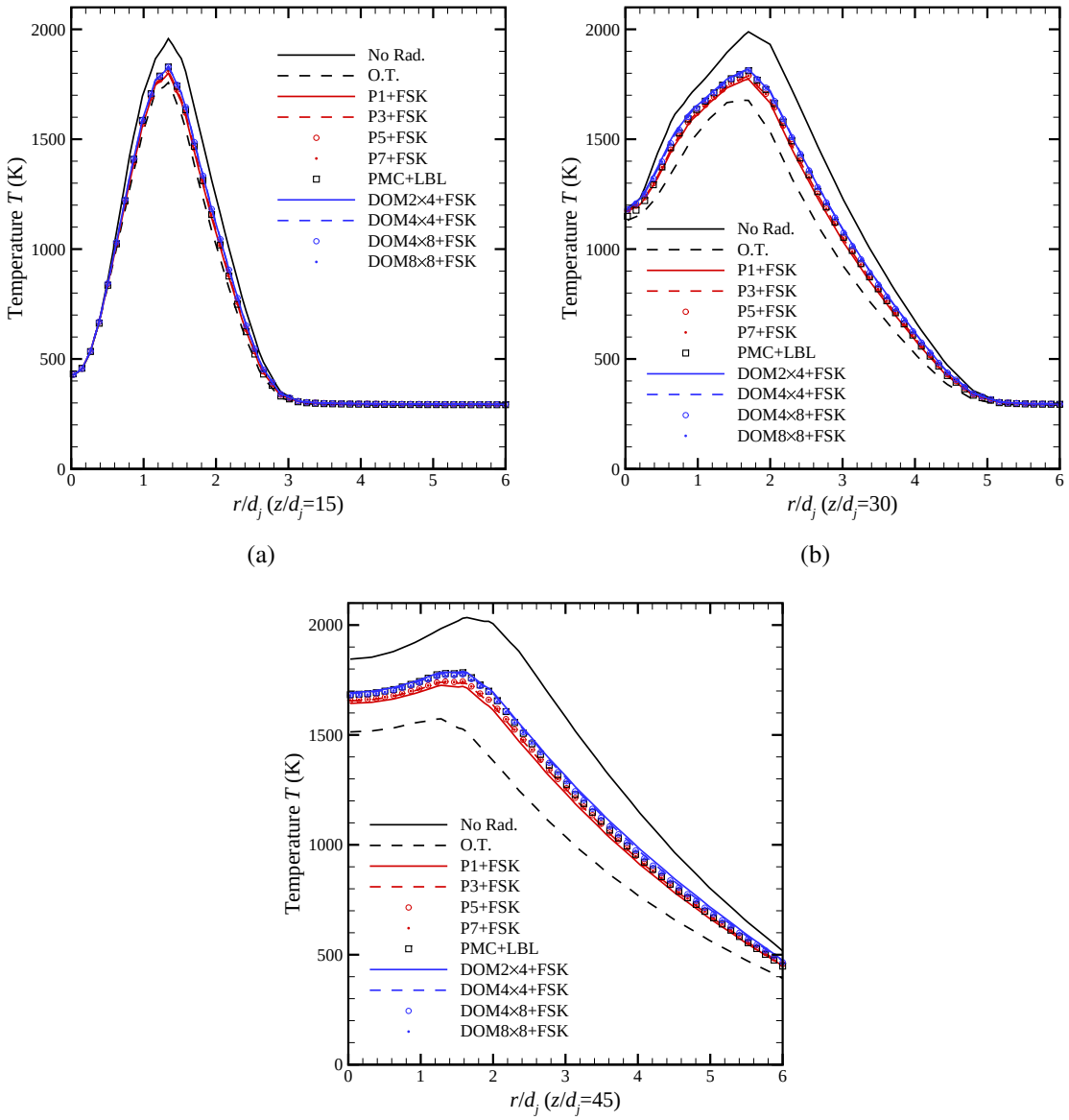

Figure 6.10: Temperature profiles at different axial locations: (a) $z/d_j = 15$, (b) $z/d_j = 30$ and (c) $z/d_j = 45$.

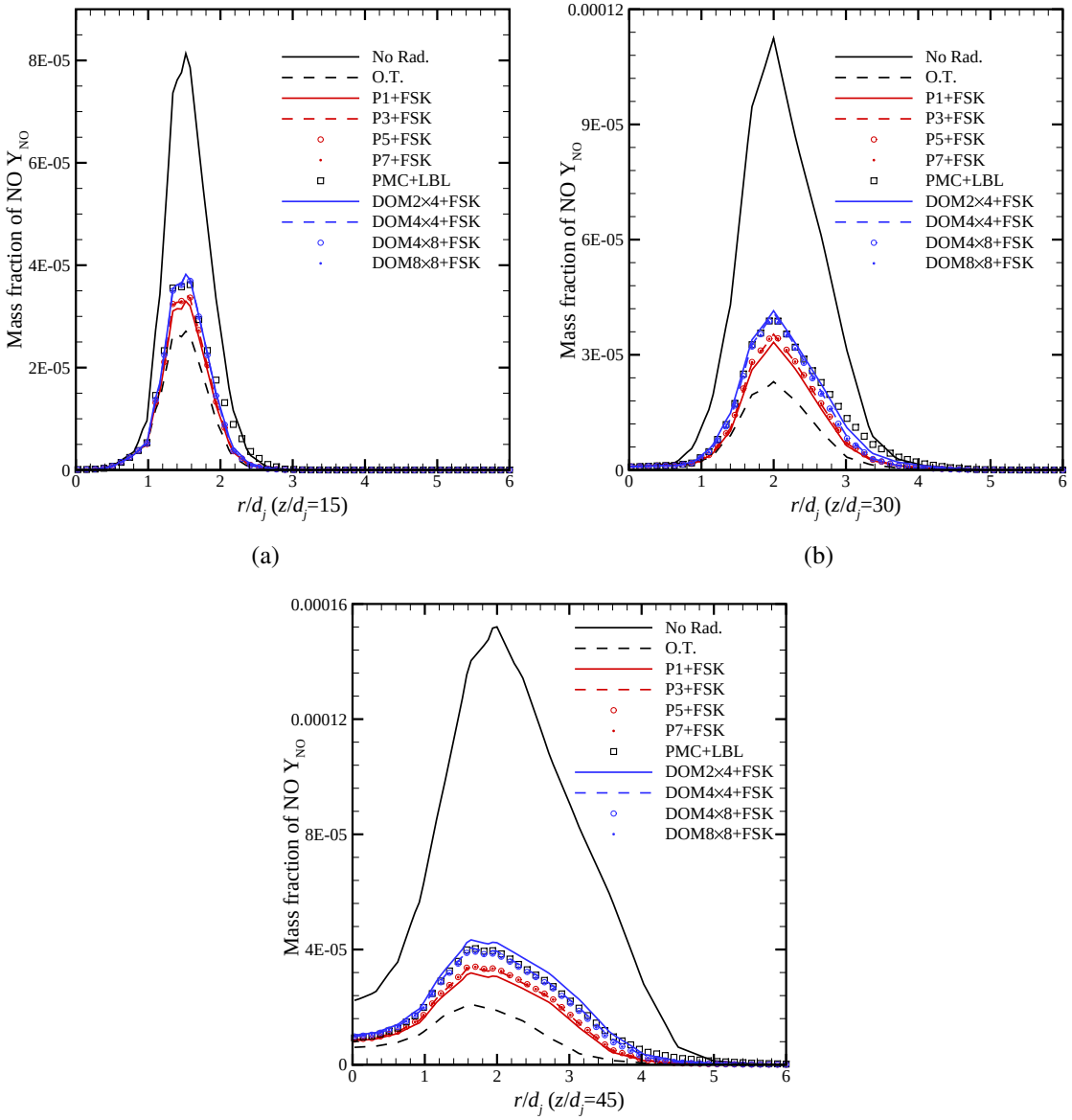

Figure 6.11: Mass fraction of NO profiles at different axial locations: (a) $z/d_j = 15$, (b) $z/d_j = 30$ and (c) $z/d_j = 45$.

Table 6.6: The resulting heat release from combustion $\dot{Q}_C$, total emission $\dot{Q}_{rad}$, net radiative heat loss $\dot{Q}_{rad}$, radiation escape ratio as $\dot{Q}_{rad}/\dot{Q}_{emi}$ and actual radiant fraction $\dot{Q}_{rad}/\dot{Q}_C$ from different radiation solvers

Radiation Solver	$\dot{Q}_C$ (kW)	$\dot{Q}_{emi}$ (kW)	$\dot{Q}_{rad}$ (kW)	$\dot{Q}_{rad}/\dot{Q}_{emi}$	$\chi_R = \dot{Q}_{rad}/\dot{Q}_C$
No Rad	68.4	/	/	/	/
O.T.	66.6	40.7	40.7	100 %	61.1 %
P1+FSK	67.3	54.4	22.5	36.7 %	33.4%
P3+FSK	67.3	63.4	20.8	32.8 %	30.9%
P5+FSK	67.3	63.7	20.7	32.4%	30.7%
P7+FSK	67.3	63.8	20.6	32.2%	30.6%
DOM 2×4+FSK	66.6	73.8	17.7	24.0 %	32.0 %
DOM 4×4+FSK	67.0	69.8	17.2	24.7 %	26.6 %
DOM 4×8+FSK	67.0	68.0	18.6	27.4 %	25.8 %
DOM 8×8+FSK	67.0	67.7	18.7	27.7 %	27.8 %
PMC+LBL	67.3	71.3	21.6	30.2 %	28.0 %

As discussed earlier, the coupling between radiative transfer and reacting flow is determined by many factors. Several quantities that describe the overall heat transfer are shown in Table 6.6. The first quantity of interest is the actual heat release from combustion, $\dot{Q}_C$, which is the integral of reaction heat over the control volume that contains the flame. If the combustion is complete, $\dot{Q}_C$ should equal to the chemical energy that is supplied to the flame in the reactants, which are quantified by $\dot{m}_F \Delta h_C$, where $\dot{m}_F$ is the mass flow rate of the fuel and Δh_C is the lower heating value of the fuel. For Sandia Flame D×4, $\dot{m}_F \Delta H_C = 70.4$ kW and the rate of incoming enthalpy from the hot pilot is around 6% of that. Two quantities related to radiative transfer are the total emission $\dot{Q}_{emi}$ and the net radiative heat loss $\dot{Q}_{rad}$. The total emission $\dot{Q}_{emi}$ and the net radiative heat loss $\dot{Q}_{rad}$ are defined as the integral of the radiative emission S_{emi} and negative radiative heat source $-S_{rad}$ over the control volume, respectively. In terms of these three quantities, the radiant fraction χ_R is defined here as the ratio of $\dot{Q}_{rad}/\dot{Q}_C$ (instead of $\dot{Q}_{rad}/\dot{m}_F \Delta H_C$) and the radiation escape ratio as $\dot{Q}_{rad}/\dot{Q}_{emi}$. The radiant fraction χ_R is a useful notion to quantify the ratio of the net radiative energy that escapes to the surroundings to the chemical energy released from the combustion and the radiation escape ratio shows the ratio of escaped radiation to the emitted.

These quantities lead to better understanding of the role of radiative transfer on the combus-

tion process. In addition to the direct cooling effects of radiation discussed earlier, adding radiation is shown to have slightly lowered the total heat release from combustion $\dot{Q}_C$ as a secondary effect resulting in less complete combustions. Total emission is found to be quite large, which is very close to the total heat release from combustion. However, what matters is the value of net radiative heat source $\dot{Q}_{rad}$, which is reasonable (around 1/3 of the total total heat release from combustion) except for O.T. results. Note that chemical reactions are taking place only at the flame zone while the radiation regions are much larger in volume. Therefore radiative transfer is very important not only in terms of peak temperature but also affects the size of flame, especially downstream of the flame.

Table 6.7 shows averaged CPU time per time step spent by both solving the equations for reacting flow and a radiation evaluation including spectral models and RTE solvers. The average $t_{RTE} + t_{overhead}$ and t_{FSK} are only shown for runs with radiation evaluated once per time step. The number of second-order elliptic PDEs for the corresponding P_N methods, the number of first-order PDEs for the corresponding DOM solvers and the number of photon bundles traced for the PMC method are also presented in the table. It is also observed that, though convergence speed is slow for the high-order P_N methods at early time steps, once convergence is reached, only one or two outer iterations are required for the RTE solution for each quadrature point at later time steps. Two empirical correlations can be obtained for the time cost of the spherical harmonics methods and the discrete ordinates methods for the simulations in which the radiation is evaluated once per time step, i.e.,

$$t_{PN} = 0.0059 \times n_{quad} \times n_{PDE} + t_{flow} + t_{FSK} + t_{overhead,PN} \tag{6.10}$$

$$t_{DOM} = 0.0015 \times n_{quad} \times n_{PDE} + t_{flow} + t_{FSK} + t_{overhead,DOM} \tag{6.11}$$

where n_{quad} is the number of quadrature points (8 for the above simulations); n_{PDE} is the number

Table 6.7: Average CPU time per time step (radiation is evaluated once per 1/10/100/250 time steps for the PN/DOM+FSK solvers and the average t_{RTE} + $t_{overhead}$ and t_{FSK} are only shown for runs with radiation evaluated once per time step)

Radiation Solver	Average CPU Time (s)	t_{RTE}+$t_{overhead}$ (s)	t_{FSK} (s)	
No Rad	0.82	/	/	
P1+FSK	0.97/0.85/0.82/0.82	0.09	0.06	1 second-order PDE
P3+FSK	1.05/0.87/0.83/0.83	0.17		4 second-order PDE
P5+FSK	1.36/0.88/0.84/0.84	0.48		9 second-order PDE
P7+FSK	1.64/0.90/0.85/0.85	0.76		16 second-order PDE
DOM 2×4+FSK	1.11/0.86/0.85/0.84	0.23		8 first-order PDE
DOM 4×4+FSK	1.20/0.87/0.85/0.84	0.32		16 first-order PDE
DOM 4×8+FSK	1.42/0.91/0.86/0.86	0.54		32 first-order PDE
DOM 8×8+FSK	1.78/0.94/0.87/0.87	0.9		64 first-order PDE
PMC+LBL	0.87	/	/	5,000 with time-blending
PMC+LBL	0.92	/	/	10,000 with time-blending

of PDEs for the corresponding RTE method; t_{flow} = 0.82 s, t_{FSK} = 0.06 s, $t_{overhead,PN}$ = 0.07 s and $t_{overhead,DOM}$ = 0.14 s. It can be seen that by storing intensity coefficients I_n^m for each time step in coupled simulations, the time cost for different orders of P_N methods is actually linearly proportional to the number of the second-order PDEs of the P_N formulation with order N. In principle and especially for this flame, DOM does not need outer iterations so that the benefit of storing intensities along each discrete ordinate is limited.

Comparison of average CPU time required for one time step with different radiation evaluation frequencies is also shown in Table 6.7. Reducing the radiation evaluation frequency for the PN/DOM+FSK solvers (or applying time blending for the case of PMC+LBL) can significantly reduce the time cost for radiation evaluations and make radiation evaluation relatively cheap compared to the computational cost of reacting flow simulations. Since the computational cost of PMC+LBL solver is proportional to the total number of photon bundles traced for a same mesh, it is not surprising that the time cost of PMC+LBL is small after applying the time-blending scheme.

6.3.3 Frozen Snapshot Study

A one-step snapshot study is carried out to isolate the radiation evaluation from the changing flow fields to study the accuracy and computational cost of different RTE solvers for one single time step, including the P_N solvers from P_1 to P_7, the $\mathrm{DOM}_{p\times a}$ solvers, with four different combinations of numbers of discrete polar (p) and azimuthal (a) ordinates, and the PMC method. The P_N and DOM methods are coupled with the FSK look-up table as the spectral model with a 8-quadrature-point evaluation. The PMC again employs the most accurate LBL calculations. In this section, the frozen scalar fields are calculated from smooth correlations to eliminate the possible effects of smoothness of the radiative properties on the performance of different RTE solvers.

Radiative calculations are conducted on a two-dimensional wedge, a three-dimensional cylinder and a three-dimensional cuboid. The size of the computational domain is $0 \le r \le 0.52$ m and $0 \le z \le 2.88$ m. For the grids of a 3-D cylinder and a 3-D cuboid, all walls are cold and black, while for the 2-D wedge, the top ($z = 2.88$ m), bottom ($z = 0$ m) and right ($r = 0.52$ m) walls are cold and black. The temperature and species concentration in the flame mimics the fully-developed Sandia Flame D×4. Equation (6.12) describes the temperature and mole fractions distributions of CO_2, H_2O and CO, whereas Fig. 6.12 shows contour plots of the scalar fields obtained from Eq. (6.12).

$$p = 1 \quad \text{bar} \tag{6.12a}$$

$$T = 1700 \times \exp\left[-\left(\frac{r}{0.05 + 0.1z}\right)^2\right] \times \exp\left[-\left(\frac{z - 1.3}{0.5z + 0.7}\right)^2\right] + 300 \quad \text{K} \tag{6.12b}$$

$$x_{\mathrm{CO_2}} = 0.08 \times \exp\left[-\left(\frac{r}{0.05 + 0.1z}\right)^2\right] \times \exp\left[-\left(\frac{z - 1.1}{0.5z + 0.6}\right)^2\right] \tag{6.12c}$$

$$x_{\mathrm{H_2O}} = 0.19 \times \exp\left[-\left(\frac{r}{0.05 + 0.1z}\right)^2\right] \times \exp\left[-\left(\frac{z - 1.0}{0.5z + 0.7}\right)^2\right] \tag{6.12d}$$

$$x_{CO} = 0.07 \times \exp\left[-\left(\frac{r}{0.05 + 0.04z}\right)^2\right] \times \exp\left[-\left(\frac{z - 1.0}{0.7}\right)^2\right] \tag{6.12e}$$

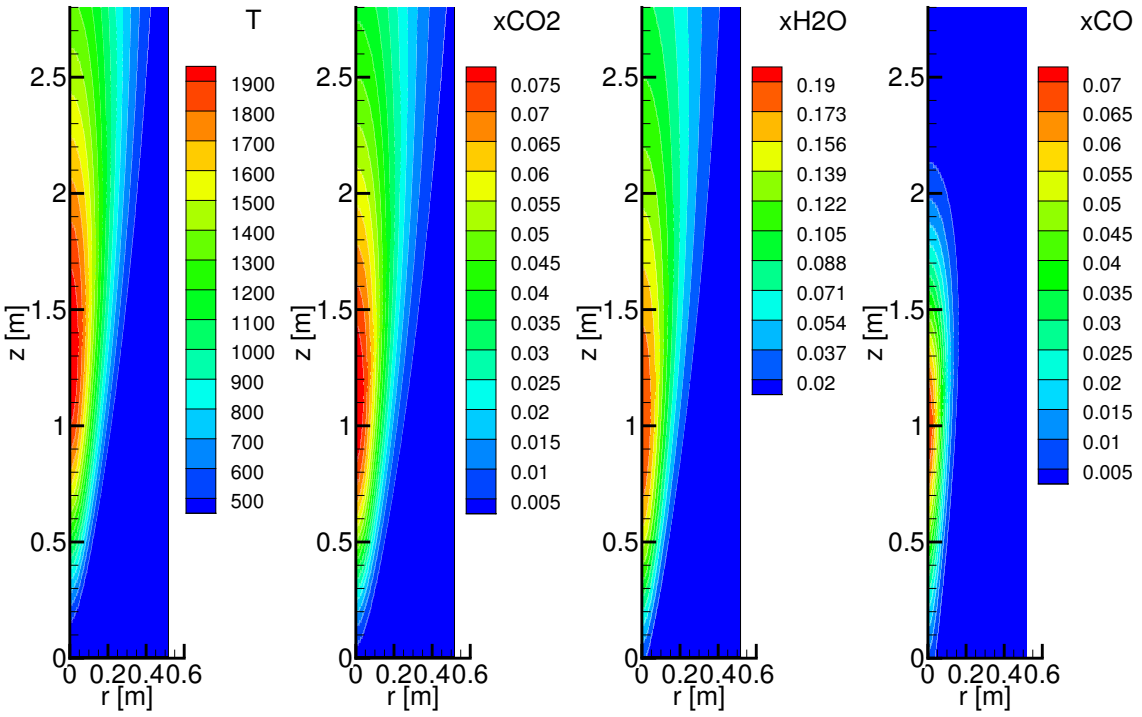

Figure 6.12: Temperature and mole fraction fields for the artificial flame.

The computational meshes are shown in Fig. 6.13, where the 2-D wedge, 3-D cylinder and cuboid have cell numbers of 5000, 0.45 million and 0.49 million, respectively. For the snapshot study, the wedge mesh is orthogonal compared with the unstructured wedge mesh used in the coupled simulation to avoid the potential error introduced by an unstructured grid. The flame profile is axisymmetric and has the same distributions of temperature and mole fractions for all three different meshes.

As a validation of the RTE solvers, the results from three geometries with the same RTE solver are compared first. Comparison of the calculated negative radiative heat sources ($\nabla \cdot \mathbf{q}$) using P7+FSK, DOM 8×8+FSK and PMC+LBL for three different meshes is presented in Fig. 6.14. The P7+FSK solutions from all three geometries are overlapping each other, which is an indication of the correctness of the P_N implementations in `OpenFOAM`® and an indication of the merit of rotational invariance of the spherical harmonics P_N methods, while for DOM 8×8+FSK and

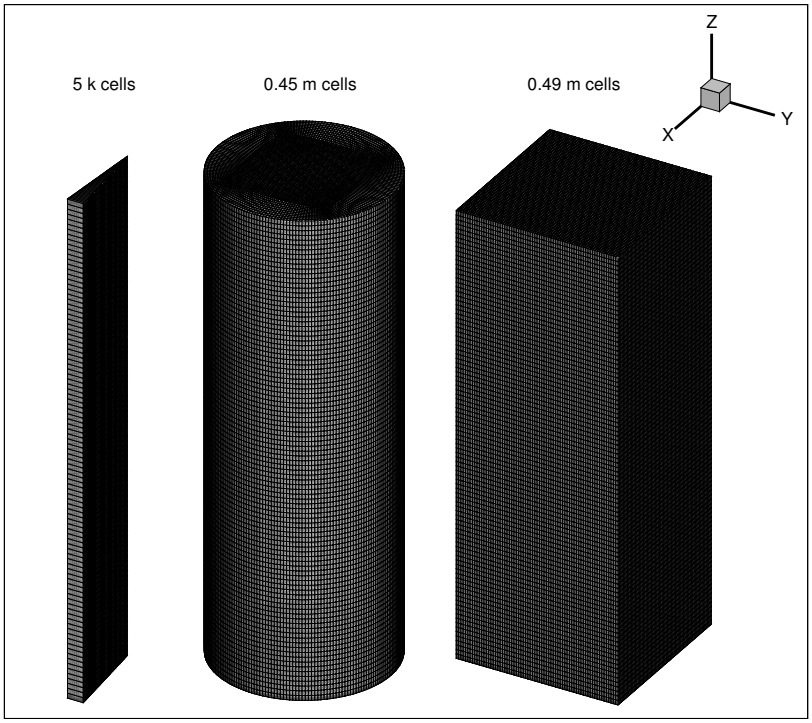

Figure 6.13: Computational geometries and meshes for the snapshot simulation of Sandia Flame D×4.

PMC+LBL solvers, all show small discrepancies between the 2-D wedge results and the results from 3-D geometries.

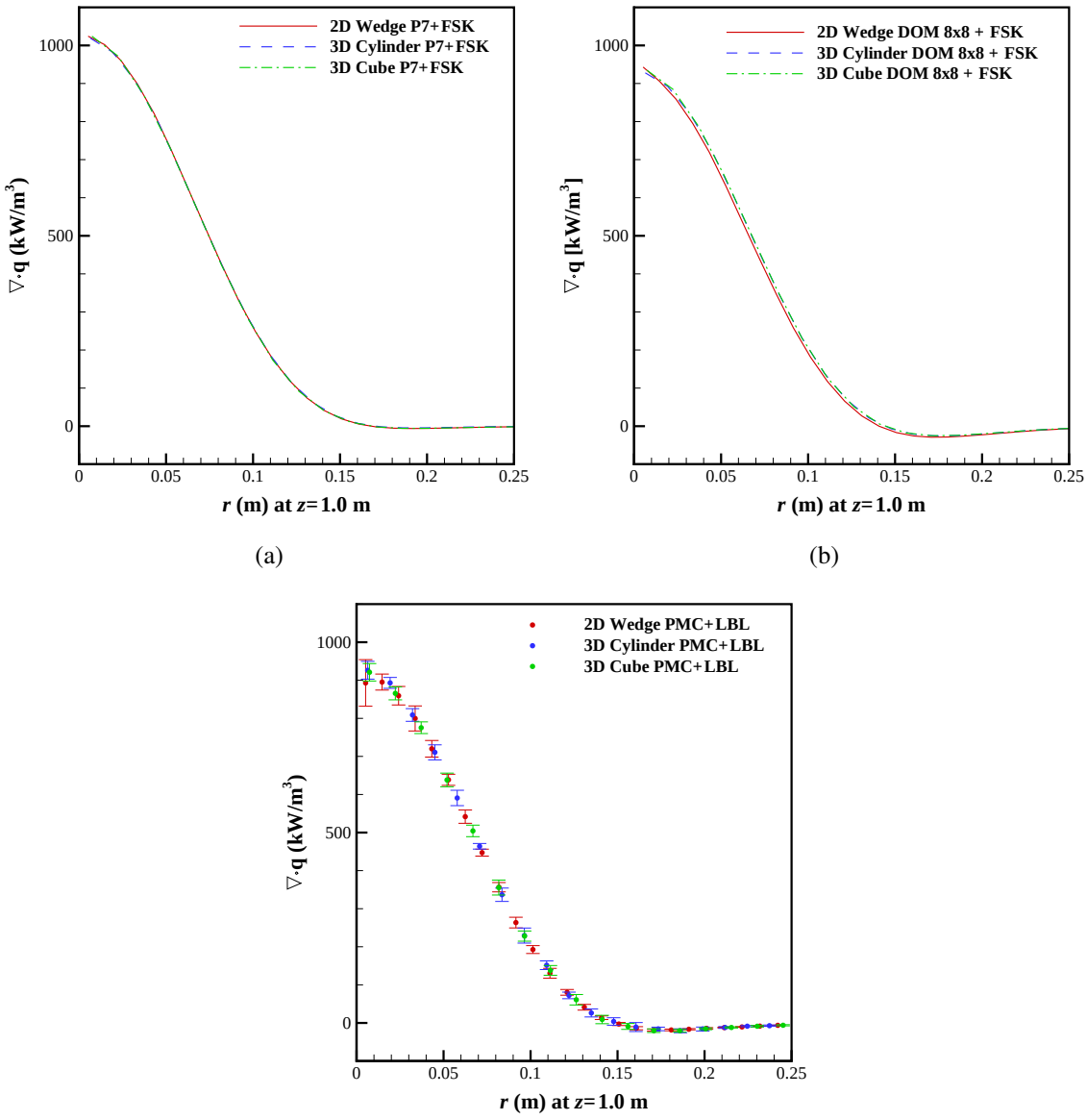

Figure 6.14: Comparison of negative radiative heat source $\nabla \cdot \mathbf{q}$ for different geometries: (a) P7+FSK, (b) DOM 8×8+FSK and (c) PMC+LBL.

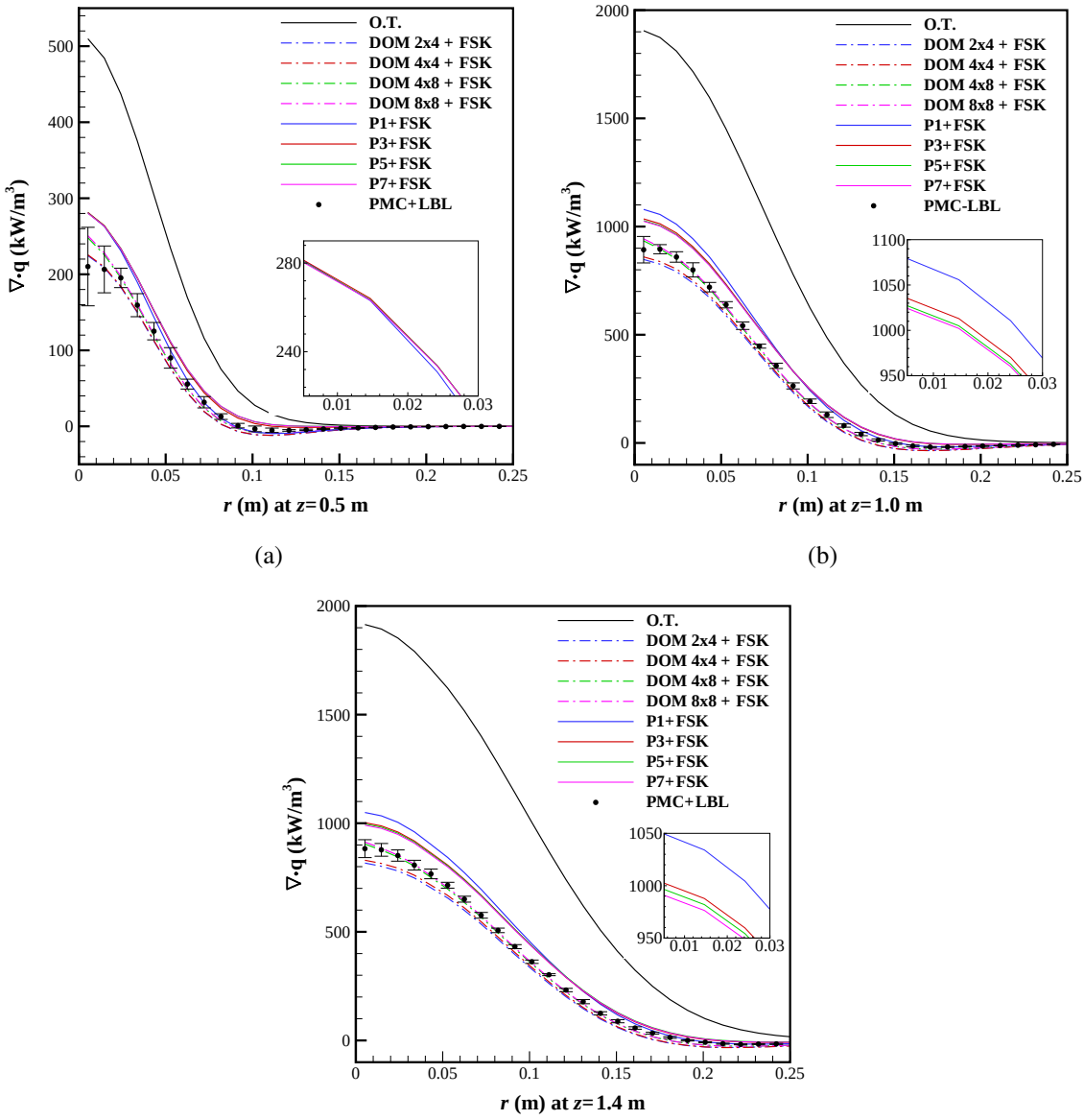

Figure 6.15: Comparison of negative radiative heat source $\nabla \cdot \mathbf{q}$ for a 2-D wedge geometry at three axial locations: (a) z=0.5 m, (b) z=1.0 m and (c) z=1.4 m.

Since all three geometries produce practically identical results, results from only the wedge geometry are shown next. The negative radiative heat sources ($\nabla \cdot \mathbf{q}$) using PN+FSK, DOM+FSK and PMC+LBL at three axial locations on the 2-D wedge geometry are shown in Fig. 6.15. All DOM+FSK calculations perform well compared to the the PMC+LBL results, which also proves the 8-quadrature FSK model is very accurate compared to LBL evaluations. As far as the accuracy of P_N methods is concerned, P_3 improves the P_1 solution to some extent, but the improvement of accuracy from P_5 and P_7 compared with P_3 is marginal and converge very slowly toward the PMC+LBL results.

To further investigate the error of the PN+FSK solver, a comparison for each special quadrature point was carried out. The optical thickness $\tau_{R,g}$ along the radius at $z = 1.0$ m and weight w_g for each quadrature point is shown in Table 6.8. The accuracy of the P_N solver for each quadrature point is shown in Figs. 6.16 and 6.17. The PMC results for each quadrature point are calculated with gray models by direct taking the k_g and $4\pi a_g I_b$ from each quadrature point as input.

For quadrature points with optically thin conditions (for this case, quadrature points 1 through 4 in Fig. 6.16), since self-absorption is a very small portion of the total emission, any RTE solver including the O.T. model can predict correct radiative heat sources. For the optically thick condition, such as the largest quadrature point 8 shown in Fig. 6.17(d), all P_N methods except P_1 capture the PMC results. The major source of errors for the high-order P_N methods are from the quadrature points in the middle, quadrature points 5–7, indicating an optically intermediate condition. This is due to the extremely anisotropic intensities resulting from this particular shape of flame. For such cases, the truncated series of spherical harmonics cannot follow the near step-function of the angular distribution of intensities for optically intermediate conditions. Much higher orders of spherical harmonics series would be required to fully resolve the discontinuity of the the angular distribution of the intensities.

At this point, it is clear that the discrepancy between the radiative heat sources from PN and PMC RTE solvers for quadrature points 5–7 shown in snapshot analysis is the root source of the

Table 6.8: Optical thickness $\tau_{R,g}$ along radius at z = 1.0 m and weights w_g for each quadrature point

Index	1	2	3	4	5	6	7	8
w_g	0.1834	0.1962	0.1624	0.1510	0.1194	0.1030	0.0606	0.0399
$\tau_{R,g}$	0.0006	0.0035	0.0120	0.03348	0.08081	0.2112	0.8327	3.5118

Table 6.9: Comparison of CPU time (s) for RTE solvers

Mesh	PN				DOM				PMC
	P_1	P_3	P_5	P_7	$DOM_{2\times4}$	$DOM_{4\times4}$	$DOM_{4\times8}$	$DOM_{8\times8}$	
2-D wedge	0.32	11.78	32.47	83.72	1.92	2.44	5.55	11.15	723 (1M×10)
3-D cylinder	430	4884	14964	40499	396	914	1577	2747	13869 (10M×10)
3-D cube	270	6998	20666	48492	533	953	1711	3210	14422 (10M×10)

errors in the flow fields in coupled simulations.

In summary, it appears that the P_3 method is the best choice for combustion simulations. For the optically thick quadrature points, it greatly improves the P_1 solution. For optically intermediate quadrature points, P_5, P_7 or even higher order approximations do not improve results a lot over P_3 solutions, but increase the number of PDEs quadratically.

The computational cost of different RTE solvers for all three geometries in this snapshot study is presented in Table 6.9. All calculations were done on a single 2.66 GHz Intel (R) Xeon (R) X7460 processor. PMC employed 100 million photon bundles for 3-D meshes and 10 million for the 2-D wedge mesh. The number of second-order PDEs for different orders of P_N methods and the number of first-order PDEs for $DOM_{p\times a}$, with respect to the number of discrete polar ordinates p and azimuthal ordinates a, are shown in Table 6.1 for reference. The coupling between the second-order PDEs for the high-order P_N in this problem is quite strong, while for DOM, there is no coupling between the first-order PDEs. For this reason, the high-order P_N methods are very inefficient due to large number of outer iterations required to resolve the coupling between PDEs. Though the computational cost of high-order P_N methods is not competitive with DOM and PMC solvers for this snapshot run, the problem is eliminated for coupled simulations as shown in the previous section.

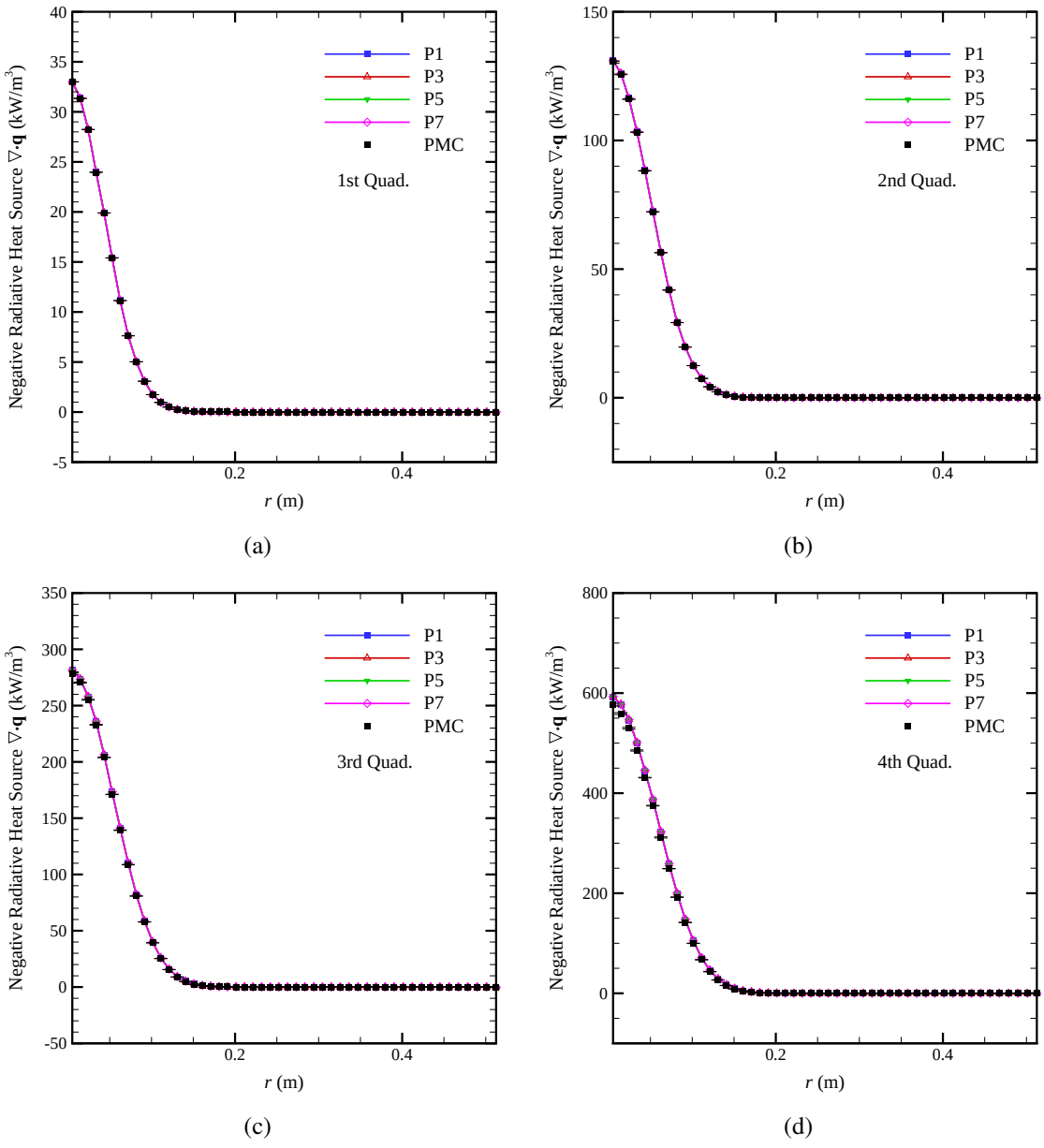

Figure 6.16: Negative radiative heat source $\nabla \cdot \mathbf{q}$ predicted from PN and PMC solvers at one axial location $z = 1.0$ m; (a) the 1st Quadrature, (b) the 2nd Quadrature, (c) the 3rd Quadrature and (d) the 4th Quadrature.

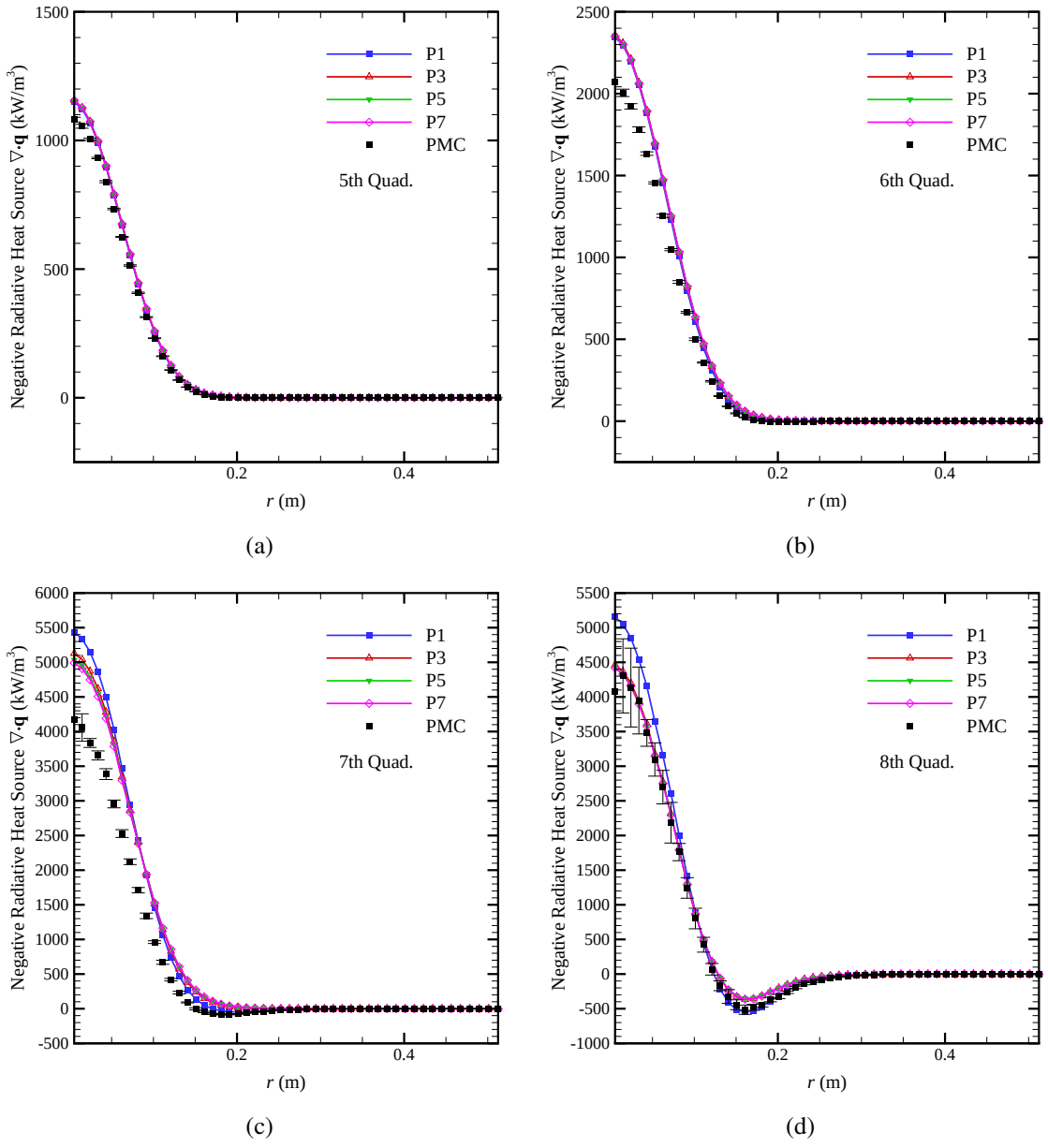

Figure 6.17: Negative radiative heat source $\nabla \cdot \mathbf{q}$ predicted from PN and PMC solvers at one axial location $z = 1.0$ m; (a) the 5th Quadrature, (b) the 6th Quadrature, (c) the 7th Quadrature and (d) the 8th Quadrature.

In summary, it appears that the P_3 method is a good choice for combustion simulations of this specific type of flames. For the optically thick quadrature points, P_3 is able to improve the P_1 solution, while for optically intermediate quadrature points, P_5, P_7 or even higher order approximations do not improve results a lot over the P_3 solution, but increase the number of PDEs quadratically.

However, the above conclusion may be limited to this specific type of flames of similar sizes without further generalization because it can be seen that the performance of P_N methods are strongly related to the radiative properties of the flame. Since the optical thickness and spatial distribution of k for each quadrature point is determined by many factors of the flame, such as the products of combustion, size of the flame, surrounding gases, etc., it is difficult to tell whether high-order P_N methods would perform better or worse for other combustion simulations. Future applications of the high-order P_N methods in combustion simulations could be studies of flames in furnaces, sheet flames and rocket plumes, etc. A high-temperature oxy-natural gas furnace will be presented next to demonstrate the strengths of the high-order P_N methods.

6.4 Oxy-Natural Gas Combustion

6.4.1 Background

Oxy-fuel combustion is the process of burning a fuel using pure oxygen instead of air as the primary oxidant. Oxy-fuel combustion has several advantages over the traditional air-fuel combustion: (1) using oxygen as the oxidizer raises the adiabatic flame temperature; (2) the products contain a high concentration of CO_2, which facilitates its sequestration; (3) production of nitrogen oxide is greatly reduced. The heat transfer characteristics in an oxy-fuel furnace are found to be quite different from those of a traditional air-fuel furnace because of resulting higher temperatures and higher concentrations of CO_2 and H_2O, which significantly increase the magnitude of radiative transfer in the furnace.

The International Flame Research Foundation has conducted a series of oxy-natural gas com-

bustion experiments under the OXYFLAME project [248, 249]. A couple of CFD simulations were carried out as part of the OXYFLAME project for better understanding of the oxy-natural combustion process as well as to validate the CFD models. Early modeling efforts have focused on chemistry and TCI models where a gray radiation model is usually employed to avoid complexity [250–252]. Later numerical studies started employing nongray spectral models, including Yin et al. [253] using a weighted sum of gray gases (WSGGM) model and Zhao et al. [254] with a LBL calculation. Zhao et al. [254] simulated a 0.8 MW oxy-natural gas burner (OXYFLAM-2A) from the OXYFLAME project. Their high-fidelity RANS study has employed a consistent hybrid Lagrangian particle/Eulerian mesh method including a transported PDF turbulence model, and PMC+LBL solver for the radiation calculation, which fully resolves TRI. Although predicted mean temperature, velocity and gas fractions are still quite different from experimental measurements, the results are considered to have captured most of the physical and chemical characteristics of the oxy-natural gas combustion processes in the furnace. Therefore, their results are used here for snapshot studies to test the performance of high-order P_N methods. The aim of the frozen snapshot study is to analyze the performance of high-order P_N solvers in the application of oxy-fuel combustions as a comparison to the less satisfactory performance of high-order P_N methods in the jet flames.

6.4.2 Frozen Snapshot Study

A one-step snapshot study is presented next to show the performance of P_N methods (up to the order of P_7) against that of the PMC method as well as the DOM. Both gray and nongray spectral models coupled with P_N, DOM and PMC RTE solvers are tested. The Planck-mean absorption coefficient is used for the gray simulation while the P_N methods and DOM are coupled with the FSK look-up table (PN+FSK and DOM+FSK) and PMC employs the most accurate LBL calculations (PMC+LBL) for the nongray simulations.

Radiative calculations are conducted on a two-dimensional wedge with 10,260 computational cells. The size of the furnace and the injector are shown in Fig. 6.18. The height and radius of the

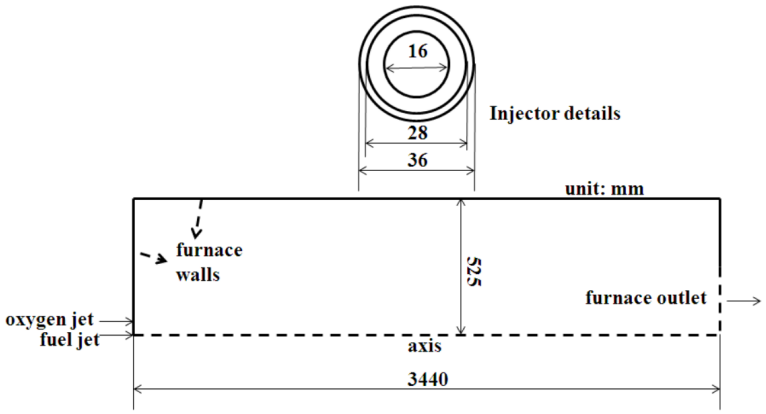

Figure 6.18: Size of the furnace and the inlet nozzle [254].

furnace are 3.44 m and 0.525 m. The unstructured mesh is refined for the flame regions and is shown in Fig. 6.19. In this study, all furnace walls are treated as cold and black. The inlet and outlet are treated as symmetry/specular reflections boundaries in P_N, DOM and PMC solvers. The contours of temperature and mole fractions of CO_2, H_2O and CO are also shown in Fig. 6.19. The furnace is filled with CO_2 and H_2O except in the flame region close to the center. The mole fraction of CO in the flame region close to the nozzle is much higher than that in an air-fuel furnaces. This oxy-natural gas flame can be generally regarded as an optically thick example because of high concentrations of CO_2 and H_2O.

In terms of radiative transfer, the furnace can be roughly divided into two regions: one is the high-temperature flame region at the center and the other is the large recirculation region where the temperature is lower. The small flame region has the highest temperature and the lowest mole fractions of CO_2 and H_2O which results in an optically thin region. The streamline plot in Fig. 6.20(a) shows the recirculation region that fills most of the furnace. The large recirculation region has relatively lower temperature and higher mole fractions of CO_2 and H_2O which is an optically thick region. These two regions are indicated by the radial distributions of radiative properties at three axial locations plotted in Fig. 6.20(b).

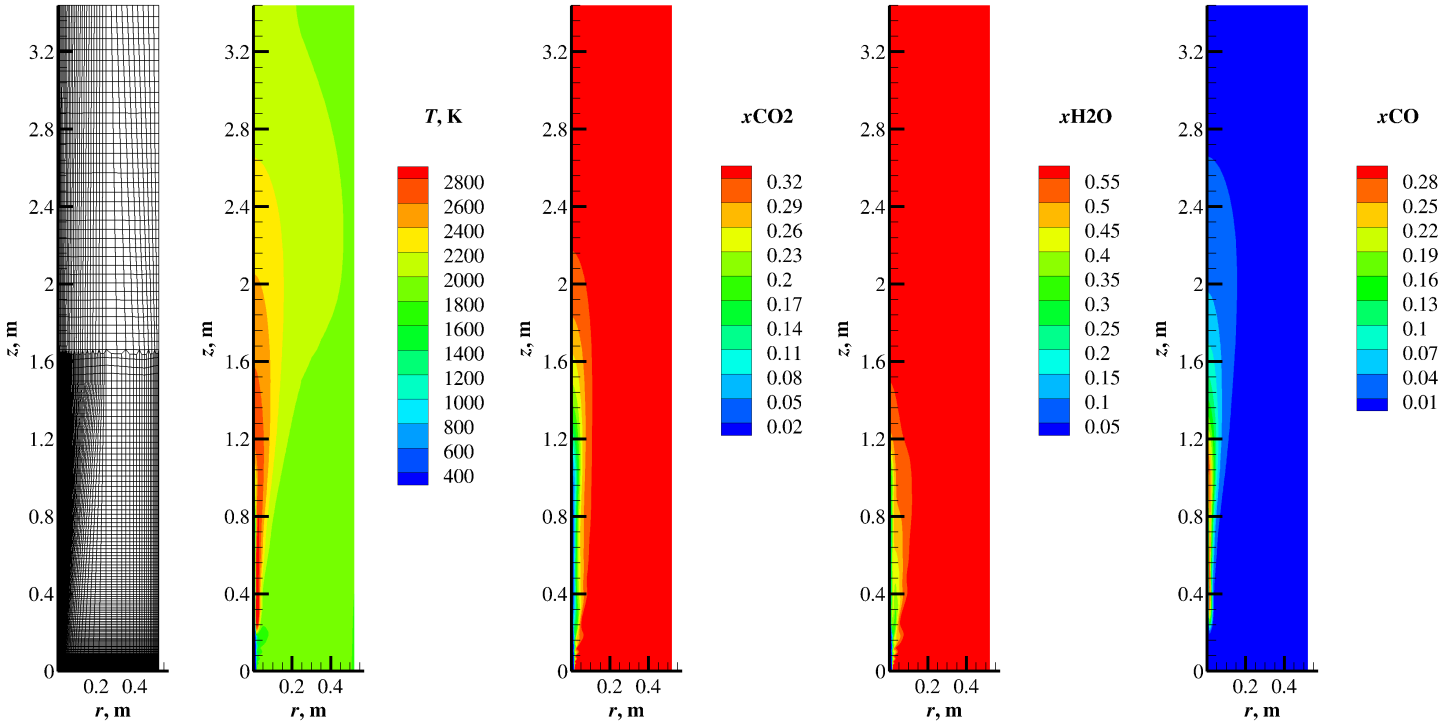

Figure 6.19: The temperature and model fraction fields for the snapshot study of a high-temperature oxy-natural gas furnace [254].

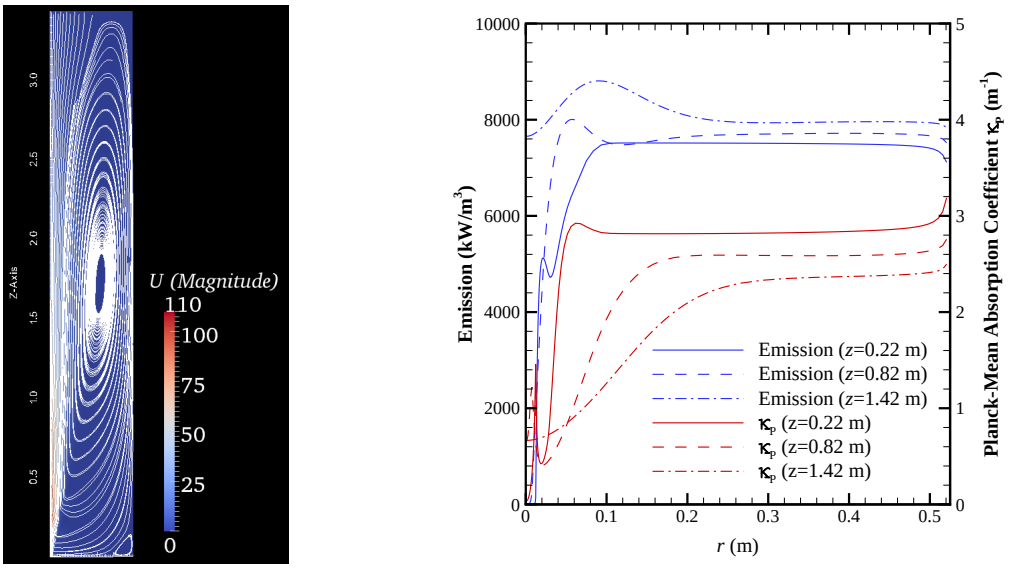

(a) (b)

Figure 6.20: (a) The streamline plot showing a large recirculation zone in the furnace and (b) the radial distributions of radiative properties at three axial locations.

The comparison of the calculated negative radiative heat sources ($\nabla \cdot \mathbf{q}$) from P_N and PMC solvers at three axial locations for the gray case is shown in Fig. 6.21. Since the same Planck-mean absorption coefficients are used, the differences between both P_N and PMC solvers are solely due to RTE in accuracies. The results show that the flame region close to the center has a negative $\nabla \cdot \mathbf{q}$ (positive radiative heat source) which indicates net absorption of radiative heat from the surroundings. At the axial location of $z = 0.22$ m, all P_N methods are found to perform well at the flame region close to the center. Compared with the PMC solution, P_1 predicts higher $\nabla \cdot \mathbf{q}$ in the recirculation region. P_3 improves P_1 results in the recirculation region to a large extent but is not very accurate at the interface of two regions around $r = 0.05$ m; P_5 and P_7 almost overlap the PMC results at this axial location. All P_N methods except P_1 are found to be almost identical to the PMC solutions at the axial location of $z = 0.82$ m. At $z = 1.42$ m, there is consistent improvement of accuracy from lower-order P_N methods to higher-order ones close to the center with P_7 almost catching the results of PMC.

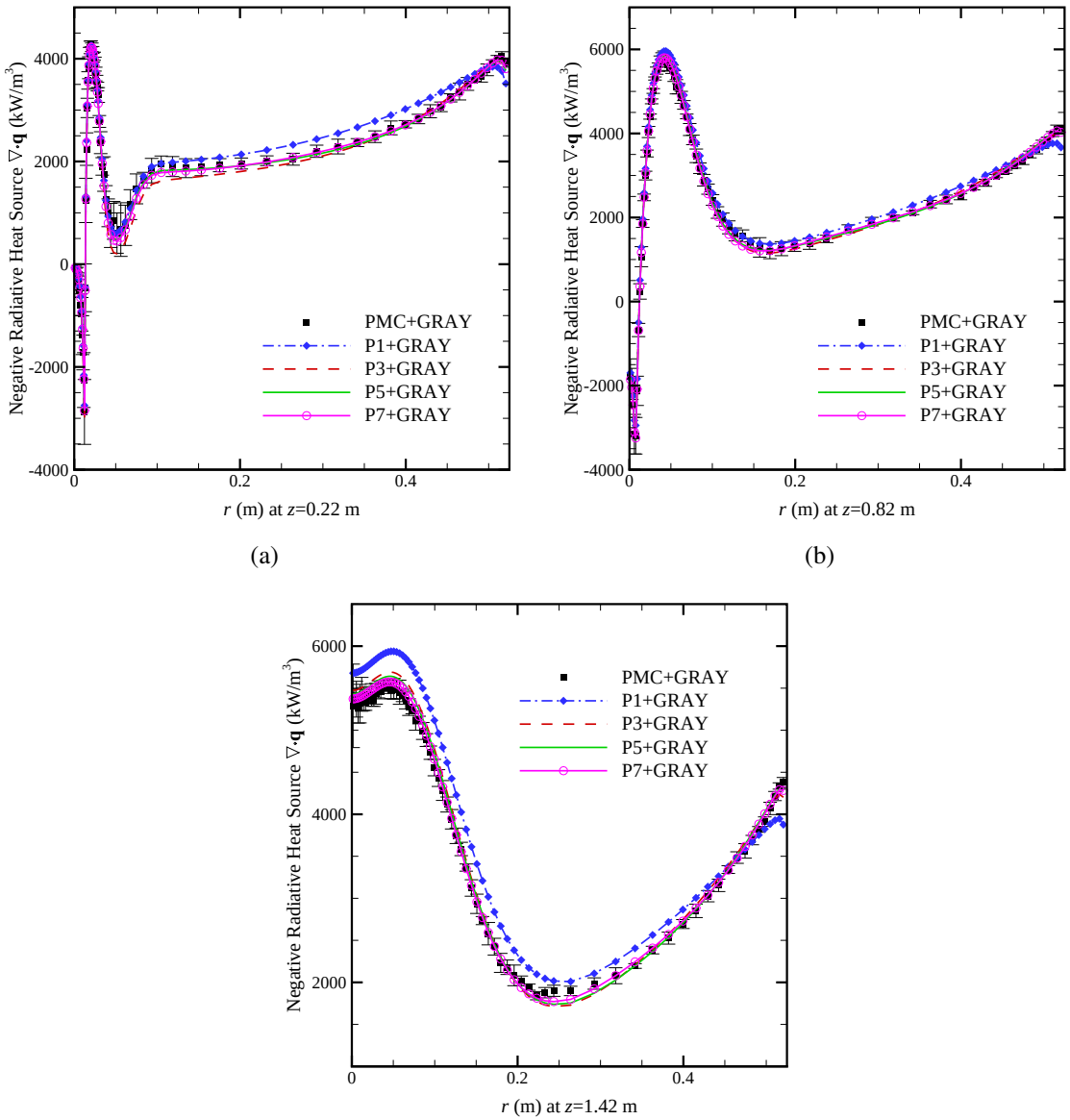

Figure 6.21: Comparison of negative radiative heat sources ($\nabla \cdot \mathbf{q}$) from P_N and PMC solvers at three axial locations for the gray case, (a) z = 0.22 m, (b) z = 0.82 m and (c) z = 1.42 m.

DOM results with four combinations of discrete polar and azimuthal ordinates for the gray case are presented in Fig. 6.22. For this problem, the results of DOM, especially $DOM_{2\times4}$ and $DOM_{4\times4}$ except for the $DOM_{2\times4}$ results in Fig. 6.22(a), are found to be less accurate than the P_1 and P_3 solvers. At the same time, $DOM_{4\times8}$ and $DOM_{8\times8}$ are found to be very accurate at all three locations compared with the PMC results.

Comparison of calculated negative radiative heat sources ($\nabla \cdot \mathbf{q}$) at the same axial locations for the nongray case is shown in Fig. 6.23 and Fig. 6.24. Compared with the gray results, more radiative heat is absorbed locally in the recirculation region so that the profile of $\nabla \cdot \mathbf{q}$ is flatter in the region $0.2 < r < 0.45$ m. The jump of $\nabla \cdot \mathbf{q}$ close to the boundary is due to a combined effect of the small drop of gas temperatures and a large increase of absorption coefficients close to the wall as shown in Fig. 6.20(b). All PN+FSK solvers perform very well compared with PMC+LBL results except that P_1 is slightly inaccurate. All DOM results are very accurate at the axial location of $z = 0.22$ m, which is shown in Fig. 6.24(a), while at the other two axial locations as shown in Fig. 6.24(b) for $z = 0.82$ m and Fig. 6.24(c) for $z = 1.42$ m, $DOM_{4\times8}$ and $DOM_{8\times8}$ perform well compared with PMC+LBL results but $DOM_{2\times4}$ and $DOM_{4\times4}$ results are still quite different from the PMC+LBL predictions and less accurate than that from the P_3 method.

The computational cost of different RTE solvers in this snapshot study is presented in Table 6.10. All computations are by a single 2.66 GHz Intel (R) Xeon (R) X7460 processor. PMC employed a total of 10 million photon bundles for the gray case and 100 million photon bundles for the nongray case. DOM is found to be still more efficient than P_N since there is no scattering involved and no wall reflections. Nevertheless, compared with the performance of high-order P_N solvers in the previous snapshot study of the jet flame (Table 6.9), the time cost of high-order P_N method for oxy-fuel flame simulation are much shorter even for this larger mesh.

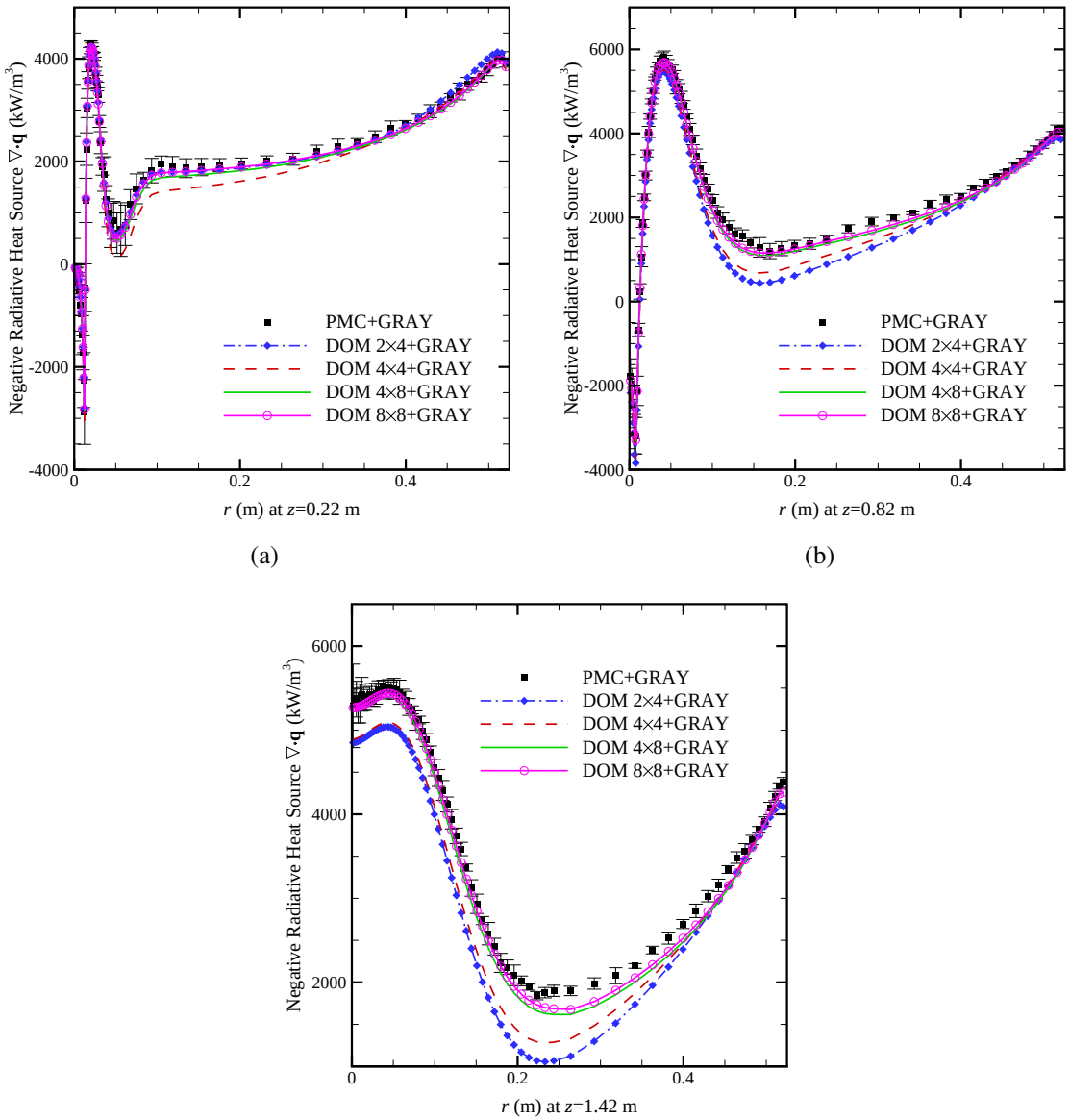

Figure 6.22: Comparison of negative radiative heat sources ($\nabla \cdot \mathbf{q}$) from DOM and PMC solvers at three axial locations for the gray case, (a) z = 0.22 m, (b) z = 0.82 m and (c) z = 1.42 m.

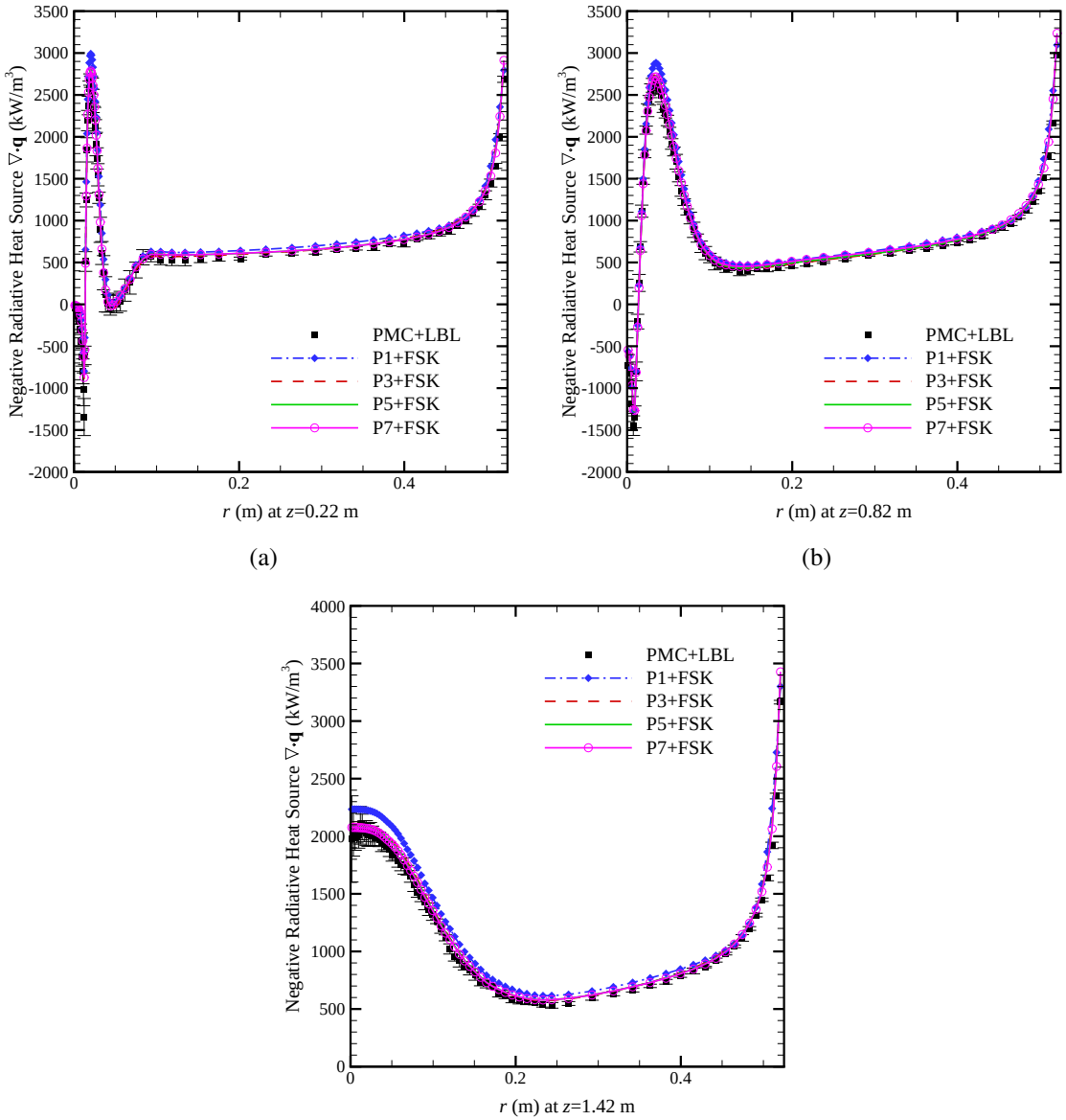

Figure 6.23: Comparison of negative radiative heat sources ($\nabla \cdot \mathbf{q}$) from P_N and PMC solvers at three axial locations for the nongray case, (a) z = 0.22 m, (b) z = 0.82 m and (c) z = 1.42 m.

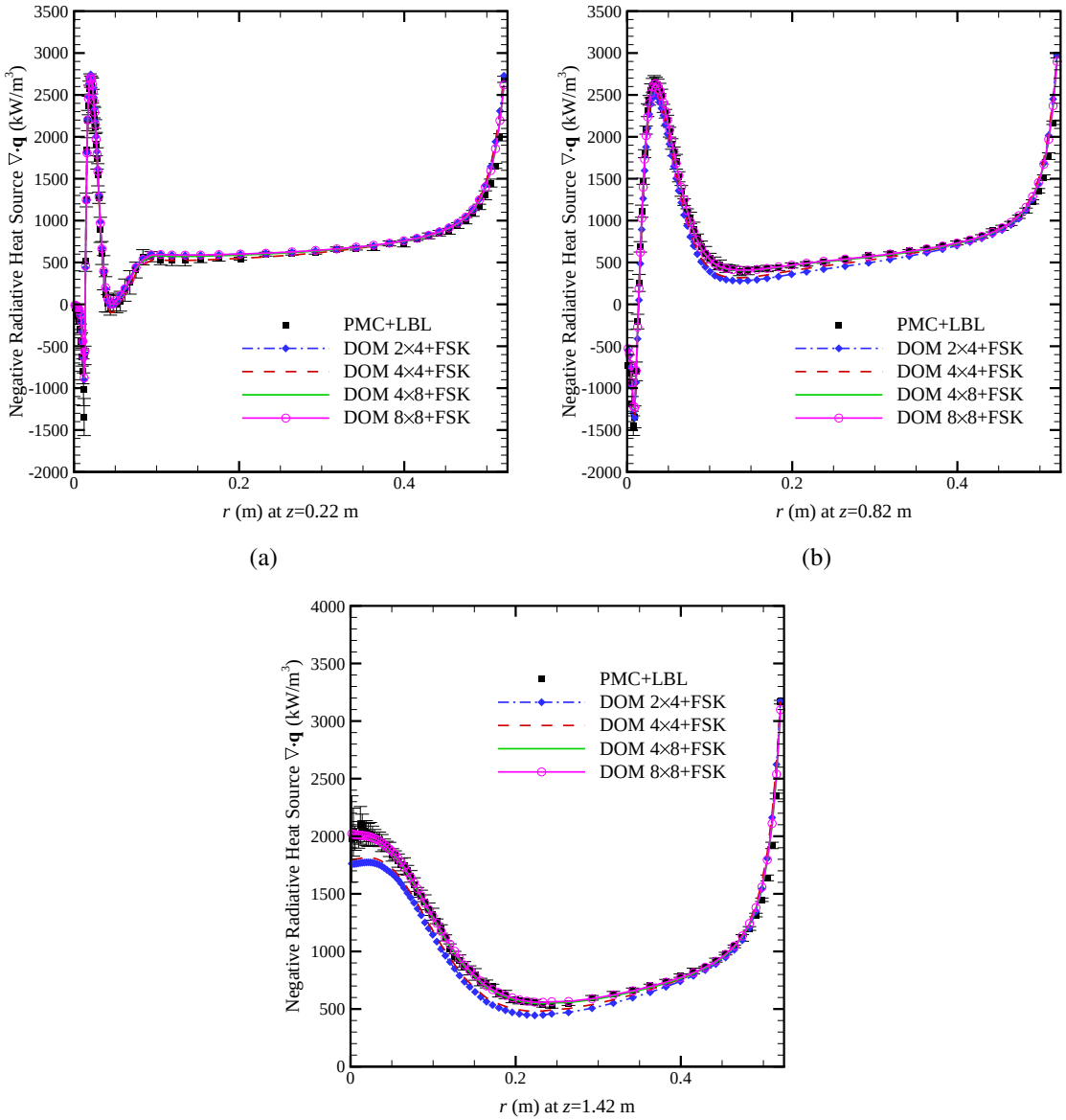

Figure 6.24: Comparison of negative radiative heat sources ($\nabla \cdot \mathbf{q}$) from DOM and PMC solvers at three axial locations for the nongray case, (a) z = 0.22 m, (b) z = 0.82 m and (c) z = 1.42 m.

Table 6.10: Comparison of CPU time (s) for RTE solvers for both the gray case and the nongray case

	P_1	P_3	P_5	P_7	$DOM_{2\times4}$	$DOM_{4\times4}$	$DOM_{4\times8}$	$DOM_{8\times8}$	PMC
Gray	0.22	2.95	10.2	27.8	4.53	5.45	6.66	13.9	223 (1M×10)
Nongray	0.95	12.8	49.7	111	13.1	25.8	39.4	77.5	1672 (10M×10)

In this section, a snapshot study was carried out for an oxy-natural gas flame. Results and computational costs show that the high-order P_N method is a very good tool to study such oxy-fuel flames. Although the benefits of high-order P_N methods such as P_5 and P_7 for the nongray simulations in this snapshot study are not obvious due to the large overall optical thickness, it can be deducted from the gray case that for a slightly optically thinner case (or a smaller oxy-fuel furnace), the high-order P_N methods would be the optimal choice for radiation simulations.

Chapter 7

Conclusions and Future Work

This chapter summarizes the research presented in this thesis on the topic of high-order spherical harmonics (P_N) methods for radiative heat transfer and applications in combustion simulations. Conclusions are drawn from this research and directions for further studies on the spherical harmonics P_N methods are also suggested.

7.1 Summary

This thesis started with a review of the second-order elliptic formulation of high-order P_N methods to the radiative transfer equation and described further development of special boundary conditions, their implementation in the finite volume-based library `OpenFOAM`® and their application in combustion simulations. Another goal of this research presented in this thesis has been to explore the accuracy and efficiency of the high-order P_N methods with emphasis on combustion-related conditions.

Chapter 1 presented a review of the importance of radiation in combustion simulations, radiative properties created by the combustion products, the radiative transfer equation (RTE), current numerical solution methods for the RTE and previous state-of-art of spherical harmonics P_N methods. Current status, difficulties and unsolved questions of these topics have been described. These

discussions provided the motivation for further exploring the high-order P_N method with regard to combustion simulations. Chapter 2 reviewed the second-order elliptic formulation of the high-order (P_N) method for general three-dimensional geometry. $N(N+1)/2$ second-order elliptic PDEs and the Marshak's boundary conditions have been formulated for arbitrary order of N. Compared to the first-order formulation with $(N+1)^2$ PDEs, the second-order formulation reduces the number of governing equations almost by half with a factor of $2(N+1)/N$. Marshak's boundary conditions have been extended to 3-D geometry for arbitrary order of N. Chapter 3 started with a review of further developments of high-order spherical harmonics P_N methods to 2-D geometries, including 2-D Cartesian geometry and 2-D axisymmetric geometry. Using the underlying geometric relationships of the intensity coefficients, the number of unknowns, governing equations and boundary conditions are reduced from $N(N+1)/2$ to $(N+1)^2/4$. Then, further development of special boundary conditions, including symmetry/specular reflection boundaries, walls with specified radiative flux, cyclic boundaries and mixed diffuse-specular surfaces are described. General formulations of these special boundary conditions for arbitrary order of P_N method in terms of intensity coefficients with even n have been developed. Chapter 4 discussed the spatial discretization of the resulting governing equations of the elliptic formulation of the high-order P_N methods (up to P_7) based on the finite volume-based software `OpenFOAM`® and the solution methods for both inner and outer iterations. The finite-volume implementations of Marshak's boundary conditions and the special boundary conditions have also been described in detail. A segregated solution sequence is employed, with which each governing equation is solved by the preconditioned conjugate gradient method, and outer iterations to resolve the coupling between the governing equations are by the Gauss-Seidel method.

Chapter 5 presented nine numerical examples in different geometries, validating the implementation as well as showing the accuracy and efficiency of the high-order P_N methods compared for a wide range of optical thicknesses and various distributions of gray radiative properties. Other reference solutions, including exact solutions through direct integration, Photon Monte Carlo (PMC)

method, analytical solutions of P_N for 1-D Cartesian geometry, finite difference method (FDM) solutions of the P_N method for 1-D cylindrical geometries and DOM are also used in different examples for comparison. The results have shown that the accuracy of high-order P_N methods are related to the overall optical thickness as well as the geometry of the problem. All P_N methods, including P_1, perform well for optically thick problem. For optically intermediate media, P_3 improves the accuracy from P_1 to a great extent. The accuracy gains from P_5 and P_7 depend on the specific case and are usually smaller than that from P_3 to P_1. For some extreme conditions, where the angular distributions of angular intensities are highly anisotropic, P_5 and P_7 are only marginally better than P_3. For optically thin media, although all P_N fail for prediction of incident radiation, they are able to predict correct radiative heat sources since there is very little self-absorption under such optical conditions. The efficiency of the P_N methods is also studied by these gray examples. The ideal CPU time is to have the time cost of different P_N methods proportional to the number of PDEs that are solved. However, the observed CPU time for these one-step simulations are far from that for optically thin and intermediate cases in multidimensional geometries. This is mostly due to the strong coupling between PDEs and a large number of outer iterations are required to obtain a converged result. In Chapter 6, the P_N methods are applied by coupling them with two combustion applications, including a turbulent jet flame and a high-temperature oxy-natural gas flame with nongray radiative media. A full-spectrum k-distribution spectral model is used to treat the nongray spectral properties of real gases, such as CO_2, H_2O and CO. For the simulations of turbulent jet flames, the RANS solver in `OpenFOAM`® was coupled with various radiation models to test the performances of high-order spherical harmonics (P_N) methods as well as to study the effects of radiation on this turbulent flame. Results from different orders of P_N methods (up to the order of 7) with the full-spectrum k-distribution (FSK) method as the spectral model were compared with line-by-line PMC calculations as well as with solutions from DOM. For the scalar predictions in coupled simulations, the P3+FSK solver is able to significantly improve the accuracy over P1+FSK results, but the improvements by P5+FSK and P7+FSK are limited and the results are still not accurate compared

with PMC+LBL results. A one-step snapshot study was also carried out to further investigate the performance of high-order P_N methods by isolating the radiation from the changing reacting flow fields. The results of the snapshot study show that high-order P_N methods are capable of obtaining the correct radiative heat source for the largest quadrature point and the small quadrature points but fail for the intermediate quadrature points. The computational costs of high-order P_N methods were also studied for both the coupled simulation and the snapshot study. Although the coupled PDEs from high-order P_N methods may take a long time to converge for the first few time steps, once initial convergence is reached, it only takes 1 or 2 outer iterations for the coupled PDEs of each quadrature for later time steps. In addition, the computational cost of high-order P_N methods can be further reduced by choosing a proper frequency for radiation evaluation. For the oxy-natural gas flame, only a frozen snapshot study was carried out to test the performance of high-order P_N method for analyzing radiative transfer within the oxy-natural gas furnace filled with the CO_2 and H_2O. The results showed that the high-order P_N method is a very good tool to study such flames in contrast to its performance in turbulent jet flames.

In terms of the choices of spectral models and RTE solvers for any specific flames, the most obvious factor is the size. For open jet flames of the sizes smaller than or similar to Sandia Flame D where the jet diameter is $d_j < 7.2$ mm, the optically thin model or even ignoring radiative transfer would probably be good enough for flame simulations. For open jet flames of size similar to Sandia Flame D×4, as shown in Section 6.2, one has to employ a nongray spectral model and high order RTE solvers or a line-by-line PMC solver. For flames enclosed by a furnace or a burner, such as the oxy-fuel flame shown in Section 6.3 or combustors of gas turbines where the CO_2 and H_2O fills the entire furnaces, the optically thin approximation would probably give wrong results. The P_N solver is expected to be preferable to PMC solutions in terms of computational cost due to larger emission from these flames. Fuel also plays an important role when choosing radiation models. For example, methane flames do not produce soot so that radiation is mostly from the gases, which are strongly nongray. Luminous flames such as ethylene flames produce certain amounts of soot, which

emits and absorbs radiation across the entire spectrum so that a gray spectral model may be feasible for analyzing radiative transfer. Since soot is always concentrated at certain locations, P_N methods may perform poorly for luminous flames. For other fuels such as hydrogen which does not produce CO_2, it is possible that the radiation effects will be lower than those from flames whose products include CO_2. For all the above flames, there is no scattering involved so that DOM with enough discrete ordinates (e.g., 8×8) is expected to be accurate for all these flames. However, DOM suffers from ray effects, false scattering and slow convergence in scattering media while scattering usually results in smoother profiles of intensities which are suitable for the P_N solvers. For simulations of such flames, e.g., rocket plumes, DOM is expected to perform poorly and inefficient compared with P_N solvers.

7.2 Future Work

Prospective areas, which need to be addressed in terms of future research and potential applications of current research will be discussed in this section.

Theoretical Study: Accuracy of the Spherical Harmonics Expansion

In this thesis, the angular distributions of intensities approximated by the truncated spherical harmonics were shown for some examples. It was found that truncated spherical harmonics expansions are incapable to approximate representative discontinuous functions (e.g., a Dirac δ function, a Heaviside step function, etc.). Two major questions are to be addressed: (1) What is the truncation error by neglecting all the intensity coefficient I_n^m with $n > N$ for both continuous and discontinuous functions? (2) What are the level of oscillations of the reconstructed intensity from the truncated spherical harmonics expansion of different orders? With these knowledges, one can probably find more desirable choices of spherical harmonics bases based on specific problems and extend maturer algorithms developed in Fourier-series analysis (e.g. Cesaro sums, Lanczos sigma factors, etc. [255]) to the spherical harmonics series to improve the accuracy and reduce the oscillations.

Also, in this way, one may be able to find a proper metric to evaluate the accuracy of RTE solvers regarding the angular profiles of radiative intensities.

Improvement of Solution Method: Preconditioning Matrix for Segregated P_N Solvers

In the implementation of P_N methods in this thesis, a Gauss-Seidel method is employed for the outer iterations, which is much slower converging than what is employed for the inner iterations: the Krylov-space based preconditioned conjugated-gradient method. As was discussed in Chapter 4, the number of outer iterations required is determined by the spectral radius of the full block matrix. Designing a preconditioning matrix **M** for the full matrix **A** is able to minimize the spectral radius. The preconditioning matrix has to satisfy two criteria: (1) the preconditioning matrix **M** itself can be efficiently inverted directly; (2) the spectral radius of the preconditioned coefficient matrix **A** has to be small. Practically, it is a process of rearranging the governing algebraic equations for better diagonal dominance for the resulting block-matrix. A proper preconditioning matrix will certainly improve the robustness and efficiency of the high-order P_N solvers.

Application: High-order P_N Methods for coupled simulations of multiphase reacting flows

In this thesis, the high-order P_N methods have been applied to two combustion problems: a turbulent jet flame and a high-temperature oxy-natural gas furnace. More studies are required to explore the strengths and weaknesses of the high-order P_N methods. In some multiphase reacting flow problems, e.g., in rocket plumes, scattering due to the particulate phase can be very strong. It is well known that DOM/FVM suffers ray effects, false scattering and slow convergence when dealing with such scattering media. In contrast, the high-order P_N methods are expected to perform very well with scattered intensity fields.

Application: High-order P_N Methods for phonon Boltzman Transport Equation

The main motivation of this thesis was to apply P_N methods for solving photon transport problems

in combustion simulations. Other physical processes, such as phonon transport problems governed by the Boltzman Transport Equation (BTE) are also direction dependent. Therefore, the high-order P_N methods discussed in this thesis can be formulated and implemented similarly for deterministic solutions of phonon transport problems as well.

Appendix A

Calculations of Half-moments of Associated Legendre Polynomials

The half-moments of associated Legendre polynomials $p^m_{n,j}$ is determined from the recursion relationship [147]:

If $n \neq j$:

$$p^m_{n,j} = \frac{(2n-1)\left[P^m_{n-1}(0)P^m_j(0) - (j-m+1)p^m_{n-1,j+1}\right] + (n+j-1)(n+m-1)p^m_{n-2,j}}{(n-j)(n-m)} \tag{A.1}$$

where the $P^m_n(0)$ are given by

$$P^m_n(0) = \begin{cases} 0 & n+m \quad \text{odd} \\ \dfrac{(-1)^{(n+m)/2}(n+m-1)!}{[(n+m)/2-1]!2^{n-1}\,[(n-m)/2]!} & n+m \quad \text{even} \end{cases} \tag{A.2}$$

When $n = j$

$$p^m_{n,n} = \frac{(n+m)!}{(2n+1)(n-m)!} \tag{A.3}$$

For nonsensical subscripts ($n < m$ or $j < m$), $p^m_{n,j} = 0$. For any given m, $p^m_{n,n}$ can be calculated from Eq. (A.3) first followed by the calculation of $p^m_{n,j}$, $n > j$ from Eq. (A.1).

When $n = j + 2$, Equation (A.1) becomes

$$p^m_{j+2,j} = \frac{-(2j+3)(j-m+1)p^m_{j+1,j+1} + (2j+1)(j+m+1)p^m_{j,j}}{2(j+2-m)} \tag{A.4}$$

where $p_{j+1,j+1}$ and $p_{j+1,j+1}$ can be calculated by Eq. (A.3), which leads to $p^m_{j+2,j} = 0$.

When $n = j + 4$,

$$p^m_{j+4,j} = \mathcal{H}_{j+4}p^m_{j+3,j+1} + \mathcal{G}_{j+4}p^m_{j+2,j} = 0 \tag{A.5}$$

where $\mathcal{H}$ and $\mathcal{G}$ are the coefficients. Since both $p^m_{j+3,j+1}$ and $p^m_{j+2,j}$ equal zero, the exact expressions of $\mathcal{H}$ and $\mathcal{G}$ are not necessary. The conclusion can be extended recursively for any $p^m_{n,j}$ with $n = j + 2k$, $k = 1, 2, 3, ...$,

$$p^m_{j+2k,j} = \mathcal{H}_{j+2k}p^m_{j+2k-1,j+1} + \mathcal{G}_{j+2k}p^m_{j+2k-2,j} = 0 \tag{A.6}$$

which can be better stated as Eq. (2.14).

Appendix B

Derivation of the Axisymmetric Formulation of P_N Method

This appendix is summarized and reorganized from the hand-written personal communications with the authors of [219].

The transformation of the P_N formulation in x-y-z Cartesian coordinate system to an axisymmetric formulation in r-z Cylindrical coordinate system is completed by (i) applying the geometric relations between the intensity coefficients $I_n^m(x, y, z)$ and $\hat{I}_n^m(r, z)$, Eq. (3.11) and (ii) converting the derivatives/operators in Cartesian coordinate system and derivatives/operators in Cylindrical coordinate system, Eqs. (3.12) and (3.20).

B.1 Governing Equations

Terms in Eq. (2.9) can be rearranged and grouped together to facilitate the derivation. The derivation of the governing equations for Y_n^m, Eq. (2.9a), is shown first, and the derivation of the governing equations for Y_n^{-m}, Eq. (2.9b), is similar to that of the former.

The terms of Eq. (2.9a) are grouped in the following manner:

$$\begin{aligned}\left(\mathcal{L}_{xx}+\mathcal{L}_{yy}\right) I^{m}_{n+4-2k} &= (\mathcal{L}_{rr}+\frac{1}{\beta r}\mathcal{L}_{r}+\frac{1}{r^2\beta^2}\frac{\partial^2}{\partial\phi^2})\cos m\phi \hat{I}^{m}_{n+4-2k} \\ &= \cos m\phi(\mathcal{L}_{rr}+\frac{1}{\beta r}\mathcal{L}_{r}-\frac{m^2}{r^2\beta^2})\hat{I}^{m}_{n+4-2k} \\ &= \cos m\phi \mathcal{A}^{+}_{m}\hat{I}^{m}_{n+4-2k} \end{aligned} \tag{B.1}$$

$$\begin{aligned}&\left(\mathcal{L}_{xx}-\mathcal{L}_{yy}\right) I^{m'}_{n+4-2k} \pm \left(\mathcal{L}_{xy}+\mathcal{L}_{yx}\right) I^{-m'}_{n+4-2k} \\ &= \cos(m'\mp 2)\phi\left\{\mathcal{L}_{rr}-\frac{1}{\beta r}\mathcal{L}_{r}+\frac{m'^2}{r^2\beta^2}\pm m'\left[\frac{2}{\beta r}\mathcal{L}_{r}-\frac{2}{\beta^2 r^2}+\frac{1}{r}\mathcal{L}_{r}\left(\frac{1}{\beta}\right)\right]\right\}\hat{I}^{m'}_{n+4-2k} \\ &= \cos(m'\mp 2)\phi(\mathcal{A}^{-}_{m'}\pm m'\mathcal{B})\hat{I}^{m'}_{n+4-2k}\end{aligned} \tag{B.2}$$

$$\begin{aligned}&\left(\mathcal{L}_{xz}+\mathcal{L}_{zx}\right) I^{m'}_{n+4-2k} \pm \left(\mathcal{L}_{yz}+\mathcal{L}_{zy}\right) I^{-m'}_{n+4-2k} \\ &= \cos(m'\pm 1)\phi\left\{\mathcal{L}_{rz}+\mathcal{L}_{zr}\mp m'\left[\frac{2}{\beta r}\mathcal{L}_{z}+\frac{1}{r}\mathcal{L}_{z}\left(\frac{1}{\beta}\right)\right]\right\}\bar{I}^{m'}_{n+4-2k} \\ &= \cos(m'\pm 1)\phi\left[C\mp m'\mathcal{D}\right]\bar{I}^{m'}_{n+4-2k}\end{aligned} \tag{B.3}$$

where $\mathcal{A}^{+}_{m}$, $\mathcal{A}^{-}_{m'}$, $\mathcal{B}$, C and $\mathcal{D}$ are simply shorthand symbols and m' is denoting $m-2$, $m-1$, etc. in the original governing equation. Applying Eqs. (B.1-B.3) to Eq. (2.9), we obtain

For each $Y_n^m : n = 0, 2, \ldots, N-1$; and $0 \le m \le n$

$$\begin{aligned}
\sum_{k=1}^{3} \Big\{ & (1+\delta_{m2}) a_k^{nm} \left[\cos m\phi (\mathcal{A}_{m-2}^{-} + (m-2)\mathcal{B}) \hat{I}_{n+4-2k}^{m-2} \right] \\
& + (1+\delta_{m1}) b_k^{nm} \left[\cos m\phi (C - (m-1)\mathcal{D}) \hat{I}_{n+4-2k}^{m-1} \right] \\
& + \frac{\delta_{m1}}{2} c_k^{nm} \left[\cos m\phi (\mathcal{A}_m^{-} + m\mathcal{B}) \hat{I}_{n+4-2k}^{m} \right] \\
& + d_k^{nm} \left[\cos m\phi (C + (m+1)\mathcal{D}) \hat{I}_{n+4-2k}^{m+1} \right] \\
& + e_k^{nm} \left[\cos m\phi (\mathcal{A}_{m+2}^{-} + (m+2)\mathcal{B}) \hat{I}_{n+4-2k}^{m+2} \right] \\
& + c_k^{nm} \cos m\phi \left(\mathcal{A}_m^{+} - 2\mathcal{L}_{zz} \right) \hat{I}_{n+4-2k}^{m} \Big\} \\
& + \cos m\phi (\mathcal{L}_{zz} - 1) \hat{I}_n^m = -(1-\omega) I_b \delta_{0n}
\end{aligned} \tag{B.4a}$$

similarly, for each $Y_n^{-m} : n = 0, 2, \ldots, N-1$; and $1 \le m \le n$:

$$\begin{aligned}
\sum_{k=1}^{3} \Big\{ & (1+\delta_{m2}) a_k^{nm} \left[\sin m\phi \left(\mathcal{A}_{m-2}^{-} + (m-2)\mathcal{B} \right) \hat{I}_{n+4-2k}^{m-2} \right] \\
& + (1+\delta_{m1}) b_k^{nm} \left[\sin m\phi \left(C - (m-1)\mathcal{D} \right) \hat{I}_{n+4-2k}^{m-1} \right] \\
& + \delta_{m1} c_k^{nm} \left[\sin m\phi \left(\mathcal{A}_m^{-} + m\mathcal{B} \right) \hat{I}_{n+4-2k}^{m} \right] \\
& + d_k^{nm} \left[\sin m\phi \left(C + (m+1)\mathcal{D} \right) \hat{I}_{n+4-2k}^{m+1} \right] \\
& + e_k^{nm} \left[\sin m\phi \left(\mathcal{A}_{m+2}^{-} + (m+2)\mathcal{B} \right) \hat{I}_{n+4-2k}^{m+2} \right] \\
& + c_k^{nm} \sin m\phi \left(\mathcal{A}_m^{+} - 2\mathcal{L}_{zz} \hat{I}_{n+4-2k}^{m} \right) \Big\} \\
& + \sin m\phi (\mathcal{L}_{zz} - 1) \hat{I}_n^m = 0.
\end{aligned} \tag{B.4b}$$

B.2 Boundary Conditions

The boundary conditions of the axisymmetric formulation can be derived by applying Eq. (3.11) to Eq. (2.24a) of $\bar{Y}_n^m$ with indices from Eq. (2.12). Observing the rotation matrices, Eq. (2.20), For $m \ge 0$ and $\alpha = \phi - \pi$, $\gamma = 0$, $\Psi_{-m}(0) = 0$ and $\Psi_m(0) = 1$, therefore

$$\bar{\Delta}_{m,m'}^{n} = \text{sign}(m') \Psi_{m'}(\pi - \phi) D'^{n}_{|m||m'|}(-\beta) \tag{B.5}$$

where

$$D'^{n}_{|m||m'|}(-\beta) = d^{n}_{|m|,|m'|}(-\beta) + (-1)^{m'} d^{n}_{|m|,-|m'|}(-\beta) \tag{B.6}$$

For $m' > 0$,

$$\bar{\Delta}^{n}_{m,m'} = \Psi_{m'}(\pi - \phi) D'^{n}_{|m||m'|}(-\beta) = \cos m'(\pi - \phi) D'^{n}_{|m||m'|}(-\beta) \tag{B.7}$$

$$\bar{\Delta}^{n}_{m,-m'} = -\Psi_{-m'}(\pi - \phi) D'^{n}_{|m||m'|}(-\beta) = -\sin m'(\pi - \phi) D'^{n}_{|m||m'|}(-\beta) \tag{B.8}$$

Therefore, together with Eq. (3.11), we obtain

$$\bar{\Delta}^{n}_{m,m'} I^{m'}_{n} + \Delta^{n}_{m,-m'} I^{-m'}_{n} = \cos \pi m' D'^{n}_{|m||m'|}(-\beta) = D^{n}_{|m||m'|}(-\beta) \hat{I}^{m'}_{n} \tag{B.9}$$

where $\cos \pi m' = (-1)^{m'}$.

Similarly, with $\gamma = 0$, $\alpha = \phi - \pi$ and $m < 0$, then $\Psi_{-m}(0) = 1$, $\Psi_{m}(0) = 0$, and $-\text{sign}(m) = 1$, the rotation matrices become

$$\bar{\Delta}^{n}_{m,m'} = \Psi_{-m'}(\pi - \phi) B'^{n}_{|m||m'|}(-\beta) \tag{B.10}$$

where

$$B'^{n}_{|m||m'|}(-\beta) = d^{n}_{|m|,|m'|}(-\beta) - (-1)^{m'} d^{n}_{|m|,-|m'|}(-\beta) \tag{B.11}$$

therefore,

$$\begin{aligned}
&\frac{\partial}{\partial \tau_{\bar{y}}} \left[\Delta^{n}_{m,m'} I^{m'}_{n} + \Delta^{n}_{m,-m'} I^{-m'}_{n} \right] \\
&= \frac{m'}{\beta r} \left[\sin m'(\pi - \phi) \sin m' \phi B'_{|m||m'|}(-\beta) - \left(\cos m'(\pi - \phi) \cos m' \phi B'_{|m||m'|}(-\beta) \right) \right] \hat{I}^{m'}_{n} \\
&= -\frac{m'}{\beta r} B_{|m||m'|}(-\beta) \hat{I}^{m'}_{n}
\end{aligned} \tag{B.12}$$

Appendix C

Note for Special Boundary Conditions

C.1 Reflections at the Wall in P_1 Approximation

When $N = 1$ and following Eq. (2.12), the Marshak's boundary conditions are characterized by the local spherical harmonics $\overline{Y}_1^0$, where $i = 1$ and $m = 0$. Substituting i and m together with values of $p_{0,1}^0 = 1/2$ and $p_{1,1}^0 = 1/3$, Equation (3.31) becomes

$$\frac{1}{2}(1 - \rho^s - \rho^d)I_0^0 + \frac{1}{3}(1 + \rho^s + \rho^d)\bar{I}_1^0 = \frac{1}{2}\epsilon I_{bw} \tag{C.1}$$

Replacing $\rho^s + \rho^d$ with $1 - \epsilon$ and applying the relation of $\bar{I}_1^0 = -\partial I_0^0/\partial\bar{\tau}_z$ from Eq. (2.31a), one simplifies Eq. (C.1) to

$$I_0^0 - \frac{2 - \epsilon}{\epsilon}\left(\frac{2}{3}\right)\frac{\partial I_0^0}{\partial\bar{\tau}_z} = I_{bw} \tag{C.2}$$

which is the Marshak's boundary condition for the P_1 approximation [21]. It can be concluded that there is no distinction between diffuse and specular reflections at reflective surfaces with the P_1 formulation.

C.2 Symmetry/Specular Boundaries

The boundary conditions for symmetry/specular boundaries can also be directly derived from Eq. (3.31), which is based on Marshak's boundary condition. When $\rho^s = 1$, Equation (3.31) becomes

$$\sum_{n=0}^{N} \left[1 - (-1)^{m+n}\right] p^m_{n,2i-1} \bar{I}^m_n = 0, \quad i = 1, 2, ..., \frac{1}{2}(N+1), \quad \text{all relevant } m \tag{C.3}$$

which does not lead to identity equations only when $m + n$ is odd. Thus it is useful to separate Eq. (C.3) for even and odd m, respectively, as

$$\sum_{l=0}^{(N-1)/2} p^m_{2l,2i-1} \bar{I}^m_{2l} = 0 \qquad \text{all relevant odd } m \tag{C.4a}$$

$$\sum_{l=1}^{(N+1)/2} p^m_{2l-1,2i-1} \bar{I}^m_{2l-1} = 0 \qquad \text{all relevant even } m \tag{C.4b}$$

$$i = 1, 2, ..., \frac{1}{2}(N+1)$$

where the relevant m are selected from Eq. (2.12). According to Eq. (2.14), $p^m_{2l-1,2i-1} = 0$ when $l \neq i$ because the sum of the subscripts of $p^m_{2l-1,2i-1}$, i.e., $2(l + i - 1)$, is even. For a given i, Eq. (C.4b) does not give an identity equation ($0 \equiv 0$) only when $l = i$. Therefore, Eq. (C.4b) leads to

$$\bar{I}^m_{2i-1} = 0 \quad i = 1, 2, ..., \frac{1}{2}(N+1), \quad \text{all relevant even } m \tag{C.5}$$

which, after applying the relationship between $\bar{I}^m_{2i-1}$ and surface normal derivatives of $\bar{I}^m_{2i}$ and $\bar{I}^m_{2i-2}$ [145], is Eq. (3.45a).

While Eq. (C.5) provides the boundary conditions for the even m, the boundary conditions for the odd m are to be obtained by Eq. (C.4a). Equation (2.13) that indicates $p^m_{2l,2i-1} = 0$ when $m > 2l$, can be applied to the expansion of Eq. (C.4a). For the case of P_3 with $N = 3$, Equation (C.4a) with

$i = 1$ and $m = \pm 1$ becomes

$$\sum_{l=0}^{1} p_{2l,1}^{\pm 1} \bar{I}_{2l}^{\pm 1} = 0$$

$$0 + p_{2,1}^{\pm 1} \bar{I}_{2}^{\pm 1} = 0$$

$$\bar{I}_{2}^{\pm 1} = 0 \tag{C.6}$$

For higher order of P_N, the rest of the boundary conditions can be developed similarly. For example, for the P_5 formulation with $N = 5$, the local spherical harmonics that characterize the Marshak's boundary conditions are $\overline{Y}_2^{\pm 1}$, $\overline{Y}_4^{\pm 1}$ and $\overline{Y}_4^{\pm 3}$, which lead to a set of equations from Eq. (C.4), which are

$2i - 1 = 2, m = \pm 1$

$$\sum_{l=0}^{2} p_{2l,2}^{1} \bar{I}_{2l}^{\pm 1} = 0$$

$$p_{2,2}^{1} \bar{I}_{2}^{\pm 1} + p_{4,2}^{1} \bar{I}_{4}^{\pm 1} = 0 \tag{C.7a}$$

$2i - 1 = 4, m = \pm 1$

$$\sum_{l=0}^{2} p_{2l,4}^{1} \bar{I}_{2l}^{\pm 1} = 0$$

$$p_{2,4}^{1} \bar{I}_{2}^{\pm 1} + p_{4,4}^{1} \bar{I}_{4}^{\pm 1} = 0 \tag{C.7b}$$

$2i - 1 = 6, m = \pm 3$

$$\sum_{l=0}^{2} p_{2l,4}^{3} \bar{I}_{2l}^{\pm 3} = 0$$

$$p_{4,4}^{3} \bar{I}_{4}^{\pm 3} = 0 \tag{C.7c}$$

Since all the remaining $p_{2l,2i-1}^{m}$ in Eq. (C.7) are nonzero, the corresponding boundary conditions are

obtained, which are $\bar{I}_2^{\pm 1} = 0$, $\bar{I}_4^{\pm 1} = 0$ and $\bar{I}_4^{\pm 3} = 0$.

As shown by the above examples, the resulting boundary conditions when m is odd are identical to Eq. (3.45b).

Bibliography

[1] Anderson, D. A., Tannehill, J. C., and Pletcher, R. H., 1984, *Computational Fluid Mechanics and Heat Transfer*, Hemisphere, New York.

[2] Launder, B. E. and Spalding, D. B., 1974, "The Numerical Computation of Turbulent Flows", *Computer Methods in Applied Mechanics and Engineering*, **3**, pp. 269–289.

[3] Pope, S. B., 2000, *Turbulent Flows*, Cambridge University Press, Cambridge.

[4] Westbrook, C. K., Mizobuchi, Y. P., Thierry, J., Smith, P. J., and Warnatz, J., 2005, "Computational Combustion", *Proceedings of the Combustion Institute*, **30**(1), pp. 125–157.

[5] Pitsch, H., 2006, "Large-Eddy Simulation of Turbulent Combustion", *Annual Review of Fluid Mechanics*, **38**, pp. 453–482.

[6] Modest, M. F. and Haworth, D. C., 2016, *Radiative Heat Transfer in Turbulent Combustion Systems*, Springer Verlag, New York.

[7] Imamori, Y., Hiraoka, K., Endo, H., and Oda, Y., 2011, "Combustion Simulations Contributing to the Development of Reliable Low-Emission Diesel Engines", *Mitsubishi Heavy Industries Technical Review*, **48**(1), p. 65.

[8] Sarofim, A. F. and Hottel, H. C., 1978, "Radiative Transfer in Combustion Chambers: Influ-

ence of Alternative Fuels", In *Proceedings of the Sixth International Heat Transfer Conference*, **6**, Washington, D.C., Hemisphere, pp. 199–217.

[9] Viskanta, R. and Mengüç, M. P., 1987, "Radiation Heat Transfer in Combustion Systems", *Progress in Energy and Combustion Science*, **13**, pp. 97–160.

[10] Nathan, G. J., Kalt, P. A. M., Alwahabi, Z. T., Dally, B. B., Medwell, P. R., and Chan, Q. N., 2012, "Recent Advances in the Measurement of Strongly Radiating, Turbulent Reacting Flows", *Progress in Energy and Combustion Science*, **38**(1), pp. 41–61.

[11] Jones, W. P. and Paul, M. C., 2005, "Combination of DOM with LES in a Gas Turbine Combustor", *International Journal of Engineering Science*, **43 (5–6)**, pp. 379–397.

[12] Schmitt, P., Poinsot, T., Schuermans, B., and Geigle, K. P., 2007, "Large-Eddy Simulation and Experimental Study of Heat Transfer, Nitric Oxide Emissions and Combustion Instability in a Swirled Turbulent High-Pressure Burner", *Journal of Fluid Mechanics*, **570**, pp. 17–46.

[13] Turns, S. R., 2000, *An Introduction to Combustion: Concepts and Applications*, McGraw-Hill, 2nd ed.

[14] Turns, S. R. and Myhr, F. H., 1991, "Oxides of Nitrogen Emissions from Turbulent Jet Flames: Part I – Fuel Effects and Flame Radiation", *Combustion and Flame*, **87**, pp. 319–355.

[15] Sivathanu, Y. R. and Gore, J. P., 1993, "Total Radiative Heat Loss in Jet Flames from Single Point Radiative Flux Measurements", *Combustion and Flame*, **94**(3), pp. 265–270.

[16] Molina, A., Schefer, R. W., and Houf, W. G., 2007, "Radiative Fraction and Optical Thickness in Large-Scale Hydrogen-Jet Fires", *Proceedings of the Combustion Institute*, **31**(2), pp. 2565–2572.

[17] Santos, A. and Costa, M., 2005, "Reexamination of the Scaling Laws for NO_x Emissions from Hydrocarbon Turbulent Jet Diffusion Flames", *Combustion and Flame*, **142**(1), pp. 160–169.

[18] Studer, E., Jamois, D., Jallais, S., Leroy, G., Hebrard, J., and Blanchetiere, V., 2009, "Properties of Large-Scale Methane/Hydrogen Jet Fires", *International Journal of Hydrogen Energy*, **34**(23), pp. 9611–9619.

[19] Hankinson, G. and Lowesmith, B. J., 2012, "A Consideration of Methods of Determining the Radiative Characteristics of Jet Fires", *Combustion and Flame*, **159**(3), pp. 781–786.

[20] Hu, L., Wang, Q., Delichatsios, M., Lu, S., and Tang, F., 2014, "Flame Radiation Fraction Behaviors of Sooty Buoyant Turbulent Jet Diffusion Flames in Reduced-and Normal Atmospheric Pressures and a Global Correlation with Reynolds Number", *Fuel*, **116**, pp. 781–786.

[21] Modest, M. F., 2013, *Radiative Heat Transfer*, Academic Press, New York, 3rd ed.

[22] Jeng, S. M., Lai, M. C., and Faeth, G. M., 1984, "Nonluminous Radiation in Turbulent Buoyant Axisymmetric Flames", *Combustion Science and Technology*, **40**, pp. 41–53.

[23] Faeth, G. M., Jeng, S. M., and Gore, J. P., 1985, "Radiation from Fires", In Lau, C. K., Jaluria, Y., and Miyasaka, K., eds., *Heat Transfer in Fire and Combustion Systems*, ASME, pp. 137–151.

[24] Gore, J. P., Jeng, S. M., and Faeth, G. M., 1987, "Spectral and Total Radiation Properties of Turbulent Carbon Monoxide/Air Diffusion Flames", *AIAA Journal*, **25**(2), pp. 339–345.

[25] Gore, J. P., Jeng, S. M., and Faeth, G. M., 1987, "Spectral and Total Radiation Properties of Turbulent Hydrogen/Air Diffusion Flames", *ASME Journal of Heat Transfer*, **109**, pp. 165–171.

[26] Faeth, G. M., Gore, J. P., Shuech, S. G., and Jeng, S. M., "Radiation from Turbulent Diffusion Flames", *Annual Review of Numerical Fluid Mechanics and Heat Transfer*.

[27] Faeth, G. M., Gore, J. P., Chuech, S. G., and Jeng, S. M., 1989, "Radiation from Turbulent Diffusion Flames", In *Annual Review of Numerical Fluid Mechanics and Heat Transfer*, **2**, Hemisphere, Washington, D.C., pp. 1–38.

[28] Zhu, X. L., Gore, J. P., Karpetis, A. N., and S., Barlow R., 2002, "The Effects of Self-Absorption of Radiation on an Opposed Flow Partially Premixed Flame", *Combustion and Flame*, **129**, pp. 342–345.

[29] Keramida, E. P., Liakos, H. H., Founti, M. A., Boudouvis, A. G., and Markatos, N. C., 2000, "Radiative Heat Transfer in Natural Gas-Fired Furnaces", *International Journal of Heat and Mass Transfer*, **43**(10), pp. 1801–1809.

[30] Stefanidis, G. D., Merci, B., Heynderickx, G. J., and Marin, G. B., 2007, "Gray/Nongray Gas Radiation Modeling in Steam Cracker CFD Calculations", *AIChE Journal*, **53**(7), pp. 1658–1669.

[31] Mehta, R. S., Modest, M. F., and Haworth, D. C., 2010, "Radiation Characteristics and Turbulence–Radiation Interactions in Sooting Turbulent Jet Flames", *Combust. Theory and Modelling*, **14**(1), pp. 105–124.

[32] Mazumder, S. and Modest, M. F., 1999, "A PDF approach to Modeling Turbulence–Radiation Interactions in Nonluminous Flames", *International Journal of Heat and Mass Transfer*, **42**, pp. 971–991.

[33] Li, G. and Modest, M. F., 2003, "Importance of Turbulence–Radiation Interactions in Turbulent Diffusion Jet Flames", *ASME Journal of Heat Transfer*, **125**, pp. 831–838.

[34] Pal, G., Gupta, A., Modest, M. F., and Haworth, D. C., 2015, "Comparison of Accuracy and Computational Expense of Radiation Models in Simulation of Nonpremixed Turbulent Jet Flames", *Combustion and Flame*, **162**(6).

[35] Ju, Y., Masuya, G., and Ronney, P. D., 1998, "Effects of Radiative Emission and Absorption on the Propagation and Extinction of Premixed Gas Flames", *Proceedings of the Combustion Institute*, **27**, pp. 2619–2626.

[36] Ebara, T., Iki, N., Takahashi, S., and Park, W., 2006, "Effect of Radiation Reabsorption on Laminar Burning Velocity of Methane Premixed Flame Containing with Steam and Carbon Dioxide", *JSME International Journal Series B Fluids and Thermal Engineering*, **49**(2), pp. 260–264.

[37] Frank, J. H., Barlow, R. S., and Lundquist, C., 2000, "Radiation and Nitric Oxide Formation in Turbulent Non-Premixed Jet Flames", *Proceedings of the Combustion Institute*, **28**, pp. 447–454.

[38] Masri, A. R., Bilger, R. W., and Dibble, R. W., 1988, "Turbulent Nonpremixed Flames of Methane near Extinction: Mean Structure from Raman Measurements", *Combustion and Flame*, **71**, pp. 245–266.

[39] Masri, A. R., Dibble, R. W., and Barlow, R. S., 1996, "The Structure of Turbulent Non-premixed Flames Revealed by Raman-Rayleigh-LIF Measurements", *Progress in Energy and Combustion Science*, **22**(4), pp. 307–362.

[40] Barlow, R. S. and Frank, J. H., 1998, "Effects of Turbulence on Species Mass Fractions in Methane/Air Jet Flames", *Proceedings of the Combustion Institute*, **27**, pp. 1087–1095.

[41] Li, G. and Modest, M. F., 2002, "Application of Composition PDF Methods in the Investigation of Turbulence–Radiation Interactions", *Journal of Quantitative Spectroscopy and Radiative Transfer*, **73**(2–5), pp. 461–472.

[42] Li, G. and Modest, M. F., 2005, "Numerical Simulation of Turbulence–Radiation Interactions in Turbulent Reacting Flows", In Sundeń, B. and Faghri, M., eds., *Modelling and Simulation of Turbulent Heat Transfer*, Ch. 3, WIT Press, Southampton, England, pp. 77–112.

[43] Coelho, P. J., 2007, "Numerical Simulation of the Interaction between Turbulence and Radiation in Reactive Flows", *Progress in Energy and Combustion Science*, **33**, pp. 311–383.

[44] Chang, H. and Charalampopoulos, T. T., 1990, "Determination of the Wavelength Dependence of Refractive Indices of Flame Soot", *Proceedings of the Royal Society (London) A*, **430**(1880), pp. 577–591.

[45] Adams, B. R. and Smith, P. J., 1995, "Modeling Effects of Soot and Turbulence–Radiation Coupling on Radiative Transfer in an Industrial Furnace", *ASME Combustion, Science and Technology Meeting*, **109**, p. 121.

[46] Wang, L., Haworth, D. C., Turns, S. R., and Modest, M. F., 2005, "Interactions among Soot, Thermal Radiation, and NOx Emissions in Oxygen-Enriched Turbulent Nonpremixed Flames: a CFD Modeling Study", *Combustion and Flame*, **141**(1-2), 170–179.

[47] Williams, A., Pourkashanian, M., and Jones, J. M., 2001, "Combustion of Pulverised Coal and Biomass", *Progress in Energy and Combustion Science*, **27**(6), pp. 587–610.

[48] Backstrom, D., Johansson, R., Andersson, K., Johnsson, F., Clausen, S., and Fateev, A., 2014, "Measurement and Modeling of Particle Radiation in Coal Flames", *Energy & Fuels*, **28**(3), pp. 2199–2210.

[49] Clements, A. G., Black, S., Szuhanszki, J., Stechly, K., Pranzitelli, A., Nimmo, W., and Pourkashanian, M., 2015, "LES and RANS of Air and Oxy-Coal Combustion in a Pilot-Scale Facility: Predictions of Radiative Heat Transfer", *Fuel*, **151**, pp. 146–155.

[50] Edge, P., Gubba, S. R., Ma., L., Porter, R., Pourkashanian, M., and Williams, A., 2011, "LES Modelling of Air and Oxy-Fuel Pulverised Coal Combustion—Impact on Flame Properties", *Proceedings of the Combustion Institute*, **33**, pp. 2709–2716.

[51] Cai, J. and Modest, M. F., 2014, "Absorption Coefficient Regression Scheme for Splitting Radiative Heat Sources across Phases in Gas-Particulate Mixtures", *Powder Technology*, **265**, pp. 76–82.

[52] Cai, J., Handa, M., and Modest, M. F., 2015, "Eulerian–Eulerian Multi-Fluid Methods for Pulverized Coal Flames with Nongray Radiation", *Combustion and Flame*, **162**(4), pp. 1550–1565.

[53] Cai, J., Zhao, X., Modest, M. F., and Haworth, D. C., 2015, "Nongray Radiation Modelings in Eulerian–Lagrangian Methods for Pulverized Coal Flames", In *Proceedings of the First Thermal and Fluids Engineering Summer Conference*.

[54] Marquez, R., Modest, M. F., and Cai, Jian, 2015, "Spectral Photon Monte Carlo With Energy Splitting Across Phases for Gas-Particle Mixtures", *ASME Journal of Heat Transfer*, **137**(12), p. 121012.

[55] Jones, W. P., Lyra, S., and Navarro-Martinez, S., 2012, "Numerical Investigation of Swirling Kerosene Spray Flames Using Large Eddy Simulation", *Combustion and Flame*, **159**, pp. 1539 – 1561.

[56] Tseng, C. C. and Viskanta, R., 2005, "Effect of Radiation Absorption on Fuel Droplet Evaporation", *Combustion Science and Technology*, **177**, pp. 1511–1542.

[57] Roy, S. P., Cai, J., and Modest, M. F., 2016, "A Multiphase Photon Monte Carlo Method for Combustion Simulations: Impact of Multiphase Radiation in High-Pressure Engine-Relevant Conditions", *Combustion Theory and Modelling*, submitted.

[58] Roy, S. P., Ge, W., Cai, J., and Modest, M. F., 2016, "Multiphase Radiative Heat Transfer Calculations in High-Pressure Spray Combustion Simulations", In *Proceedings of the 8th International Symposium on Radiative Transfer*, Cappdocia, Turkey.

[59] Howell, J. R. and Perlmutter, M., 1964, "Monte Carlo Solution of Thermal Transfer through Radiant Media between Gray Walls", *ASME Journal of Heat Transfer*, **86**(1), pp. 116–122.

[60] Howell, J. R. and Perlmutter, M., 1964, "Monte Carlo Solution of Thermal Transfer in a Non-grey Nonisothermal Gas with Temperature Dependent Properties", *AIChE Journal*, **10**(4), pp. 562–567.

[61] Perlmutter, M. and Howell, J. R., 1964, "Radiant Transfer through a Gray Gas Between Concentric Cylinders Using Monte Carlo", *ASME Journal of Heat Transfer*, **86**(2), pp. 169–179.

[62] Modest, M. F. and Poon, S. C., 1977, "Determination of Three-Dimensional Radiative Exchange Factors for the Space Shuttle by Monte Carlo", ASME paper no. 77-HT-49.

[63] Modest, M. F., 1978, "Determination of Radiative Exchange Factors for Three Dimensional Geometries with Nonideal Surface Properties", *Numerical Heat Transfer*, **1**, pp. 403–416.

[64] Walters, D. V. and Buckius, R. O., 1992, "Monte Carlo Methods for Radiative Heat Transfer in Scattering Media", In *Annual Review of Heat Transfer*, **5**, Hemisphere, New York, pp. 131–176.

[65] Howell, J. R., 1998, "The Monte Carlo Method in Radiative Heat Transfer", *ASME Journal of Heat Transfer*, **120**(3), pp. 547–560.

[66] Farmer, J. T. and Howell, J. R., 1998, "Comparison of Monte Carlo Strategies for Radiative Transfer in Participating Media", In Hartnett, J. P. and Irvine, T. F., eds., *Advances in Heat Transfer*, **31**, Academic Press, New York.

[67] Wong, B. T. and Mengüç, M. P., 2004, "Monte Carlo methods in Radiative Transfer and Electron-Beam Processing", *Journal of Quantitative Spectroscopy and Radiative Transfer*, **84**, pp. 437–450.

[68] Wang, A. and Modest, M. F., 2006, "Photon Monte Carlo Simulation for Radiative Transfer in Gaseous Media Represented by Discrete Particle Fields", *ASME Journal of Heat Transfer*, **128**, pp. 1041–1049.

[69] Wang, A. and Modest, M. F., April 2006, "An Adaptive Emission Model for Monte Carlo Ray-Tracing in Participating Media Represented by Statistical Particle Fields", In *Proceedings of Eurotherm Seminar 78*, Poitiers, France, Elsevier.

[70] Huang, B., Mielikainen, J., Oh, H., and Huang, H. A., 2011, "Development of a GPU-Based High-Performance Radiative Transfer Model for the Infrared Atmospheric Sounding Interferometer (IASI)", *Journal of Computational Physics*, **230**(6), pp. 2207–2221.

[71] Santos, P. D. and Lani, A., 2016, "An Object-Oriented Implementation of a Parallel Monte Carlo Code for Radiation Transport", *Computer Physics Communications*, **202**, pp. 233–261.

[72] Larsen, E. W. and Mercer, B., 1987, "Analysis of a Monte Carlo Method for Nonlinear Radiative Transfer", *Journal of Computational Physics*, **71**(1), pp. 50–64.

[73] Hottel, H. C. and Cohen, E. S., 1958, "Radiant Heat Exchange in a Gas-Filled Enclosure: Allowance for Nonuniformity of Gas Temperature", *AIChE Journal*, **4**, pp. 3–14.

[74] Lockwood, F. C. and Shah, N. G., 1981, "A New Radiation Solution Method for Incorporation in General Combustion Prediction Procedures", In *Eighteenth Symposium (International) on Combustion*, The Combustion Institute, pp. 1405–1409.

[75] Coelho, P. J. and Carvalho, M. G., 1997, "A Conservative Formulation of the Discrete Transfer Method", *ASME Journal of Heat Transfer*, **119**, pp. 118–128.

[76] Mishra, S. C., Kim, M. Y., and Maruyama, M., 2012, "Performance Evaluation of Four Radiative Transfer Methods in Solving Multi-Dimensional Radiation and/or Conduction Heat Transfer Problems", *International Journal of Heat and Mass Transfer*, **55**, pp. 5819–5835.

[77] Chandrasekhar, S., 1960, *Radiative Transfer*, Dover Publications, New York.

[78] Lee, C. E., 1962, "The Discrete S_N Approximation to Transport Theory", Technical Information Series Report LA2595, Lawrence Livermore Laboratory.

[79] Carlson, B. G. and Lathrop, K. D., 1968, "Transport Theory—The Method of Discrete Ordinates", In Greenspan, H., Kelber, C. N., and Okrent, D., eds., *Computing Methods in Reactor Physics*, Gordon & Breach, New York.

[80] Tsai, J. R., Özişik, M. N., and Santarelli, F., 1989, "Radiation in Spherical Symmetry with Anisotropic Scattering and Variable Properties", *Journal of Quantitative Spectroscopy and Radiative Transfer*, **42**(3), pp. 187–199.

[81] Chai, J. C., Lee, H. S., and Patankar, S. V., 1994, "Finite Volume Method for Radiation Heat Transfer", *Journal of Thermophysics and Heat Transfer*, **8**(3), pp. 419–425.

[82] 2011, *ANSYS FLUENT Computational Fluid Dynamics Software*, ANSYS Corp., Canonsburg, Pennsylvania.

[83] 2012, *COMSOL multiphysics user guide (Version 4.3 a)*, COMSOL Inc., Burlington, MA.

[84] Jasak, H., Jemcov, A., and Tukovic, Z., 2007, "OpenFOAM: A C++ Library for Complex Physics Simulations", In *International Workshop on Coupled Methods in Numerical Dynamics*, Dubrovnik, Croatia, IUC, pp. 1–20.

[85] Thynell, S. T., 1998, "Discrete-Ordinates Method in Radiative Heat Transfer", *International Journal of Engineering Science*, **36**(12), pp. 1651–1675.

[86] Chai, J. C., Lee, H. S., and Patankar, S. V., 1993, "Ray Effect and False Scattering in the Discrete Ordinates Method", *Numerical Heat Transfer – Part B: Fundamentals*, **24**, pp. 373–389.

[87] Coelho, P. J., 2002, "The Role of Ray Effects and False Scattering on the Accuracy of the Standard and Modified Discrete Ordinates Methods", *Journal of Quantitative Spectroscopy and Radiative Transfer*, **73(2–5)**, pp. 231–238.

[88] Tagne, K. and Herve, T., 2014, "Ray Effects Elimination in Discrete Ordinates and Finite Volume Methods", *ASME Journal of Heat Transfer*, **29**(2), pp. 306–318.

[89] McClarren, R. G. and Hauck, C. D., 2010, "Robust and Accurate Filtered Spherical Harmonics Expansions for Radiative Transfer", *Journal of Computational Physics*, **229**(16), pp. 5597–5614.

[90] Olfe, D. B., 1967, "A Modification of the Differential Approximation for Radiative Transfer", *AIAA Journal*, **5**(4), pp. 638–643.

[91] Modest, M. F., 1989, "The Modified Differential Approximation for Radiative Transfer in General Three-Dimensional Media", *Journal of Thermophysics and Heat Transfer*, **3**(3), pp. 283–288.

[92] Pal, G. and Modest, M. F., 2015, "Advanced Differential Approximation Formulation of the P_N Method for Radiative Transfer", *ASME Journal of Heat Transfer*, **137**(7), p. 072701.

[93] Jeans, J. H., 1917, "The Equations of Radiative Transfer of Energy", *Monthly Notices Royal Astronomical Society*, **78**, pp. 28–36.

[94] Eddington, A. S., 1926, *The Internal Constitution of the Stars*, Cambridge University Press, England, (also Dover Publications, New York, 1959).

[95] Murray, R. L., 1957, *Nuclear Reactor Physics*, Prentice Hall, Englewood Cliffs, NJ.

[96] Davison, B., 1958, *Neutron Transport Theory*, Oxford University Press, London.

[97] Weinberg, A. M., Wigner, P., and Wigner, E. K., 1958, *The physical Theory of Neutron Chain Reactors*, University of Chicago Press, Chicago.

[98] Meghreblian, R. V. and Holmes, D. K., 1960, *Reactor Analysis*, McGraw-Hill, New York.

[99] Mark, J. C., 1944, "The Spherical Harmonics Method, Part I", Technical Report Atomic Energy Report No. MT 92, National Research Council of Canada.

[100] Mark, J. C., 1945, "The Spherical Harmonics Method, Part II", Technical Report Atomic Energy Report No. MT 97, National Research Council of Canada.

[101] Marshak, R. E., 1947, "Note on the Spherical Harmonics Method as Applied to the Milne Problem for a Sphere", *Phys. Rev.*, **71**, pp. 443–446.

[102] Greenspan, H., Kelber, C. N., and Okrent, D., 1968, *Computing methods in reactor physics*, Gordon and Breach Science Publishers, New York.

[103] Kourganoff, V., 1963, *Basic Methods in Transfer Problems*, Dover Publications, New York.

[104] Pomraning, G. C. and Clark, M., 1963, "The Variational Method Applied to the Monoenergetic Boltzmann Equation. Part I", *Nuclear Science and Engineering*, **16**(2), pp. 147–154.

[105] Pomraning, G. C. and Clark, M., 1963, "The Variational Method Applied to the Monoenergetic Boltzmann Equation. Part II", *Nuclear Science and Engineering*, **16**(2), pp. 155–164.

[106] Davis, J. A., 1966, "Variational Vacuum Boundary Conditions for a PN Approximation", *Nuclear Science and Engineering*, **25**(2), pp. 189–197.

[107] Yvon, J, 1957, "La Diffusion Macroscopique des Neutrons une Methode d'Approximation", *Journal of Nuclear Energy*, **4**(3), pp. 305–318.

[108] Gelbard, E., Davis, J., and Pearson, J., 1959, "Iterative Solutions to the Pl and Double-Pl Equations", *Nuclear Science and Engineering*, **5**, pp. 36–44.

[109] Schmidt, E. and Gelbard, E. M., 1966, "A Double P_N Method for Spheres and Cylinders", *Trans. Am. Nucl. Soc.*, **9**, pp. 432–433.

[110] Wang, C., 1967, *Double Spherical Harmonics Approximation for Cylindrical and Spherical Geometries*, PhD thesis, University of Wisconsin–Madison.

[111] Cheng, P., 1965, *Study of the Flow of a Radiating Gas by a Differential Approximation*, PhD thesis, Stanford University, Stanford, CA.

[112] Cheng, P., 1966, "Dynamics of a Radiating Gas with Application to Flow Over a Wavy Wall", *AIAA Journal*, **4**(2), pp. 238–245.

[113] Arpaci, V. S. and Gozum, D., 1973, "Thermal Stability of Radiating Fluids: the Bénard Problem", *Physics of Fluids*, **16**(5), pp. 581–588.

[114] Canosa, J. and Penafiel, H. R, 1973, "A Direct Solution of the Radiative Transfer Equation: Application to Rayleigh and Mie Atmospheres", *Journal of Quantitative Spectroscopy and Radiative Transfer*, **13**(1), pp. 21–39.

[115] Dave, J. V. and Canosa, J., 1974, "A Direct Solution of the Radiative Transfer Equation: Application to Atmospheric Models with Arbitrary Vertical Nonhomogeneities", *Journal of the Atmospheric Sciences*, **31**(4), pp. 1089–1101.

[116] Bayazitoğlu, Y. and Higenyi, J., 1979, "The Higher-Order Differential Equations of Radiative Transfer: P_3 Approximation", *AIAA Journal*, **17**, pp. 424–431.

[117] Higenyi, J. K. D., 1980, *Higher Order Differential Approximation of Radiative Energy Transfer in a Cylindrical Gray Medium*, PhD thesis, Rice University.

[118] Tong, T. W. and Swathi, P. S., 1987, "Radiative Heat Transfer in Emitting–Absorbing–Scattering Spherical Media", *Journal of Thermophysics and Heat Transfer*, **1**(2), pp. 162–170.

[119] Ymeli, G. L. and Kamdem, H. T. T., 2015, "High-Order Spherical Harmonics Method for Radiative Transfer in Spherically Symmetric Problems", *Computational Thermal Sciences: An International Journal*, **7**(4), pp. 353–371.

[120] Ou, S. C. S. and Liou, K. N., 1982, "Generalization of the Spherical Harmonic Method to Radiative Transfer in Multi-Dimensional Space", *Journal of Quantitative Spectroscopy and Radiative Transfer*, **28**(4), pp. 271–288.

[121] Condiff, D., 1987, "Anisotropic Scattering in Three Dimensional Differential Approximation of Radiation Heat Transfer", In *Fundamentals and Applications of Radiation Heat Transfer*, **HTD-72**, ASME, pp. 19–29.

[122] Brenner, H., 1967, "The Stokes Resistance of a Slightly Deformed Sphere — II Intrinsic Resistance Operators for an Arbitrary Initial Flow", *Chemical Engineering and Science*, **22**, p. 375.

[123] Ratzel, A. C., 1981, *PN Differential Approximation for Solution of One–and Two–Dimensional Radiation and Conduction Energy Transfer in Gray Participating Media*, PhD thesis, University of Texas at Austin.

[124] Ratzel, A. C. and Howell, J. R., 1983, "Two-Dimensional Radiation in Absorbing–Emitting–Scattering Media Using the P-N Approximation", *ASME Journal of Heat Transfer*, **105**, pp. 333–340.

[125] Mengüç, M. P. and Viskanta, R., 1985, "Radiative Transfer in Three-Dimensional Rectangular Enclosures Containing Inhomogeneous, Anisotropically Scattering Media", *Journal of Quantitative Spectroscopy and Radiative Transfer*, **33**(6), pp. 533–549.

[126] Mengüç, M. P., 1985, *Modeling of Radiative Heat Transfer in Multidimensional Enclosures Using Spherical Harmonics Approximation*, PhD thesis, Purdue University.

[127] Mengüç, M. P. and Viskanta, R., 1986, "Radiative Transfer in Axisymmetric, Finite Cylindrical Enclosures", *ASME Journal of Heat Transfer*, **108**, pp. 271–276.

[128] Maeder, C., 1968, "A Three-Dimensional PN Spherical Harmonics Theory in Cylindrical Geometry", *Nuclear Science and Engineering*, **33**(1), pp. 128–138.

[129] Nakamura, S., 1972, "New Formulation and Coarse–Mesh Acceleration for Two–Dimensional DSN and PN Methods", In *Proc. Seminar on Numerical Reactor Calculations*, Vienna, Austria, IAEA.

[130] Blomquist, R. N. and Lewis, E. E., 1980, "A Rigorous Treatment of Transverse Buckling Effects in Two-Dimensional Neutron Transport Computations", *Nuclear Science and Engineering*, **73**(2), pp. 125–139.

[131] Ziver, A. K. and Goddard, A. J. H., 1981, "A Finite Element Method for Multigroup Diffusion-Transport Problems in Two Dimensions", *Annals of Nuclear Energy*, **8**(11–12), pp. 489–698.

[132] Fenstermacher, T. E., 1981, *Method of Solution of the Neutron Transport Equation in Multidimensional Cartesian Geometries Using Spherical Harmonics and Spatially Orthogonal Polynomials*, PhD thesis, University of Maryland.

[133] Fletcher, J. K., 1977, "The Solution of the Time-Independent Multi-Group Neutron Transport Equation Using Spherical Harmonics", *Annals of Nuclear Energy*, **4**(9), pp. 401–405.

[134] Fletcher, J. K., 1983, "The Solution of the Multigroup Neutron Transport Equation Using Spherical Harmonics", *Nuclear Science and Engineering*, **84**(1), pp. 33–46.

[135] Fletcher, J. K., 1986, "Recent Developments of the Transport Theory Code MARC/PN", *Progress in Nuclear Energy*, **18**(1), pp. 75–83.

[136] Fletcher, J. K., 1986, "A Solution of the Multigroup Transport Equation using Spherical Harmonics", *Transport Theory and Statistical Physics*, **15**(1-2), pp. 157–179.

[137] Kobayashi, K., Oigawa, H., and Yamagata, H., 1986, "The spherical harmonics method for the multigroup transport equation in x–y geometry", *Annals of Nuclear Energy*, **13**(12), pp. 663–678.

[138] Kobayashi, K., 1988, "An Acceleration Method of the Iteration Calculation Using the Padé Approximation in the Spherical Harmonics Method", *Annals of Nuclear Energy*, **15**(5), pp. 236–240.

[139] Inanc, F., 1989, *A Modular Nodal Method for Solving the Neutron Transport Equation Using Spherical Harmonics in Two Dimensions*, PhD thesis, Iowa State University.

[140] Inanc, F., 1992, "Coefficients of Second Order Spherical Harmonic Equations Using Automatic Generation", *Annals of Nuclear Energy*, **19**(1), pp. 39–50.

[141] Khouaja, H., Edwards, D. R., and Tsoulfanidis, N., 1997, "Spherical Harmonics-Finite Element Treatment of Neutron Transport in Cylindrical Geometry", *Annals of Nuclear Energy*, **24**(7), pp. 515–531.

[142] Brunner, T. A., 2000, *Riemann Solvers for Time-Dependent Transport Based on the Maximum Entropy and Spherical Harmonics Closures*, PhD thesis, University of Michigan.

[143] Brunner, T. A. and Holloway, J. P., 2001, "One-Dimensional Riemann Solvers and the Maximum Entropy Closure", *Journal of Quantitative Spectroscopy and Radiative Transfer*, **69**(5), pp. 543–566.

[144] Eaton, M. D., 2007, *A High-Resolution Riemann Method for Solving Radiation Transport Problems on Unstructured Meshes*, PhD thesis, University of London.

[145] Modest, M. F. and Yang, J., 2008, "Elliptic PDE Formulation and Boundary Conditions of the Spherical Harmonics Method of Arbitrary Order for General Three-Dimensional Geometries", *Journal of Quantitative Spectroscopy and Radiative Transfer*, **109**, pp. 1641–1666.

[146] Yang, J. and Modest, M. F., 2007, "High-Order *P-N* Approximation for Radiative Transfer in Arbitrary Geometries", *Journal of Quantitative Spectroscopy and Radiative Transfer*, **104**(2), pp. 217–227.

[147] Modest, M. F., 2012, "Further Developments of the Elliptic P_N-Approximation Formulation and its Marshak Boundary Conditions", *Numerical Heat Transfer – Part B: Fundamentals*, **62**(2–3), pp. 181–202.

[148] Ravishankar, M., Mazumder, S., and A., Kumar., 2010, "Finite-Volume Formulation and Solution of the P_3 Equations of Radiative Transfer on Unstructured Meshes", *ASME Journal of Heat Transfer*, **132**(2), p. 023402.

[149] Ravishankar, M., 2009, "Spherical Harmonics Based Techniques for Solution of the Radiative Transfer Equation", Master's thesis, The Ohio State University.

[150] Ge, W., Marquez, R., Modest, M. F., and Roy, S. P., 2015, "Implementation of High Order Spherical Harmonics Methods for Radiative Heat Transfer on OpenFOAM", *ASME Journal of Heat Transfer*, **137**(5), p. 052701.

[151] Ge, W., Modest, M. F., and Marquez, R., 2015, "Two-dimensional Axisymmetric Formulation of High Order Spherical Harmonics Methods for Radiative Heat Transfer", *Journal of Quantitative Spectroscopy and Radiative Transfer*, **156**, pp. 58–66.

[152] Roy, S. P., Cai, J., Ge, W., and Modest, M. F., 2015, "Computational Cost and Accuracy Comparison of Radiation Solvers with Emphasis on Combustion Simulations", In *Proceedings of CHT-15. 6th International Symposium on ADVANCES IN COMPUTATIONAL HEAT TRANSFER*, Rutgers University, New Brunswick, NJ, USA, Begell House Inc.

[153] Ge, W., Modest, M. F., and Roy, S. P., 2016, "Development of High-Order PN Models for Radiative Heat Transfer in Special Geometries and Boundary Conditions", *Journal of Quantitative Spectroscopy and Radiative Transfer*, **172**, pp. 98–109.

[154] Ge, W., T., Ren, Modest, M. F., Roy, S., and Haworth, D. C., 2017, "Application of High-Order Spherical Harmonics Methods for Radiative Transfer in Simulation of a Turbulent Jet Flame", In *Proceedings of CHT-17. 7th International Symposium on ADVANCES IN COMPUTATIONAL HEAT TRANSFER*, Napoli, Italy.

[155] McClarren, R. G. and Hauck, C. D., 2010, "Simulating Radiative Transfer with Filtered Spherical Harmonics", *Physics Letters A*, **374**(22), pp. 2290–2296.

[156] Boyd, J. P., 2000, *Chebyshev and Fourier Spectral Methods*, Dover Publications, New York.

[157] Ryan, W. H. and Elaine, S. O., 2015, "Effect of Radiation on the Propagation of Planar Coal Dust Flames in Air", In *Proceedings of the 25th international colloquium on the dynamics of explosions and reactive systems*, Leeds, UK.

[158] Taine, J., 1983, "A Line-by-Line Calculation of Low-Resolution Radiative Properties of CO_2–CO–Transparent Nonisothermal Gases Mixtures up to 3000 K", *Journal of Quantitative Spectroscopy and Radiative Transfer*, **30**(4), pp. 371–379.

[159] Hartmann, J.-M., Levi Di Leon, R., and Taine, J., 1984, "Line-by-Line and Narrow-Band Statistical Model Calculations for H_2O", *Journal of Quantitative Spectroscopy and Radiative Transfer*, **32**(2), pp. 119–127.

[160] Rothman, L. S., Gordon, I. E., Barber, R. J., Dothe, H., Gamache, R. R., Goldman, A., Perevalov, V. I., Tashkun, S. A., and Tennyson, J., 2010, "HITEMP, the High-Temperature Molecular Spectroscopic Database", *Journal of Quantitative Spectroscopy and Radiative Transfer*, **111**(15), pp. 2139–2150.

[161] Rothman, L. S., Gordon, I. E., Babikov, Y., Barbe, A., Benner, D. Chris, Bernath, P. F., Birk, M., Bizzocchi, L., Boudon, V., Brown, L. R., Campargue, A., Chance, K., Cohen, E. A., Coudert, L. H., Devi, V. M., Drouin, B. J., Fayt, A., Flaud, J.-M., Gamache, R. R., Harrison, J. J., Hartmann, J.-M., Hill, C., Hodges, J. T., Jacquemart, D., Jolly, A., Lamouroux, J., Roy, R. J. Le, Li, G., Long, D. A., Lyulin, O. M., Mackie, C. J., Massie, S. T., Mikhailenko, S., Mller, H. S. P., Naumenko, O. V., Nikitin, A. V., Orphal, J., Perevalov, V., Perrin, A., Polovtseva, E. R., Richard, C., Smith, M. A. H., Starikova, E., Sung, K., Tashkun, S., Tennyson, J., Toon, G. C., Tyuterev, Vl. G., and Wagner, G., 2013, "The HITRAN 2012 Molecular Spectroscopic Database", *Journal of Quantitative Spectroscopy and Radiative Transfer*, **130**, pp. 4–50.

[162] Tashkun, S. A. and Perevalov, V. I., 2011, "CDSD-4000: High-Resolution, High-Temperature Carbon Dioxide Spectroscopic Databank", *Journal of Quantitative Spectroscopy and Radiative Transfer*, **112**(9), pp. 1403–1410, available from ftp://ftp.iao.ru/pub/CDSD-4000.

[163] Ren, T., 2015, *Determination of Temperature and Concentration from Radiometric Measurements in Combustion Systems*, PhD thesis, University of California, Merced.

[164] Arking, A. and Grossman, K., 1972, "The Influence of Line Shape and Band Structure on Temperatures in Planetary Atmospheres", *Journal of the Atmospheric Sciences*, **29**, pp. 937–949.

[165] Denison, M. K. and Webb, B. W., 1993, "A Spectral Line Based Weighted-Sum-of-Gray-

gases Model for Arbitrary RTE Solvers", *ASME Journal of Heat Transfer*, **115**, pp. 1004–1012.

[166] Pierrot, L., Rivière, Ph., Soufiani, A., and Taine, J., 1999, "A Fictitious-gas-based Absorption Distribution Function Global Model for Radiative Transfer in Hot Gases", *Journal of Quantitative Spectroscopy and Radiative Transfer*, **62**, pp. 609–624.

[167] Modest, M. F., 2003, "Narrow-Band and Full-Spectrum *k*-Distributions for Radiative Heat Transfer—Correlated-*k* vs. Scaling Approximation", *Journal of Quantitative Spectroscopy and Radiative Transfer*, **76**(1), pp. 69–83.

[168] Zhang, H. and Modest, M. F., 2002, "A Multi-Scale Full-Spectrum Correlated-*k* Distribution For Radiative Heat Transfer in Inhomogeneous Gas Mixtures", *Journal of Quantitative Spectroscopy and Radiative Transfer*, **73**(2–5), pp. 349–360.

[169] Wang, A. and Modest, M. F., 2005, "High-Accuracy, Compact Database of Narrow-Band *k*-Distributions for Water Vapor and Carbon Dioxide", *Journal of Quantitative Spectroscopy and Radiative Transfer*, **93**, pp. 245–261.

[170] Cai, J. and Modest, M. F., 2013, "Improved Full-Spectrum *k*-Distribution Implementation for Inhomogeneous Media Using a Narrow-Band Database", *Journal of Quantitative Spectroscopy and Radiative Transfer*, **141**, pp. 65–72.

[171] Modest, M. F. and Riazzi, R. J., 2005, "Assembly of Full-Spectrum *k*-Distributions from a Narrow-Band Database; Effects of Mixing Gases, Gases and Nongray Absorbing Particles, and Mixtures with Nongray Scatterers in Nongray Enclosures", *Journal of Quantitative Spectroscopy and Radiative Transfer*, **90**(2), pp. 169–189.

[172] Cai, J., Marquez, R., and Modest, M. F., 2014, "Comparisons of Radiative Heat Transfer Calculations in a Jet Diffusion Flame Using Spherical Harmonics and *k*-Distributions", *ASME Journal of Heat Transfer*, **136**, p. 112702.

[173] Wang, C., Ge, W., Modest, M. F., and He, B., 2016, "A Full-Spectrum *k*-Distribution Look-Up Table for Radiative Transfer in Nonhomogeneous Gaseous Media", *Journal of Quantitative Spectroscopy and Radiative Transfer*, **168**, pp. 46–56.

[174] Wang, C., Modest, M. F., and He, B., 2016, "Full-Spectrum *k*-Distribution Look-Up Table for Nonhomogeneous Gas-Soot Mixtures", *Journal of Quantitative Spectroscopy and Radiative Transfer*, **176**, pp. 129–136.

[175] Wang, C., Modest, M. F., and He, B., 2016, "Improvement of Full-Spectrum *k*-Distribution Method Using Quadrature Transformation", *International Journal of Thermal Science*, **108**, pp. 100–107.

[176] Singer, J. M. and Grumer, J., 1959, "Carbon Formation in Very Rich Hydrocarbon–Air Flames—I: Studies of Chemical Content, Temperature, Ionization and Particulate Matter", In *Seventh Symposium (International) on Combustion*, The Combustion Institute, pp. 559–572.

[177] Wersborg, B. L., Howard, J. B., and Williams, G. C., 1972, "Physical Mechanisms in Carbon Formation in Flames", In *Fourteenth Symposium (International) on Combustion*, The Combustion Institute, pp. 929–940.

[178] Kunugi, M. and Jinno, H., 1966, "Determination of Size and Concentration of Soot Particles in Diffusion Flames by a Light-Scattering Technique", In *Eleventh Symposium (International) on Combustion*, The Combustion Institute, pp. 257–266.

[179] Sarofim, A. F. and Hottel, H. C., 1978, "Radiative Transfer in Combustion Chambers: Influence of Alternative Fuels", In *Proceedings of the Sixth International Heat Transfer Conference*, **6**, Washington, D.C., Hemisphere, pp. 199–217.

[180] Pagni, P. J. and Okoh, C. I., 1985, "Soot Generation within Radiating Diffusion Flames", In *Twentieth Symposium (International) on Combustion*, **20**, Elsevier, pp. 1045–1054.

[181] Becker, A., 1909, *Annalen der Physik*, **28**, p. 1017.

[182] Millikan, R. C., 1961, "Optical Properties of Soot", *Journal of the Optical Society of America*, **51**, pp. 698–699.

[183] Millikan, R. C., 1961, "Sizes, Optical Properties and Temperatures of Soot Particles", In *The Fourth Symposium on Temperature, Its Measurement and Control in Science and Industry*, **3**, pp. 497–507.

[184] Minutolo, P., Gambi, G., and D'alessio, A., 1996, "The Optical Band Gap Model in the Interpretation of the UV-Visible Absorption Spectra of Rich Premixed Flames", In *Twenty-Sixth Symposium (International) on Combustion*, **26**, Elsevier, pp. 951–957.

[185] Gaydon, A. G. and Wolfhard, H. G., *Flames: Their Structure, Radiation and Temperature*, 3rd ed.

[186] Köylü, Ü.Ö. and Faeth, G. M., May 1993, "Radiative Properties of Flame-Generated Soot", *ASME Journal of Heat Transfer*, **115**(2), pp. 409–417.

[187] Manickavasagam, S. and Mengüç, M. P., 1997, "Scattering Matrix Elements of Fractal-Like Soot Agglomerates", *Journal of Applied Physics*, **36**(6), pp. 1337–1351.

[188] Tien, C. L. and Drolen, B. L., 1987, "Thermal Radiation in Particulate Media with Dependent and Independent Scattering", In *Annual Review of Numerical Fluid Mechanics and Heat Transfer*, **1**, Hemisphere, New York, pp. 1–32.

[189] Smoot, L Douglas and Smith, Philip J, 2013, *Coal Combustion and Gasification*, Springer Science & Business Media, New York.

[190] Buckius, R. O. and Hwang, D. C., 1980, "Radiation Properties for Polydispersions: Application to Coal", *ASME Journal of Heat Transfer*, **102**, pp. 99–103.

[191] Foster, P. J. and Howarth, C. R., 1968, "Optical Constants of Carbons and Coals in the Infrared", *Carbon*, **6**, pp. 719–729.

[192] Viskanta, R., Ugnan, A., and Mengüç, M. P., 1981, "Predictions of Radiative Properties of Pulverized Coal and Fly-Ash Polydispersions", ASME paper no. 81-HT-24.

[193] Dombrovsky, L. A. and Baillis, D., 2010, *Thermal Radiation in Disperse Systems: An Engineering Approach*, Begell House, New York.

[194] Dunkel, R. V., 1965, "Emissivity and Inter-Reflection Relationships for Infinite Parallel Specular Surfaces", In Katzoff, S., ed., *Symposium on Thermal Radiation of Solids NASA SP55*, pp. 39 – 44.

[195] Dombrovsky, L. A., 2002, "Spectral Model of Absorption and Scattering of Thermal Radiation by Diesel Fuel Droplets", *High Temperature*, **40**(2), pp. 242–248.

[196] Dombrovsky, L. A., Sazhin, S. S., Mikhalovsky, S. V., Wood, R., and Heikal, M. R., 2003, "Spectral Properties of Diesel Fuel Droplets", *Fuel*, **82**(1), pp. 15–22.

[197] Faeth, G. M., 1996, "Spray Combustion Phenomena", *Proceedings of the Combustion Institute*, **26**(1), pp. 1593–1612.

[198] Bermúdez, A., Ferrín, J. L., Linan, A., and Saavedra, L., 2011, "Numerical Simulation of Group Combustion of Pulverized Coal", *Combustion and Flame*, **158**(9), pp. 1852–1865.

[199] Libby, P. A. and Williams, F. A., 1994, *Turbulent Reacting Flows*, Academic Press, San Diego.

[200] Fox, R. O., 2003, *Computational Models for Turbulent Reacting Flows*, Cambridge University Press, Cambridge.

[201] Smith, G. P., Golden, D. M., Frenklach, M., Moriarty, N. W., Eiteneer, B., Goldenberg, M., Bowman, C. T., Hanson, R., Song, S., Gardiner, W. C., Lissianski, V., and Qin, Z., 1999, "GRI-Mech 3.0", Available at http://www.me.berkeley.edu/gri_mech.

[202] Mehl, M., Pitz, W. J., Westbrook, C. K., and Curran, H. J., 2011, "Kinetic Modeling of Gasoline Surrogate Components and Mixtures under Engine Conditions", *Proceedings of the Combustion Institute*, **33**(1), pp. 193–200.

[203] Magnussen, B. F. and Hjertager, B. H., 1977, "On Mathematical Modeling of Turbulent Combustion with Special Emphasis on Soot Formation and Combustion", In *Sixteenth Symposium (International) on Combustion*, Elsevier, pp. 719–729.

[204] Peters, N., 1988, "Laminar Flamelet Concepts in Turbulent Combustion", In *Twenty-First Symposium (International) on Combustion*, **21**, Elsevier, pp. 1231–1250.

[205] Karlsson, A., 1995, *Modeling Auto-Ignition, Flame Propagation and Combustion in Non-Stationary Turbulent Sprays*, PhD thesis, Chalmers University of Technology.

[206] Magnussen, B. F., 2005, "The Eddy Dissipation Concept: A Bridge between Science and Technology", In *ECCOMAS Thematic Conference on Computational Combustion, Lisbon, Portugal*.

[207] Haworth, D. C., 2010, "Progress in Probability Density Function Methods for Turbulent Reacting Flows", *Progress in Energy and Combustion Science*, **36**, pp. 168–259.

[208] Poinsot, T. and Veynante, D., 2005, *Theoretical and Numerical Combustion*, R. T. Edwards, Inc., 2nd ed.

[209] Versteeg, H. K. and Malalasekera, W., *Flames: Their Structure, Radiation and Temperature*, 2nd ed.

[210] MacRobert, T. M., 1967, *Spherical Harmonics*, Pergamon Press, New York, 3rd ed.

[211] Boas, M. L., 1966, *Mathematical Methods in the Physical Sciences*, Wiley, New York.

[212] Arfken, G. B. and Weber, H. J., 2001, *Mathematical method for physicists*, Harcourt/Academic Press, London, 5th ed.

[213] Pellaud, B., 1966, "Numerical Comparison of Different Types of Vacuum Boundary Conditions for the P_N Approximation", *Trans. Am. Nucl. Soc.*, **9**, pp. 434–435.

[214] McClarren, R. G., 2007, *Spherical Harmonics Methods for Thermal Radiation Transport*, PhD thesis, University of Michigan.

[215] Euler, Leonhard, 1775, "Formulae Generales Pro Translatione Quacunque Corporum Rigidorum", *Novi Acad. Sci. Petrop*, **20**, pp. 189–207.

[216] Varshalovich, D. A., Moskalev, A. N., and Khersonskii, V. K., 1981, *Quantum Theory of Angular Momentum*, World Scientific, Singapore.

[217] Blanco, M. A., Flórez, M., and Bermejo, M., 1997, "Evaluation of the Rotation Matrices in the Basis of Real Spherical Harmonics", *Journal of Molecular Structure (Theochem)*, **49**, pp. 19–27.

[218] *FlexPDE software*, PDE Solutions Inc., Antioch.

[219] Marquez, R. and Modest, M. F., 2013, "Two-Dimensional Axisymmetric Formulation of Higher Order P_N-Approximations", Kharagpur, India, 22nd National and 11th International ISHMT–ASME Heat and Mass Transfer Conference 2013.

[220] Modest, M. F., 1976, "Photon-Gas Formulation of the Differential Approximation in Radiative Transfer", *Letters in Heat and Mass Transfer*, **3**, pp. 111–116.

[221] Patankar, S. V., 1980, *Numerical Heat Transfer and Fluid Flow*, Hemisphere Publishing Corporation, New York, 1st ed.

[222] Anderson, D. A., Tannehill, J. C., and Pletcher, R. H., 2011, *Computational Fluid Mechanics and Heat Transfer*, CRC Press, Florida, 3rd ed.

[223] Ferziger, J. H. and Peric, M., 2012, *Computational Methods for Fluid Dynamics*, Springer, Berlin, 3rd ed.

[224] Mazumder, S., 2015, *Numerical Methods for Partial Differential Equations: Finite Difference and Finite Volume Methods*, Academic Press.

[225] Patankar, S. V. and Spalding, D. B., 1972, "A Calculation Procedure for Heat, Mass and Momentum Transfer in Three-Dimensional Parabolic Flows", *International Journal of Heat and Mass Transfer*, **15**(10), pp. 1787–1806.

[226] Van Doormall, J. P. and Raithby, G. D., 1985, "An Evaluation of the Segregated Approach for Predicting Incompressible Fluid Flows", In *National Heat Transfer Conference*, Denver, Colorado.

[227] Weller, H. G., Tabor, G., Jasak, H., and Fureby, C., 1998, "A Tensorial Approach to Computational Continuum Mechanics Using Object-Oriented Techniques", *Computers in Physics*, **12**(6), pp. 620–631.

[228] Eaton, J. W., Bateman, D., and Hauberg, S., 2016, *GNU Octave Version 3.0.1 Manual: A High-Level Interactive Language for Numerical Computations*, CreateSpace Independent Publishing Platform, ISBN 1441413006.

[229] Press, W. H., Teukolsky, S. A., Vetterling, W. T., and Flannery, B. P., 2007, *Numerical Recipes – The Art of Scientific Computing*, Cambridge University Press, Cambridge, 3rd ed.

[230] Jacob, D. A. H., 1980, *Preconditioned Conjugate Gradient Methods for Solving Systems of Algebraic Equations*, Central Electricity Research Laboratories.

[231] Jasak, H., 1996, *Error Analysis and Estimation for the Finite Volume Method with Applications to Fluid Flows*, PhD thesis, Imperial College of Science, Technology and Medicine.

[232] Chen, K, 2005, *Matrix Preconditioning Techniques and Applications*, Cambridge University Press.

[233] Hackbusch, W., 2012, *Iterative Solution of Large Sparse Systems of Equations*, Springer Science & Business Media.

[234] Salari, K. and Knupp, P., 2000, "Code Verification by the Method of Manufactured Solutions", Technical report, Sandia National Labs., Albuquerque, NM (US); Sandia National Labs., Livermore, CA (US).

[235] Roache, P. J., 2002, "Code Verification by the Method of Manufactured Solutions", *Journal of Fluids Engineering*, **124**(1), pp. 4–10.

[236] Wolfram Research, Inc., 2016, *Mathematica, Version 11.0*, Wolfram Research, Inc., Champaign, Illinois.

[237] Wang, A., 2007, *Investigation of Turbulence–Radiation Interactions in Turbulent Flames Using a Hybrid FVM/Particle-Photon Monte Carlo Approach*, PhD thesis, The Pennsylvania State University, University Park, PA.

[238] Zhang, H. and Modest, M. F., 2003, "Full-Spectrum k-Distribution Correlations for Carbon Dioxide Mixtures", *Journal of Thermophysics and Heat Transfer*, **17**(2), pp. 259–263.

[239] Modest, M. F. and Mehta, R. S., 2004, "Full spectrum k-distribution correlations for CO_2 from the CDSD-1000 spectroscopic databank", *International Journal of Heat and Mass Transfer*, **47**, pp. 2487–2491.

[240] Modest, M. F. and Singh, V., 2005, "Engineering Correlations for Full Spectrum k-Distribution of H_2O from the HITEMP Spectroscopic Databank", *Journal of Quantitative Spectroscopy and Radiative Transfer*, **93**, pp. 263–271.

[241] Gelbard, E. M., 1961, "Simplified Spherical Harmonics Equations and Their Use in Shielding Problems", Technical Report WAPD-T-1182, Bettis Atomic Power Laboratory.

[242] Modest, M. F., Cai, J., Ge, W., and Lee, E., 2014, "Elliptic Formulation of the Simplified Spherical Harmonics Method in Radiative Heat Transfer", *International Journal of Heat and Mass Transfer*, in print.

[243] Barlow, R. S. and Frank, J. H., 1998, "Effects of Turbulence on Species Mass Fractions in Methane/Air Jet Flames", In *Twenty-seventh Symposium (International) on Combustion*, **27**, The Combustion Institute, pp. 1087–1095.

[244] Barlow, R. S., "International Workshop on Measurement and Computation of Turbulent Non-premixed Flames (TNF)", website: http://www.sandia.gov/TNF/abstract.html.

[245] Pal, G., 2010, *Spectral Modeling of Radiation in Combustion Systems*, PhD thesis, The Pennsylvania State University, University Park, PA.

[246] Bowman, C. T., Hanson, R. K., Gardiner, W. C., Lissianski, V., Smith, G. P., Golden, D. M., Frenklach, M., Eiteneer, B., and Goldenberg, M., 1995, "GRI-Mech 2.21", Available at http://www.me.berkeley.edu/gri_mech.

[247] Cai, J., Roy, S., and Modest, M. F., 2016, "A Comparison of Specularly Reflective Boundary Conditions and Rotationally Invariant Formulations for Discrete Ordinate Methods in Axisymmetric Geometries", *Journal of Quantitative Spectroscopy and Radiative Transfer*, **182**, pp. 75–86.

[248] Lallemant, N., Breussin, F., Weber, R., Ekman, T., Dugue, J., Samaniego, J.M., Charon, O., Van Den Hoogen, A. J., Van Der Bemt, J., and Fujisaki, W., 2000, "Flame Structure, Heat Transfer and Pollutant Emissions Characteristics of Oxy-Natural Gas Flames in the 0.7-1 MW Thermal Input Range", *Journal of the Institute of Energy*, **73**(469), pp. 169–182.

[249] Lallemant, N., Dugue, J., and Weber, R., 2003, "Measurement Techniques for Studying Oxy-Natural Gas Flames", *Journal of the Institute of Energy*, **76**(507), pp. 38–53.

[250] Breussin, F., Lallemant, N., and Weber, R., 2000, "Computing of Oxy-Natural Gas Flames Using Both a Global Combustion Scheme and a Chemical Equilibrium Procedure", *Combustion Science and Technology*, **160**(1), pp. 369–397.

[251] Brink, A., Hupa, M., Breussin, F., Lallemant, N., and Weber, R., 2000, "Modeling of Oxy-Natural Gas Combustion Chemistry", *Journal of Propulsion and Power*, **16**(4), pp. 609–614.

[252] Kim, G. and Kim, Y., 2005, "Non-Adiabatic Flamelet Modeling for Combustion Processes of Oxy-Natural Gas Flame", *Journal of Mechanical Science and Technology*, **19**(9), pp. 1781–1789.

[253] Yin, C., Rosendahl, L. A, and Kær, S. K., 2011, "Chemistry and Radiation in Oxy-Fuel Combustion: A Computational Fluid Dynamics Modeling Study", *Fuel*, **90**(7), pp. 2519–2529.

[254] Zhao, X. Y., Haworth, D. C., Ren, T., and Modest, M. F., 2013, "A Transported Probability Density Function/Photon Monte Carlo Method for High-Temperature Oxy–Natural Gas Combustion with Spectral Gas and Wall Radiation", *Combustion Theory and Modelling*, **17**(2), pp. 354–381.

[255] Chu, Eleanor, 2008, *Discrete and Continuous Fourier Transforms: Analysis, Applications and Fast Algorithms*, CRC Press, Boca Raton, Florida.